UNIVERSIDAD COMPLUTENSE DE MADRID

FACULTAD DE CIENCIAS FÍSICAS

TESIS DOCTORAL

Metamateriales sublongitud de onda para gestión modal y de potencia en circuitos integrados

———————

Subwavelength metamaterials for integrated power and modal management

MEMORIA PARA OPTAR AL GRADO DE DOCTORA

PRESENTADA POR

Raquel Fernández de Cabo

DIRIGIDA POR

Aitor Villafranca Velasco
David González Andrade

UNIVERSIDAD COMPLUTENSE DE MADRID

FACULTAD DE CIENCIAS FÍSICAS

TESIS DOCTORAL

Metamateriales sublongitud de onda para gestión modal y de potencia en circuitos integrados

Subwavelength metamaterials for integrated power and modal management

MEMORIA PARA OPTAR AL GRADO DE DOCTORA

PRESENTADA POR

Raquel Fernández de Cabo

DIRECTORES

Aitor Villafranca Velasco

David González Andrade

"Simply because we were licked a hundred years before we started is no reason for us not to try to win."

- Harper Lee

ACKNOWLEDGEMENTS

I am truly grateful to Dr. Aitor Villafranca Velasco for the opportunity to begin my research career within his esteemed research group four years ago. Collaborating with him has not only helped me grow as a researcher but also enriched me as an individual, thanks to his unwavering dedication to social causes. Aitor, I am deeply thankful for your sincere trust in my capabilities, for giving me the opportunity to explore my ideas, and, most importantly, for guiding me through the challenges encountered along this journey. I would like to express my sincerest gratitude to Dr. David González Andrade for his inestimable support, meticulous attention to detail, and invaluable guidance. David, your profound professionalism and admirable character have been a constant source of inspiration. Thank you for your constant presence and the countless meaningful experiences we have shared throughout the years.

I sincerely appreciate the warm welcome extended to me by Dr. Juan Diego Ania Castañón at the Instituto de Óptica. I am grateful for his support and dedication to ensuring progress and improvement in all endeavors. I would also like to express my gratitude to my colleagues from Torres Quevedo: Pedro Corredera, José Luis de Miguel, Conchi Pulido, Belén García, Joaquín Campos, Alejandro Rosado, Alejandro Ferrero, Pablo Santafé, and Hugo Fidalgo. The moments we shared during the coffee breaks have been invaluable throughout my journey. Jaime and Inés, I sincerely appreciate your support and understanding throughout the challenges of the PhD journey. Your friendship and encouragement have been invaluable, and I am grateful for your presence every step of the way. Furthermore, I would like to recognize my colleagues at IOPTICA for instilling in me the importance of outreach and making science accessible to diverse audiences.

To Dr. Pavel Cheben, I extend my sincere gratitude for his invaluable teachings and insightful discussions on the papers. His expertise and guidance have significantly enhanced my knowledge and understanding of this research field.

I have also had the opportunity to work at the Centre de Nanosciences et de Nanotechnologies (C2N) for three months. I would like to express my sincere thanks to Dr. Carlos Alonso Ramos and Dr. Daniele Melati for this unique opportunity. It has been an honor to work with the entire MINAPHOT team, and during my time there, it felt like my second home. I want to specially thank Prof. Delphine Marris-Morini, Prof. Eric Cassan, Dr. Laurent Vivien, Paula Nuño, Zindine Mokeddem, Yijun Yang, Nhi

Nguyen, and David Medina. I also want to thank Alejandro Sánchez, who shared the experience at the C2N with me.

I would also like to extend my gratitude to Dr. Vladimir and Dr. Lina Stankovic, as well as their entire group at Strathclyde University, for their support during my time in Glasgow.

During this period, I had the pleasure of collaborating with numerous talented individuals whose contributions were invaluable to me. I am grateful to Prof. Alejandro Ortega Moñux, Dr. Robert Halir, and Dr. José Manuel Luque González for welcoming me into their group at Málaga University.

On the financial side, I would like to acknowledge the support from the Spanish Ministry of Science, Innovation and Universities (formerly Ministry of Science and Innovation) through grants PID2020-115353RA-I00, the Spanish State Research Agency and the European Social Fund Plus under grant PRE2021-096954, the Community of Madrid—FEDER funds (S2018/NMT-4326), the European Union's Horizon Europe program through the Marie Sklodowska-Curie grant agreement No. 734331 and No. 101062518 and HADEA grant agreement No. 101135523.

These closing lines are dedicated to those dearests to me: my family and loved ones. I am profoundly grateful for each of you, and mere words cannot adequately convey my appreciation. Your love and support have been invaluable throughout this journey. To my parents, Eliseo and Bini, and my sister Sara, I am deeply thankful for your sacrifices and encouragement, without which I would not have been able to complete this thesis. I deeply appreciate all your advices and sacrifices, without which I would not have been able to accomplish this thesis. To Alba and Miguel, who have become like a second family to me, I extend my heartfelt gratitude for your constant support. Thank you for being there whenever I needed someone to lean on. Your presence in my life has been a source of strength and comfort, and I am grateful for your friendship and support.

TABLE OF CONTENTS

LIST OF FIGURES

LIST OF ACRONYMS

BOX: Buried-oxide 3

CMOS: Complementary metal-oxide-semiconductor.....4

DC: Duty cycle..... 16

DUV: Deep ultraviolet.....8

E-beam: Electron beam 8

EL: Excess loss..... 10

ER: Extinction ratio 10

FDTD: Finite-difference time-domain 9

FOM: Figure of merit..... 49

GC: Grating coupler 19

LIDAR: Light detection and ranging 5

MDM: Mode division multiplexing 6

MFS: Minimum feature size 7

MMI: Multimode interference.....3

MZI: Mach-Zhender interferometer..... 25

PDM: Polarization division multiplexing 86

PIC: Photonic integrated circuit 2

PM: Polarization maintaining 59

SEM: Scanning-electron microscope.....3

SOI: Silicon-on-insulator.....4

SWG: Subwavelength grating 7

TE: Transverse-electric.....3

TM: Transverse-magnetic 3

WDM: Wavelength division multiplexing.....6

WG: Waveguide 3

ABSTRACT

Introduction and objectives

Integrated photonics, born from the success of optical communications and driven by the limitations of electronic interconnects, emerged as a groundbreaking technology in the 1970s. This pioneering innovation opened the possibility of manipulating and controlling light signals on a miniature scale, leading to the development of compact and highly efficient optical systems. Photonic integrated circuits (PICs) enable high-speed data transmission and broad bandwidth capacity systems in a miniaturized semiconductor chip. Silicon photonics, distinguished by its compatibility with complementary metal-oxide-semiconductor (CMOS) fabrication processes and monolithic integration, has become the dominant platform for PICs. Its applications extend to diverse fields such as neuromorphic photonics, 5G-6G communications, quantum photonics, the Internet of Things, light detection and ranging, spectrometry, and sensing. Despite the promising potential of silicon photonics technology, challenges such as birefringence and fabrication limitations persist, impeding the development of fundamental integrated building blocks. To address these challenges, ongoing research is required to enhance the performance of photonic components, thereby unlocking new applications, and enabling next-generation PICs.

The primary aim of this thesis is to design, optimize, and experimentally characterize novel components for integrated silicon photonics, with a special focus on minimizing losses, ensuring broad operational bandwidths, facilitating multimode operation, and maintaining robust fabrication tolerances. Broadband operation, a critical requirement for most applications, poses a significant challenge due to chromatic dispersion in the silicon-on-insulator (SOI) platform. To tackle this challenge, subwavelength grating metamaterials through periodic nanostructuration has been deeply investigated in this thesis. Specifically, the thesis endeavors to develop high-performance power and modal management building blocks to drive forward next-generation silicon photonics applications.

Results of the research

During the development of the present thesis, significant advances have been reported in the fields of power and modal management. In terms of power management, the primary goal of the present thesis is to achieve efficient power splitting with ultra-broadband multimode operation and low excess losses, essential for applications in data communication networks, sensing systems, and quantum information processing. On the other hand, the objective for modal management is to optimize the conversion between optical modes to mitigate signal degradation, which is particularly relevant in

high-speed communication systems, nonlinear photonics, and quantum computing. The following devices have been developed with these targets in mind:

- A novel Y-junction architecture based on full subwavelength grating metamaterial waveguides. This first proposed power splitter has been developed for two different lithographic resolutions of 50 nm and 100 nm. The device exhibits a high-performance and large fabrication tolerances. Full three-dimensional finite-difference time-domain (3D FDTD) simulations show a fundamental mode excess loss (EL) below 0.1 dB in an ultra-broad bandwidth of 300 nm (1400 — 1700 nm) when optimized for a fabrication resolution of 50 nm, and under 0.3 dB in a 350 nm extended bandwidth (1350 — 1700 nm) for a 100 nm resolution. Exhaustive measurements over a 260 nm bandwidth (1420 — 1680 nm) show fundamental transverse-electric mode (TE_0) excess loss under 0.3 dB considering a high-resolution lithographic process (i.e., 50 nm) and below 0.5 dB for a standard-resolution scenario (i.e., 100 nm). Subwavelength Y–junctions with artificially induced errors of ±10 nm further demonstrate the robustness to fabrication deviations of this design. The proposed splitter also exhibits first-order transverse-electric mode (TE_1) excess loss lower than 1.5 dB within a 170 nm bandwidth (1420 — 1590 nm) in both 50 nm and 100 nm resolution scenarios, hence enabling multimode power splitting configurations.
- The second device developed in this thesis is an achromatic splitter based on a Y-junction assisted by SWG metamaterials. The proposed SWG-assisted device yields the broadest bandwidth reported to date for a nanophotonic silicon power splitter. Operation over an outstanding 700 nm bandwidth was obtained through 3D FDTD simulations, covering an extensive wavelength range from 1300 nm to 2000 nm. The device design was optimized for both TE_0 and the TE_1 modes, and it also exhibits a remarkable performance for the fundamental transverse-magnetic (TM_0) mode. Specifically, 3D FDTD simulations predict minimal excess loss (< 0.2 dB) for both TE_0 and TE_1 modes over a 700 nm bandwidth (1300 — 2000 nm), and less than 0.3 dB for the TM_0 mode within the 1300 — 1800 nm wavelength range. Experimental measurements validate simulation results, confirming low excess losses for the three modes in the 1430 — 1680 nm wavelength range along with robust fabrication tolerances for etching errors up to ±10 nm.
- The third device developed in this thesis is an innovative mode converter architecture based on two mirrored symmetric Y-junctions connected through SWG metamaterials. The geometrical parameters of the device are further refined through an inverse design optimization algorithm, maximizing the modal field conversion between the fundamental and second-order transverse-electric (TE_2) modes. The device, optimized through 3D FDTD, shows EL below 0.75 dB and extinction ratio (ER) exceeding 10 dB over a broad bandwidth of 350 nm (1350 nm to 1700 nm). Furthermore, within a 150 nm wavelength range (1472–1622 nm), the ER exceeds 20 dB while EL remains below 0.3 dB. Experimental validation confirms efficient mode

conversion, with EL as low as 0.4 dB and ER exceeding 18 dB over a broadband of 149 nm, extending from 1471 nm to 1620 nm. To the best of our knowledge, the proposed mode converter exhibits the broadest bandwidth experimentally ever reported experimentally for TE_0 – TE_2 exchange.

Conclusions

The devices and results reported in this thesis represent a major breakthrough in the field of integrated photonics, introducing pioneering building blocks enabled through subwavelength metamaterials. These achievements not only indicate progress toward a new frontier of high-performance on-chip applications but also hold potential for significant enhancements across various domains: from enhancing high-capacity communication networks to applications in nonlinear photonics, quantum computing, LIDAR, and sensing.

RESUMEN

Introducción y objetivos

La fotónica integrada, nacida a raíz del éxito de las comunicaciones ópticas e impulsada por las limitaciones de las interconexiones electrónicas, emergió como una tecnología revolucionaria en la década de 1970. Esta tecnología innovadora abrió la posibilidad de manipular y controlar señales de luz en una escala en miniatura, permitiendo el desarrollo de sistemas ópticos compactos y muy eficientes. Los circuitos fotónicos integrados (PIC) permiten la transmisión de datos a alta velocidad y los sistemas de gran ancho de banda en un chip semiconductor miniaturizado. distinguida por su compatibilidad con los procesos de fabricación de óxido de metal complementario (CMOS) y la integración monolítica, se ha consolidado como la plataforma dominante para los PICs. Sus aplicaciones se extienden a diversos campos, como la fotónica neuromórfica, las comunicaciones 5G-6G, fotónica cuántica, el internet de las cosas, la detección y el alcance de la luz (LIDAR), la espectrometría, y sensores. A pesar del prometedor potencial de la tecnología fotónica de silicio, todavía persisten desafíos como la birrefringencia y las limitaciones de fabricación, que impiden el desarrollo de los componentes integrados fundamentales. Para hacer frente a estos retos, es necesario proseguir la investigación con el fin de incrementar el rendimiento de los componentes fotónicos, desbloqueando así nuevas aplicaciones y haciendo posible la próxima generación de PICs.

El objetivo principal de esta tesis es diseñar, optimizar y caracterizar experimentalmente componentes innovadores para la fotónica de silicio integrada, con especial enfoque en minimizar las pérdidas, garantizar anchos de banda operativos amplios, facilitar el funcionamiento multimodo y mantener tolerancias de fabricación robustas. Un requisito fundamental de los dispositivos fotónicos integrados es el funcionamiento de banda ancha, lo que supone un reto importante debido a la dispersión cromática asociada a la plataforma de silicio sobre aislante (SOI). Para abordar este reto, en esta tesis se han investigado en profundidad los metamateriales de rejilla de sublongitud de onda basados en la nanoestructuración periódica. En concreto, el objetivo de esta tesis es el desarrollo de componentes de gestión modal y de potencia de alto rendimiento que permitan el desarrollo de aplicaciones fotónicas integradas de la siguiente generación.

Resultados de la investigación

Durante el desarrollo de la presente tesis se han conseguido importantes logros en las tareas de gestión de potencia y gestión modal. En cuanto a la gestión de la potencia, el objetivo principal de esta tesis pretende conseguir una división eficiente de la potencia con un funcionamiento multimodo de banda ultra-ancha con un bajo exceso de pérdidas, esencial para aplicaciones en redes de comunicación de datos, sistemas de detección y procesamiento cuántico de la información. Por otro lado, el objetivo de la gestión modal es optimizar la conversión entre distintos modos ópticos para mitigar la degradación de la señal, lo que resulta especialmente relevante en sistemas de comunicación de alta velocidad, fotónica no lineal y computación cuántica. Con estos objetivos en mente se han desarrollado los siguientes dispositivos:

- Una novedosa arquitectura de unión en Y construida a partir de guías de onda totalmente basadas en metamateriales sublongitud de onda. Esta primera propuesta de divisor de potencia se ha desarrollado considerando dos resoluciones litográficas diferentes: 50 nm y 100 nm. El dispositivo demuestra un alto rendimiento con grandes tolerancias de fabricación en un ancho de banda ultra-ancho. Las simulaciones tridimensionales utilizando el método de diferencias finitas en el dominio del tiempo (3D FDTD) muestran una pérdida de exceso (EL) para el modo fundamental inferior a 0.1 dB en un ancho de banda de 300 nm (1400 — 1700 nm) cuando se optimiza para una resolución de fabricación de 50 nm, e inferior a 0.3 dB en un ancho de banda extendido a 350 nm (1350 — 1700 nm) para una resolución de 100 nm. Tras realizar una serie de medidas exhaustivas en un ancho de banda de 260 nm (1420 — 1680 nm), se observa una pérdida de exceso inferior a 0.3 dB para el modo transversal eléctrico fundamental considerando un proceso litográfico de alta resolución (es decir, 50 nm) e inferior a 0.5 dB en un escenario de resolución estándar (es decir, 100 nm). Las medidas de uniones en Y sublongitud de onda con errores inducidos artificialmente de ±10 nm demuestran además la fiabilidad de este diseño frente a desviaciones durante la fabricación. El divisor propuesto también presenta una EL para el modo transversal-eléctrico de primer orden (TE_1) inferior a 1.5 dB en un ancho de banda de 170 nm (1420 — 1590 nm), tanto en escenarios de resolución de 50 nm como de 100 nm, permitiendo así el funcionamiento multimodo del divisor de potencia.
- El segundo dispositivo que se ha desarrollado en esta tesis es un divisor de potencia acromático basado en una estructura de unión en Y asistida por metamateriales SWG. Este dispositivo asistido por SWG proporciona el mayor ancho de banda registrado hasta la fecha para un divisor de potencia nanofotónico de silicio. Las simulaciones 3D FDTD han demostrado que el dispositivo funciona en un ancho de banda de 700 nm, cubriendo el extenso rango de longitudes de onda de 1300 nm a 2000 nm. El diseño del dispositivo se optimizó para los modos TE_0 y TE_1, presentando a su vez un rendimiento destacable para el modo transversal-magnético fundamental (TM_0). Específicamente, las simulaciones 3D FDTD estiman pérdidas mínimas (< 0.2 dB) para los modos TE_0 y TE_1 en un ancho de banda de

700 nm (1300 — 2000 nm), y menos de 0.3 dB para el modo TM_0 en el rango de longitudes de onda de 1300 — 1800 nm. Las medidas experimentales validan los resultados de simulación, confirmando pérdidas de exceso mínimas para los tres modos en la banda de longitud de onda de 1430 — 1680 nm, así como tolerancias de fabricación robustas para errores de grabado de hasta ±10 nm.

- El tercer dispositivo desarrollado en esta tesis es una novedosa arquitectura de conversión modal basada en dos uniones en Y simétricas enfrentadas y conectadas a través de metamateriales SWG. Los parámetros geométricos del dispositivo han sido ajustados mediante un algoritmo de optimización de diseño inverso, maximizando la conversión de campo modal entre los modos fundamental y transversal-eléctrico de segundo orden (TE_2). El dispositivo, optimizado mediante simulaciones 3D FDTD, ofrece una EL inferior a 0.75 dB y una ratio de extinción (ER) superior a 10 dB en un amplio ancho de banda de 350 nm (1350 nm a 1700 nm). La validación experimental confirma la eficiente conversión de modo, con una EL menor a 0.4 dB y una ER por encima de 18 dB en un ancho de banda de 149 nm, que se extiende desde 1471 nm hasta 1620 nm.

Conclusiones

Los resultados obtenidos en esta tesis representan un avance importante en el campo de la fotónica integrada, al proponer bloques de construcción pioneros gracias a los metamateriales sublongitud de onda. Estos avances no sólo suponen el avance hacia una nueva era de aplicaciones de alto rendimiento en chip, sino que estos avances prometen mejoras significativas para diversos campos: desde la mejora de las redes de comunicación de alta capacidad hasta su aplicación en la fotónica no lineal, la computación cuántica, LIDAR y sistemas de sensado.

Chapter I:

SILICON PHOTONICS OVERVIEW

The present thesis covers the design, optimization and experimental demonstration of novel high-performance photonic integrated building blocks based on subwavelength metamaterials. These developments have been the result of national and international collaborations between the Spanish National Research Council (CSIC) - Institute of Optics "Daza de Valdés" (IO) and other renowned institutions such as the Centre for Nanoscience and Nanotechnology (C2N), the National Research Council of Canada (NRC), the University of Málaga (UMA), and the University of Strathclyde. In this introductory chapter, the main insights of the thesis are presented and contextualized by discussing their applicability and relevance for current state-of-the-art technology.

Section 1.1 provides a historical background on integrated photonics. In Section 1.2, the scientific and industrial impact of silicon photonics is addressed, revealing its pivotal role as an enabling technology for telecom, datacom, and next-generation applications. Section 1.3 introduces the main outcomes of this thesis, while Section 1.4 outlines the organizational structure of the document.

1.1. The rise of integrated photonics

1.1.1. Microelectronics: evolution and frontiers

Prior to the 1950s, the landscape of electronic components consisted of independent entities that, in response to a potential difference, generated a flow of electric current. A revolutionary era in the electronics industry began with the inception of the transistor in 1948. This breakthrough paved the way for further advances in the field, most notably after the development of integrated circuits. With millions of transistors on a single chip, integrated circuits drove the industry forward enabling the advent of the microprocessor and the realization of modern information technology [1].

The evolution of classic microprocessors, driven by the ever-increasing transistor density following Moore's Law [2], encountered a turning point in 2003 with the emergence of the 3 GHz clock speed limit [3]. Despite efforts to diminish transistor size, some issues arose: processor overheating and reduced efficiency of transistors with sizes of less than 10 nm. At this scale, insulator regions reduce to just a few hundred atoms and hence electrons exhibit susceptibility to quantum tunnelling into these insulators [4]. While multi-core processing provided a remedy, the need for efficient system interconnects for parallel processing became crucial [5]. Subsequently, another challenge manifested in the form of an electronic interconnect bottleneck, emphasizing the urgent need for high-speed data transmission. Conventional electronic interconnections, relying on copper/dielectric assemblies, pose challenges concerning power dissipation and signal integrity when elevated data rates are demanded. This bottleneck made the conventional practice of data transmission from a computer chip to either memory or another computer chip via copper wires unsustainable regardless of proximity.

In face of the increasing complexity of circuits and demands for higher data rates in a myriad of applications, industry has been searching for solutions. Integrated photonics emerged as a promising alternative inspired by the success of optical communications based on optical fibers. The concept of photonic integrated circuits (PIC) was first introduced by Stewart E. Miller in 1969 [6], thereby establishing the roots of integrated optics. Miller acknowledged the potential of dielectric waveguides for guiding light beams and building circuits embedded in a single substrate. This pioneering innovation opened the possibility of manipulating and controlling light signals on a miniature scale, leading to the development of compact and highly efficient optical systems. Integrated photonics benefits from the inherent advantages of optical fibers, such as high-speed data transmission, broad bandwidth capacity, and further extends these advantages to the scale of a miniaturized semiconductor chip. PICs enable the encoding of data onto optical waves, particularly useful for high-speed data communication and interconnected applications. Optical signals are not affected by electromagnetic interference, whereas electrical signals in electronic circuits are vulnerable to it. Hence, optical communication systems offer high-speed and efficient data transfer over long distances with minimal signal degradation, enabling the transmission of large volumes of data [7], [8]. Nowadays, optical interconnection within data centers covers distances ranging from intra-chip connections up to 10 km, effectively overcoming the limitations of electronic interconnection [9], [10].

1.1.2. Integrated photonics: from fundamentals to applications

Integrated optics relies on waveguides (WGs) as foundational components, guiding light beams within a semiconductor or dielectric material. Optical WGs operate on the principle of total internal reflection, where light transitions from a higher refractive index medium to a lower refractive index (Δn) at an angle beyond the critical angle. Figure I.1 displays a full PIC [11] in panel (a), followed by a scanning-electron microscope (SEM) image of a routing circuit in panel (b), and a fundamental wire WG constituent in panel (c). The WG core material has a higher refractive index (n_{core}), placed over a buried-oxide (BOX) layer and covered with the cladding material with lower refractive index (n_{clad}). A high refractive index contrast enhances light confinement inside the WG and, hence, allows for compact dimensions and large integration capability. These WGs support two different orthogonal set of solutions of Maxwell equations, i.e., quasi transverse-electric (TE) and quasi transverse-magnetic (TM) polarizations, characterized by the direction of the main component of the propagating electric field. The main electric field of quasi-TE modes is oriented parallel to the chip surface, while quasi-TM modes have most of the electric field in the component perpendicular to the chip surface. Therefore, optical modes are defined as the different field distributions allowed, usually referred to as TE and TM modes.

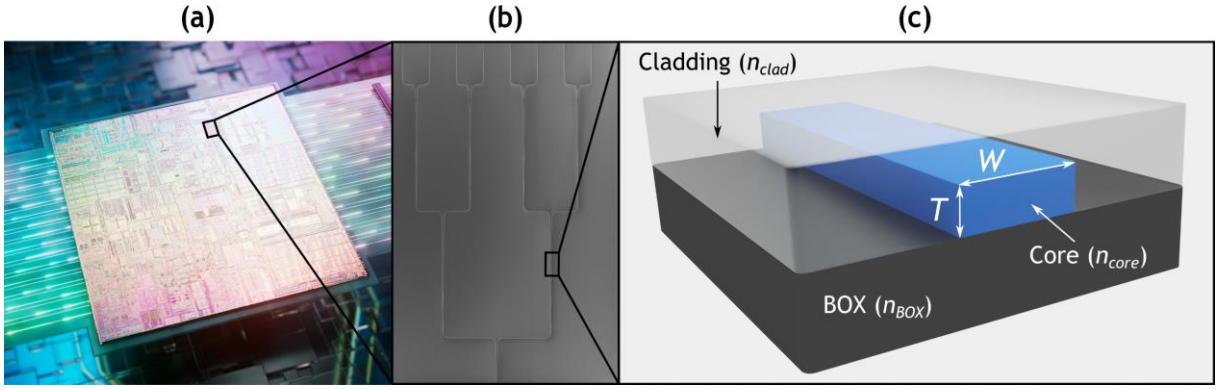

Figure I.1. (a) Complete PIC [11], (b) SEM image of a circuit part, (c) and basic wire WG.

PICs consist of several fundamental building blocks that can be active or passive. Passive devices operate without the need for an energy source and some examples are waveguides, directional couplers, multimode interference (MMI) couplers, Mach–Zehnder interferometers, Bragg gratings, ring resonators, to name a few. Active devices require external energy sources to operate, such as silicon-based lasers, silicon modulators, and detectors. By combining different building blocks, it becomes possible to perform complex on-chip optical functionalities, such as signal generation, modulation, amplification, routing, and detection [12]. Different materials have been adopted for the design and fabrication of PICs, each having its own particular advantages and limitations, to suit specific academic and technological purposes [13].

1.1.3. Materials and platforms for integrated photonics

One the most engaging material platforms for the development of integrated active components is the compound of two III-V semiconductors: indium phosphide (InP). InP-based PICs can integrate both active and passive components on a single chip. InP is particularly suitable for applications such as long-haul telecom, optical fiber networks, and high-speed optical communication systems. However, waveguides based on InP suffer from higher propagation losses than those based on group IV materials [14]. Other combinations of group III-V such as gallium arsenide (GaAs) or indium gallium arsenide (InGaAs) have been widely used in PICs, but their fabrication costs are elevated. Polymer-based WGs utilize organic materials, such as polymers and copolymers, offering integration with multiple optical components, e.g., lasers, detectors, modulators, and multiplexers [15]. Some polymer materials, particularly those with biocompatible properties or specific surface modifications, find application in bio-photonics for biomedical sensing or lab-on-a-chip devices [16]. Even with these advantages, organic polymers are limited by their low refractive index contrast, which hinders the realization of dense, compact integrated devices. A crystal with exceptional electro-optic properties is lithium niobate (LiNbO3), providing integrated optics platforms that have been used predominantly for the implementation of active components such as high-speed electro-optic modulators, switches, and frequency converters. LiNbO3 exhibits strong nonlinear properties, which expands its potential applications in nonlinear optics. Unfortunately, bulk LiNbO3 waveguides have large footprints, and the fabrication technology is not compatible with complementary metal-oxide-semiconductor (CMOS) technology [17], [18].

The alignment of silicon (Si) with the mature and well-established fabrication methods of CMOS technology reinforces its position as the preferred material for integrated photonics. Silicon PICs provide the advantage of monolithic integration with electronic components and compatibility with fiber optics applications. Silicon photonics encompasses different fabrication platforms such as silicon-on-insulator (SOI), silicon nitride (SiN), silica-on-silicon, germanium-on-silicon (GOS) or silicon oxynitride (Hydex), among others. Today, the reference Si photonics platform either in technological development or commercial adoption is the SOI platform. While Si has intrinsic limitations in light emission and detection as a consequence of its indirect bandgap, Si photonics platforms offer the prospect of integrating other materials. The combination of Si with other platforms to overcome their limitations is commonly referred to as hybrid or heterogeneous integration. This approach has the potential to yield large-scale hybrid devices, as demonstrated by the development of InP/Si lasers [19], [20].

The potential to miniaturize and integrate optical components on a chip has opened up a realm of possibilities for cutting-edge technologies, expanding the scope of PICs —particularly on silicon platforms— beyond its initial focus on datacom and telecom applications. In the domain of sensing technology, PICs play a notable role, particularly in biosensing and environmental monitoring, where they contribute to the creation of compact and highly sensitive sensors for detecting biological or chemical substances [21], [22]. In the field of medical imaging, PICs enable advanced techniques such as optical coherence tomography, providing high-resolution and non-invasive imaging capabilities for medical diagnostics [23]. Integrated photonics is also instrumental in for quantum computing, where

PICs are leveraged to generate, manipulate, and detect quantum states of light, thus advancing the development of quantum processors and communication systems [24], [25]. Beyond these applications, integrated photonics finds use in light detection and ranging (LIDAR) and laser radar systems for autonomous vehicles, environmental mapping, and surveillance [26], [27]. These diverse applications underscore the versatility of integrated photonics in addressing technological challenges across numerous industries.

1.2. Guiding the future: silicon photonics technology

As the electronics industry has evolved, billions of dollars and decades of research have been devoted to studying every facet of silicon semiconductor device processing and manufacturing, resulting in a highly mature, cost-effective, high-yield, and reliable process. Silicon, owing to its compatibility with well-established CMOS fabrication processes, stands out as the preferred material for the development of PICs [28], allowing for cost-effective and large-scale production [29], [30]. Moreover, silicon-based PICs allow the monolithic integration of photonic devices in close proximity to electronic components on a single chip [31], which is essential for two main reasons. First, it facilitates the simultaneous achievement of the required levels of performance, scalability, and complexity in electronic-photonic (optoelectronic) systems. Second, this approach significantly enhances system-level innovation by providing a common design environment to realize advanced optoelectronic systems. Specific applications could thus benefit by leveraging the strengths of each technology, electronics or photonics, to achieve optimal performance and functionality [32].

The inception of silicon photonics can be traced back to the seminal 1985 paper authored by Soref and Larenzo [33]. In subsequent years, advancements included the demonstration of low-loss waveguides in a thick silicon-on-insulator process in 1991–92, as well as the development of various optical integrated devices, modulators, and photodetectors [34]. SOI platform consists of a three-layer structure on a thick silicon substrate: a silicon layer that forms the waveguide core for light propagation, a silicon dioxide (SiO_2) BOX layer, and a top cladding layer (typically SiO_2) covering the waveguides. Two approaches to Si layer thickness are commonly used in SOI platforms: thin and thick. Thin SOI platforms feature a device layer thickness ranging from 220 nm to 300 nm, while thick SOI employs a waveguide core layer with a thickness on the order of a few microns. This thesis focuses on a standard SOI platform with 220-nm-thick Si layer. Both Si and SiO_2 exhibit transparency bands that initiate at wavelengths around $\lambda_{Si} \sim$ 1100 nm and $\lambda_{SiO2} \sim$ 200 nm, respectively, and extending up to $\lambda_{Si} \sim$ 8000 nm and $\lambda_{SiO2} \sim$ 3500 nm. Consequently, in this wavelength range Si photonics benefit from the extensive knowledge and infrastructure of the fiber optics industry, as these wavelength ranges cover the important telecom bands (i.e., O, C and L)[(*1)], up to short wavelengths of the mid-infrared bands. Moreover, the removal of SiO_2 surrounding the Si core to create suspended waveguides presents the opportunity to expand the low-loss SOI wavelength range up to around 8000 nm. This approach opens up possibilities for new applications, encompassing communication

networks, sensing, and nonlinear systems. The SOI platform has a large refractive index difference between the Si and the SiO_2: n_{Si} = 3.45 and n_{SiO2} = 1.46 at λ = 1550 nm. This high refractive index difference strongly confines the electromagnetic field into the Si layer, enabling high-density integration of photonic components integration with propagation losses as low as 1-2 dB/cm [35].

1.2.1. Evolution and challenges in silicon photonics

In the field of communication, which has been the essential market driver for PICs, silicon photonics has transformed from a challenger technology in the small-scale integration —with 1-to-10 components on a PIC— to a dominant technology in recent years for intra-, and inter-datacenter interconnects, and it is poised to become the reference technology in the next few years [34]. Silicon photonics-based transceivers for data communication have undergone remarkable progress, evolving from conceptualization to achieving a production scale of several million units annually. Figure I.1 provides a comprehensive overview of the technological evolution across five generations of data transceivers [36]. This progression aims for ever denser optical integration and foresees a future peak of innovation with the advent of 3D co-packaged optics with on-chip integrated lasers.

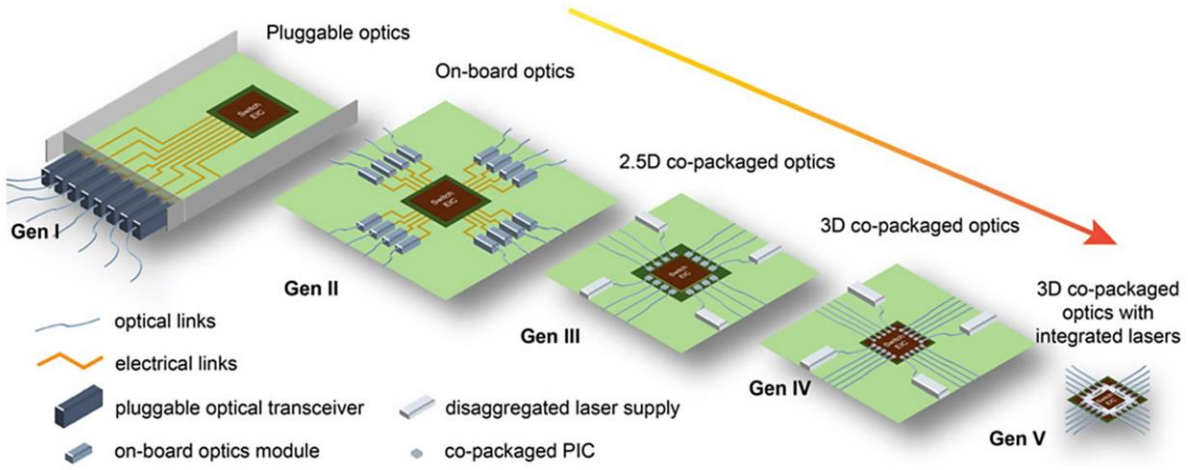

Figure I.2. The evolution of optics through different generations and the advancement of co-packaging technologies in data centre applications [36].

Over the past few years, wavelength division multiplexing (WDM) was the primary technology for silicon photonic optical transceivers, using different wavelength as data channels [37]. However, there has been a considerable development of mode division multiplexing (MDM) systems, which are capable of increasing data transmission capacity by simultaneously transmitting multiple signals through different optical modes within the same waveguide [38], [39]. Furthermore, recent research advances have demonstrated on-chip hybrid platforms that integrate MDM with WDM. This innovative combination of multiplexing technologies allows to increase the bandwidth density of on-chip optical interconnects without scaling the number of waveguides per chip [40]. Additionally, the exploration of multimode silicon photonics, particularly involving higher-order modes, is proving to be a valuable

*(*1)O band: 1260 — 1360 nm, C band: 1530 — 1565 nm, and L band: 1565 — 1625 nm.*

avenue in emerging fields such as quantum information processing [41], and on-chip nonlinear photonics [42].

As discussed upon in this section, SOI PICs allows for high-density integration and cost-effective production [43]. These properties have boosted ultra-fast data transmission in integrated optical transceivers and are now playing a crucial role in a wide spectrum of emerging applications such as neuromorphic photonics [44], 5G-6G communications [45], quantum photonics [46], the Internet of Things [47], light detection and ranging [26], spectrometry [48], and sensing [49]. In order to address the needs of all these applications development of novel and efficient Si-integrated components is sought. High-performance integrated building blocks are essential for maintaining signal integrity and ensuring optimal power consumption, crucial for efficient optical signal transmission and low-power applications. These devices are expected to offer compact sizes, low losses, robust fabrication tolerances, and to be capable of operating over broad bandwidths for different optical modes and polarizations. Nevertheless, the development of fundamental photonic building blocks that can meet all these requirements is still a significant challenge. The high refractive index contrast of SOI platform results in a high birefringence between TE- and TM- polarized modes, high thermal dependence, chromatic dispersion, and susceptibility to fabrication deviations. In addition, available fabrication processes are subject to resolution limitations in terms of the minimum feature sizes (MFSs) that can be realized and can introduce small dimensional deviations from device's nominal designs, compromising their performance. Therefore, performance improvements in fundamental building blocks are key to unlocking novel applications and thereby driving technological advancements in integrated photonics.

1.3. Objectives and contributions of this thesis

The main objective of the present thesis is the design, optimization and characterization of new key components exhibiting minimal losses, broad operational bandwidths, and multimode operation along with robust fabrication tolerances. A key requirement for integrated photonic devices is broadband operation, i.e., flat response over wide wavelength ranges, which is difficult to accomplish as a consequence of the chromatic dispersion of the SOI platform. To meet all these requirements, the original devices developed in this thesis rely on periodic nanostructuration at the subwavelength scale, also known as subwavelength grating (SWG) metamaterials.

More specifically, the main goal of this thesis is to create novel high-performance power and modal management building blocks that enable the evolution of next-generation applications, thereby pushing the field of integrated photonics forward. The objective related to power management is to achieve efficient power splitting with ultra-broadband multimode operation and low excess loss, addressing the diverse demands of emerging applications such as data communication networks, sensing systems, and quantum information processing. On the other hand, the aim for modal management is to optimize the conversion between different optical modes and ensure low signal

degradation (with emphasis on modal dispersion mitigation) to be implemented in high-speed communication systems. To demonstrate the impact of these contributions beyond simulations, rigorous experimental characterizations were carried out to validate the outstanding performance of these cutting-edge building blocks. The devices were developed using a standard SOI platform with a BOX thickness of 2 µm and a 220-nm-thick silicon layer. The visual representation in Figure I.4 provides an overview of the three building blocks conceived in this thesis.

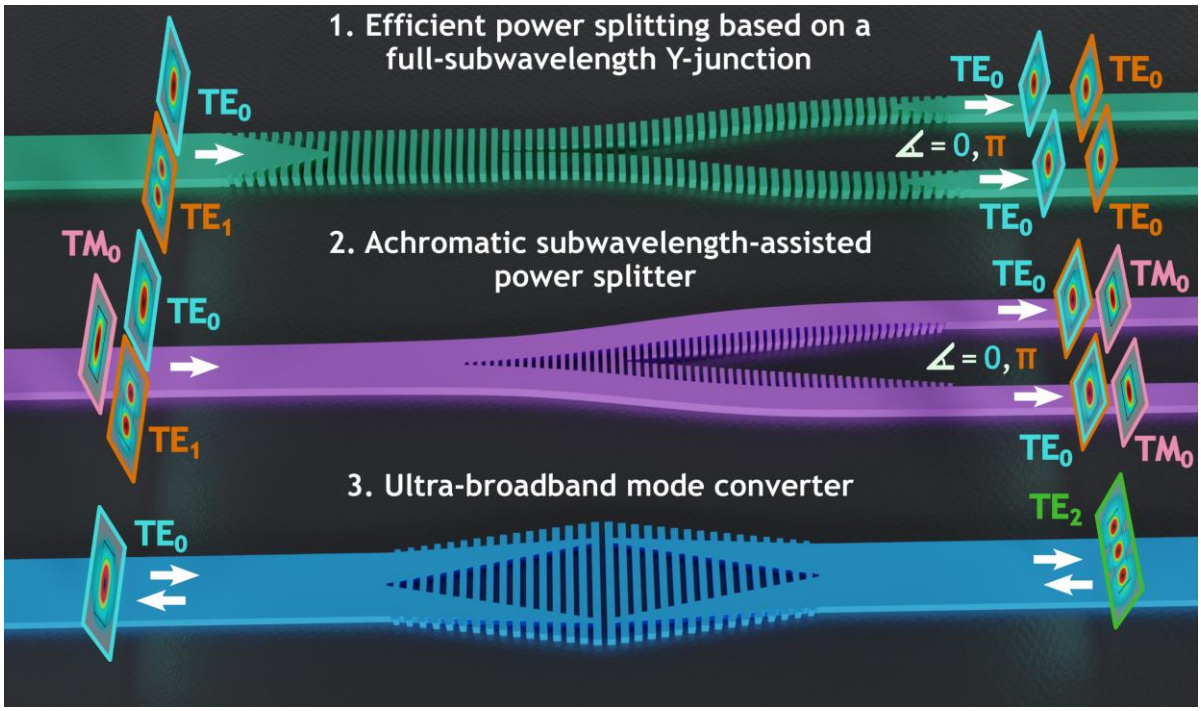

Figure I.3. Graphical abstract showing the main devices developed in this thesis.

1.3.1. Efficient power splitting based on a full-subwavelength Y-junction

Efficient power division is a fundamental functionality in silicon photonic integrated circuits, being 3-dB optical power splitters extensively used in light distribution or as building blocks for more intricate arrangements. Moreover, power splitters are often concatenated sequentially to build 1×N dividers, evidencing the necessity of compact and low-loss designs that operate over large bandwidths and have relaxed fabrication tolerances. But current state-of-the-art power-division architectures are hampered by limited operational bandwidths, high sensitivity to fabrication errors or large footprints.

Symmetric Y-junctions, among multiple power splitting architectures, are characterized by their theoretically polarization- and wavelength-independent spectral response along with their simple design. However, current lithography techniques have a limited resolution leading to a minimum feature size between the two Y-junction arms (i.e., a tip between the arms). This is particularly restrictive in deep ultraviolet (DUV) lithography, with a substantially larger minimum feature size compared to electron-beam (e-beam) technology. In addition, since the Y-junction tip is located at the midpoint of the stem waveguide, coinciding with the fundamental mode power maximum, deviations from the tip nominal design particularly penalize the fundamental mode losses.

In this thesis, a novel Y-junction enhanced with subwavelength gratings metamaterials has been developed for two different lithographic resolutions of 50 nm and 100 nm. The device exhibits a high-performance and large fabrication tolerances over an ultra-wide bandwidth. Full three-dimensional finite-difference time-domain (3D FDTD) simulations show a fundamental mode excess loss below 0.1 dB in an ultra-broad bandwidth of 300 nm (1400 — 1700 nm) when optimized for a fabrication resolution of 50 nm, and under 0.3 dB in a 350 nm extended bandwidth (1350 — 1700 nm) for a 100 nm resolution. Exhaustive measurements over a 260 nm bandwidth (1420 — 1680 nm) show fundamental transverse-electric mode (TE_0) excess loss under 0.3 dB considering a high-resolution lithographic process (i.e., 50 nm) and below 0.5 dB for a standard-resolution scenario (i.e., 100 nm). Subwavelength Y-junctions with artificially induced errors of ±10 nm further demonstrate the robustness to fabrication deviations of this design. The proposed splitter also exhibits first-order transverse-electric mode (TE_1) excess loss lower than 1.5 dB within a 170 nm bandwidth (1420 — 1590 nm) in both 50 nm and 100 nm resolution scenarios, hence enabling multimode power splitting configurations.

1.3.2. Achromatic subwavelength-assisted power splitter

The strong demand for high performance and ultra-broadband power splitters, especially for multimode and dual polarization operation, is paramount for a myriad of applications. The second device developed in this thesis is an achromatic power splitter. The proposed SWG-assisted device yields the broadest bandwidth reported to date for a nanophotonic power divider. Operation over an outstanding 700-nm bandwidth was obtained through 3D FDTD simulations, covering an extensive wavelength range from 1300 nm to 2000 nm.

The device design was optimized for both TE_0 and the TE_1 modes, and it also exhibits a remarkable performance for the fundamental transverse-magnetic (TM_0) mode. Specifically, 3D FDTD simulations predict minimal excess loss (< 0.2 dB) for both TE_0 and TE_1 modes over a 700 nm bandwidth (1300 — 2000 nm), and less than 0.3 dB for the TM_0 mode within the 1300 — 1800 nm wavelength range. Experimental measurements validate simulation results, confirming low excess losses for the three modes in the 1430 — 1680 nm wavelength range along with robust fabrication tolerances for etching errors up to ±10 nm.

This SWG-assisted symmetric Y-junction is expected to unlock new possibilities for a myriad of applications in both traditional and emerging areas of silicon photonics, including mode-division multiplexing, quantum key distribution, and neural networks. Moreover, the proposed design strategy can be applied to other high-index contrast material platforms. The operating bandwidth for TM_0 could be extended with a thicker BOX layer for the SOI platform and higher-order modes could also be potentially supported just by increasing the device's dimensions.

1.3.3. Ultra-broadband mode converter

The exponential growth of global Internet traffic and the rising bandwidth-hungry applications accentuate the necessity for the telecom industry to move towards next-generation optical systems. MDM techniques provide improved data rates by simultaneously transmitting several signals in optical modes of different orders within a single waveguide. Multimode silicon photonics, leveraging mode-division multiplexing technologies, offer strong prospects to increase capacity of large-scale multiprocessing systems for on-chip optical interconnects. Moreover, these technologies have implications not only for telecom and datacom applications but are also useful for emerging fields such as integrated quantum and nonlinear photonics. Thus, the development of compact, low-loss and low-crosstalk mode converters is crucial for effective on-chip mode manipulation.

The third device developed in this thesis is an innovative mode converter architecture based on two symmetric Y-junctions in back-to-back configuration connected through SWG metamaterials. The geometrical parameters of the design are further refined through Powell's gradient-free optimization algorithm, maximizing the modal field conversion between the fundamental and second-order transverse-electric (TE_2) modes. The device, optimized through 3D FDTD, shows excess loss (EL) below 0.75 dB and extinction ratio (ER) exceeding 10 dB over a broad bandwidth of 350 nm (1350 nm to 1700 nm). Furthermore, within a 150 nm wavelength range (1472–1622 nm), ER exceeds 20 dB while EL remains below 0.3 dB. Experimental validation confirms efficient mode conversion in both cases, TE_0 - TE_2 and TE_2 - TE_0, with EL as low as 0.4 dB and ER exceeding 18 dB over a broadband of 149 nm, extending from 1471 nm to 1620 nm. The demonstrated mode converter is a pioneering solution in the field, which stands out for its notable combination of increased bandwidth, efficiency, and compact design compared to other state-of-the-art solutions. These compelling attributes underline the device's considerable potential in ultrahigh-density MDM systems for advanced multimode optical communication and signal processing applications.

1.4. Document organization

The structure of this thesis is organized as follows:

- **Chapter I** is devoted to the introduction.
- **Chapter II** introduces the fundamental principles of light-wave propagation through periodic dielectric structures, focusing on the subwavelength grating regime. The objective of this chapter is to provide a comprehensive understanding of the essential concepts and practical applications of SWG metamaterials, laying the basis for their implementation in the design of the proposed devices.
- **Chapter III** presents an in-depth review of state-of-the-art power splitting and mode conversion devices, including a complete discussion of their strengths, limitations, ongoing advances, and current challenges.
- **Chapter IV** describes the design and characterization of a broadband power splitter based on full SWG metamaterials, developed for the SOI platform. The principle of operation, design considerations, and optimization procedures of the proposed device are explained.

Subsequently, the fabrication process and the extensive experimental characterization are explained.

- **Chapter V** presents the achromatic power splitting architecture assisted by SWG metamaterials, for multimode and dual-polarization operation. This chapter covers theoretical considerations, simulation results, fabrication details, and exhaustive characterization of this innovative device.
- **Chapter VI** focuses on the broadband mode converter. The device design process involves a refined gradient-free optimization method combined with SWGs. The description of the fabrication process of the novel mode-converter device is included, and insights from both simulated and experimental measurements are discussed.
- **Chapter VII** draws the conclusions obtained from this thesis and discusses future lines of research.

Chapter II:

LIGHT DYNAMICS IN PERIODIC STRUCTURES

This chapter explores the fundamental nature of periodic dielectric waveguides in integrated photonic circuits. These structures are a versatile design tool capable of operating as optical metamaterials for an appropriate wavelength-to-period ratio. Specifically, the emphasis is on the utilization of periodic dielectric structures when they remain unaffected by diffractive effects, commonly referred to as subwavelength grating metamaterials. Recognized for their tailorable optical properties, SWG metamaterials prove themselves to be an excellent resource for engineering photonic components, especially in those fabrication platforms constrained by limitations in available material such as SOI.

Section 2.1 introduces the basis for understanding light behavior in wire waveguides and, consequently, the underlying concepts of periodic waveguides. In Section 2.2, the theoretical foundations of wave propagation along periodic structures are described, including their inherent photonic band structure. Building on this basis, Section 2.3 describes SWGs as uniaxial crystals to model their response as an equivalent metamaterial. Section 2.4 discusses the different engineering approaches of SWG metamaterials for photonic design. The chapter concludes in Section 2.5 by summarizing the main insights derived from the concepts presented.

2.1. Introduction to photonic wire waveguides

This section aims to establish a solid foundation in the principles of uniform wire waveguides. The fundamental principles describing the behavior of light's electromagnetic field in integrated photonic wire waveguides establish the basis for approaching and understanding more advanced structures, in particular periodic waveguides.

The macroscopic behavior of an electromagnetic field is governed by Maxwell's equations. A conventional waveguide can be conceptualized as a dielectric medium characterized by its non-magnetic, linear, isotropic, and non-homogeneous properties. In the absence of free charges and under the assumption of a sinusoidal regime, the governing equations for such waveguides are as follows [50]:

$$\nabla \times \vec{E} = -j\omega_0\mu_0\vec{H} \tag{2.1}$$

$$\nabla \times \vec{H} = j\omega\varepsilon_0\epsilon\vec{E} \tag{2.2}$$

$$\nabla \cdot \overrightarrow{\epsilon E} = 0 \tag{2.3}$$

$$\nabla \cdot \vec{H} = 0 \tag{2.4}$$

The electromagnetic fields, electric ($\vec{E}$) and magnetic ($\vec{H}$), propagate with an angular frequency ω_0 in a medium with vacuum magnetic permeability μ_0 and dielectric permittivity ε_0. The relative dielectric tensor ϵ is related to the refractive index of the material as $\epsilon = n^2$. The vacuum wavenumber is then given by the angular frequency and the speed of light in vacuum: $k_0 = \frac{\omega_0}{c}$.

Let's consider a monochromatic light wave propagating in the x direction within a conventional dielectric wire waveguide, as shown in Figure II.1(a). Because of the translational symmetry of this WG, the expressions for the electric ($\vec{E}$) and magnetic ($\vec{H}$) fields can be separated into the transversal ($\vec{E}_t = \vec{E}_y + \vec{E}_z$; $\vec{H}_t = \vec{H}_y + \vec{H}_z$) and longitudinal ($\vec{E}_x$; $\vec{H}_x$) components [51]. In addition, the EM field solutions are characterized by its wavevector component in the propagation direction, $\vec{k} = k_x\hat{x}$. A set of solutions to Maxwell's equations permits to disaggregate the field components as a function of the transverse components, with a general form [51]:

$$\vec{E}_m(x,y,z) = \vec{E}_{t,m}(y,z) \cdot e^{j(\omega_0 t - k_{x,m}x)} \tag{2.5}$$

$$\vec{H}_m(x,y,z) = \pm\vec{H}_{t,m}(y,z) \cdot e^{j(\omega_0 t - k_{x,m}x)} \tag{2.6}$$

where m identifies the solutions with different field distribution and propagation constant $k_{x,m}$, i.e., the different propagating modes. The field, or harmonic solutions, $\vec{E}_{t,m}(y,z)$ and $\vec{H}_{t,m}(y,z)$, are completely determined for each mode of order m. Upon substituting these field solutions into Maxwell's equations, the transversal components can be expressed as functions of their longitudinal components, and the longitudinal components can be derived. The resulting equations for the

longitudinal components of the electric and magnetic fields, referred to as the reduced wave equations or modal equations, are then formulated as follows [51]:

$$\frac{\partial^2 E_x}{\partial y^2} + \frac{\partial^2 E_x}{\partial z^2} = [k_x^2 - \epsilon k_0^2] E_x \tag{2.7}$$

$$\frac{\partial^2 H_x}{\partial y^2} + \frac{\partial^2 H_x}{\partial z^2} = [k_x^2 - \epsilon k_0^2] H_x \tag{2.8}$$

The complex eigenvalue of th0e modal equations is the wavenumber associated to each mode, $k_x = k_x^{re} + j\, k_x^{im}$, and is related to the effective index of the modes as $k_x = k_0\, n_{eff} = \frac{\omega_0}{c} n_{eff}$. The real component of the eigenvalue (k_x^{re}) corresponds to the phase variation experienced by the propagating mode, while the imaginary component (k_x^{im}) accounts for its attenuation or loss. It is important to note that wire waveguides support two types of modes depending on the light polarization direction, as shown in Figure II.1. The solutions for quasi-transverse-electric modes in wire waveguides consist of harmonic solutions where the dominant component of the electric field is E_y, with the component E_x being negligible, and $H_y = 0$. Similarly, quasi-transverse-magnetic modes present an electric field that is primarily polarized along the z-direction. Thus, the calculation of propagating modes in wire waveguides entails solving the modal equations while considering the appropriate boundary conditions that ensure the fields at the interfaces are satisfied.

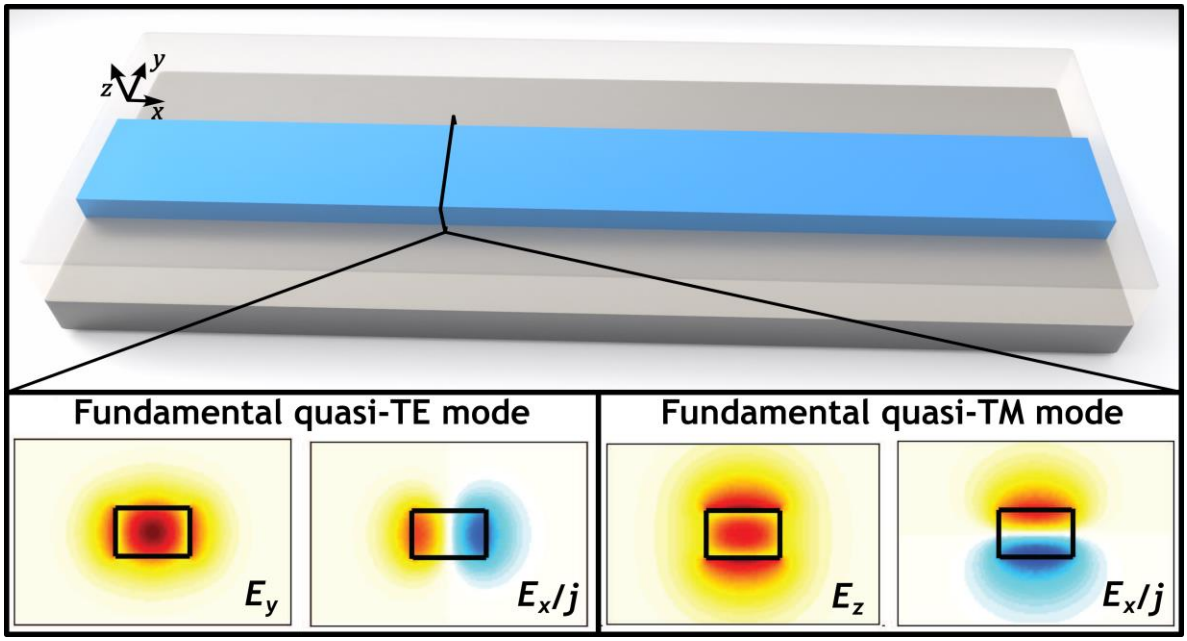

Figure II.1 Schematic representation of a wire waveguide with insets of the $E_y(E_z)$ and E_x components of the fundamental quasi-TE(TM) mode supported. Graded yellow and blue colors are utilized to indicate a π-phase difference [52].

2.2. Light propagation in periodic dielectric media

Now consider a monochromatic light wave propagating in the positive x direction ($\vec{k} = k_x\hat{x}$) of a dielectric periodic waveguide, as shown in Figure II.1(c). For simplicity only the electric field solutions will be developed, the procedure being similar for the magnetic field. The periodic waveguide core consists of different dielectric segments of a material with refractive index n_{core}, width W and thickness T, spaced with a period Λ. The amount of core material present in a period, i.e., the length of the core segments (a), is defined by the duty cycle (DC) as: $a = DC \cdot \Lambda$. Gaston Floquet [53] and Felix Bloch [54] set the foundations on wave propagation in periodic structures. The Floquet-Bloch theorem introduces the solution of EM waves propagating along the periodicity direction, which can be expressed as a Fourier series expansion:

$$\vec{E}(x,y,z) = \vec{E}_F(y,z)\, e^{-jk_x x} = \left(\sum_{m=-\infty}^{\infty} \vec{E}_{F,m}(y,z) e^{-jm\frac{2\pi}{\Lambda}x} \right) e^{-jk_x x} \tag{2.9}$$

The field profile is defined over a single period and satisfies $E_F(x,y,z) = E_F(x \pm \Lambda, y, z)$ since the grating structure is characterized by its periodicity in the x direction $\epsilon(x,y,z) = \epsilon(x \pm \Lambda, y, z)$. The solution for this field is the sum of an infinite series of harmonic plane waves. The series involves the product of two components: a periodic function in the direction of propagation, with the same period as the grating WG, and an exponential function with dependence on the direction of propagation. The exponential function can be combined as:

$$\vec{E}(x,y,z) = \sum_{m=-\infty}^{\infty} \vec{E}_{F,m}(y,z)\, e^{-jk_{F,x} x} \tag{2.10}$$

where $k_{F,x} = k_x + m\frac{2\pi}{\Lambda}$ is the complex Floquet-Bloch wavenumber and it can be rewritten as $k_{F,x} = k_{F,x}^{re} + jk_{F,x}^{im}$. Similar to the propagation of a mode in a conventional photonic wire, here $k_{F,x}^{im}$ is associated with the attenuation of the Floquet-Bloch mode, while $k_{F,x}^{re}$ is related to the phase constant. Thus, the effective index of a Floquet-Bloch mode can be denoted as: $n_{eff,F} = \frac{k_{F,x}}{k_0} = \frac{k_{F,x}^{re}}{k_0} + j\frac{k_{F,x}^{im}}{k_0} = n_{eff,F}^{re} + jn_{eff,F}^{im}$.

There are no analytical solutions for Floquet-Bloch modes in a 3D medium, but accurate numerical methods are available for this purpose, including finite-difference time-domain or eigenmode expansion approaches [55]. The main simulations conducted on this thesis employ the 3D FDTD method. This approach discretizes both space and time into a grid, calculating the electric and magnetic field values at each grid point. The method iteratively updates these values based on Maxwell's equations and boundary conditions. Through repetitive iterations, the simulation computes the evolution of electromagnetic fields over time in a given three-dimensional scenario.

2.2.1. Periodicity and wavevector: photonic band structure

Similar to the conventional mode profile propagating with its respective wavenumber, $\vec{E}_F(y,z)$ can be understood as a mode profile that propagates with wavevector $\overrightarrow{k_F} = k_{F,x}\hat{x}$ along the x-axis. An important consideration is that the Floquet-Bloch mode profile, rather than being constant in the propagation direction, is cyclic in the periodicity direction. Therefore, for periodic waveguides it is enough to calculate the eigenvalues for the wavevectors $\overrightarrow{k_F}$ within just one period: the primitive unit cell. This is widely known as the first Brillouin zone in solid state physics [56]. In periodic photonic waveguides, $\overrightarrow{k_F} = k_{F,x}\hat{x} = \left(k_x + m\frac{2\pi}{\Lambda}\right)\hat{x} = (k_x + mG)\hat{x}$, where G is the primitive reciprocal lattice. The first Brillouin zone is thus delimited within the region $k_{F,x} \in [-\frac{G}{2}, +\frac{G}{2}]$ and any other wavenumber is equivalent under translation by a multiple of $G = \frac{2\pi}{\Lambda}$. Furthermore, the first Brillouin zone may itself be redundant if the periodic structure presents additional symmetries, such as mirror planes. The range $-\frac{G}{2} < k_{F,x} < 0$ is the reverse of $0 < k_{F,x} < \frac{G}{2}$, then the irreducible Brillouin zone is $k_{F,x} \in [0, +\frac{G}{2}]$ [56]. The uniform wire waveguide (Figure II.1(a)), can be considered a special case of the Floquet-Bloch formalism for a period $\Lambda \to 0$, so the Brillouin zone of the wavevector is unbounded ($k_{F,x} \to \infty$). The band structure of the uniform wire waveguide is presented in Figure II.1(b), while Figure II.1(d) illustrates the diverse light behaviors within a periodic structure (Figure II.1(c)).

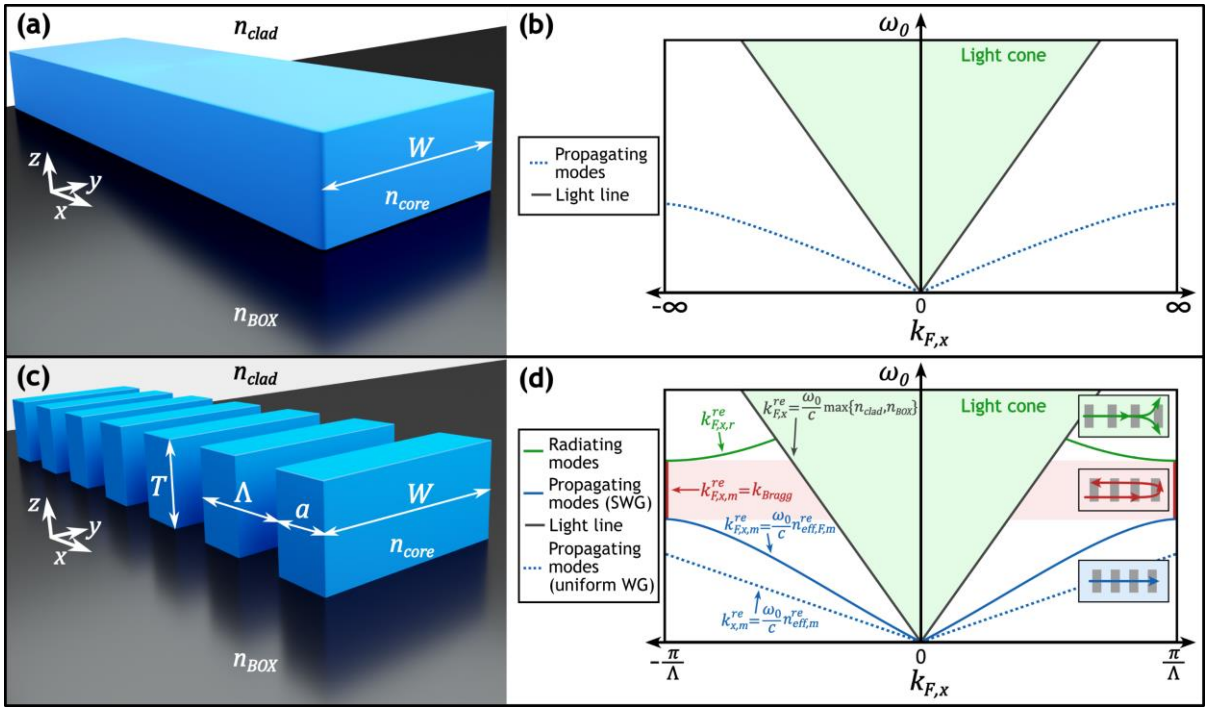

Figure II.2. Illustrations of (a) a uniform wire waveguide and (c) a periodic waveguide. Note that the cladding is omitted in panels (a) and (c) for the sake of clarity. Band diagrams of both uniform wire and periodic WGs are plotted in panels (b) and (d), respectively. The subwavelength (blue), Bragg (red) and radiation (green) regimes are also depicted in panel (d).

2.2.2. Bragg regime

In periodic waveguides, there is a perturbation-induced coupling between the modes at $k_{F,x} = -\frac{G}{2}$ and $k_{F,x} = \frac{G}{2}$, which results in the small band gaps at the edge of the zone, as illustrated by a red vertical line in Figure II.1(d). Within these gaps, the light is cannot propagate along the periodic waveguide since there are no permitted propagating $k_{F,x}$ solutions [56]. The Bragg condition offers a straightforward explanation of this phenomenon: multiple reflections from various unit cells collaborate to interfere destructively within the structure [57]. Consider two Floquet-Bloch modes characterized by wave vectors $k^{re}_{F,x,m}$ and $k^{re}_{F,x,m'}$. In order for reflection to occur without mode conversion the mode of order m may be the same mode as m', and the phase constant of the Floquet-Bloch mode propagating in the positive x-direction ($k^{re}_{F,x,m}$) must match the phase constant of the backward-propagating ($k^{re}_{F,x,m'} < 0$) mode: $k^{re}_{F,x,m} = -k^{re}_{F,x,m'}$ [58]. This condition for phase matching is expressed as follows:

$$k^{re}_{F,x,m} = k^{re}_{F,x,m'} + l\frac{2\pi}{\Lambda} = -k^{re}_{F,x,m} + l\frac{2\pi}{\Lambda} \rightarrow 2k^{re}_{F,x,m} = l\frac{2\pi}{\Lambda} \tag{2.11}$$

Therefore, the Bragg regime can be expressed for each band gap of order l as the range of frequencies satisfying the following equality:

$$k_{Bragg} = \frac{\omega_0}{c} n_{l,Bragg} = l\frac{\pi}{\Lambda} \tag{2.12}$$

In the frequency range corresponding to the photonic bandgap, light is prevented from propagating through the structure and $k^{re}_{F,x,m}$ remains constant. Bragg gratings find widespread application as narrowband reflection filters for datacom [59], sensing-related systems [60], and emerging areas such as nonlinear optics [61] and quantum photonics [57].

2.2.3. Radiation regime

The modes above the light line ($k_{F,x} = k_0 \cdot \max\{n_{clad}, n_{BOX}\}$) describe the propagation of light within the cladding or BOX and are considered radiation modes. These modes are characterized by a continuous spectrum, visually represented by the green cone in Figure II.1(d). The bands located above the bandgap and below the cladding light line, represent the leaky modes, as illustrated by the green lines in Figure II.1(d). Leaky modes are especially relevant for the design of fiber-chip input/output light coupling devices, such as grating couplers that radiate a portion of the guided Floquet-Bloch mode. In this radiation regime, the mode experiences an upward or downwards partial diffraction (z-direction) when it is phase-matched to the radiation mode supported by the cladding. This process is characterized by an emission angle θ_r respect to the vertical axis (z-direction). The grating equation dictates the phase matching condition for the diffracted Floquet-Bloch mode:

$$k_d \sin(\theta_r) = k^{re}_{F,x,r} = k^{re}_x + r\frac{2\pi}{\Lambda} = k_0 n^{re}_{eff} + r\frac{2\pi}{\Lambda} \tag{2.13}$$

where k_d is the wavenumber of the radiation mode in the cladding ($k_d = k_0 n_{clad}$), considering only the emission in the xz-plane for simplicity. The integer number r corresponds to the mode order. To operate in the radiation regime described in Equation (2.13), two criteria must be met. First, the angle θ_r must be a real value. Second, only eigenvalues characterized by a negative order ($r < 0$) can be emitted by the grating, as $n_{eff}^{re} > n_{clad}$.

Surface grating couplers (GCs) facilitate efficient light coupling between optical fibers and chip waveguides. For this purpose, the optical fiber is placed above radiating grating structures on the chip surface, as shown in Figure II.2. A surface GC changes the out-of-plane wave vector direction of the light to align with the in-plane waveguide direction, coupling the light into the waveguide and acting as a mode-size converter [62], [63].

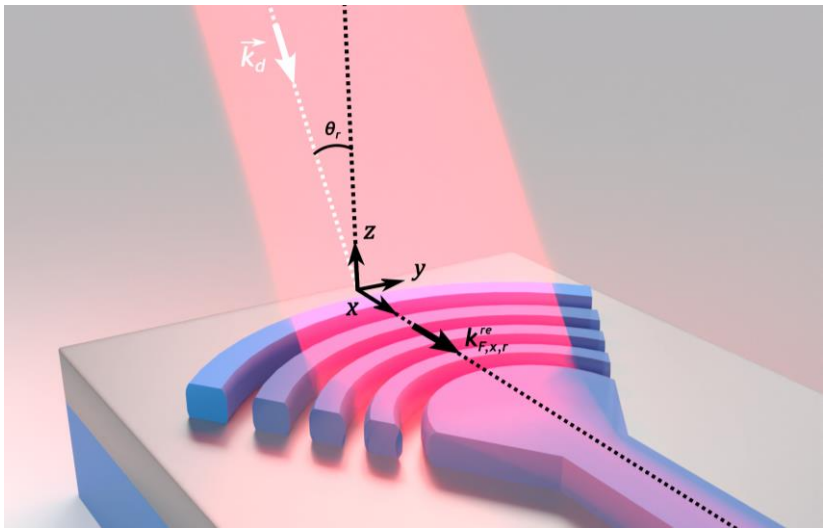

Figure II.3. Schematic of a typical focusing grating coupler based on curved periodic structures.

2.2.4. Subwavelength regime

In the subwavelength regime, radiative and reflective effects are suppressed, and the propagation of the Floquet-Bloch mode is lossless: $k_{F,m}^{im} = 0$, and hence $k_{F,m} = k_{F,m}^{re}$ [64]. This regime is illustrated in Figure II.1(d) below the first band gap or Bragg regime, where the Floquet-Bloch mode propagates through the periodic waveguide.

$$k_{F,m} = \frac{2\pi}{\lambda_0} n_{eff,F} < k_{Bragg}(l = 1) = \frac{\pi}{\Lambda} \tag{2.14}$$

Rewriting Equation (2.14) gives the condition for the period of the periodic waveguide to operate in the subwavelength regime:

$$\Lambda_{\mathrm{SWG}} < \frac{\lambda_0}{2n_{eff,F}} \tag{2.15}$$

Equation (2.15) labels this regime as subwavelength, referring to the significantly shorter periodicity of the structure relative to the wavelength of light. The region where the Floquet-Bloch mode is linear ($k_{F,x} \to 0$) is known as deep-subwavelength regime, which will be further explained in the following sections. Within the SWG regime, the Floquet-Bloch modes have a lower effective refractive index compared to modes of the same order and polarization propagating in an equivalent uniform wire waveguide with identical width and thickness. In other words, the equivalent uniform wire WG corresponds to the case of a periodic WG in which the duty cycle is fixed at 1. Moreover, the effective refractive index of the modes propagating in the SWG regime is higher than the refractive index of the first Bragg regime:

$$n_{l=1,Bragg} < n_{eff,F,m} < n_{eff,m} \tag{2.16}$$

As mentioned above, it is important to note that the value $n_{eff,F,m}$ is influenced not only by the grating period but also by the duty cycle. This can be interpreted as follows: as more silicon is present in a period ($DC \to 1$), $n_{eff,F,m}$ increases and converges toward $n_{eff,m}$. Conversely, when there is less silicon in a period ($DC \to 0$), the value of $n_{eff,F}$ decreases, approaching $n_{l=1,Bragg}$. Thus, in the subwavelength regime, the grating WG behaves as a new uniform material (referred to as metamaterial through this thesis) with a refractive index (n_{eq}) lower than the refractive index of the core material: $n_{eq} < n_{core}$.

2.3. Subwavelength grating metamaterials

The optical properties of SWG gratings described in the previous section hold remarkable potential for the implementation of metamaterials. The term "metamaterial" is defined in the literature as an artificial medium that exhibits properties different from those available in natural materials [64]. Subwavelength gratings inherently behave as engineered metamaterials, as they are nanostructures which exhibit unique and tailored properties that are not intrinsic to their individual components. The effective optical properties of the SWG metamaterial are influenced by both the constituent materials and the specific topology of the nanostructures [65]. By precisely designing grating WGs at the subwavelength scale, a wide range of refractive indices can be synthesized as well as controlling light dispersion and anisotropy. To fully harness the design advantages offered by subwavelength nanostructures, it is important to understand the conditions under which they behave as equivalent uniform materials and to characterize the properties of these metamaterials. In the following section a mathematical model to describe the optical properties of periodic SWG waveguides is introduced.

2.3.1. SWGs as uniaxial crystal

Uniaxial crystals are anisotropic materials with a single optical axis, which means that light travels through the crystal with different velocities in each direction [66]. The periodic waveguide in Figure II.1(c) can be conceived as a "slice" of an infinite laminar material as shown in Figure II.3(a) [67]. In the subwavelength regime, this layered structure acts according to an equivalent

homogeneous anisotropic material, i.e., as a uniaxial crystal (Figure II.3(b)). Thus, the SWG waveguide can be effectively modeled as a homogeneous waveguide made of the equivalent uniaxial crystal material (see Figure II.3(c)).

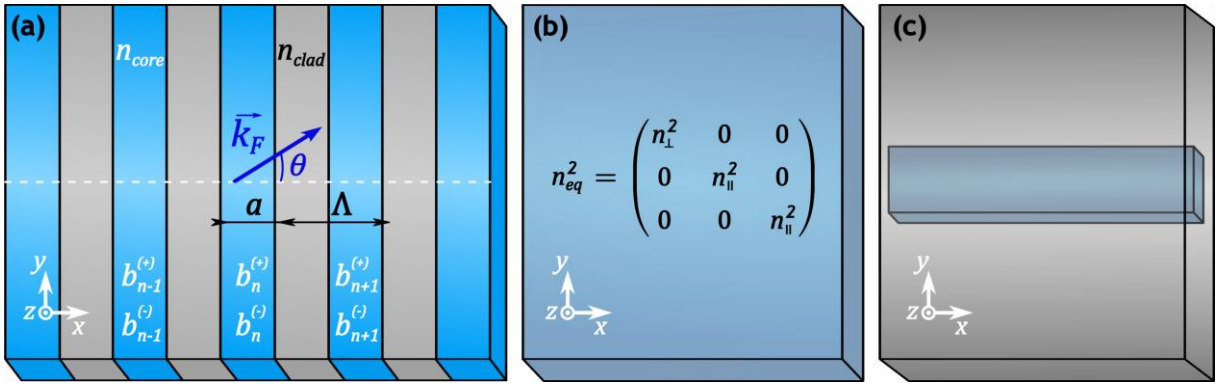

Figure II.4. (a) Infinite laminar medium composed of alternating layers of the waveguide core and cladding material. (b) Equivalent uniform anisotropic material in the subwavelength regime. (c) Metamaterial model of the periodic structure.

Let's consider a monochromatic plane wave that propagates in the x-y plane with a wave vector $\overrightarrow{k_F}$ forming an angle θ relative to the x-axis, as depicted in Figure II.3(a). The electric field solution can be expressed using the Floquet-Bloch theorem (Equation (2.9)) as:

$$\vec{E}(x,y) = \vec{E}_F(x)e^{-jk_{F,x}x}e^{-jk_{F,y}y} \tag{2.17}$$

Note that here $\vec{E}_F$ only depends on x since the laminar material extends infinitely through y and z directions. The wavenumbers in the x and y directions are related to the wavenumber as $k_{F,x} = k_F\cos(\theta)$ and $k_{F,y} = k_F\sin(\theta)$. Equation (2.17) can be rewritten and simplified by considering the electric field distribution within each homogeneous layer as a sum of an incident plane wave and a reflected plane wave, as proposed by Yeh in [68]. Hence, a Floquet-Bloch mode in the n-th core layer is given by:

$$\vec{E}(x,y) = \left[\left(b_0^{(+)}e^{-jk_x^{core}(x-n\Lambda)} + b_0^{(-)}e^{jk_x^{core}(x-n\Lambda)}\right)e^{-jk_x n\Lambda}\right]e^{-jk_{F,y}y} \tag{2.18}$$

Using Equation (2.18) in the modal or dispersion equation to obtain the relation between k_y, k_x and k_0, results in:

$$\cos(k_{F,x}\Lambda) = \cos(k_x^{core}a)\cos(k_x^{clad}(\Lambda-a)) - \Delta\sin(k_x^{core}a)\sin(k_x^{clad}(\Lambda-a)), \tag{2.19}$$

where $k_x^{core} = \sqrt{(k_0 n_{core})^2 - k_{F,y}^2}$ and $k_x^{clad} = \sqrt{(k_0 n_{clad})^2 - k_{F,y}^2}$ are the wavenumbers of the core and cladding in the periodicity direction (x-direction), respectively. The factor Δ is a term dependent on polarization as well as core and cladding materials:

$$\Delta_{\mathrm{TE}} = \frac{1}{2}\left(\frac{n_{clad}^2\, k_x^{core}}{n_{core}^2\, k_x^{clad}} + \frac{n_{core}^2\, k_x^{clad}}{n_{clad}^2\, k_x^{core}}\right) \tag{2.20}$$

$$\Delta_{\mathrm{TM}} = \frac{1}{2}\left(\frac{k_x^{core}}{k_x^{clad}} + \frac{k_x^{clad}}{k_x^{core}}\right) \tag{2.21}$$

In the deep-subwavelength limit, i.e., $\Lambda \ll \lambda_0$, it is satisfied that $k_x \Lambda \ll 1$ and hence, $k_x^{core} a \ll 1$ and $k_x^{clad}(\Lambda - a) \ll 1$. Under this approximation, Equation (2.19) can be reduced for each polarization to [67]:

$$\frac{k_{F,x}^2}{n_{\parallel}^2} + \frac{k_{F,y}^2}{n_{\perp}^2} = \frac{k_{F,\mathrm{TE}}^2 \cos^2(\theta)}{n_{\parallel}^2} + \frac{k_{F,\mathrm{TE}}^2 \sin^2(\theta)}{n_{\perp}^2} = k_{0,\mathrm{TE}}^2 \tag{2.22}$$

$$\frac{k_{F,x}^2}{n_{\parallel}^2} + \frac{k_{F,y}^2}{n_{\parallel}^2} = \frac{k_{F,\mathrm{TM}}}{n_{\parallel}} = k_{0,\mathrm{TM}}^2 \tag{2.23}$$

Equations (2.21) and (2.22) are the dispersion relations of TE and TM plane waves propagating along the xy plane of a uniaxial anisotropic crystal. For this crystal, $n_{\parallel}$ and $n_{\perp}$ are the ordinary and extraordinary indices of refraction, respectively. The electric field of TE-polarized light lies within the xy-plane, whereas for TM polarization the electric field is orthogonal to the periodicity (i.e., in the z-direction). In other words, a plane wave propagating through a laminar periodic structure in the deep-subwavelength regime propagates as if it were a homogeneous uniaxial crystal described by the diagonal permittivity tensor:

$$\epsilon = {n_{eq}}^2 = \begin{bmatrix} n_{\perp}^2 & 0 & 0 \\ 0 & n_{\parallel}^2 & 0 \\ 0 & 0 & n_{\parallel}^2 \end{bmatrix} \tag{2.24}$$

Moreover, the metamaterial properties are found to be independent of both period and wavelength in this regime, allowing to simplify the permittivity tensor components to Rytov's equations [69]:

$$n_{\parallel}^2 = DC\; n_{core}^2 + (1 - DC) n_{clad}^2 \tag{2.25}$$

$$n_{\perp}^2 = \left(\frac{DC}{n_{core}^2} + \frac{(1 - DC)}{n_{clad}^2}\right)^{-1} \tag{2.26}$$

As Rytov's equations intuitively imply, a high duty cycle corresponds to permittivity tensor components closely aligned with n_{core}^2, while a low duty cycle aligns with components approximating n_{clad}^2. This principle is fundamental to leveraging subwavelength materials for refractive index engineering.

An improved method to model the equivalent metamaterial in the full subwavelength regime was proposed in [67]: the slab model. This model incorporated the WG core thickness in the calculation to obtain the permittivity tensor, describing the complete subwavelength regime. Initially, the

calculation involves determining the effective indices for the 2D periodic slab waveguide, considering mode propagation along the y- and the x-axis. The plane waves propagating along these two axes exhibit effective refractive indices $n_{eff,y}$ and $n_{eff,x}$. To translate these effective indices into refractive indices, one must compute the equivalent homogeneous slab that generates these modes. Subsequently, an isotropic 2D slab waveguide considering different refractive indices of the core material ($n_{eq} = \sqrt{n_{eq,x}^2 + 2n_{eq,y}^2}$) is solved, yielding a mapping function. Then mapping the effective indices $n_{eff,x}$ and $n_{eff,y}$ to the equivalent refractive indices $n_{eq,x}$ and $n_{eq,y}$, the permittivity tensor of the equivalent metamaterial is:

$$\epsilon = {n_{eq}}^2 = \begin{bmatrix} n_{eq,x}^2 & 0 & 0 \\ 0 & n_{eq,y}^2 & 0 \\ 0 & 0 & n_{eq,y}^2 \end{bmatrix} \tag{2.27}$$

Here, the parameters $n_{eq,x}$ and $n_{eq,y}$ are analogous to $n_\perp$ and $n_\parallel$ in the deep-subwavelength regime approximation, respectively. Henceforth, the terms $n_{eq,x}$ and $n_{eq,y}$ are used instead of $n_\perp$ and $n_\parallel$.

2.4. Subwavelength metamaterials for nanophotonic device design

SWG metamaterials have been successfully applied to the design of a wide variety of high-performance devices [65]. Three fundamental properties of SWG metamaterials are typically exploited for the design of high-performance photonic devices: refractive index, dispersion, and anisotropy engineering. As detailed in the following sub-sections, the selection of the engineering technique depends on the specific purpose and application of each device.

Nevertheless, regardless of the particular engineering technique, there are several practical considerations involved in the design of subwavelength metamaterials. The first consideration is the choice of an appropriate period. Smaller periods result in $n_{eq,y}$ and $n_{eq,x}$ values nearly wavelength independent but requires smaller feature sizes that can be more difficult to fabricate. For example, for an SWG with silicon core (n_{Si} = 3.476) and silicon dioxide BOX and cladding (n_{SiO2} = 1.444) operating at a wavelength of λ_0 = 1550 nm, a commonly used period is Λ = 200 nm. These period values adhere to the MFS achievable with certain technologies, such as electron-beam lithography (see Annex A) if a duty cycle between 25% and 75% is considered, since the MFS would be 50 nm in the worst case. The second consideration arises when small duty cycles are employed, resulting in smaller equivalent rates for the metamaterial. Consequently, this leads to weak waveguide guidance, raising a potential risk of leakage loss towards the silicon substrate [70]. The final considerations only apply to wide SWG waveguides with tight mode confinement. In such scenarios, a few nanometers of jitter in the placement of each grating segment may introduce significant transmission losses [71] as the jitter disturbs the periodicity on which the propagation of the Floquet-Bloch mode is based.

2.4.1. Refractive index engineering

As discussed in the previous section, one of the key functionalities of SWG waveguides lies in their ability to manipulate the refractive index of the equivalent metamaterial. According to Equations (2.25) and (2.26), it is possible to synthesize the equivalent refractive indices $n_{eq,y}$ and $n_{eq,x}$ by modifying the geometrical parameters of the grating. Refractive index engineering achieves a broad spectrum of refractive index values, ranging from those of the core to the cladding materials. Controlling the refractive index profile of the equivalent metamaterial waveguide provides the means to manipulate the confinement properties of guided modes within the waveguide. This additional degree of freedom in the design introduces flexibility and addresses a notable limitation in integrated optics: the fixed values of the refractive indices of the material platforms. This control over the refractive index is essential for optimizing the performance of photonic devices [72], [73], which is highly desirable for building sophisticated microphotonic circuits.

To visually illustrate refractive index engineering, Figure II.5 shows two SWG waveguides, characterized by $DC_1 = a_1/\Lambda$ in panel (a) and $DC_2 = a_2/\Lambda$ in panel (c), where $DC_2 > DC_1$. Their respective equivalent metamaterials with refractive indices $n_{eq,1}$ and $n_{eq,2}$ are included in Figure II.5(b) and (d), respectively. The insets in panels (b) and (d) provide a closer look at the fundamental TE mode ($|E_y|$ field profile) within each metamaterial structure. From the insets, it can be easily seen that TE_0 mode is more confined in the structure with higher DC, since $n_{eq,2} > n_{eq,1}$.

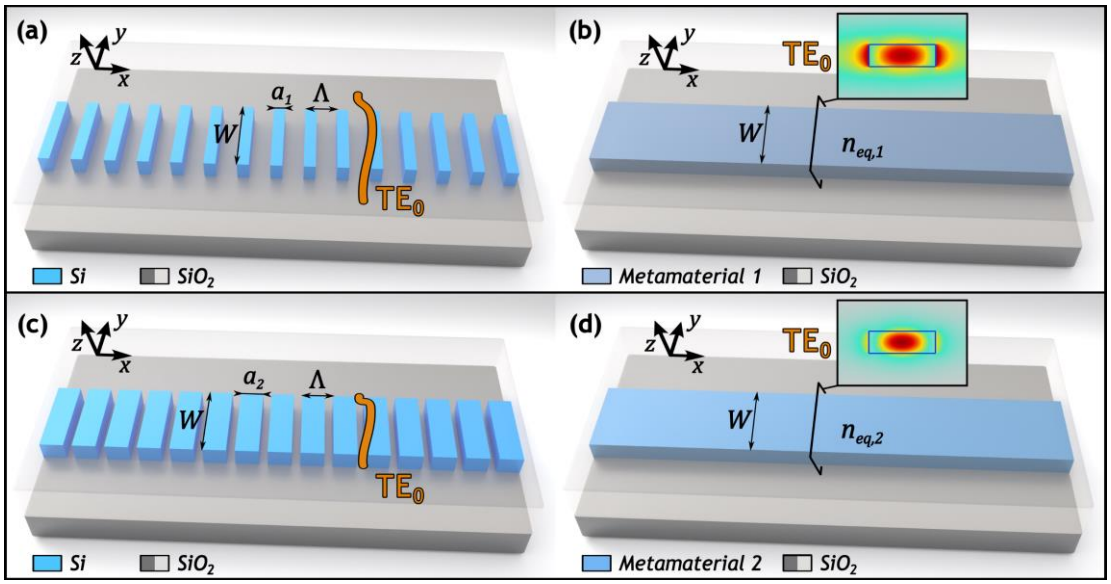

Figure II.5. Schematic representations of SWG waveguides with (a) low duty cycle and (c) high duty cycle. Their corresponding equivalent metamaterial models are shown in panels (b) and (d), respectively. For a waveguide of W = 500 nm and thickness 220 nm, the fundamental TE mode $|E_y|$ field profile is included in the insets for (b) $n_{eq,1}$ = 2.5 and (d) $n_{eq,2}$ = 3.2.

The high index contrast of the SOI platform enables strong modal confinement within the WGs, critical for dense integration of on-chip devices and low propagation losses. However, the confinement of optical modes can limit the interaction between light and adjacent materials, which is desired for certain optical functionalities. Refractive index-engineered SOI waveguides based on SWG provide a solution by accomplishing both robust mode confinement and substantial light-matter

interaction. For instance, light-matter interaction plays a fundamental role in integrated photonic sensors, which commonly depend on the evanescent field [74] of a propagating mode extends into the cladding, enabling the detection of variations in this material. Therefore, variations in the cladding induce changes in the n_{eq} of the equivalent metamaterial. This can be quantified through different methods, including a power difference in the context of a Mach-Zehnder interferometers (MZIs) [75] or a shift in the resonance wavelength for ring resonators [76].

2.4.2. Dispersion engineering

The chromatic dispersion of SWG metamaterial waveguides, representing the variation of the effective index of the Floquet-Bloch mode with wavelength, is governed by the wavelength-to-pitch ratio of the periodic structure. Within the SWG regime, two zones with qualitatively different dispersion behavior can be identified, as illustrated in Figure II.1(d). First, the deep subwavelength regime, where chromatic dispersion is negligible and $n_{eff,F}$ remains nearly constant. In this regime, the major source of dispersion arises from the dispersion of its constituent materials. Second, the region where the Floquet-Bloch mode transitions toward the Bragg regime and chromatic dispersion becomes noticeable, starting to contribute to the overall dispersion characteristics. As k_0 increases, the slope of the $n_{eff,F}$ curve experiences a rapid increase, leading the SWG to exhibit characteristics resembling a material with substantial and tunable chromatic dispersion [73].

Dispersion engineering is a powerful tool for the realization of integrated photonic devices with broad operational bandwidths. By engineering the structural parameters of the SWG, dispersion-dependent design parameters can be achieved to have an ultra-flat profile over a wide range of wavelengths. The analysis presented in [77], which examines a multimode SWG interference structure as a case study, provides a comprehensive overview of dispersion engineering principles. The analysis investigates a SWG multimode-interference structure as a case study and delves into the dispersion equation of a broad anisotropic metamaterial waveguide, with a particular focus on TE polarization. The parameters $n_{eq,x}$ and $n_{eq,y}$ of Equation (2.27), which are analogous to $n_{\perp}$ and $n_{\parallel}$, can be used in Equation (2.22) for an improved description. The propagation wavenumber for the m-th order mode, using a first order Taylor expansion in Equation (2.22) and assuming paraxiality (i.e., $k_{y,m} \ll k_0$), can be approximated as follows [77]:

$$k_{x,m} = n_{eq,y}\left(k_0 - \frac{k_y^2}{2k_0 n_{eq,x}^2}\right) = n_{eq,y}\left(\frac{2\pi}{\lambda} - \frac{\lambda k_y^2}{4\pi n_{eq,x}^2}\right) \tag{2.28}$$

Assuming that the guided modes are well confined in the metamaterial WG, the lateral component y of the wavevector is given by [78]:

$$k_{y,m} = \frac{m\pi}{W_e} \tag{2.29}$$

In this context, the effective width $W_e = W + \frac{\lambda}{\pi}\sqrt{n_{eq}^2 - n_{clad}^2}$ considers the lateral penetration depth of each mode field. The effective refractive index for that Floquet-Bloch mode can be obtained as $n_{eff,F,m} = \frac{\lambda}{2\pi}k_{x,m}$, and the dispersion is calculated by its variability with the wavelength:

$$n_{eff,F,m} = n_{eq,y} - m^2 \frac{\lambda^2 n_{eq,y}}{8W_e^2 n_{eq,x}^2} \tag{2.30}$$

By judiciously engineering the values of $n_{eq,y}$ and $n_{eq,x}$, a value of $n_{eff,F,m}$ independent of the wavelength can be achieved. Dispersion engineering has been successfully applied to different nanophotonic components, providing unprecedented broadband devices, including waveguides [79], phase shifters [80], beam splitters [77], [81], and focusing grating couplers [82], to name a few. Furthermore, it has also been employed to demonstrate the phenomenon of slow light in SWG waveguides, i.e., periodic WGs with a significantly reduced group velocity of light [83].

2.4.3. Anisotropy engineering

The inherent high index contrast of the SOI platform, combined with the prevalent use of waveguides with non-square rectangular cross sections, leads to different light propagation behaviors for TE and TM polarizations. This effect is formally identified as birefringence and is quantified by the expression $B = n_{eff}^{TE} - n_{eff}^{TM}$, where n_{eff}^{TE} and n_{eff}^{TM} are the effective indices of the TE and TM modes, respectively. Novel SWG metamaterial topologies provide extra degrees of freedom to adjust the refractive index allows the index difference between n_{eff}^{TE} and n_{eff}^{TM} to be decreased, facilitating birefringence management. Examples of polarization management devices based on such SWG structures include polarization filters [84], polarization beam splitters [85], [86], rotators[87], [88], and splitter-rotators [89], [90]. Two main advanced SWG topologies have been successfully demonstrated for anisotropy engineering: tilted SWGs [91] and bricked SWGs [92].

2.4.3.1. Tilted subwavelength gratings

Equations (2.22) and (2.23) reveal that for a TM plane wave, the magnitude of the $k_{F,\mathrm{TM}}$ vector is practically independent of the incident angle θ since its electric field is oriented in z-direction. However, a TE plane wave (xy-plane polarized) is strongly dependent on θ because the electric field orientation changes from perpendicular to parallel to the core segment interfaces. Hence, the wavenumber of a TE plane wave varies between $k_{F,\mathrm{TE}}(\theta = 0) = n_{eq,x}k_0$ and $k_{F,\mathrm{TE}}(\theta = 90) = n_{eq,y}k_0$, when the direction of propagation shifts from x to y. Therefore, tilting the silicon segments primarily affects the TE (in-plane) modes, with minimal impact on the TM (out-of-plane) modes, as illustrated in Figure II.5(a). When tilting the segments in the SWG waveguide, the period along the propagation direction (Λ_x) is given by $\Lambda_x = \Lambda/cos(\theta)$. Extending the equivalence between a periodic structure and a uniaxial crystal, the tilted SWG waveguide can be modelled as a uniform waveguide, as shown in Figure II.5(b). The tilt of SWG segments is expressed by a rotation of the permittivity tensor, losing its diagonality in the new nondiagonal tensor [91]:

$$\tilde{\epsilon}(\theta) = \mathrm{T}^{-1}(\theta)\,\epsilon\,\mathrm{T}(\theta) = \begin{bmatrix} \tilde{n}^2_{eq,x}(\theta) & \tilde{n}^2_{eq,xy}(\theta) & 0 \\ \tilde{n}^2_{eq,xy}(\theta) & \tilde{n}^2_{eq,y}(\theta) & 0 \\ 0 & 0 & \tilde{n}^2_{eq,z} \end{bmatrix} \tag{2.31}$$

The rotation matrix in the xy plane is $\mathrm{T}(\theta)$. The elements of the tensor $\tilde{\epsilon}$ are calculated from the tensor components of the non-tilted SWG as [91]:

$$\tilde{n}^2_{eq,x}(\theta) = n^2_{eq,y}\sin^2(\theta) + n^2_{eq,x}\cos^2(\theta) \tag{2.32}$$

$$\tilde{n}^2_{eq,y}(\theta) = n^2_{eq,y}\cos^2(\theta) + n^2_{eq,x}\sin^2(\theta) \tag{2.33}$$

$$\tilde{n}^2_{eq,xy}(\theta) = \left(n^2_{eq,x} - n^2_{eq,y}\right)\cos(\theta)\sin(\theta) \tag{2.34}$$

$$\tilde{n}^2_{eq,z}(\theta) = n^2_{eq,y} \tag{2.35}$$

The component $\tilde{n}^2_{eq,z}(\theta)$ of the tensor remains invariant when tilting the SWG structure. This property allows direct control of the modal birefringence by simply adjusting the tilt angle at a constant duty cycle.

2.4.3.2. Bricked subwavelength gratings

For a brick SWG waveguide as depicted in Figure II.5(c), the SWG silicon segments are also subdivided periodically along the y-axis, characterized by a period Λ_y. The resulting silicon bricks are alternately translated in the x-direction a specific distance Δx. The permittivity tensor $\epsilon(\overline{\Delta x})$ characterizes the behavior of this bricked periodic structure as a uniform anisotropic medium as a function on the normalized translation $\overline{\Delta x} = \Delta x/\Lambda_x$ as [92]:

$$\epsilon(\overline{\Delta x}) = \begin{bmatrix} n^2_{eq,x}(\overline{\Delta x}) & 0 & 0 \\ 0 & n^2_{eq,y}(\overline{\Delta x}) & 0 \\ 0 & 0 & n^2_{eq,z}(\overline{\Delta x}) \end{bmatrix} \tag{2.36}$$

The component of the permittivity tensor $n^2_{eq,z}$ is independent of the block translation, and $n^2_{eq,x}(\overline{\Delta x})$ and $n^2_{eq,y}(\overline{\Delta x})$ are expressed by [92]:

$$n^2_{eq,x}(\overline{\Delta x}) = \frac{n^2_{eq,y}n^2_{eq,x}}{(A + B\,cos(2\pi\overline{\Delta x}))^2} \tag{2.37}$$

$$n^2_{eq,y}(\overline{\Delta x}) = (A + B\,cos(2\pi\overline{\Delta x}))^2 \tag{2.38}$$

$$n^2_{eq,z}(\overline{\Delta x}) = n^2_{eq,y} \tag{2.39}$$

Here A and B are derived from the boundary conditions of $\overline{\Delta x} = 0$ and $\overline{\Delta x} = 0.5$ and are defined as $A = 0.5(n_{eq,y} + \sqrt{n_{eq,y}n_{eq,x}})$ and $B = 0.5(n_{eq,y} - \sqrt{n_{eq,y}n_{eq,x}})$. Comparable to tilted SWG metamaterials, a diverse range of birefringence can be achieved for a fixed period and duty cycle by properly adjusting the translation of the structure.

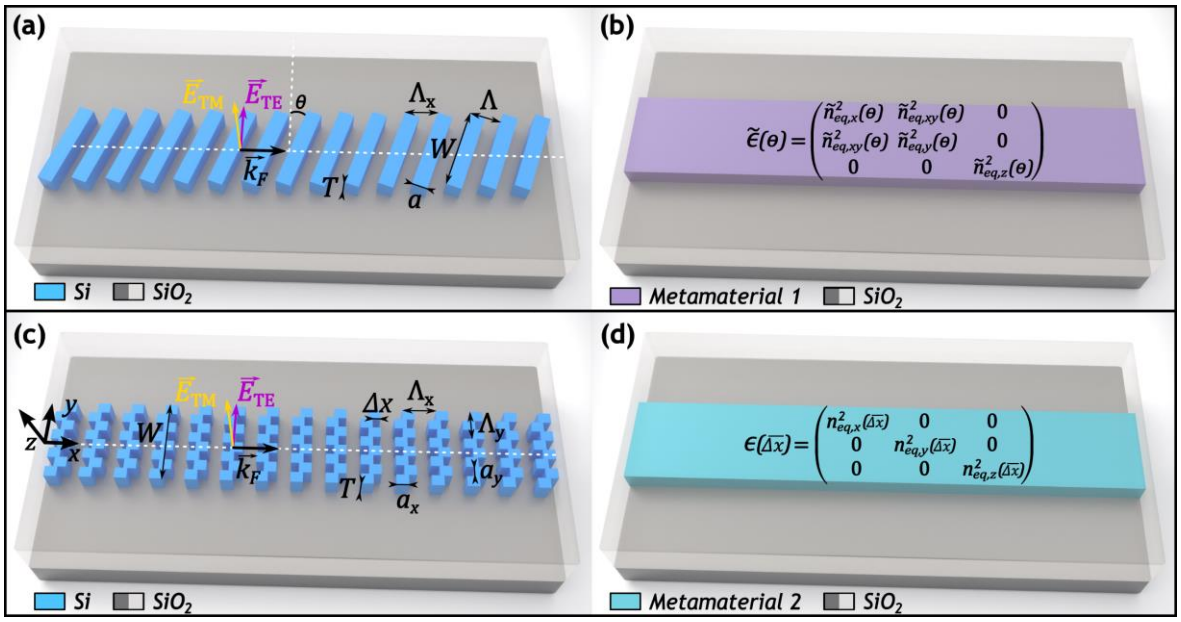

Figure II.6. Schematic representations of (a) tilted SWG waveguides and (b) its equivalent metamaterial; (c) bricked SWG waveguides and (d) its equivalent metamaterial.

2.5. Conclusions

In less than two decades since its inception, SWG metamaterials have witnessed a meteoric rise thanks to their inherent properties and the additional degrees of freedom they offer for the design of photonic components. Manipulation of refractive index, dispersion, and anisotropy within SWG metamaterials has opened the door to the creation of devices with properties that are challenging or beyond the reach of conventional wire or rib waveguides. Their successful implementation in the development of ultra-broadband, low-loss, and fabrication-tolerant building blocks, along with their ability to create polarization management devices, has established SWG metamaterials as an indispensable tool in the design of state-of-the-art silicon photonic devices [67], [93].

Given the rapid evolution of SWG nanostructures, interest arises in exploiting optimization algorithms to explore the vast design space of these metamaterials further efficiently. This places the spotlight on the use of both gradient-free algorithms, based on heuristics such as genetic optimization or direct search, and gradient algorithms, such as the adjoint method. The use of advanced optimization strategies constitutes the cornerstone of the advancement of these breakthrough metamaterials, enabling them to unleash their full potential and, consequently, shaping the future landscape of PICs.

This thesis exploits the innate potential of SWG metamaterials to generate innovative, high-performance Si photonic devices. The results obtained in the field of SWG metamaterial engineering include the realization of a broadband power divider conceived for the first two TE modes

as well as the successful development of a dual-polarized, multimode achromatic power divider. In addition, a novel architecture for efficient and broadband mode conversion is introduced through the synergic application of a gradient-free optimization algorithm and the concepts of SWG metamaterials.

Chapter III:

STATE-OF-THE-ART POWER AND MODAL MANAGEMENT DEVICES

Chapter III offers a thorough exploration of power and modal management nanophotonic devices in the state of the art, examining the diverse structures used for these purposes and the underlying physics governing their operation. In addition, the chapter provides an overview of inverse design optimization techniques and highlights their potential for optimizing device structures to achieve superior performance suitable for next-generation on-chip applications.

Section 3.1 provides an overview of the role of nanophotonic power splitting and mode conversion devices in both emerging and mature on-chip applications. Next, Section 3.2 delves into passive power splitting architectures, presenting the principal structures used for this task in contemporary designs, along with their operating principles. Similarly, Section 3.3 discusses mode converters and their impact on multimode integrated photonics, describing the basic physical principles underlying their realization, as well as their advantages and limitations. The chapter concludes with Section 3.4, which examines device performance enhancement through inverse design optimization techniques. This section describes the principles and methods of inverse design optimization and its relevance to photonics, providing valuable insights into optimizing device structures tailored for next-generation on-chip.

3.1. Introduction

The intrinsic high refractive index contrast of the SOI platform has not only enabled to minimize propagation losses but has also concurrently allowed high-density integration, thereby unlocking the potential for ultra-high-speed data transmission[43], [94]. Beyond its traditional role in telecom and datacom, the unique characteristics of the SOI platform have expanded and revolutionized the landscape of Si photonics. As a result, the potential to realize diverse emerging cutting-edge applications with far-reaching implications on a single silicon chip has ushered in a new era for photonics integration. Some of these applications include neuromorphic photonics [44], 5G-6G communications [45], quantum photonics [41], [46], the Internet of Things [47], LIDAR [26], spectrometry [48], sensing [49], optical processors [42], and on-chip nonlinear photonics [95], [96].

To effectively integrate the aforementioned functionalities into on-chip photonic circuits, it is imperative to develop fundamental building blocks that exhibit minimal losses across broad operational bandwidths, support multiple modes and polarizations, and demonstrate relaxed fabrication tolerances. Despite the impressive progress accomplished in the field of Si photonics, it still remains a significant challenge to meet all of these high-performance requirements simultaneously, especially when involving multiple optical modes or polarization. These challenges mostly arise from the inherent characteristics of dispersion and birefringence, which are strongly related to the high refractive index contrast of the SOI platform.

During the upcoming sections, a comprehensive review of fundamental silicon photonics building blocks is conducted, focused on power splitting and modal management components. This review covers multiple device architectures, discusses design considerations for each structure in relation to their principle of operation, and provides a close look at their advantages and limitations. This approach aims to (i) provide an understanding of the main operation principles and their associated design complexities, (ii) provide a comprehensive view of the related state of the art in order to enable a comparison framework for our own developments, and (iii) identify possible optimization strategies that can be exploited by incorporating subwavelength metamaterials.

3.2. Passive power division architectures

Power splitters stand as indispensable components within virtually every photonic circuit, as they perform fundamental signal handling tasks that are critical to the overall circuit functionality. These essential components are pivotal for controlling the distribution and routing of optical signals in general PICs, as well as for the design of more intricate topologies, such as those within complex large-scale optical networks [97]. Notably, several key on-chip structures heavily depend on power splitters, in particular on 3-dB power splitters. For example, Mach-Zehnder interferometer modulators [98] and multiplexing/demultiplexing systems [99], [100] use power splitters to divide and combine the light, which is a crucial task directly involved in both processes. Other optical devices such as switches [101] or phased arrays [102], [103] benefit from the capabilities of splitters for routing, redirecting and, hence, controlling signal paths. Therefore, power splitters are critical to

provide the flexibility and scalability required to meet the demands of contemporary data transmission systems.

In order to successfully address the ever-increasing data transmission demands, power splitters that operate over ultra-broad bandwidths and support multiple spatial eigenmodes are required. Performance requirements are especially stringent when used in applications such as mode-division multiplexing [100], quantum key distribution [46], and neural networks [104]. Moreover, the development of polarization-independent power splitters is of particular interest to achieve cost-effective and compact transceivers [105], in line with the requisites for high-capacity and low-latency of 5G and next-generation networks [106]. The high-performance of optical power splitters, particularly in terms of losses, operational bandwidth and fabrication robustness, is of utmost importance to ensure the integrity of high-speed optical signals [103].

Numerous power splitting architectures have been proposed in recent years. These architectures can be primarily categorized, based on their operational principles, into multimode interference structures, directional couplers, adiabatic couplers, inverse design structures, and Y-junctions. Each type represents a distinctive power-splitting design paradigm, offering its own advantages and limitations that will be further discussed hereafter.

3.2.1. Multimode interference structures

Multimode interference devices consist of a multimode waveguide as central structure with multiple input and output access waveguides, usually single-mode, to launch and recover light from the multimode region. Depending on the number of inputs (*N*) and the number of outputs (*M*), these devices are defined as *N*×*M* MMI couplers. That is, in a typical 1×2 configuration, light is inserted into a single input port and the power is divided between the two output ports.

MMI devices exploit the self-imaging effect discovered by Talbot [107], where an input field profile is reproduced in single or multiple images periodically along the propagation direction of the light. Ulrich found self-image formation in multimode waveguide [108], and his results constitute the basis for the subsequent contributions of Soldano [78] towards the development of the first MMI devices. The conclusions reached by Soldano can be summarized as follows: high index contrast waveguides where the light propagates through the waveguide core and penetrates the cladding minimally, manifest *Q* multiple images of the input field at certain positions related to the beat length L_π [109]:

$$L_\pi(\lambda) = \frac{\lambda}{2(n_{eff,0}(\lambda) - n_{eff,1}(\lambda))} \tag{3.1}$$

Where $n_{eff,0}$ and $n_{eff,1}$ are the effective indices of the fundamental and the first-order modes (TE_0 and TE_1) of the multimode waveguide of width W_{MMI}, respectively. In a conventional MMI, under the paraxial approximation and considering a two-dimensional (xy plane) approach, the beat length is given by [77]:

$$L_\pi(\lambda) \simeq \frac{4W_e^2}{3\lambda} n_{eff,MMI} \tag{3.2}$$

In the multimode region, the 2D effective index of the multimode waveguide is $n_{eff,MMI}$ and the effective width taking into account the penetration of well-confined optical modes into the cladding is W_e (Equation (2.29)) [78]. W_e is assumed to be identical for all modes and invariant with wavelength. The usual configurations for MMIs as power splitters are 1×N and 2×N, i.e., 1 or 2 inputs and N output waveguides. As an example, in 1×N configuration, the first single image appears at $x_1 = \frac{3L_\pi}{4}$ and Q multiple images of the input field are reproduced at distances in the direction of propagation of $x_q = \frac{3L_\pi}{4Q}$, as illustrated in Figure III.1 [110]. Therefore, a 1×2 MMI power splitter can be designed by selecting a multimode region length of $L_{MMI} = x_2 = 3L_\pi/8$.

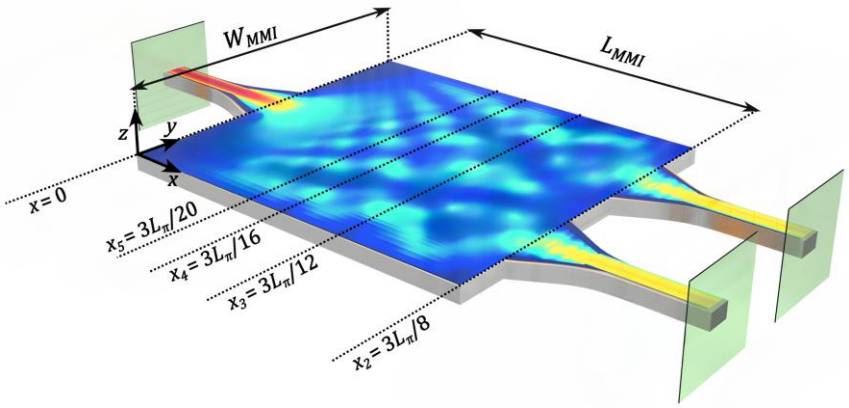

Figure III.1. Schematic representations of a 1×2 MMI power splitter [110].

MMI devices offer numerous advantages, e.g. relatively small size and robust fabrication tolerances, thus ensuring their highly efficiency in applications such as mode multiplexing [100] and polarization splitting [111]. But despite their remarkable characteristics, the operating bandwidth of these devices is limited by the dispersive properties of SOI materials. Since the beat length is inversely proportional to the wavelength, the position of the self-images of each spectral component is different, resulting in performance degradation away from the central design wavelength. To reduce sensitivity to fabrication imperfections and overcome wavelength-dependence, various optimized solutions have been put forth, with the most relevant devices described in [77], [112], [113]. In the approach of Nair et al. [112], the multimode region was carefully designed to control the evolution of the optical field achieving a dual-polarization operation over a broad bandwidth of 400 nm. The splitter designed by Hassan et al. [113] entailed an increase in the waveguide core thickness, from the standard 220 nm to 340 nm, thereby achieving polarization-insensitive operation with low losses.

The broadest bandwidth demonstrated for a MMI structure was obtained by Halir et al. in [77], showing low losses in a wavelength range covering 500 nm. The key strategy to achieve a flat response for their 2×2 MMI power splitter involved leveraging the anisotropy of SWGs and using dispersion engineering to accomplish a wavelength-independent beating length. In their proposed design, shown in Figure III.2, the effective refractive index for the mth mode within the SWG metamaterial can be

approximated to Equation (2.30) [77]: $n_{eff,F,m} = n_{eq,y} - m^2 \frac{\lambda n_{eq,y}}{8W_e^2 n_{eq,x}^2}$. Using this expression into Equation (3.1), the beat length of the SWG metamaterial results in:

$$L_\pi^{SWG}(\lambda) \simeq \frac{4W_e^2}{3\lambda}\frac{n_{eq,x}^2}{n_{eq,y}} \tag{3.3}$$

Halir et al. [77] demonstrates that through a careful selection of the SWG geometric parameters, it is possible to tailor the ratio $n_{eq,x}^2/n_{eq,y}$ to be directly proportional to λ. Therefore, L_π^{SWG} do not depend on the wavelength, mitigating the dispersive effects of conventional MMIs in SOI platform.

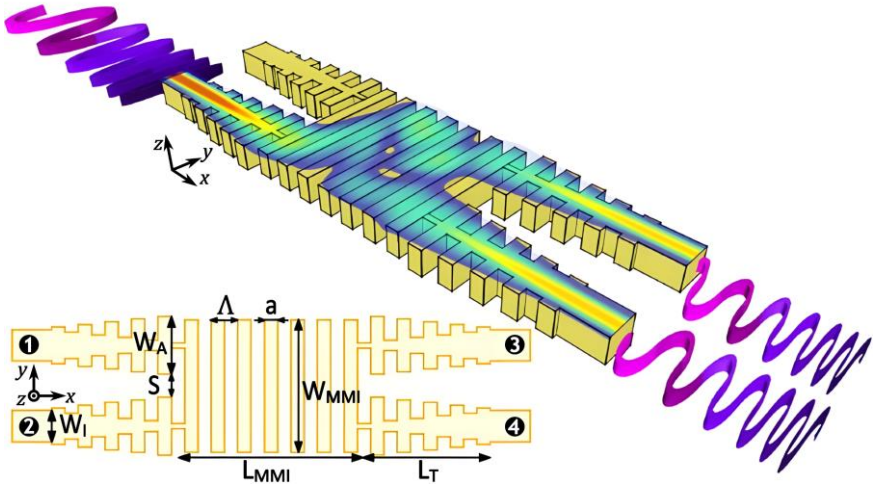

Figure III.2. Schematic representation of the 2×2 MMI power splitter engineered through SWG metamaterials proposed in [77].

3.2.2. Coupling structures

When two or more waveguides are situated in close proximity to each other, a phenomenon known as evanescent coupling enables power transfer between them. This interaction occurs for a certain distance of interaction, often referred to as the coupling length or interaction length. The concept of evanescent coupling was first formally addressed by Marcatili in 1969 [114], later refined in 1986 [115]. The principle of evanescent coupling involves transferring optical power between different waveguides through the evanescent field, that is, the part of the electromagnetic fields that exponentially decays beyond the waveguide core. Considering two parallel waveguides with the same width and thickness, the power in the first waveguides (WG1) is totally coupled to the second waveguide (WG2) at a certain distance of interaction. Therefore, at any arbitrary position, the fraction of the power coupled from WG1 to WG2 is dependent on the length of the interaction region between the waveguides and their separation.

There are two main optical coupling structures that depend on periodic evanescent coupling between parallel waveguides, albeit with distinct design principles, which will be further discussed in the next subsections.

3.2.2.1. *Directional couplers*

Let's consider two waveguides that are laid out physically close to each other. By treating both waveguides as a single composite waveguide structure, a comprehensive analysis of the guided modes is allowed. The field expressions therein adhere to Maxwell's equations and fulfill all boundary conditions pertinent to the composite structure. The resulting modes, referred to as the supermodes of the composite waveguide, accurately depict the electromagnetic behavior within the structure. If the two waveguides are identical (i.e., same shape, width, and thickness), the normal mode fields exhibit either symmetric or antisymmetric profiles with respect to the centerline of the composite structure (dash-dot-dash line in Figure III.3). Figures III.3(a) and 3(b) illustrate the field distributions of the two lowest-order symmetric and antisymmetric supermodes of two equal coupled waveguides, respectively. The symmetric supermode $\vec{E}_S$, with effective index $n_{eff,S}$, and antisymmetric supermode $\vec{E}_A$ with effective index $n_{eff,A}$. The expression of the total propagating field ($\vec{E}_T$, along the x direction) can be expressed as the addition of each supermode field [116]:

$$\vec{E}_T(x,y,z) = \vec{E}_S(y,z)e^{-j\frac{2\pi}{\lambda}n_{eff,S}\,x} + \vec{E}_{AS}(y,z)e^{-j\frac{2\pi}{\lambda}n_{eff,A}\,x} \tag{3.4}$$

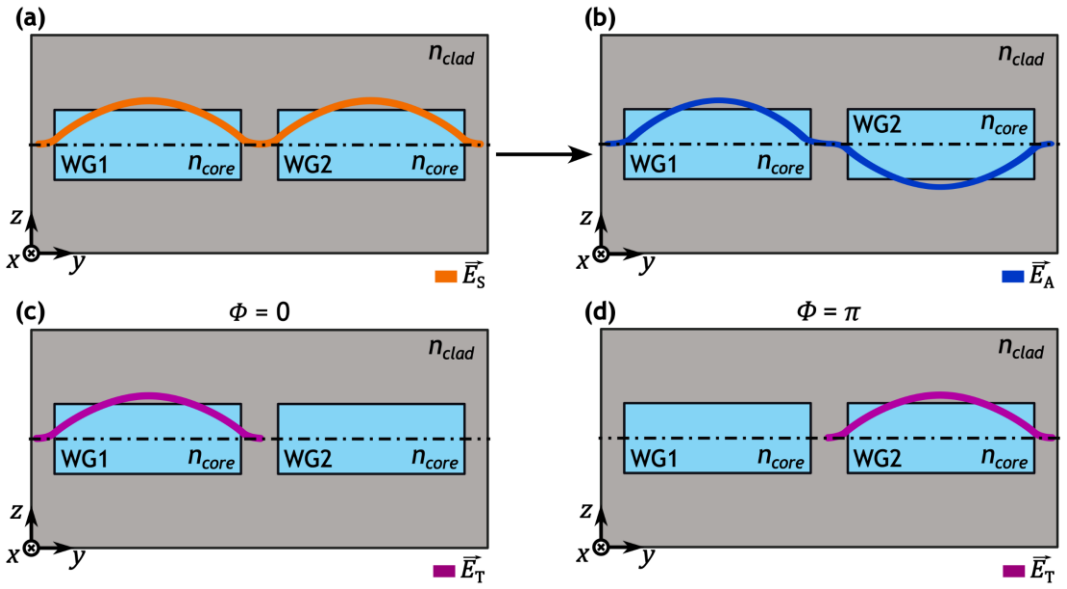

Figure III.3. Schematic of directional coupler supermodes for (a) symmetric and (b) antisymmetric supermode field distributions. The total field of the modal overlap is presented in purple for different phase shifts between the supermodes: (c) $\phi = 0$, (d) $\phi = \pi$.

If two supermodes of equal power are considered, the phase shift difference between them, denoted as $\phi = \frac{2\pi}{\lambda}(n_{eff,S} - n_{eff,A})$, will establish where power is localized in the composite waveguide structure. When the two supermodes are in phase ($\phi = 0$) the power becomes localized in WG1, as depicted in Figure III.3(c). Conversely, if the two supermodes are in counter phase, $\phi = \pi$, the power is localized in WG2, as shown in Figure III.3(c). The minimal interaction length required for a complete power crossover between the two waveguides is referred to as the coupling length (L_C). L_C is as a quantitative measure of interaction or coupling strength and can be determined using the equation provided by reference [12].

$$L_C(\lambda) = \frac{\lambda}{2(n_{eff,S}(\lambda) - n_{eff,A}(\lambda))} \tag{3.5}$$

Then, complete power crossover occurs at discrete locations which are odd integer multiples of L_C: $x_C = (2n+1)L_C$. In the case where the two waveguides are not identical, the fields do not exhibit symmetric or antisymmetric behavior and the subscripts S and A lack physical significance. The extensive mathematical development for the analysis of non-identical waveguides can be found in the referenced literature [117], as it exceeds the scope of this thesis.

Directional couplers can be easily designed to split power into different ratios, such as 90:10, 60:40, or 50:50, by readily modifying their interaction length. In particular, directional power splitters can achieve equal power division (commonly known as the 3 dB configuration) by setting an interaction length of $Lc/2$, as shown in Figure III.4 [118]. Looking into Equation (3.5), it is easy to see that directional couplers suffer from the same bandwidth limitation as MMIs structures and exhibit high sensitivity to fabrication errors. Nonetheless, these devices have demonstrated remarkable results in applications including mode conversion [119], mode multiplexing [120] and biosensing [121].

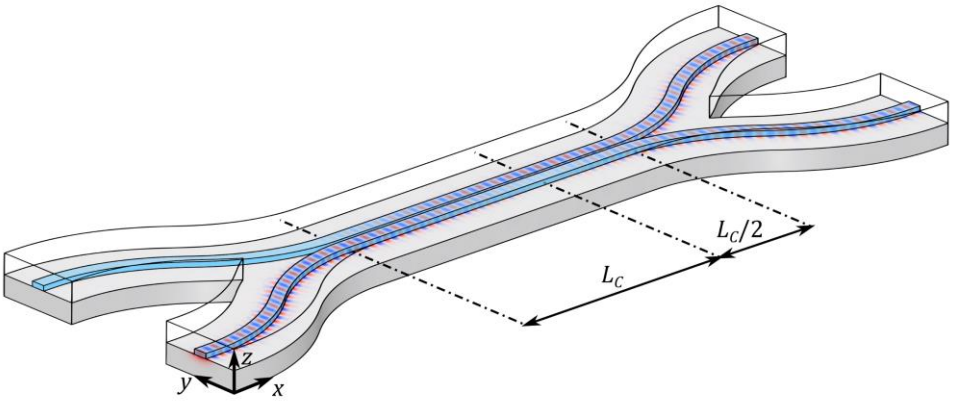

Figure III.4. Schematic of a 3-dB directional coupler power splitter [118].

In order to address the wavelength dependency inherent in conventional directional coupler splitters, multiple solutions have been proposed using geometric design strategies. Bent directional couplers use curved waveguides within the coupling region [122], while asymmetric directional couplers feature waveguides with distinct cross-sectional shapes and dimensions [123], allowing for tailored light coupling behaviors. In [124], Gupta et al. utilize shallow-etched coupling waveguides, that is, the waveguides within the power coupling region are partially etched and present a rib waveguide structure in this area. These design enhancements contribute to polarization-insensitive responses, although with operational bandwidths typically not exceeding 100 nm.

Directional couplers have been effectively demonstrated using SWG metamaterials [81], [125], [126]. Ye and Dai [126] presented a compact broadband 2×2 3-dB power splitter by utilizing an SWG-assisted asymmetric directional coupler, illustrated in Figure III.5(a). Their splitter achieves an

operational bandwidth of 300 nm in simulations and experimentally validated 200 nm with subdecibel loss for the TE_0 mode. The straight coupling region of the device integrates SWG metamaterials to engineer mode dispersion, thereby increasing the operational bandwidth of the device. Specifically, the SWG region, that can be seen in Figure III.5(b), reduces the effective index contrast of the optical waveguides. The use of SWG in their design results in improved coupling strength and a shorter coupling length.

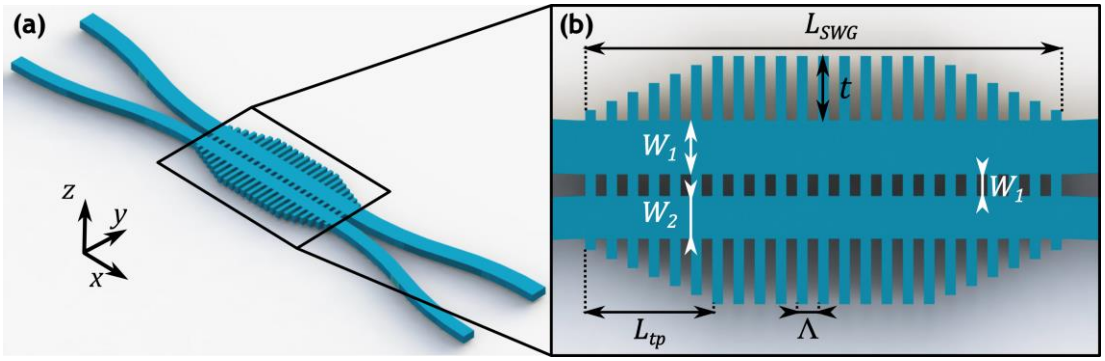

Figure III.5. (a) Schematic of the 3-dB SWG-assisted asymmetric directional coupler demonstrated in [126] with (b) an inset of the SWG coupling region.

3.2.2.2. *Adiabatic couplers*

Adiabatic couplers rely on the gradual transition of the guided mode characteristics as the waveguide geometry changes, referred to as mode evolution. This evolution occurs adiabatically, without significant mode coupling or radiation loss. These structures use tapered waveguides to ensure smooth and adiabatic transitions. The key physics involved include the conservation of energy and the avoidance of abrupt transitions. As the waveguide geometry varies, such as in tapering or bending, the mode adapts to these changes by redistributing its energy. This process relies on a slow variation of the waveguide parameters compared to the characteristic wavelength of the guided mode. If the changes occur too rapidly, non-adiabatic transitions may lead to energy loss or mode conversion. Achieving adiabatic mode evolution is essential for efficient light confinement and propagation in integrated optical devices.

The main difference between adiabatic and directional couplers lies in their approach to achieving efficient power transfer and mode preservation. Adiabatic couplers operation is based on the evolution of a single normal mode, driven by the gradual change in the device shape over distance, rather than the interference between two modes. These couplers are inherently low-loss, polarization-insensitive, and tolerant to fabrication imperfections. However, adiabatic operation usually requires an increased device length, typically greater than 100 µm [127], [128]. Recent advances have led to the development of compact adiabatic couplers that employ linear tapered profiles. For instance, the splitter proposed by Wang et al. in [129] has just a 5 µm length with a 30 nm MFS, beyond the DUV lithography limit of state-of-the-art silicon photonics foundries. In [130], Ozcan et al. device achieve minimal measured losses within a 100 nm bandwidth for a compact 14-µm-long device.

Significant achievements have been made using SWG metamaterials for the development of compact and broadband adiabatic couplers. An interesting approach was reported in [131] by Yun et al., using

SWG-assisted strip waveguides with a narrow central strip waveguide flanked by wide symmetric subwavelength fins. These waveguides are engineered to present higher refractive indices than conventional SWG waveguides but significantly lower refractive indices than conventional strip/rib waveguides. This design facilitates a compact configuration with a total length of 35 μm and achieves a broad measured bandwidth of 185 nm. A SEM image of the fabricated device is depicted in Figure III.6(a). Recently, in the study by Hu et al. [132], another significant achievement was presented: a 3-dB directional coupler using trapezoidal SWGs and a reversely tapered wire waveguide, specifically designed for TE_0 mode operation. This coupler, shown in the SEM image of Figure III.6(b), exhibited minimal measured losses over a bandwidth of 270 nm and a total length of 24.4 μm. The design of this coupler consists of a trapezoidal SWG waveguide coupled to an inversely tapered wire waveguide. The narrow part of the trapezoidal subwavelength segments is gradually reduced to adjust the coupling strength between the two waveguides. This variation of the coupling strength along the propagation direction decreases wavelength sensitivity, expanding the operational bandwidth of the device.

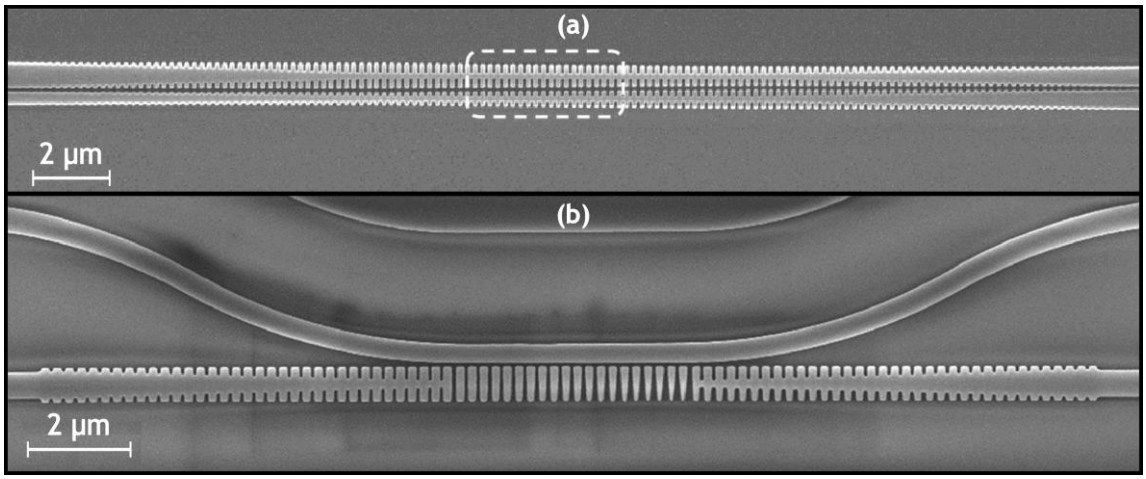

Figure III.6. SEM images of the fabricated 3-dB SWG adiabatic couplers proposed in (a) Ref. [131] and (b) Ref. [132].

3.2.3. Y-junctions

Y-junctions receive their name from their peculiar "Y" topology and consist of a stem waveguide that branches into two or more diverging arms. Y-junctions are one of the most widespread components in photonic systems, providing multiple functionalities including beam splitting and modal conversion. Their structure can have symmetric or antisymmetric characteristics, depending on their particular application. The functionality of asymmetric and symmetric Y-junctions, as well as their ability to split multiple modes at the junction, is highly dependent on the number of modes supported by the stem waveguide [133]. As will be discussed later in this section, this consideration has a major impact on the operating principles and performance characteristics of Y-junction devices.

3.2.3.1. *Asymmetric Y-junctions*

The asymmetric configuration [134] of Y-junctions is characterized by having arm waveguides with different widths. To understand the operation of asymmetric Y-junctions, let's consider the scenario where a single-mode stem waveguide (port 1) splits into two arm waveguides, one wider (port 2) and the other narrower (port 3). Considering TE polarization, an input TE_0 mode travels through the stem waveguide with an effective index $n_{eff,0}^{(1)}$ and, upon reaching the junction, it transitions to the TE_0 mode of the wider arm with an effective index $n_{eff,0}^{(2)}$. This transition occurs because $n_{eff,0}^{(1)}$ is closer to the index of the wide arm than to the index of the narrow arm ($n_{eff,0}^{(3)}$): $|n_{eff,0}^{(1)} - n_{eff,0}^{(2)}| < |n_{eff,0}^{(1)} - n_{eff,0}^{(3)}|$. This index-matching principle also determines the behavior of asymmetric Y-junctions with a multimode stem waveguide: each mode in the stem exhibits a strong preference for the arm that supports a mode with a similar effective index to that of the stem mode. The mode-sorting for an asymmetric Y-junction with a multimode stem waveguide that supports the three lowest-order TE modes and single-mode arm waveguides is illustrated in Figure III.7. It is important to note that as the mode order increases, its effective index decreases compared to modes of lower order: $n_{eff,0}^{(1)} > n_{eff,1}^{(1)} > n_{eff,2}^{(1)}$. On the other hand, the effective index of the fundamental mode in the wider arm is higher than the index in the narrower arm: $n_{eff,0}^{(2)} > n_{eff,0}^{(3)} > n_{eff,0}^{(4)}$. Hence, in this specific example, the TE_0 mode of the stem transitions into the TE_0 mode of the wider arm, while the TE_1 mode of the stem transforms into the TE_0 mode of the middle arm, and the TE_2 mode of the stem converts into the TE_0 mode of the narrower arm.

Although less prevalent than their symmetric counterparts, asymmetric Y-junctions have found applications in diverse areas such as mode converters and multiplexers [135], and as variable power splitters [136], among others.

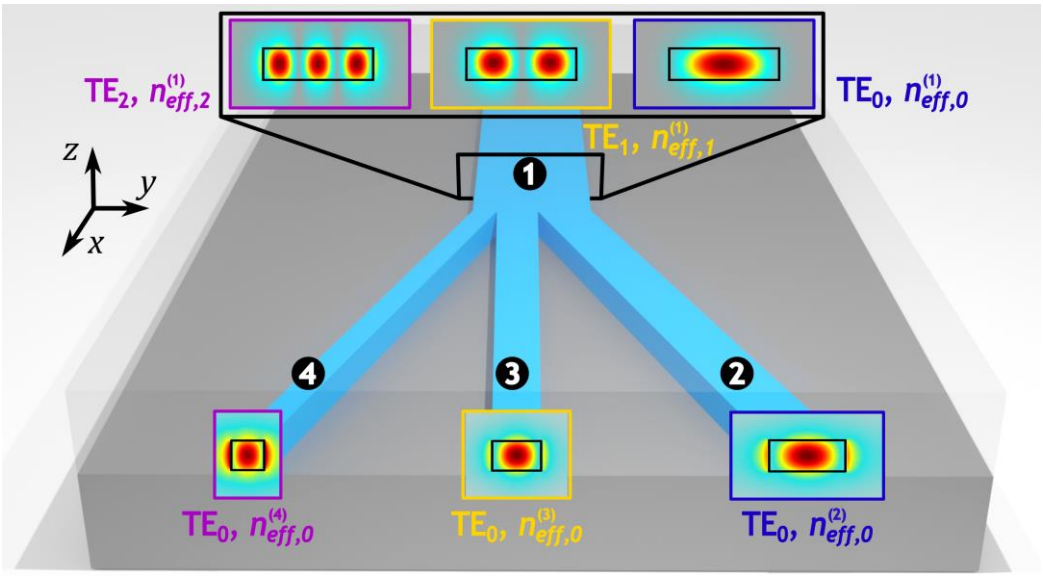

Figure III.7. Schematic of an asymmetric Y-junction configuration with a multimode stem supporting the three lowest-order TE modes. Each mode profile ($|E_y|$) is shown in insets, and its evolution into the corresponding arm waveguide according to the index-matching principle is represented.

3.2.3.2. Symmetric Y-junctions

In symmetric configuration, the Y-junction comprise a stem waveguide that branches into two diverging arm waveguides of equal width and their main function is power splitting [133]. The typical symmetric Y-junction configuration to develop 3-dB power splitter comprises two output arms of equal width, with a given angle between the branching arms (2θ). An ideal adiabatic transition in symmetric Y-junctions minimizes losses and ensures a polarization- and wavelength-independent spectral response for supported modes. This adiabaticity is only possible when the angle θ is small enough to achieve a smooth transition [137].

For a symmetric Y-junction with a multimode stem waveguide of width W_S, each spatial mode exhibits specific behavior. Consider a symmetric Y junction supporting both fundamental and first order modes in the stem waveguide, as shown in Figure III.8. The power distribution of the fundamental mode is equally divided into two in-phase fundamental modes, one on each output arm, as a consequence of the symmetry of the device. Similarly, for the first-order mode, the power is evenly distributed between the fundamental modes of the output arms, but the relative phase between them (φ) is π.

When analyzing symmetric Y-junctions that support higher-order modes beyond the first-order mode, it is crucial to consider their optical mode evolution and conversion properties [137], [138], [139]. To facilitate this analysis, Y-junctions are treated as a two-dimensional planar layer configuration, as shown in Figure III.9.

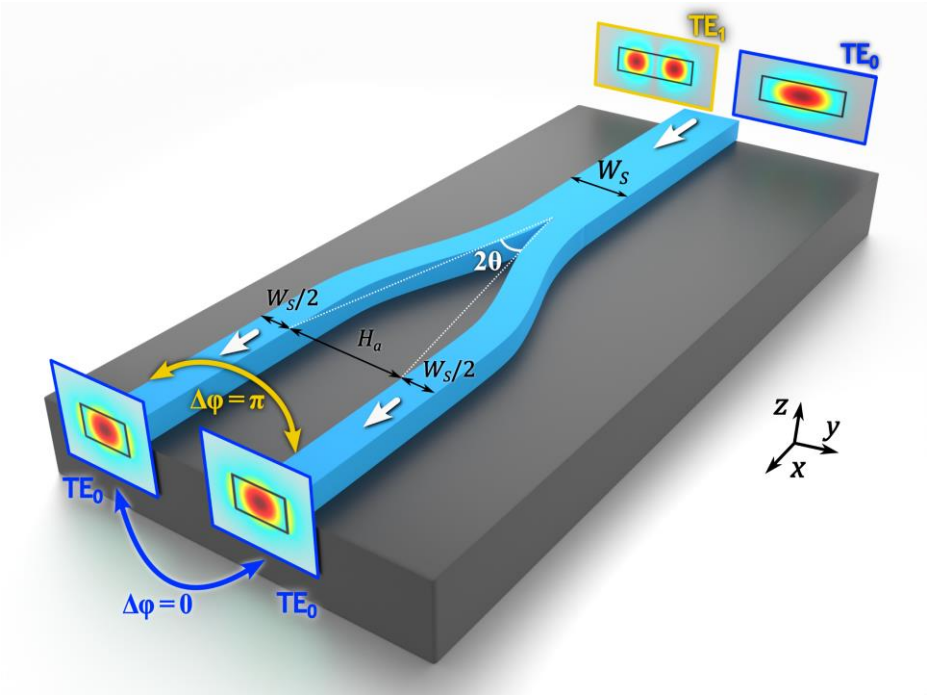

Figure III.8. Schematic of a symmetric Y-junction configuration with a multimode stem supporting the two lowest-order TE modes. Each mode profile ($|E_y|$) is shown in insets, and its evolution with the corresponding phase difference ($\Delta\varphi$). The cladding has been omitted for clarity.

The input stem section is structured as a typical slab waveguide (see Figure III.9), comprising three dielectric layers with different refractive indices arranged as cladding – core – cladding (n_{clad} - n_{core} - n_{clad}). Similarly, the output arm waveguides in a conventional double-arm Y-junction feature a five-layer symmetric structure: cladding – core – cladding – core - cladding (n_{clad} - n_{core} - n_{clad} - n_{core} - n_{clad}). In this approach, the separation between the arm waveguides ($2d$) is a function of the distance to the junction tip (x_T): $d = x_T tan(\theta)$.

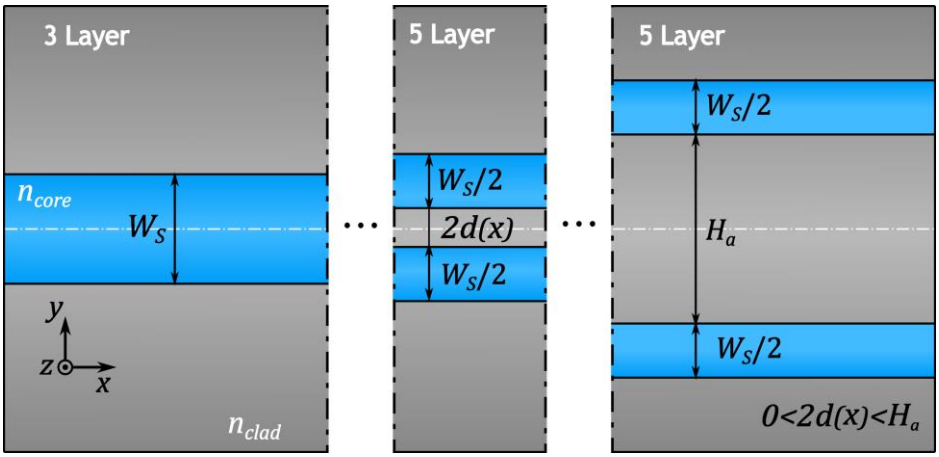

Figure III.9. Symmetric Y-junction representation as a 2D dielectric layer structure.

When the modal transition at the stem-arms interface is not perfectly adiabatic, such as for angle values not sufficiently small, these devices induce modal conversion. This means that a portion of the power from the mode of order m is converted into the mode of order m'. Mode conversions are limited to either even-to-even or odd-to-odd modes because of the intrinsic symmetry of these devices [140]. The calculated overlap integral at the interface between the stem and arm waveguides, which includes the incident and transmitted fields, determines the amount of power conversion between modes [137]:

$$c^t_{m,m'} = \frac{1}{\omega\mu_0}\frac{k^i_{x,m}k^t_{x,m'}}{k^i_{x,m}+k^t_{x,m'}}\int_{-\infty}^{\infty} E^i_{z,m}(E^t_{z,m'})^* dy \tag{3.6}$$

The quantification of transmitted power between the input mode of order m into the output mode of order m' is contingent upon the branching angle and the difference between its wave vectors in the propagation direction (k_x) in the three-layer ($k^i_{x,m}$) and five-layer ($k^t_{x,m'}$) guided wave mode. The incident field (E^i_z) corresponds to that present in a typical three-layer slab waveguide. Then, the field transmitted to the output branching arms waveguides can be approximated by [137]:

$$E^t_z(y) = B(d)E_z(y,d)e^{\left(-j\cos\theta\int_0^x k_x(x')dx'\right)}e^{(-jk_x|y|\sin\theta)} \tag{3.7}$$

The electric field $E_z(y,d)$ is the corresponding guided-TE mode in a symmetric five-layer waveguide and $B(d)$ is a normalizing factor.

If the modal transition at the junction is completely adiabatic, the behavior of symmetric Y-junction for high-order modes can be described as follows. When an input mode of order m propagates through the stem, it splits at the junction into the two modes of order $m/2$ of each arm when m is even, and

into the two modes of order $(m-1)/2$ of each arm when m is odd. The relationship between the output modes in the arms is determined by changes in modal symmetry at the stem-arms transition. When an even mode in the stem transitions to two even modes at the arms, the resulting output modes are in phase. In contrast, if an even mode in the stem transitions into two odd modes at the arms, the two output modes have a π phase difference between them. Likewise, when an odd mode in the stem transitions to two odd modes at the arms, the resulting output modes are in phase; whereas if an odd mode in the stem transitions into two even at the arms, the two output modes have a π phase difference between them.

To visualize this behavior, Figure III.10 displays a symmetric Y-junction operating for the first four-order modes. The operation for TE_0 (blue) and TE_1 (yellow) modes remains consistent with the explanation provided in Figure III.8. In the case of TE_2 (purple) and TE_3 (green) modes injected through the stem waveguide, they produce two anti-phase TE_1 and two in-phase TE_1 modes at the arms, respectively.

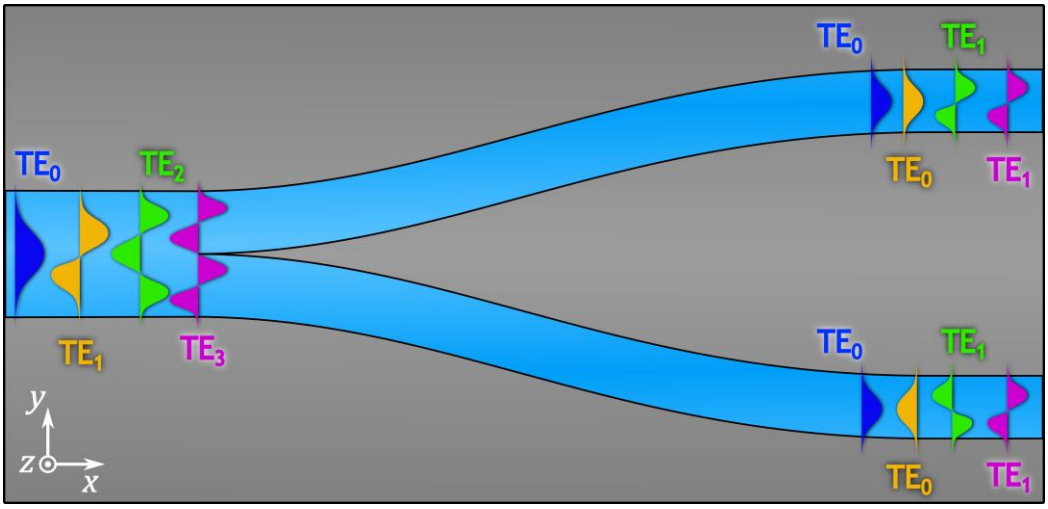

Figure III.10. Schematic and principle of operation of a multimode symmetric Y-junction for a four-mode stem waveguide.

In ideal Y-junction structures, the tip between the arm waveguides gradually widens from zero spacing. This is challenging given the MFS limitations of current fabrication technologies, yielding an imperfect tip [141]. This constraint on MFS results in significant losses for even modes, as the maximum of their power profile is aligned with the junction tip. Conversely, this effect is negligible for odd modes, as they present a zero-power profile at the stem waveguide center. Different optimized solutions have been proposed to mitigate the impact of the MFS at the tip, ranging from tapered and slotted waveguides [130], [142], [143], [144], inverse design algorithms [141], [145], and photonic crystals [146], [147].

Despite the plethora of power splitter architectures proposed to date, performance improvements are still sought after. In particular, there is still the need for a low-loss compact device for multiple modes over an ultra-broad bandwidth along with relaxed fabrication tolerances.

3.3. Mode conversion architectures

Mode converters are key components in multimode photonic systems, enabling the transformation of a given spatial mode into any other desired mode and vice versa. The conversion between two modes can be mathematically described by the following mode-coupling equations [35]:

$$-\frac{\partial A}{\partial x} = j\kappa_{ab} B e^{j(k_{x,a} - k_{x,b})x} \tag{3.8}$$

$$-\frac{\partial B}{\partial x} = j\kappa_{ba} A e^{j(k_{x,b} - k_{x,a})x} \tag{3.9}$$

where A and B are the amplitudes of waveguide modes of order a and b, respectively. The propagation constants of the two modes are $k_{x,a}$ and $k_{x,b}$. The coupling coefficients representing the power exchange are κ_{ab} and κ_{ba} from mode a to b and from b to a, respectively.

Mode conversion is an indispensable function for multimode silicon photonic systems, which is a powerful approach for the development of both emerging and established fields. For example, modal manipulation enabled by mode converters is useful to advance practical applications, including on-chip nonlinear photonics [42], [95], [96] and quantum information processing [41], [148]. In MDM systems, mode converters are essential at both transmitting and receiving ends [149]. MDM techniques allow for the simultaneous transmission of multiple signals through different-order optical modes within a single waveguide. Some studies have also explored strategies that combine WDM with broadband MDM systems for on-chip and off-chip high-bandwidth-density interconnects [40].

Considering this wide range of potential applications, broadband, low-loss, low-crosstalk and compact sizes are critical specifications for mode converters. Four main types of mode converters have been proposed, each employing different designs based on their respective operation principle: phase matching, beam shaping, constructive interference of coherent scattering and induced gradient phase [35].

3.3.1. Phase matching

In the context of mode converters, phase matching is a crucial concept that involves aligning the effective indices of modes with different orders. To further understand this phenomenon, consider the transition of a mode from a narrower waveguide to a wider one. This transition induces a shift in the effective refractive index of the mode, caused by the change in geometric dimensions and possible variations in material properties between the waveguides. In certain configurations, the effective refractive index of the mode in the narrower waveguide matches the effective refractive index of another mode within the wider waveguide, allowing mode conversion. This statement implies that the energy carried by the mode in the narrower waveguide can be effectively transferred to the mode in the wider waveguide. Phase matching is not only dependent on the dimensions of the waveguides but is also affected by variables such as wavelength, polarization, and material properties. Hence,

careful design strategies and optimization techniques are critical for achieving efficient mode conversion by satisfying phase-matching conditions.

In [150], [151], Dai et al. proposed a mode (de)multiplexer comprising mode converter structures, based on adiabatic asymmetric directional couplers, at the input and output waveguides. The mode conversion structure transforms the fundamental mode in the narrow input/output waveguide of width $W_b(x)$ into the ith-order mode of the multimode bus waveguide of width $W_a(x)$ over a bandwidth of ~90 nm. Figure III.11 shows the design of Dai's mode converter structure for the specific scenario of TE_0-to-TE_1 conversion.

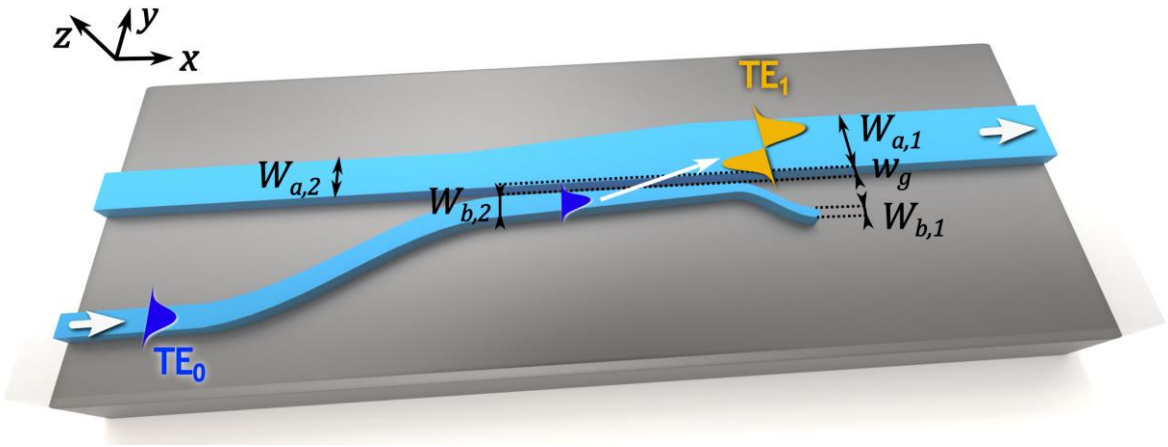

Figure III.11. Schematic and principle of operation for TE_0-to-TE_1 conversion of the device proposed in [150].

Mode conversion between the TM fundamental mode and first-order TE modes, based on the phase-matching technique, was proposed in [152] using adiabatic tapers. This device yields robust fabrication tolerances and a broad bandwidth, at the expense of a total length of almost 300 μm to satisfy the adiabaticity criterion. Mode converters based on adiabatic couplers possess the advantage of high performance and scalability of the number of channels, at the cost of stringent precision requirement on the coupling length and coupling strength, as well as a relatively long conversion length. Other mode conversion approaches that rely on the phase-matching condition have been proposed, such as directional grating couplers [153] and contra-directional grating-assisted couplers [154]. An adiabatic directional coupler based on SWGs was also introduced in [155] to achieve a TE_0-to-TE_{12} mode converter with losses below 1.5 dB across a 75 nm bandwidth, while also benefiting from relaxed fabrication tolerances. Although these approaches allow for the realization of compact devices, their bandwidths are typically limited to a few nanometers owing to their resonant coupling nature.

3.3.2. Beam shaping

Beam shaping is a versatile method for manipulating the mode order in multimode systems, involving the combination of optical modes from separate waveguide branches, each with its own phase, to

form the desired mode in a multimode bus waveguide. Careful control of mode evolution within each branching waveguide, including modifications to phase relationships and power distribution among the branches, is necessary to achieve mode-order conversion between the different supported modes. The practical implementation of this method requires precise design of the geometry, dimensions, and refractive indices of the branching waveguides to control mode evolution and interference patterns.

For instance, the mode order converter proposed in [156] consists of a waveguide-based Mach-Zehnder interferometer, as depicted in Figure III.12. It comprises two single-mode waveguide arms with an optical path difference denoted by $\Delta\varphi$. In a TE_0-to-TE_1 mode conversion scenario, the input waveguide only supports the fundamental mode while the output waveguide is a multimode optical waveguide capable of accommodating both TE_0 and TE_1 modes. The device is dependent on the optical path difference, which is inversely proportional to the wavelength, and thus exhibits a limited operational bandwidth.

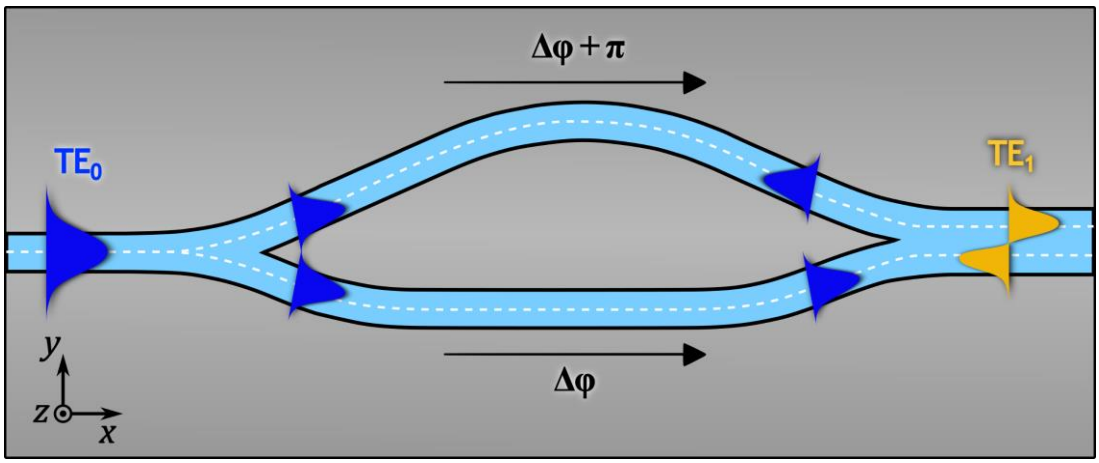

Figure III.12. Schematic and principle of operation for TE_0-to-TE_1 conversion of the device proposed in [156].

Differential waveguides in an MZI structure can provide a broad bandwidth, as shown in [157], but at the cost of compactness. The work in [158] introduces a mode conversion device that transforms the fundamental mode into higher order modes for TM polarization. The device, shown in Figure III.13(a), uses asymmetric graded index structures, which rely on the refractive index variations of two distinct asymmetric gradient profiles implemented through periodic structures commonly known as photonic crystals. While this technology allows for more compact device designs, simulated transmission efficiency is only about 80%. As mentioned in the previous section (3.2.3.1), asymmetric Y-junctions can be used for mode conversion, also referred to as mode sorting in these devices. The study in [159] showcased aggregate bandwidths of 20 Gb/s and 60 Gb/s for on-chip links employing MDM and MDM-WDM, respectively, using asymmetric Y-junctions as illustrated in Figure III.13(b), with measured power penalties below 0.7 dB.

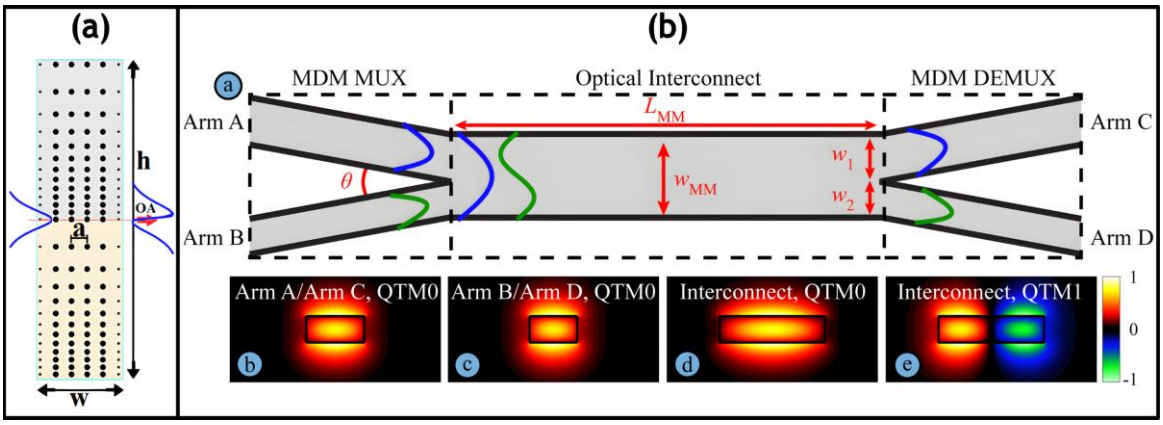

Figure III.13. Schematic and principle of operation for TE_0-to-TE_1 conversion of the device proposed in (a) [158] (b) and the MDM system demonstrated in [159].

3.3.3. Constructive interference of coherent scattering

Mode conversion based on the constructive interference of coherent scattering lies in the transformation of an input mode into multiple high-order modes. These modes interact within a multimode interference region, resulting in a distinct mode profile at the output of the interference area. This method was first implemented in MMI couplers with conversion lengths of several hundred microns [160]. Recently, a two-mode converter and (de)multiplexer based on a SWG-MMI, a symmetric Y-junction and a 90º phase shifter was demonstrated in [100], as shown in Figure III.14. This device combines the previous method of beam shaping with constructive interference of coherent scattering. Coherent scattering occurs within the MMI, while the Y-junction is used for power distribution, acting as the beam-shaping component. González-Andrade et al. achieved simulated operational bandwidth of 300 nm, shortening the length of the MMI structure to tens of microns [100].

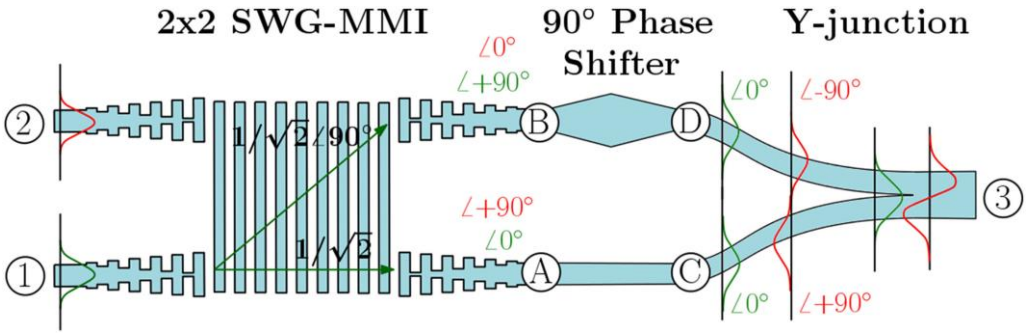

Figure III.14. Schematic and principle of operation of the two-mode converter and (de)multiplexer based on a SWG-MMI, a symmetric Y-junction and a 90◦ phase shifter, proposed in [100].

Nevertheless, the total channel capacity is limited by the number of output ports in the MMI coupler, analogous to branching waveguide mode converters. Alternative approaches based on engineered waveguide structures have been proposed to achieve mode conversion over very short distances, typically only a few microns. These include the introduction of defects into photonic crystal waveguides [161] and the use of computer-designed nanostructures based on inverse design

algorithms [162]. Despite being the most compact devices reported to date, these structures typically involve reduced MFSs that require high-precision fabrication techniques, making them less attractive for practical applications.

3.3.4. Induced gradient phase

Mode conversion in a waveguide can also be accomplished by perturbing its refractive index, causing a phase imbalance in the propagating light. This perturbation, which can be achieved by methods such as introducing defects, changing the material composition, or modifying the waveguide geometry, induces a phase gradient. Metasurfaces or metamaterials, for example, can introduce this phase gradient, resulting in a non-uniform phase distribution along the waveguide length to drive mode conversion between two specific modes.

The device reported in [163] utilizes a graded index co-directional grating coupler. This coupler has a periodic variation in refractive index along the propagation direction and a graded index profile along the transverse direction. These design elements enable the realization of a 20-μm-long mode converter. In [164], two compact mode converters are engineered for the exchange between TE_0-to-TE_1 and TE_0-to-TE_2 modes through the utilization of silicon metamaterial structures, illustrated in Figure III.15(a) and (b), respectively. The fabricated devices demonstrate measured losses ranging from 0.2 to 0.3 dB across a wavelength span of 87 nm. In [165], TE_0-to-TE_1 and TE_0-to-TE_2 mode converters have also been proposed and experimentally demonstrated all-dielectric metasurface structure with tilted SWGs, represented in Figure III.15(c) and (d), respectively.

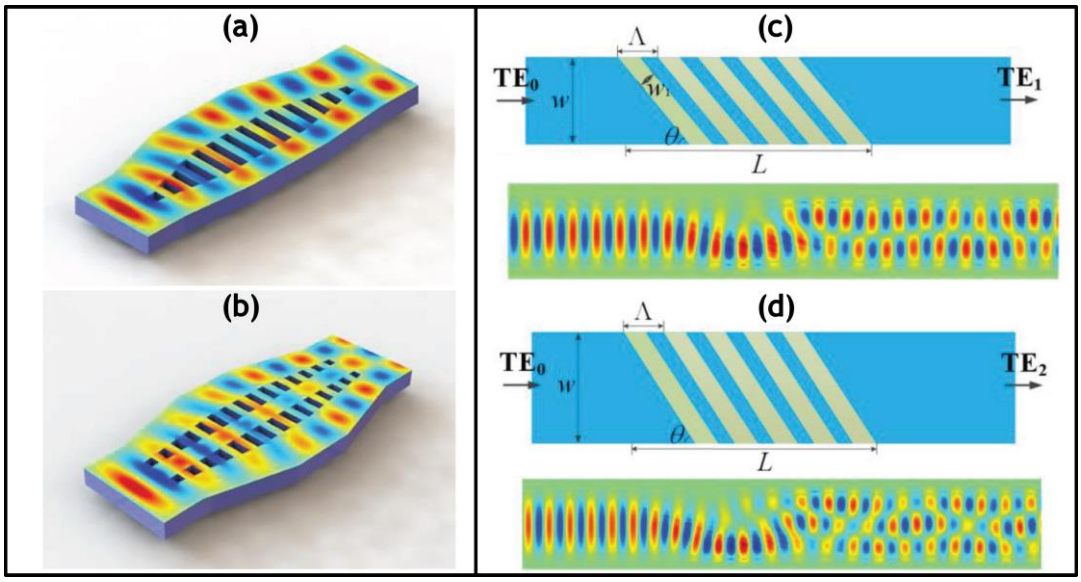

Figure III.15. Schematic of the mode converter structures proposed for TE_0-to-TE_1 operation in (a) and (c), and TE_0-to-TE_2 operation in (b) and (d). The designs from [164] are illustrated in panels (a)-(b), while (c)-(d) depict the configurations from [165].

Mode converters based on this principle are compact and can efficiently exchange power between different modes over broad wavelength ranges with robust fabrication tolerances. This method has the potential to provide high quality mode conversion, and thus it is recently attracting research interest.

3.4. Enhancing device performance: Inverse design optimization

The development of novel devices has traditionally relied on the theoretical study of the underlying physics to create structures that yield suitable responses. The design parameter space is explored sequentially, typically by computing performance metrics. However, this approach faces computational limitations and is only effective for structures involving small sets of design parameters. The escalating demands for high-performance nanophotonic devices impose severe challenges on conventional design approaches. Devices integrating metamaterials [65], [166] or subject to topological engineering [141] often present multiple reciprocal design parameters, hindering sequential exploration and requiring simultaneous multi-parameter optimizations. Optimization through inverse design offers unprecedented opportunities to push the boundaries of device performance and functionality for integrated photonics. Inverse design methods first establish the desired performance metrics for the device, then iteratively optimize the device structure. By leveraging computational algorithms and optimization strategies, inverse design approaches enable the development of novel device topologies tailored to address specific performance objectives.

The inverse design process adopts a function-based approach to optimize a figure of merit (FOM) associated with the target physical response. An iterative optimization algorithm is then used to minimize or maximize the FOM. This results in the design structure corresponding to the optimal physical response. Thus, inverse design methods provide devices with a high degree of freedom in their optimization, facilitating the realization of nanophotonic devices with high-performance and ultra-compact dimensions. Inverse design automates the design of nanophotonic devices by initially assuming a structure without the need for physical principles, thus reducing the need for human intervention. However, the quality of the initial structure and the selection of variable parameters are decisive for algorithmic convergence and optimization effectiveness. These elements significantly affect the overall efficiency of the optimization process and the achievement of the desired performance criteria. Therefore, the role of the designer is still pivotal for the best exploitation of inverse design methods.

Optimization algorithms are fundamental in the inverse design process and can be categorized into three main groups: heuristic optimization algorithms, gradient-based algorithms, and deep learning [167].

- Heuristic optimization algorithms employ approximation strategies inspired by natural phenomena, human intuition, or problem-specific knowledge to efficiently navigate large solution spaces and find satisfactory solutions. These algorithms use heuristics to guide the search for solutions, but do not guarantee optimality. They are often preferred for handling real-world problems characterized by high-dimensional, nonlinear, or noisy objective functions. These techniques include direct binary search [168], genetic algorithms [141], [145], [169], and particle swarm optimization algorithms [145], [169].

- Gradient-based optimization algorithms, such as the adjoint method [170], transform the inverse design problem into an abstract mathematical problem. In this approach, optimization parameters and the mapping between these parameters and the distribution of dielectric constants in the design region are determined. The FOM derivative represents the device performance with respect to the optimization parameters and is obtained using methods like the adjoint analysis. Finally, the optimal distribution of dielectric constants in the design region is computed using methods such as the steepest descent method [171]. Gradient-based optimization algorithms can be divided into three categories: shape optimization [170], topology optimization [172] and objective-first [173].

- Deep learning employs nonlinear models and machine learning techniques to gradually transform low-level design into high-level structures through multilayer processing. When machine learning techniques are applied to an initial noisy set of optimized designs, instead of finding a singular optimized solution, a lower dimensional design subspace containing high-performance designs is revealed [174]. The detailed analysis of this region, which includes all conceivable high-performance designs, elucidates their performance, structural variations, and constraints. Such a comprehensive understanding of the design space allows for the recognition of optimal designs tailored to specific application requirements.

Inverse design optimized structures present promising prospects for broadband and compact devices. For example, in [175] Wang et al. used a direct Y-junction design as initial structure for an inverse design optimization, achieving an ultra-broadband power splitter with low losses. However, in this study, part of the structure is automatically generated by the algorithm, resulting in mosaic patterns with small MFSs, as illustrated in Figure III.16. This mosaic pattern is derived through topology optimization, a methodology that conceptualizes the design space as a bitmap. In this bitmap representation, each pixel undergoes iterative updates in the direction of gradient descent until the gradients diminish to a sufficiently small magnitude. Nevertheless, these complex patterns pose a challenge for high-resolution fabrication processes and impact performance under fabrication errors. Therefore, it is still desirable to control the geometric parameters modified by the algorithm according to certain design constraints.

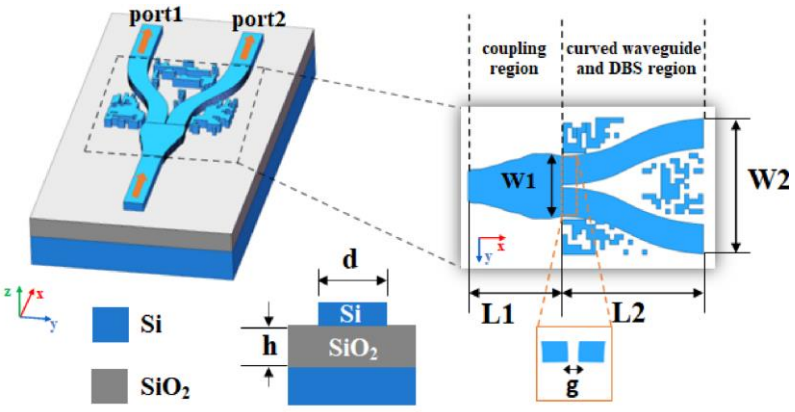

Figure III.16. Schematic of the Y-junction power splitter proposed in [175] using inverse design algorithms.

Chapter IV:

EFFICIENT POWER SPLITTING BASED ON A FULL-SUBWAVELENGTH Y-JUNCTION

This chapter introduces a novel power splitter engineered through SWG metamaterials to achieve an ultra-broad bandwidth for the SOI platform. The developed splitter architecture is based on a dual-mode symmetric Y–junction comprising SWG waveguides in both stem and arms waveguides. This design strategy effectively reduces mode confinement around the junction tip to mitigate fundamental mode loss. Section 4.1 provides a critical review of the strengths and limitations of current Y-junction power splitters. Section 4.2 describes the principle of operation, design, and optimization strategy, including simulation results. Experimental measurements of the fabricated power splitter are detailed in Section 4.3. Finally, section 4.4 offers a comprehensive discussion of the obtained results.

4.1. Introduction
4.2. Principle of operation and device design
4.3. Fabrication and experimental characterization
4.4. Conclusions

4.1. Introduction

As further discussed in the preceding chapter, 3-dB optical power splitters serve as pivotal components that are extensively used in different systems for light distribution or as fundamental components to construct more intricate optical structures. Therefore, there is a strong demand for power splitters characterized by low loss, compactness, and relaxed fabrication tolerances while operating over broad spectral ranges for multiple optical modes. Diverse power division architectures have been reported based, among others, on symmetric Y–junctions [141], [142], MMI couplers [112], [176], inverse tapers [177], adiabatic tapers [129], directional and adiabatic couplers [122], [123], [178], slot waveguides [144] and photonic crystal [146], [179].

Symmetric Y-junctions are one of the most popular solutions available because of their polarization- and wavelength-independent operation besides their intuitive design. However, these splitters tend to suffer from significant radiation losses at the junction tip for fundamental modes, especially as the tilt angle between the two branching arms increases [180]. This resulting radiation loss hence depends on the operating mode and can be ascribed to two main mechanisms. The first mechanism relates to the wavefront inclination as the mode in the stem waveguide propagates through the junction, resulting from gradual tilting in the propagation direction. The second mechanism involves changes in the mode profile along the branching. Radiation loss for odd modes is generally lower compared to even modes. This discrepancy arises because odd modes exhibit a zero-power field profile at the midpoint of the stem waveguide, whereas even modes have maximum power field profile in this region. For instance, the TE_0 mode presents a field profile characterized by a single lobe in the center of the stem waveguide, which then transitions into a two-lobe distribution with one lobe extending to each arm waveguide. In contrast, the field profile of the TE_1 mode has two lobes, with a zero-field value at the center of the stem waveguide that naturally separate into two lobes within the arms [181]. Note that the loss mechanism related to the wavefront inclination is predominantly influenced by the tilt angle, while the mechanism related to the mode profile change is sensitive to the sharpness of the junction tip, a parameter constrained by the resolution of the fabrication processes. This contributes to further increase radiation loss and introduces additional back reflections, particularly affecting the fundamental mode as its field profile is maximum at the center of the stem waveguide and aligns with the abrupt tip at the junction. There are numerous optimized Y-junction design approaches proposed to circumvent the effect of MFS at the tip, including tapered and slotted waveguides [142], [178], or particle swarm optimization algorithms [144]. Nevertheless, ultra-broadband, low-loss and fabrication-tolerant solutions are still sought after.

SWG metamaterials are a powerful design tool to enhance the performance of photonic devices [64], [166], [182], as explained in detail in Chapter II. In particular, SWG engineering has been successfully applied to several power splitters such as asymmetric directional couplers [126], three-guide directional couplers [183], inverse tapers [184], slot adiabatic waveguides [185], MMI devices [77], and Y–junctions [186]. This chapter presents a novel power splitting architecture based on a dual-mode Y–junction engineered with subwavelength metamaterials to effectively reduce mode confinement around the junction tip, mitigating fundamental mode loss penalty caused by MFS limitations [187], [188].

Two different resolution scenarios have been taken into account for the optimization of the SWG Y-junction. First, with an MFS of 100 nm, corresponding to current deep-UV fabrication process (dry lithography) [189], [190]. The second scenario is considered for high-resolution e-beam lithography and emerging processes in photonic foundries like immersion lithography, both with an MFS of 50 nm [191]. Full 3D FDTD simulations show negligible fundamental mode excess losses within an ultra-broad bandwidth in excess of 300 nm for both MFS scenarios [187]. Extensive experimental characterization yields measured TE_0 mode excess loss (EL_{TE0}) of less than 0.3 dB within the $1420 - 1680$ nm wavelength range and exhibits excess loss for TE_1 mode (EL_{TE1}) lower than 1.5 dB within a 170 nm bandwidth ($1420 - 1590$ nm) considering a resolution scenario with MFS of 100 nm [188].

4.2. Principle of operation and device design

Consider a conventional symmetric Y-junction as shown in Figure IV.1(a) as a reference model. The device consists of an input multimode stem waveguide that supports both TE_0 and TE_1 modes, characterized by a width W_0 and length L_s. The design features two single-mode output arm waveguides with an S-bend shape to reduce the branching angle at the junction and minimize losses due to wavefront tilt mismatch. Each arm has a width $W = W_0/2$, length L_b and are finally separated by a distance H_a. An adiabatic taper of length L_t is also included to adapt the stem waveguide to the width of both arms at the junction ($W_T = 2W + H_{off}$). When the tilt angle between the two arms is small enough to consider an adiabatic transition [133], the input TE_0 mode injected at the stem is divided into two in-phase TE_0 modes at the output arms due to the symmetry of the device. Upon injection of the TE_1 mode, the power is again equally distributed and converted into two TE_0 modes at the output arms, but with a π phase difference (ϕ) between them. A gap of width H_{off} is considered between the two arm waveguides at the junction tip to account for the MFS resolution of the fabrication process.

Figure IV.1(b) presents the schematic of the proposed device, which operates analogously to a conventional symmetric Y-junction but incorporates SWG metamaterials in both input and output waveguides. The SWG region plays a crucial role in reducing the modal confinement of the TE_0 mode, thereby minimizing radiation losses at the junction. Furthermore, the use of subwavelength structures circumvents the need of a junction tip, allowing us to define geometrical parameters (Λ, DC and H_{off}) with values above the considered MFS. As in its conventional counterpart, the power distribution of the fundamental mode in the SWG Y-junction is equally divided into two in-phase fundamental modes, one on each output arm. For the first-order mode, the power is evenly distributed between the fundamental modes of the output arms, but the relative phase between them ($\Delta\varphi$) is π.

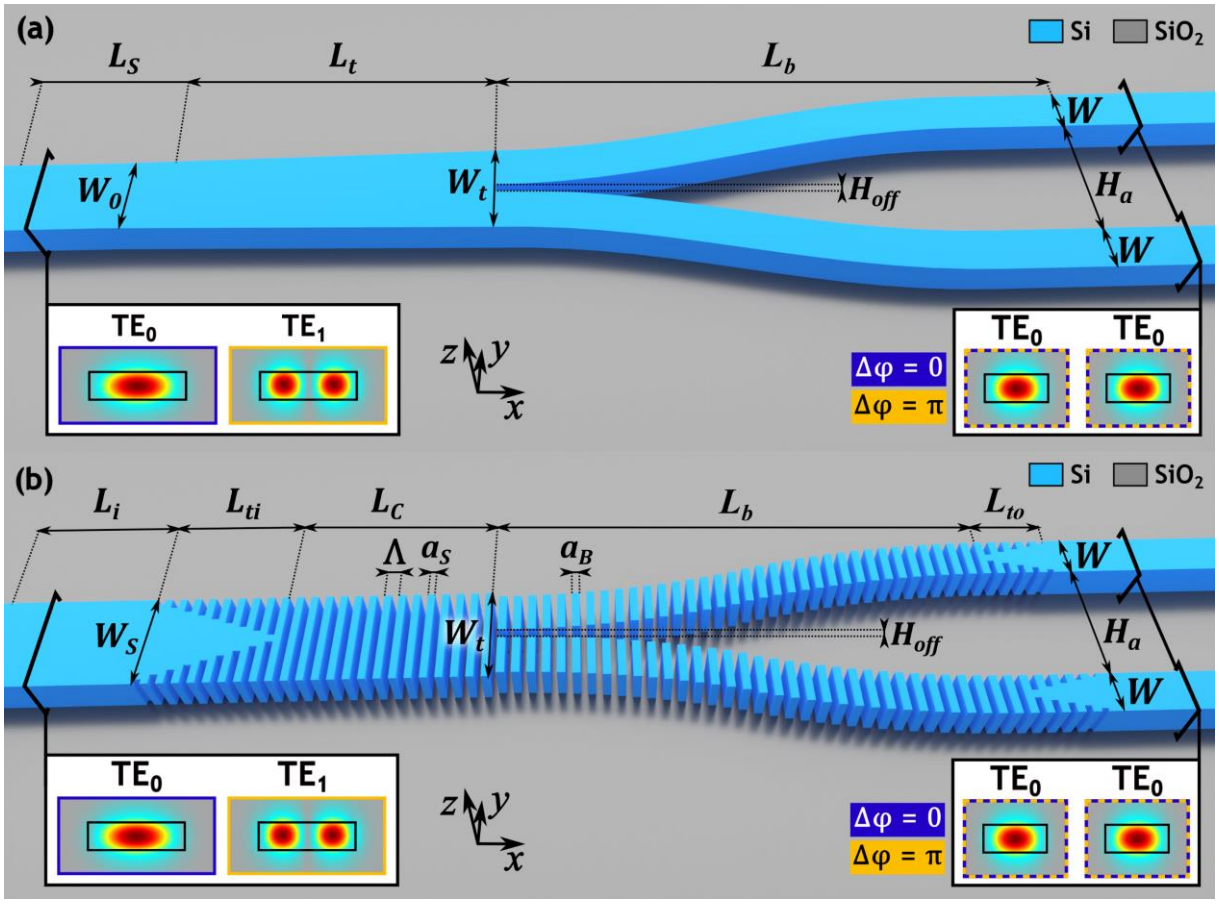

Figure IV.1. Schematic of (a) a conventional symmetric Y-junction and (b) SWG Y-junction. This pair of devices operate for TE_0 and TE_1 modes.

For the sake of comparison, the same arm offset (H_{off}), arm width (W) and final separation (H_a) are preserved identical as in its conventional counterpart. The input strip waveguide of length L_i and width W_S evolves into an SWG waveguide of length L_C through an adiabatic taper (length L_{ti}). Adiabatic tapers, each with a length denoted as L_{to}, are also implemented on both arms to ensure a smooth transition from the SWG structure into the strip output waveguides. In order to minimize mode effective index mismatch at the junction, different duty cycles are defined for the stem and arms waveguides: $DC_S = a_S/\Lambda$ and $DC_A = a_A/\Lambda$, respectively. Here, a_S represents the length of the silicon segments in the stem, and a_A denotes the length of the silicon segments in the arms, considering a constant period Λ.

4.2.1. Optimization process

Both the reference conventional Y-junction and the proposed SWG splitter were optimized for an SOI platform with a core waveguide thickness of 220 nm and top and buried silicon dioxide layers. The device was simulated using a commercial 3D FDTD solver [192] for two distinct fabrication processes, each designed with MFSs of 100 nm and 50 nm. Therefore, the parameter H_{off} is modified accordingly to each MFS scenario. Both Y-junctions' arms are designed for compatibility with conventional interconnect waveguides with a width of $W = 500\,nm$. A grating period of Λ = 220 nm is selected to avoid radiation and Bragg regimes and ensure subwavelength propagation within the

wavelength range of interest, spanning from 1300 nm to 1700 nm. Table 1 lists the remaining geometric design parameters for both conventional and SWG Y-junctions.

Table 1. Conventional and SWG Y-junction geometrical parameters.

Design	Parameter	Symbol	Value [μm]
SWG and conventional Y-junctions	Arm width	W	0.5
	Arm final separation	H_a	1.5
	Arm length	L_b	12.3
Conventional Y-junction	Stem waveguide width	W_0	1.0
	Taper length	L_S	13.0
	Stem waveguide length	L_t	4.0
SWG Y-junction	Input strip width	W_S	1.2
	Input strip length	L_i	2.0
	Input SWG taper	L_{ti}	10.0
	Output SWG taper	L_{to}	6.0
	Central SWG section	L_C	13.0

Once the geometry of input and output waveguides is defined, the main design challenge is to optimize the SWG geometry of both the stem and the arms. First, the width of the SWG stem waveguide was optimized to prevent weak confinement of the Floquet-Bloch TE_1 mode, which would result in TE_1 mode radiation and leakage towards the silicon substrate under the BOX layer. The performance of TE_1 mode splitting could be improved by selecting a wider SWG stem waveguide width. However, this improvement for TE_1 comes at the expense of increased confinement of the Floquet-Bloch TE_0 mode, resulting in higher excess losses for the fundamental mode. Figure IV.2 shows the effective index of the Floquet-Bloch TE_1 mode ($n_{eff,1}$) supported by the SWG stem waveguide as a function of the waveguide width. The effective index of the Floquet-Bloch TE_0 mode ($n_{eff,0}$) supported by the arms is also shown with a dotted blue line. As a compromise between EL_{TE0} and EL_{TE1}, a width of the SWG stem waveguide of W_S = 1200 nm was selected.

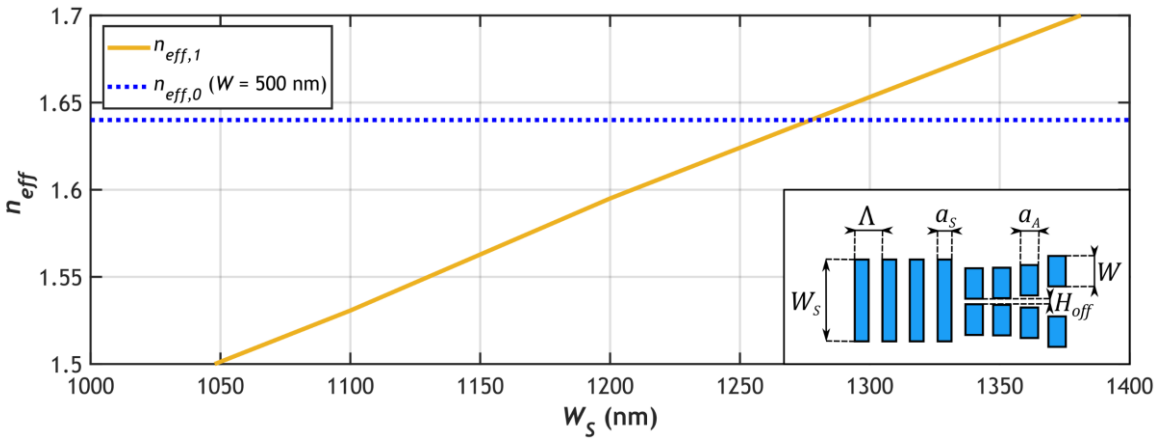

Figure IV.2. Effective index of the Floquet-Bloch TE_1 mode for different widths of the SWG stem waveguide. The effective index of the Floquet-Bloch TE_0 mode within a 500-nm-wide SWG waveguide at a wavelength of 1550 nm is represented with a dotted blue line.

Mode-matching at the interface between the stem and the arms waveguides was further optimized by judiciously adjusting the duty cycle on each side of the junction. For this purpose, the EL was swept for different DC_A values while keeping a constant DC_S of 50% (see Figure IV.3). Two additional restrictions were considered. Firstly, the chosen DC_A value must not violate the MFS. Secondly, the selected DC_A may not necessarily ensure the minimum value for both EL_{TE0} and EL_{TE1} simultaneously. For the MFS of 100 nm, DC_A is set to 55% to ensure a separation between the silicon segments ($1 - DC_A \cdot \Lambda$) of 99 nm and minimum EL for TE_1 mode (see Figure IV.3(a)). For the MFS of 50 nm, the optimal loss balance for both TE_0 and TE_1 modes was achieved with a DC_A = 60% (see Figure IV.3(b)).

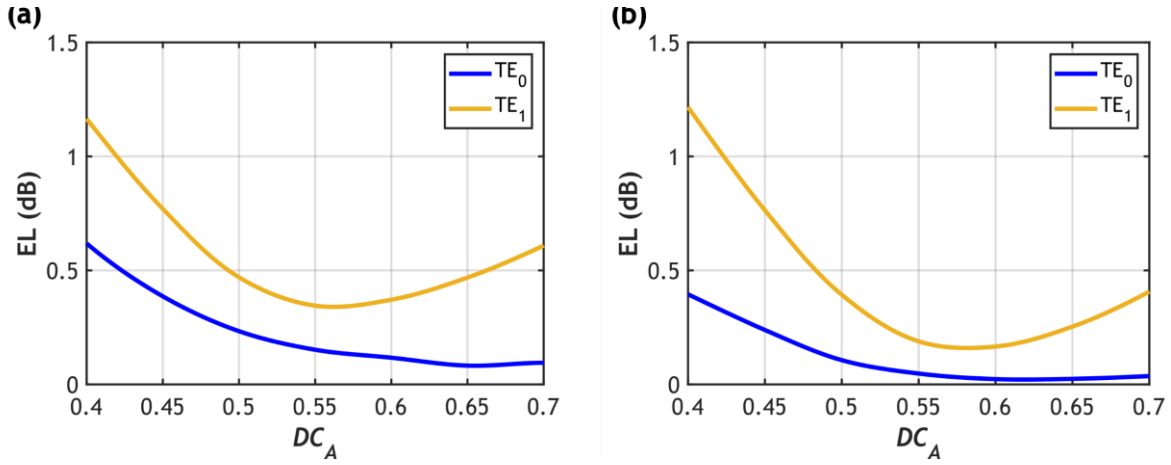

Figure IV.3. Calculated excess loss of the SWG Y-junction for variable DC_A, for (a) MFS = 100 nm and (b) MFS = 50 nm, maintaining DC_S = 50% at a wavelength of 1550 nm.

4.2.2. Simulation results

Simulated excess loss comparison between the optimized SWG Y-junction (solid line) and its conventional counterpart (dashed line) is shown in Figure IV.4, with EL_{TE0} in blue and EL_{TE1} in yellow. To simplify the notation, herein $EL_{TEm}^{D,MFS}$ will be used to represent the excess loss of both conventional ($D = Conv$) and SWG ($D = SWG$) splitters operating for TE_0 ($m = 0$) or TE_1 ($m = 1$) modes considering the two MFS values, which can be either 100 nm or 50 nm. For the SWG Y-junction, Figure IV.4(a) showcases the results considering the MFS of 100 nm, demonstrating $EL_{TE0}^{SWG,100}$ as low as 0.3 dB in a 350 nm bandwidth (1350 – 1700 nm) and $EL_{TE1}^{SWG,100}$ under 0.45 dB in a 300 nm wavelength range (1300 – 1600 nm). A significant reduction for EL_{TE0} is achieved across the full simulated bandwidth of 300 nm. Particularly, at the nominal design wavelength of 1550 nm, the reduction is notable, dropping from 0.99 dB for the conventional Y-junction to 0.12 dB for the SWG Y-junction. Considering the MFS of 50 nm (Figure IV.4(b)), the SWG device exhibits an excellent performance in a broad bandwidth of 300 nm, with $EL_{TE0}^{SWG,50}$ below 0.1 dB for a wavelength range from 1400 nm to 1700 nm, and under 0.3 dB for TE_1 mode in a 1300 – 1600 nm spectrum. In terms of overall performance, $EL_{TE0}^{SWG,50}$ decreased 0.35 dB in a 250 nm bandwidth (1350 – 1600 nm) relative to the conventional splitter, while $EL_{TE1}^{SWG,50}$ experiences only a marginal increment.

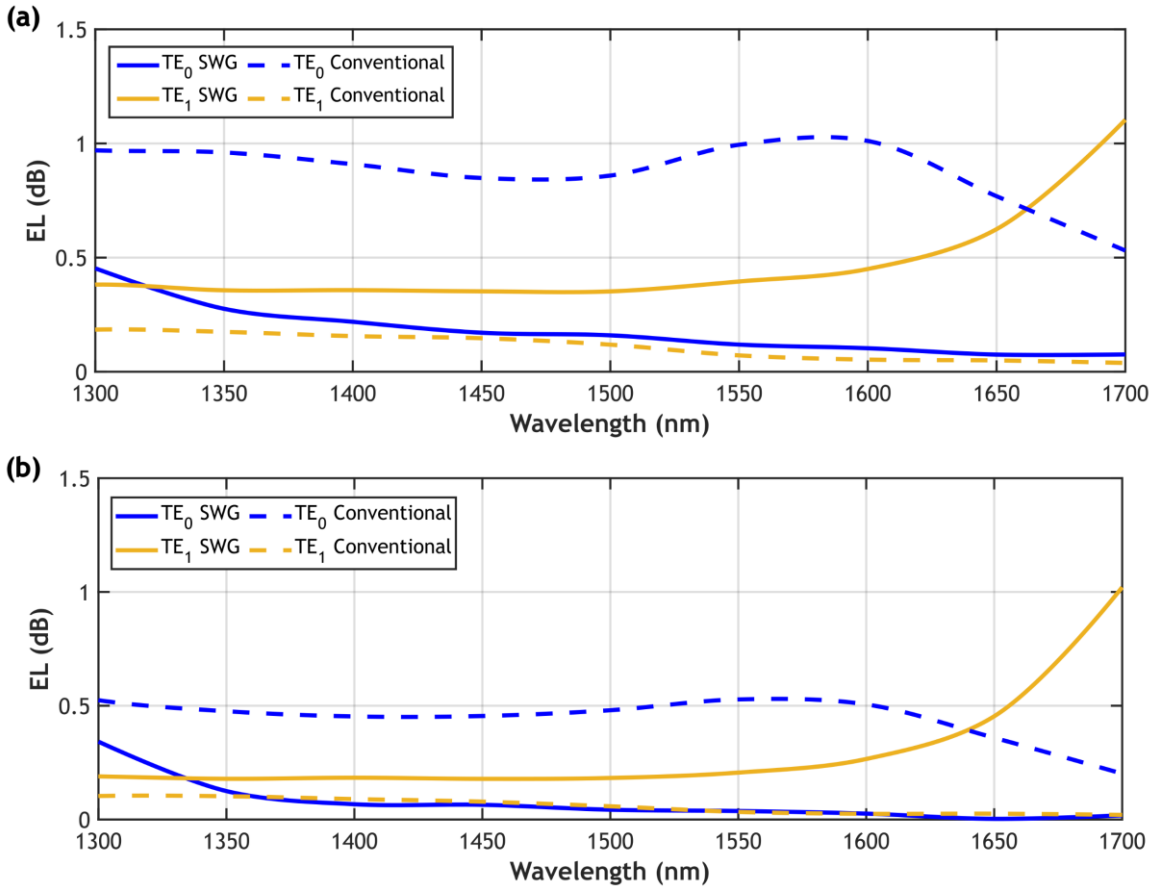

Figure IV.4. Simulated excess loss for TE_0 (blue) and TE_1 (yellow) modes of the SWG Y-junction (solid lines) compared to the conventional Y-junction (dashed lines): (a) MFS = 100 nm, optimized SWG Y-junction with DC_A = 55%; (b) MFS = 50 nm, optimized SWG Y-junction with DC_A = 60%.

The sum of both TE_0 and TE_1 EL values is significantly reduced for the proposed SWG device compared to its conventional counterpart. Therefore, the SWG Y-junction ensures consistent performance for both modes for the two 100 nm and 50 nm MFS designs. This enhanced performance is maintained over a broad bandwidth of 300 nm (1300 – 1600 nm), with the figure of merit $EL_{TE0}^{SWG,100} + L_{TE1}^{SWG,100}$ under 0.5 dB for the SWG device under the most stringent MFS design. It is noteworthy that the performance of the conventional Y-junction deteriorates rapidly as the MFS becomes more restrictive, with $EL_{TE0}^{Conv,100} + L_{TE1}^{Conv,100}$ reaching up to 1.5 dB within the simulated wavelength range.

In order to evaluate the consequences of under- and over-etching effects during fabrication, the entire device was resized by incorporating the corresponding deviation to the length and width of the silicon segments, since fabrication errors are absolute variations of the waveguide dimensions as shown in Figure IV.5. As such, $a_S' = a_S + \Delta\delta$ and $a_A' = a_A + \Delta\delta$ are the lengths of the silicon segments at the stem and the arms of the SWG Y-junction, and the width of the stem and the arms are $W_S' = W_S + \Delta\delta$ and $W_A' = W + \Delta\delta$, respectively.

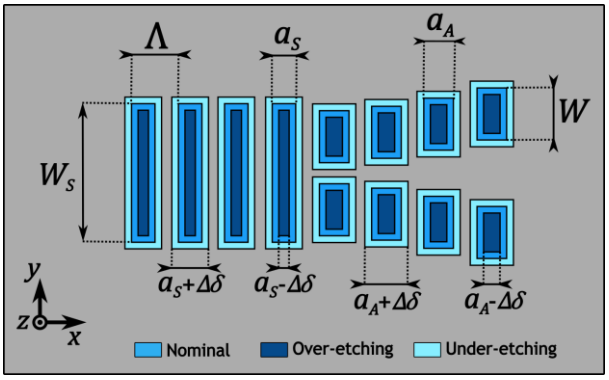

Figure IV.5. Redimensioning of the device to account for under-etching and over-etching deviations during fabrication process.

3D FDTD simulations on the SWG Y-junction tolerance to etching errors of $\Delta\delta$ = ± 10 nm and $\Delta\delta$ = ± 20 nm from the nominal design were performed, as illustrated in Figure IV.6. For both MFS values of 100 nm (Figure IV.6(a)) and 50 nm (Figure IV.6(b)), the SWG Y-junction performance degradation is observed predominantly for the TE_1 mode when $\Delta\delta$ is negative, i.e. for over-etching errors. The observed behavior for over-etching errors stems from a decrease in dimensions, which significantly deconfines the TE_1 mode within the stem waveguide. This leads to weak guidance and consequently mode radiation. By contrast, the TE_0 mode exhibits robust tolerances, particularly for the MFS = 50 nm. Simulations also confirmed that the effect of temperature changes on device performance were negligible for variations of ±10 K for either mode (TE_0 or TE_1), and for the two MFS designs.

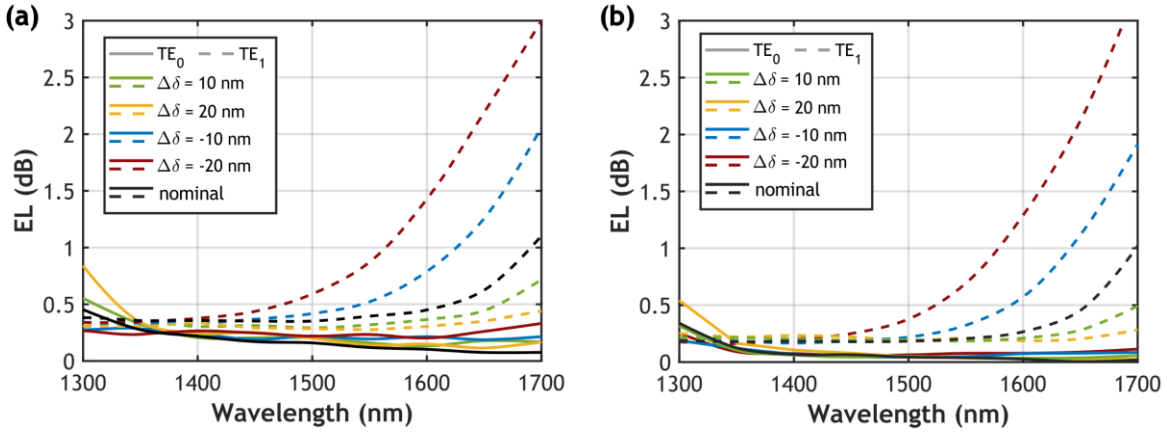

Figure IV.6. Tolerances to fabrication errors of $\Delta\delta$ = ± 10, ± 20 nm for TE_0 (solid lines) and TE_1 (dashed lines) modes for the SWG Y-junction with (a) MFS = 100 nm and (b) MFS = 50 nm.

4.3. Fabrication and experimental characterization

The device was fabricated using electron-beam lithography in a commercial foundry [191]. The SOI wafer comprises a silicon layer thickness of 220 nm and a 2-µm-thick BOX. The mask pattern was defined by exposing the resist to a 100 keV e-beam lithography system, followed by an anisotropic reactive ion etching process that transfers the pattern to the Si layer. A SiO_2 cladding with a thickness of 2.2 µm was deposited by chemical vapor deposition. Finally, a deep etch process was applied to smooth the chip facets, enabling efficient fiber-chip edge coupling by using high-efficiency broadband

SWG edge couplers [193]. A more in-depth description of the fabrication method can be found in Annex A.

Experimental characterization was carried out using two tunable lasers to sweep the wavelength range from 1420 — 1680 nm, fully covering the S, C, L and U telecom bands, and partially the E-band. A schematic of the setup is shown in Figure IV.7. Polarization at the chip input was controlled through a three-paddle fiber polarizer followed by a linear polarizer, a half-wave plate and a polarization maintaining (PM) lensed optical fiber. The PM lensed optical fiber was mounted on a micropositioning stage and attached to a fiber rotator to direct its output linearly polarized light onto the chip plane. When the linearly polarized light is aligned along the y-direction, it excites TE polarization on the chip waveguides (see Figure IV.7 axis). Conversely, rotating the linearly polarized light to the z-direction allows to excite TM polarization in the chip waveguides. The chip is placed on a holder capable of precise movement within the xy-plane. Output light from the chip is collected using a 40x achromatic microscope objective and filtered through a Glan-laser calcite polarizer mounted on another micropositioning stage. Precise positioning stages facilitated alignment of the chip waveguides with the PM fiber and the microscope objective. A broadband dielectric mirror, mounted on a folding frame, enables the redirection of the polarized light beam to either an infrared camera or a germanium photodetector. The photodetector has an operating wavelength range from 0.78 μm to 1.8 μm and is connected to a digital power meter. Moreover, a free-space polarimeter can be placed before the photodetector to verify the polarization state in the entire wavelength range (1420 — 1680 nm).

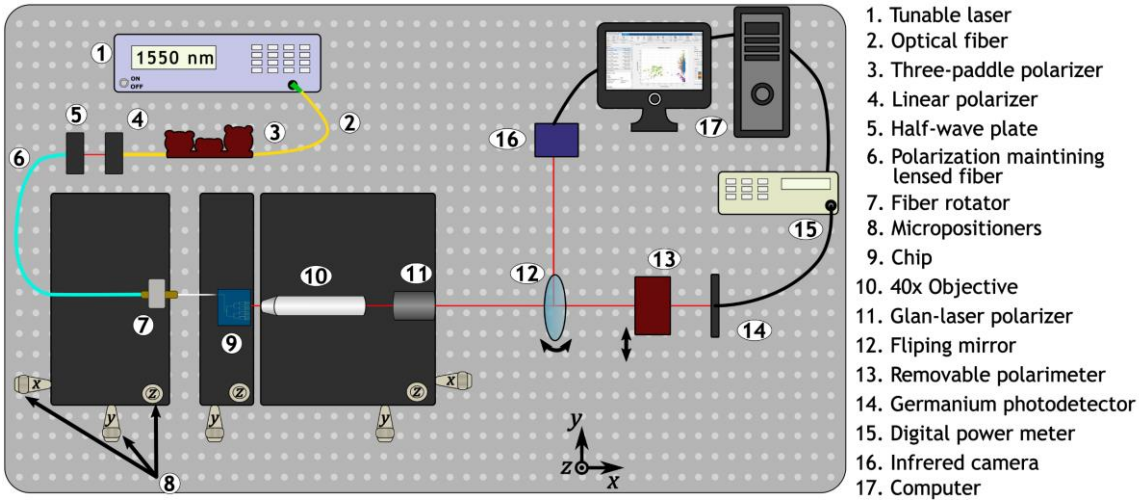

Figure IV.7. Schematic of the measurement setup used to characterize the fabricated devices.

4.3.1. Fundamental transverse-electric mode

4.3.1.1. Proof-of-concept characterization

For a first proof-of-concept characterization, the device was fabricated in a multi-project wafer fabrication run at a commercial foundry. Figure IV.8 shows SEM images of the fabricated devices prior

to upper cladding deposition. Figure IV.8(a) shows an SEM image of the SWG Y-junction with an MFS of 100 nm, with a more detailed view of the tip in Figure IV.8(b). Figures IV.8(c) and (d), following the previous arrangement, provide SEM images of the splitter with MFS of 50 nm. Detailed SEM image analysis reveals a slight over-etching, with deviations below $\Delta\delta$ < -10 nm in SWG segments of both arms and stem. A Mach-Zehnder interferometer comprising two SWG Y-junctions was used to evaluate the power splitter performance.

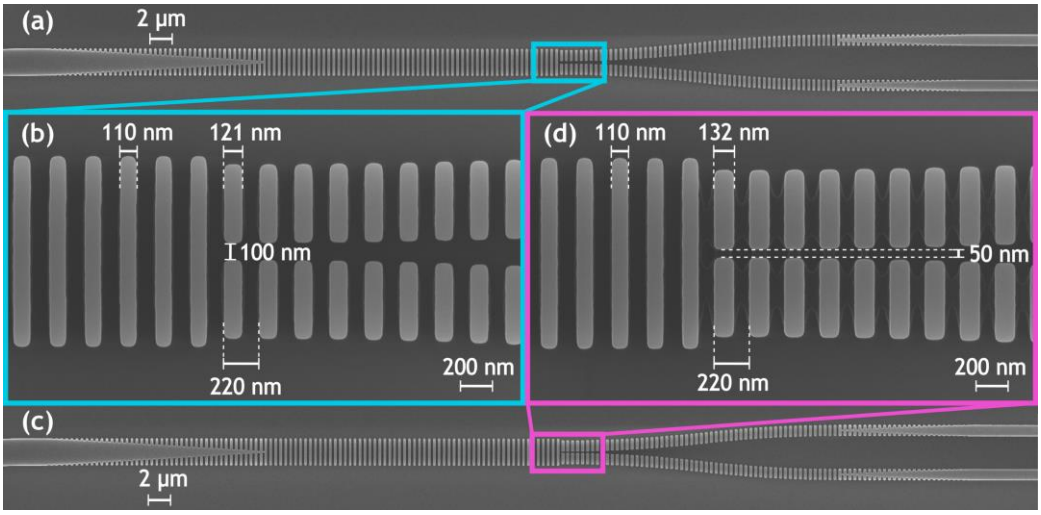

Figure IV.8. Scanning electron microscope images of (a) the complete SWG Y-junction and (b) a detailed view of the junction tip for an MFS of 100 nm. SEM images of (c) the entire device and (d) the junction tip for an MFS of 50 nm.

Figure IV.9 shows the spectral response of the MZI structure including two SWG Y-junction considering an MFS = 50 nm. The difference between the transmittance of the measured MZI transmittance maxima (P_{MZI}^{max}) and a reference structure (P_{ref}) allowed us to estimate the excess loss due to the two SWG Y-junction: $2EL = 10 \cdot \log_{10}(P_{MZI}^{max}/P_{ref})$. The reference structure contains a sequence of waveguides with the same length, width and number of bends as the MZI structure. In order to conduct a conservative evaluation of the device's performance, the reference waveguide with the highest power transmission among those available, as shown in Figure IV.9, was used for comparison.

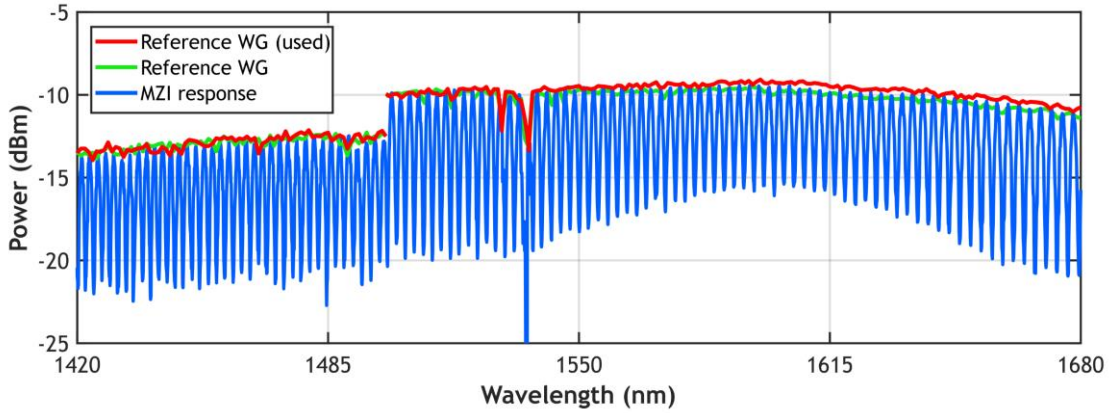

Figure IV.9. Measured power transmittance of the MZI structure, which includes two SWG Y-junctions with an MFS of 50 nm, alongside reference waveguides. Note that the discontinuity at 1505 nm results from the laser change during the wavelength scan.

Two conventional Y-junctions with MFS of 100 nm and 50 nm were also characterized in the 1420 – 1680 nm range to compare the performance of the SWG Y-junction with that of the conventional counterpart. The measured loss EL_{TE0} is shown in Figure IV.10(a) for an MFS = 100 nm and (b) for an MFS = 50 nm. The fabricated SWG Y-junction shows $EL_{TE0}^{SWG,100}$ under 0.72 dB over the full bandwidth of 260 nm (1420 – 1680 nm) and is further reduced below 0.5 dB in a 210 nm bandwidth (1470 – 1680 nm). For the MFS = 50 nm, $EL_{TE0}^{SWG,50}$ decreases to less than 0.4 dB for the entire measured wavelength range, and under 0.22 dB in a 195 nm bandwidth (1485 – 1680 nm), as plotted in Figure IV.10(b).

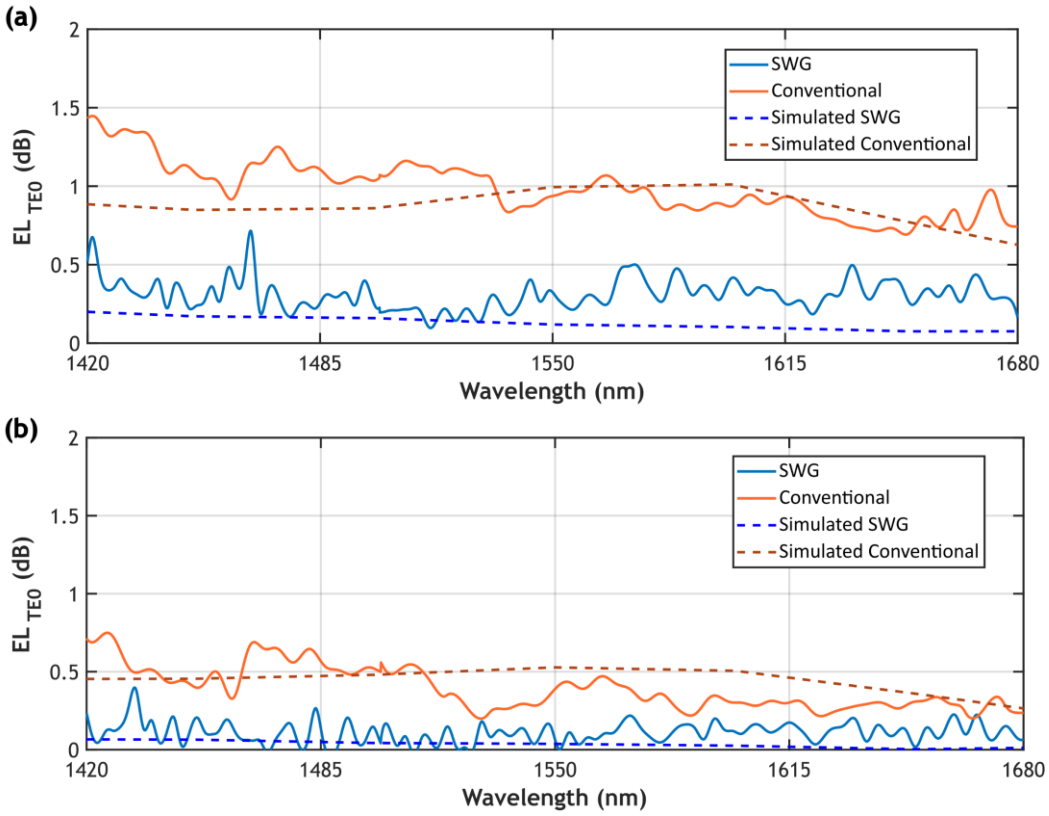

Figure IV.10. Measured EL for the TE_0 mode for the SWG (blue) and the conventional (orange) Y-junctions for (a) an MFS = 100 nm and (b) an MFS = 50 nm. Simulation results are also included for reference in all cases (dashed lines).

The proof-of-concept experimental evaluation demonstrates a substantial performance improvement for the SWG device over its conventional counterpart in both MFS scenarios, especially for the 100 nm MFS design. The conventional Y-junction exhibits high EL across the entire measured spectrum, stronger deterioration observed for shorter wavelengths. This phenomenon occurs because the optical mode is more confined within the waveguide at shorter wavelengths, thus increasing its sensitivity to the effect of the tip MFS, producing power radiation. These measurements reinforce the potential of SWG technology to overcome the constraints imposed by fabrication resolution limitations.

4.3.1.2. Extended characterization using cascaded structures

Following the success of the proof of concept, a second round of multi-project wafer chips were fabricated in the same foundry for an extended characterization of the device excess losses associated with both TE_0 and TE_1 modes and analysis of fabrication tolerances. In this second round, the chip included cascaded structures with increasing numbers of concatenated Y-junctions. Specifically, configurations of 1×2 (stage 1), 1×4 (stage 2), 1×8 (stage 3), and 1×16 (stage 4) divisions were utilized for this purpose. The SEM image presented in Figure IV.11(a) illustrates the 1×16 structure, providing a comprehensive description of the four stages. Figure IV.11(b) presents a close-up view of the SWG Y-junction within the structure. The chip also contained reference waveguides with the same width, length, and bend configurations as those of the cascaded structures, in order to serve as test structures for evaluating the EL generated by the Y-junctions.

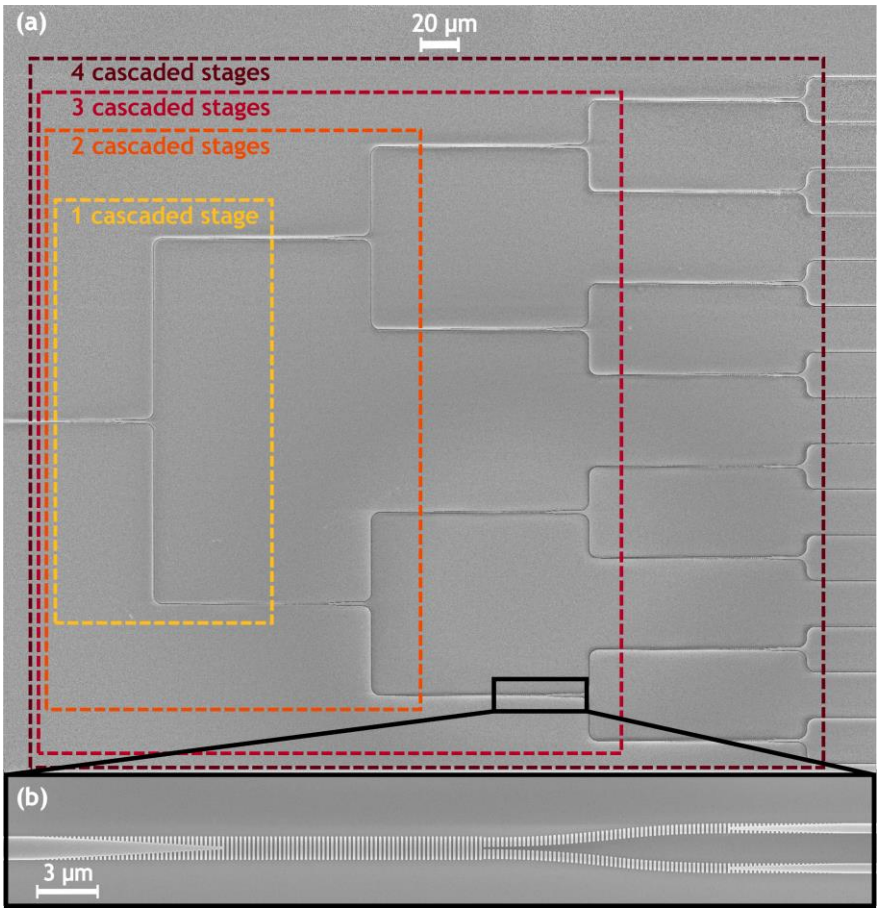

Figure IV.11. SEM images of the SWG Y-junction in (a) a 1×16 cascaded configuration and (b) inset of the device.

The measured excess loss for different cascaded Y-junctions is presented in Figure IV.12. The EL_{TE0} of the SWG and conventional Y-junctions designed with an MFS of 100 nm ($EL_{TE0}^{SWG,100}$ and $EL_{TE0}^{Conv,100}$) are plotted in Figure IV.12(a). For the designs considering an MFS of 50 nm, $EL_{TE0}^{SWG,50}$ and $EL_{TE0}^{Conv,50}$ are represented in Figure IV.12(b). Although conventional Y-junctions with H_{off} = 0 nm were also included and measured, these results were equivalent to the 50 nm MFS case, and they have not been included for the sake of clarity in Figure IV.12. For both designs accounting for MFSs of 50 nm and 100 nm, the SWG splitter has substantially reduced EL_{TE0} compared to conventional Y-junction. Figure IV.13 shows

the EL_{TE0} per splitter. This value has been calculated through a linear regression analysis of the measured losses at each stage. The SWG Y-junction (solid line) exhibits a consistent flat response across the entire measured bandwidth ranging from 1420 nm to 1680 nm. Specifically, for the SWG Y-junction, $EL_{TE0}^{SWG,50}$ remains below 0.3 dB and $EL_{TE0}^{SWG,100}$ stays under 0.5 dB over the full wavelength

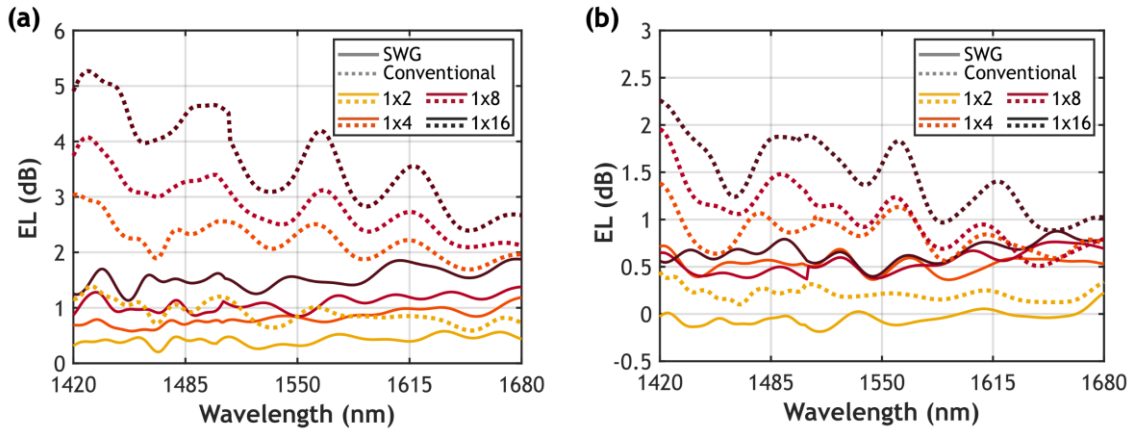

Figure IV.12. Excess loss of the 1×2, 1×4, 1×8 and 1×16 cascaded structures, for SWG (solid lines) and conventional (dotted lines) Y-junctions with MFS of (a) 100 nm and (b) 50 nm.

range of 260 nm. In contrast, especially for a 100 nm MFS, the performance of the conventional Y-junction (dotted line) degrades with decreasing wavelength, resulting in significant loss penalty. Considering the high-resolution fabrication with an MFS of 50 nm, the SWG device consistently outperforms the conventional Y-junction, with $EL_{TE0}^{SWG,50}$ < 0.23 dB in a 215 nm bandwidth (1420 — 1635 nm) as presented in Figure IV.13. As the MFS increases to 100 nm, the detrimental effect on the performance of the conventional Y-junction becomes more pronounced, with an $EL_{TE0}^{Conv,100}$ above 0.57 dB in the 1420 — 1680 nm window. In contrast, the SWG device yields high-performance over the entire measured bandwidth with $EL_{TE0}^{SWG,100}$ below 0.46 dB.

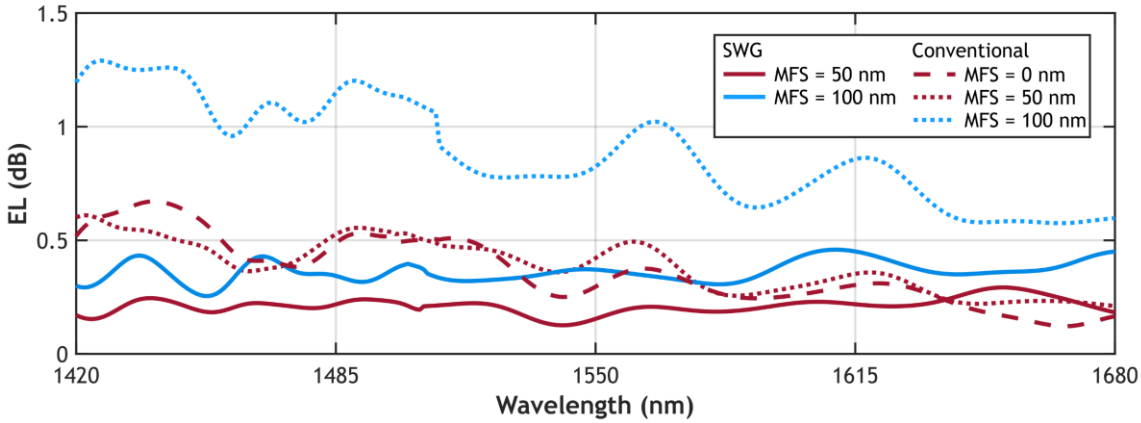

Figure IV.13. Excess loss per splitter measured through linear regression of the response of four cascaded stages for SWG (solid lines) and conventional (dotted lines) Y-junctions, for both MFS of 100 nm and 50 nm. Results obtained for the conventional splitter with ideal resolution (MFS = 0 nm) are also shown (dashed lines).

Devices with deterministically induced dimensions variations of ±10 nm were integrated into the chip to assess the resilience of the SWG Y-junction to fabrication errors. Figure IV.14(a) shows $EL_{TE0}^{SWG,50}$ and $EL_{TE0}^{SWG,100}$, indicating that the performance remains consistent despite the geometric variations. $EL_{TE0}^{SWG,100}$ exhibits a slight improvement for under-etching deviations of +10 nm and degrades towards longer wavelengths for $\Delta\delta$ = -10 nm (SEM images shown in Figures IV.14(b) and (c), respectively). In contrast, for the MFS of 50 nm, $EL_{TE0}^{SWG,50}$ is slightly improved for devices with over-etching deviations of -10 nm and maintains consistent with the nominal design for $\Delta\delta$ = +10 nm (SEM images shown in Figures IV.14(d) and (e), respectively)). The largest fabrication bias was observed in the SWG stem waveguide width, narrowing the nominal value (W_s = 1200 ± 10 nm) by approximately 40 nm.

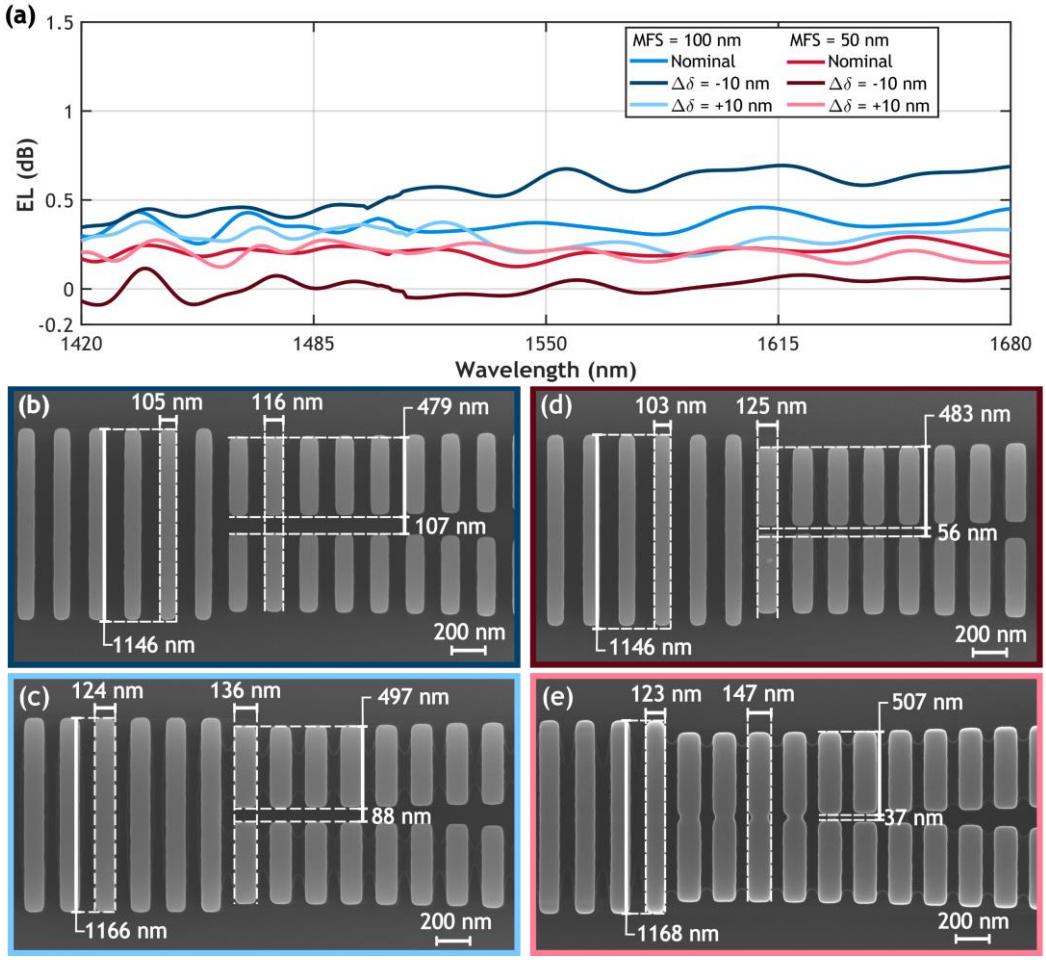

Figure IV.14. Tolerances to fabrication errors of $\Delta\delta$ = ±10 nm for the SWG Y-junction with MFS of 100 nm (blue lines) and of 50 nm (red lines). (a) Excess loss per splitter was measured through linear regression of cascaded stages. SEM images of devices for an MFS of 100 nm with (b) $\Delta\delta$ = -10 nm and (c) $\Delta\delta$ = +10 nm. SEM images of devices for an MFS of 50 nm with (d) $\Delta\delta$ = -10 nm and (e) $\Delta\delta$ = +10 nm.

4.3.2. First-order transverse-electric mode

In order to characterize the TE_1 mode division, in the second fabrication round auxiliary test structures with mode multiplexers [150] were included, as shown in Figure IV.15. When TE_0 is injected through the upper input port of the mode multiplexer, the TE_0 mode is generated at the output

multimode waveguide. Conversely, when the lower input port is excited with TE_0, TE_1 is generated at the mode multiplexer output. Reference structures with the same waveguide length, width and number of bends were included on the chip to compare with the measured power measured of the structures including the mode multiplexer and the Y-junctions (P_{MM+Y}) and obtain the excess loss of the structure: $EL_{MM+Y} = 10 \cdot \log_{10}(P_{MM+Y}/P_{ref})$. In addition, the power of two mode multiplexers in back-to-back (P_{MM}) was measured to extract the losses associated to each mode multiplexer: $2EL_{MM} = 10 \cdot \log_{10}(P_{MM}/P_{ref})$. The TE_1 mode excess loss corresponding to the Y-junctions can thus be obtained as: $EL = EL_{MM+Y} - EL_{MM}$.

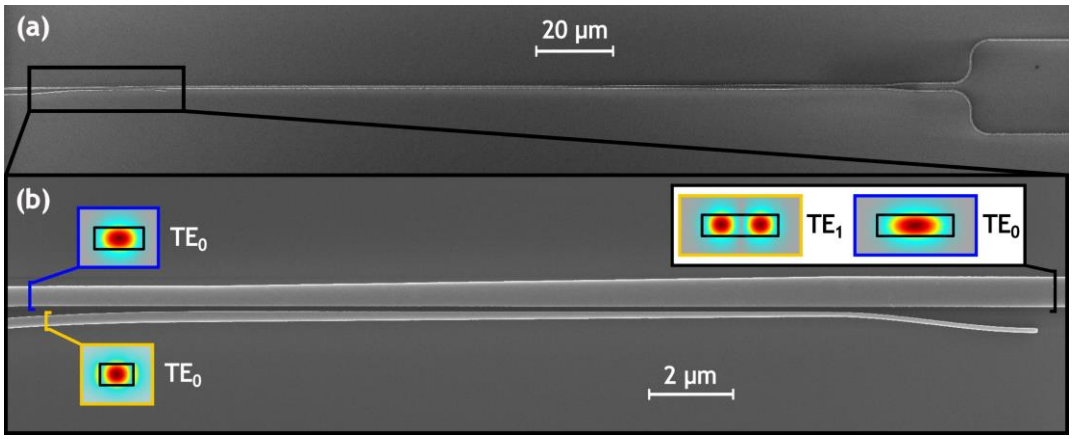

Figure IV.15 SEM images of the structure employed for the characterization of TE_1, (a) mode multiplexer and SWG Y-junction and (b) zoomed image of the mode multiplexer.

Figure IV.16 shows EL_{TE1} measurements for MFS = 50 nm for both SWG ($EL_{TE1}^{SWG,50}$) and conventional ($EL_{TE1}^{Conv,50}$) Y-junctions, as well as for the conventional Y-junction with H_{off} = 0 nm. Similarly, EL_{TE1} for MFS = 100 nm for SWG ($EL_{TE1}^{SWG,100}$) and conventional ($EL_{TE1}^{Conv,100}$) Y-junctions are plotted in the same figure. As previously explained, $EL_{TE1}^{Conv,50}$ and $EL_{TE1}^{Conv,100}$ are negligible due to TE_1 mode odd symmetry, with a power minimum at the center of the multimode stem. The proposed device exhibits an $EL_{TE1}^{SWG,50}$ below 1 dB over a 100 nm bandwidth, covering the wavelength range between 1475 nm and 1575 nm. Within a 170 nm bandwidth (1420 — 1590 nm), $EL_{TE1}^{SWG,50}$ and $EL_{TE1}^{SWG,100}$ only increase 0.5 dB compared to the conventional Y-junction. This degradation of the performance for the TE_1 mode arises from the selection of the stem waveguide width of W_S = 1200 nm, as a compromise between EL_{TE0} and EL_{TE1}. Note that increasing the width of the SWG stem waveguide results in stronger modal confinement that prevents TE_1 mode radiation, but increasingly penalizes TE_0 due to the resulting mode profile at the junction tip [187].

SWG Y-junctions with $\Delta\delta$ = ±10 nm were also included in combination with the mode multiplexer structures to study fabrication tolerances to study fabrication tolerances for TE_0 and TE_1 modes and are shown in Figure IV.17. Figure IV.17(a) shows that $EL_{TE0}^{SWG,100}$ remain <1 dB for $\Delta\delta$ = -10 nm and <0.7 dB for $\Delta\delta$ = +10 nm, for the 1420 — 1680 nm wavelength range. Figure IV. 17(b) shows that $EL_{TE0}^{SWG,50}$ is lower than 0.5 dB for both under- and over-etching errors in the full measured bandwidth

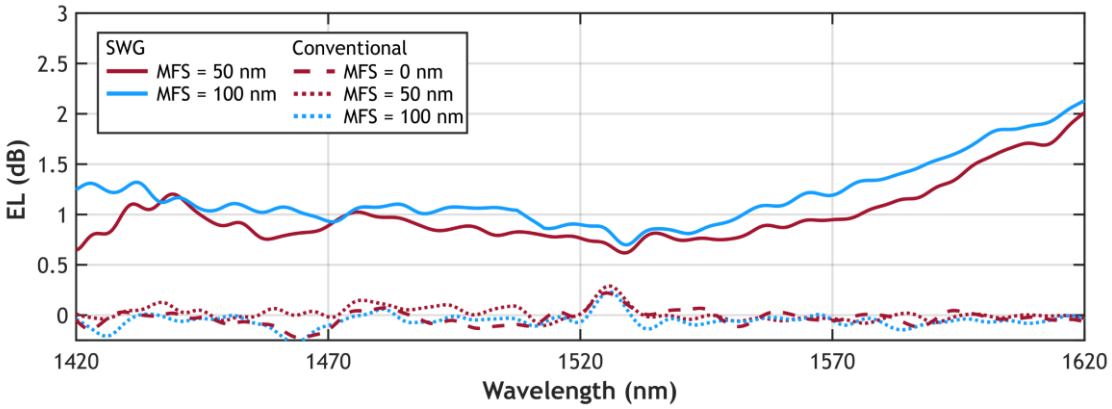

Figure IV.16. EL_{TE1} measurements for SWG (solid lines) and conventional (dotted lines) Y-junctions for MFS of 50 nm (red) and 100 nm (blue). Conventional Y-junction with MFS = 0 nm (dashed lines) is also shown.

(1420 — 1680 nm). These results corroborate the robustness of the SWG Y-junction to fabrication errors for TE_0 mode, discussed in section 4.4.1.2 (see Figure IV.14(a)). The performance for TE_1 mode division is more sensitive to fabrication errors in the width of the SWG stem owing to the weaker confinement of the Floquet-Bloch TE_1 mode compared to the Floquet-Bloch TE_0 mode. While under-etching results in $EL_{TE1}^{SWG,50}$ < 2.1 dB and $EL_{TE1}^{SWG,100}$ <1.7 dB within the entire measured bandwidth, over-etching errors are negligible at shorter wavelengths and increase towards longer wavelengths.

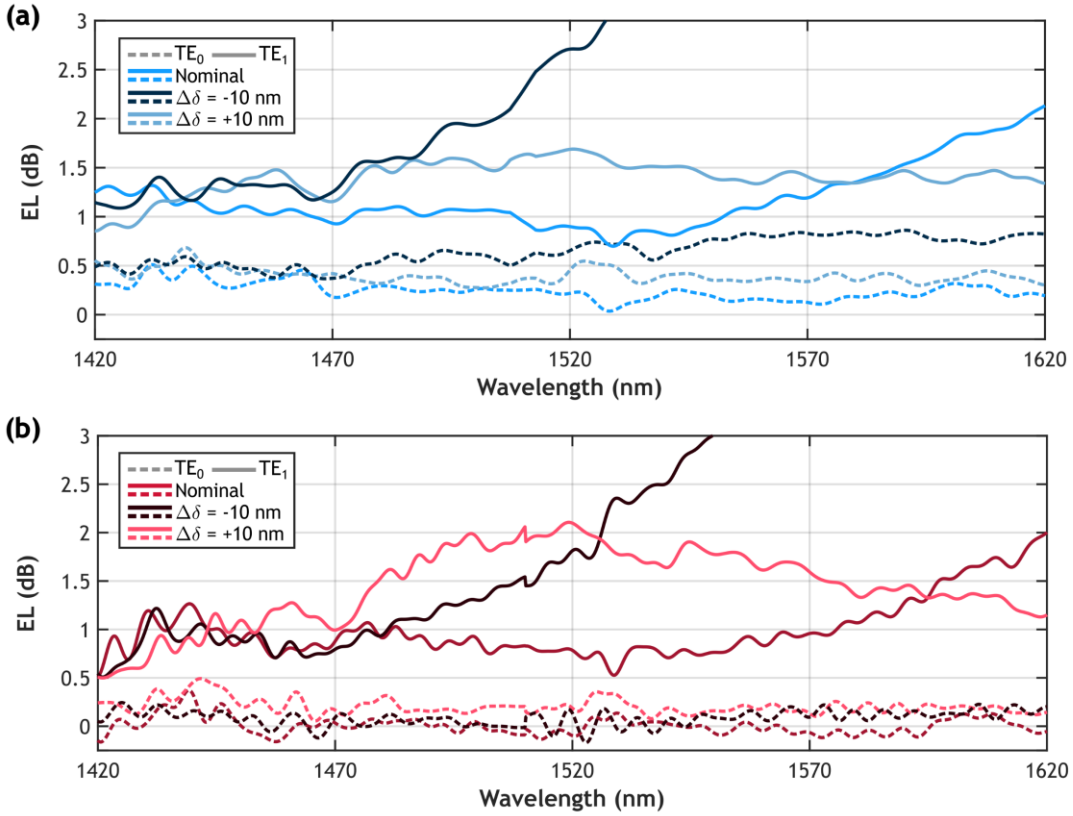

Figure IV.17. Tolerances to fabrication errors of the SWG Y-junction for TE_0 (dashed line) and TE_1 (solid line) polarizations, for MFS of (a) 100 nm and (b) 50 nm.

4.4. Conclusions

Optical power splitters are fundamental building blocks in almost every integrated photonic circuit. Meeting modern technology demands requires low-loss, compact splitters tolerant to fabrication processes while operating over wide spectral ranges for multiple optical modes. One of the most widespread power splitter architectures is the symmetric Y-junction due to their simplicity and versatility. However, these devices suffer from increased losses, especially for fundamental modes, due to fabrication resolution limitations. In this chapter, a novel high-performance power splitter based on a Y-junction engineered with subwavelength metamaterials has been presented. This innovative approach effectively mitigates mode confinement near the junction tip, thereby alleviating losses stemming from limited fabrication resolution. The device is designed to accommodate two different fabrication processes: a high-resolution process with an MFS of 50 nm and a more stringent resolution of 100 nm.

Simulated excess losses for the fundamental TE mode are below 0.1 dB across a broad bandwidth of 300 nm (1400 — 1700 nm) for the 50 nm MFS, and under 0.3 dB for the first-order TE mode within a 1300 — 1600 nm window. With a 100 nm MFS, the proposed design yields excess losses for both TE_0 and TE_1 modes below 0.5 dB across a 300 nm bandwidth (1300 — 1600 nm). Notably, compared to a conventional Y-junction, this results in a significant reduction in TE_0 loss at the central design wavelength (1550 nm), from 0.99 dB to 0.12 dB, with negligible impact on TE_1 loss.

The experimental characterization was carried out by means of two fabrication runs, considering both MFS resolutions of 100 nm and 50 nm. In the first run, a proof-of-concept device was characterized using an MZI structure to extract fundamental TE mode losses. In the second run, a comprehensive characterization employing cascaded structures was performed for the TE_0 mode. Furthermore, a structure combining a mode multiplexer with SWG Y-junctions was used to assess TE_1 mode loss. The measurements demonstrate the broadband performance and relaxed fabrication tolerances of SWG-based Y-junctions. Accurate measurements of the cascaded splitters show excess loss for the fundamental TE mode below 0.3 dB for MFS = 50 nm and under 0.5 dB for MFS = 100 nm, covering a 260 nm bandwidth (1420 — 1680 nm). In addition, excess loss for the TE_1 mode remains below 1 dB over a 100 nm bandwidth (1475 — 1575 nm) for the 50 nm MFS. SWG Y-junctions subjected to deterministically induced errors of ±10 nm were also measured to evaluate resilience to over- and under-etching errors, demonstrating robust fabrication tolerances for the fundamental TE mode.

The performance of the SWG Y-junction demonstrated in this thesis significantly outperforms other state-of-the-art power splitters. A comprehensive comparison of its performance against alternative architectures for dual-mode splitting is provided in Table 2 of Chapter V in the discussion section. For example, some of the best-performing experimentally demonstrated alternatives, such as [194], exhibit a bandwidth of 80 nm with EL <0.15 dB, while [195] operates within a 100 nm wavelength range with EL <0.65 dB. In contrast, the developed splitter exceeds the operating bandwidth by 70 nm

with EL <1.5 dB. In exclusive consideration of operation for the fundamental mode, it outperforms the aforementioned alternatives by an extended margin of 160 nm, while maintaining EL below 0.5 dB. Despite the performance advancements accomplished through the use of SWG metamaterials in the stem and arms waveguides of a Y-junction, the TE_1 mode exhibits higher losses than expected. This decrease in TE_1 mode performance is a consequence of the SWG stem waveguide width selected as a compromise between TE_0 and TE_1 mode performance optimization. Therefore, a second strategy has been proposed and described in Chapter V.

The SWG-engineered Y-junction presented in this chapter demonstrates the potential of SWG metamaterials for developing high-performance integrated photonics power splitters. Moreover, this SWG splitter holds promise for enhancing the functionality of diverse silicon photonic applications, including high-bandwidth on-chip communication systems and broadband spectroscopic systems.

Chapter V:

ACHROMATIC SUBWAVELENGTH-ASSISTED POWER SPLITTER

This chapter introduces a new power splitter that utilizes a Y-junction assisted by SWG metamaterials, achieving an unprecedented ultra-broad bandwidth in the SOI platform. The proposed design strategy effectively mitigates the adverse effects of junction tip-induced losses by employing SWG metamaterials, facilitating smooth modal transitions within the device structure. This device operates not only for the fundamental and first-order TE modes but also demonstrates compatibility with the fundamental TM mode. Section 5.1 outlines the need for high-performance multimode power splitters characterized by broad bandwidths. Section 5.2 describes the principle of operation, optimization strategy, and final design as well as the simulation results. Experimental measurements of the fabricated power splitter for the three operating modes are detailed in Section 5.3. Section 5.4 offers a comprehensive discussion of the obtained results and a comparison with other state-of-the-art power splitters.

5.1. Introduction
5.2. Principle of operation and device design
5.3. Fabrication and experimental characterization
5.4. Discussion and conclusions

5.1. Introduction

In the previous chapter, a broadband multimode power splitter was demonstrated and experimentally validated. However, the discrepancy observed between the expected performance of the first-order TE mode in simulations and actual measurements reveals the need to improve multimode performance. The SWG Y-junction presented in Chapter IV shows degradation for the TE_1 mode as a consequence of a compromise between excess losses for TE_0 and TE_1 modes intrinsic to the design. That is, the selection of the SWG stem waveguide width is critical, as it directly affects modal confinement. Higher SWG stem width values lead to stronger modal confinement, preventing TE_1 mode radiation. However, this exacerbates the inherent penalties of TE_0 mode due to the change on the mode profile at the junction tip.

Therefore, in this chapter a novel strategy to realize a 3-dB power splitter tailored for the SOI platform is presented. This device relies on a symmetric Y-junction with conventional waveguides as arms and stem but features a SWG-metamaterial-assisted transition between them. The use of SWG-metamaterials to assist the stem-to-arms transition allows flexible control of the modal transition at the junction tip. This ensures that the modes propagating through each branching arm waveguide do not experience an abrupt refractive index change. As a result, the device showcases low losses across multiple modes with relaxed fabrication tolerances over an unprecedented ultra-broad bandwidth. Moreover, this innovative design facilitates dual-polarization operation.

Simulations yield for the SWG-assisted Y-junction minimal excess loss (<0.2 dB) for both TE_0 mode and TE_1 modes over a remarkable 700 nm bandwidth (1300 — 2000 nm), and less than 0.3 dB for the TM_0 mode within the 1300 — 1800 nm wavelength range. Experimental measurements validate the simulation results, confirming low excess losses for the three modes in the 1430 — 1680 nm wavelength range along with robust fabrication tolerances for etching errors up to ±10 nm.

5.2. Principle of operation and device design

As discussed in the previous chapter, there are two main basic mechanisms responsible for radiation loss at the tip in symmetric Y-junctions: the wavefront mismatch due to the abrupt tilt angle, and the transformation of the mode profile in the interface between the stem and arms. Thus, loss for the first-order mode is typically lower than for the fundamental mode. The first loss-inducing mechanism is mainly determined by tilt angle (θ) and hence, the arm waveguides length and final separation. The second mechanism is driven by the minimum separation between the arms, which in turn is limited by the resolution of fabrication processes. To further understand the loss induced by the junction, the stem-to-arms interface is treated as a transition from a three-layer waveguide structure to a five-layer waveguide structure, as explained in more detail in Chapter III (section 3.2.3.2). The transmitted power between the input mode of order m into the output mode of order m' is contingent upon the branching angle and the difference between its propagation constant (k_x) in the three-layer ($k_{x,m}^{i}$) and five-layer ($k_{x,m'}^{t}$) guided wave mode, given by Equation (3.7). In the

five-layer structure, the separation between the branching waveguides ($2d$) increases gradually with the tilt of the arm waveguides and the distance to the junction x: $d = x\,tan(\theta)$.

It is important to note that mode evolution and mode conversion in Y-junctions are also two important phenomena to take into account [137], [138], [139]. Mode conversion is the process of exchanging optical power between different-order modes through interaction and typically occurs in asymmetric Y-junctions. This process in symmetric configurations is restricted to even-to-even and odd-to-odd modes [140]. For example, only coupling between TE_0 and TE_2 or TE_1 and TE_3 would be possible. However, by further preventing TE_2 and higher-order modes operation through waveguide width design, no mode conversion is allowed. Under this condition, the behavior of symmetric Y-junctions is hence primarily governed by mode evolution. Mode evolution involves the transition of optical modes from the stem to the arm waveguides within the splitter structure. When an input TE_0 mode propagates through the stem, it is divided equally into two in-phase TE_0 modes at the output arms due to the device's inherent symmetry. An input TE_1 mode is similarly equally split into two TE_0 modes of equal amplitude at the output arms, but with a π phase difference (φ) between them. The evolution of the TM_0 mode is analogous to that of the TE_0 mode.

All these abovementioned factors are therefore considered when designing the novel SWG-assisted splitter that is schematized in Figure V.1. The splitter comprises a stem waveguide of width W_S supporting both fundamental and first-order transverse-electric modes, and two S-bend output arms of width W with SWG metamaterials between them. The SWG metamaterials between the arms reduce the main radiation loss mechanism inherent to symmetric Y-junctions that is attributed to the transformation of the mode profile along the branching. The use of S-bend shaped waveguides for the arms of the Y-junction reduces considerably the tilt angle ($\theta \sim 0$), thus drastically decreasing the radiation loss caused as demonstrated in [196], [197].

The SWG section of length L_{SWG} is divided in two different regions to take better advantage of the grating geometry. The first section of length L_{S1} comprises SWG segments located at the beginning of the branching, whose width increases with arm spacing. In the second section of length L_{S2}, the SWG segments are split along the waveguide of each output arm, while linearly decreasing in size. This allows for improved light splitting by using SWG metamaterials to manipulate the beam according to the shape and spacing of the arm waveguides. To be more specific, the SWG metamaterials implemented between the arms ensure a nearly invariant $k_{x,m'}^{t}$ with x at the junction proximity to reduce the difference between the propagation constants at the stem-to-arms interface. Similar to the operation described in Chapter IV, the input fundamental mode has a field profile with one lobe

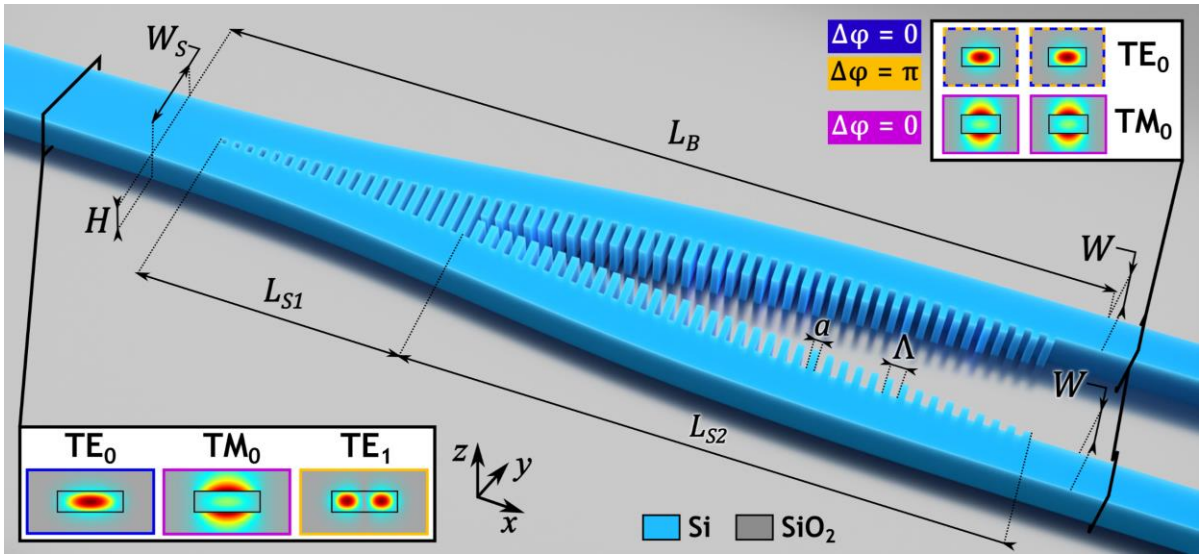

Figure V.1. Three-dimensional schematic of the SWG-assisted Y-junction comprising two S-shaped arms and an SWG-metamaterial-assisted transition. The SiO_2 upper cladding is not shown for clarity. Insets: field distribution within the stem and arm waveguides of the fundamental and first-order transverse-electric modes ($\Re\{E_y\}$), as well as of the fundamental TM mode ($\Re\{E_z\}$).

in the center of the stem waveguide, which transforms into a two-lobe distribution (with one lobe in each arm waveguide), while the field profile of the first-order mode has two lobes with a zero-power value at the center of the stem waveguide. This behavior is illustrated in Figure V.2, showing the field propagations of fundamental modes in panels (a) and (c) for TE and TM polarization, respectively. Also, the two-lobe field distribution of TE_1 mode propagating through the Y-junction is depicted in Figure V.2 (b).

The device was optimized for an SOI platform with a 220-nm-thick silicon core layer through rigorous 3D FDTD simulations. An MFS of 100 nm was considered in the entire structure to ensure compatibility with state-of-the-art DUV fabrication processes and also higher resolution processes such as e-beam lithography [190]. The stem waveguide width was set to W_S = 0.5 μm for monomode operation for wavelengths above 1300 nm. The SWG metamaterial properties are primarily defined by two key geometric parameters: the pitch or period and the duty cycle. First, the selection of an appropriate Λ value is crucial. This value should be small enough to avoid Bragg regime, ensuring propagation within the subwavelength regime: $\Lambda_{\mathrm{SWG}} < \lambda_0/2n_{eff}$, where n_{eff} is the effective refractive index for each optical mode. Conversely, excessively small periods lead to reduced minimum feature sizes. The SWG period was set to 200 nm with a DC = 50% to maximize the MFS.

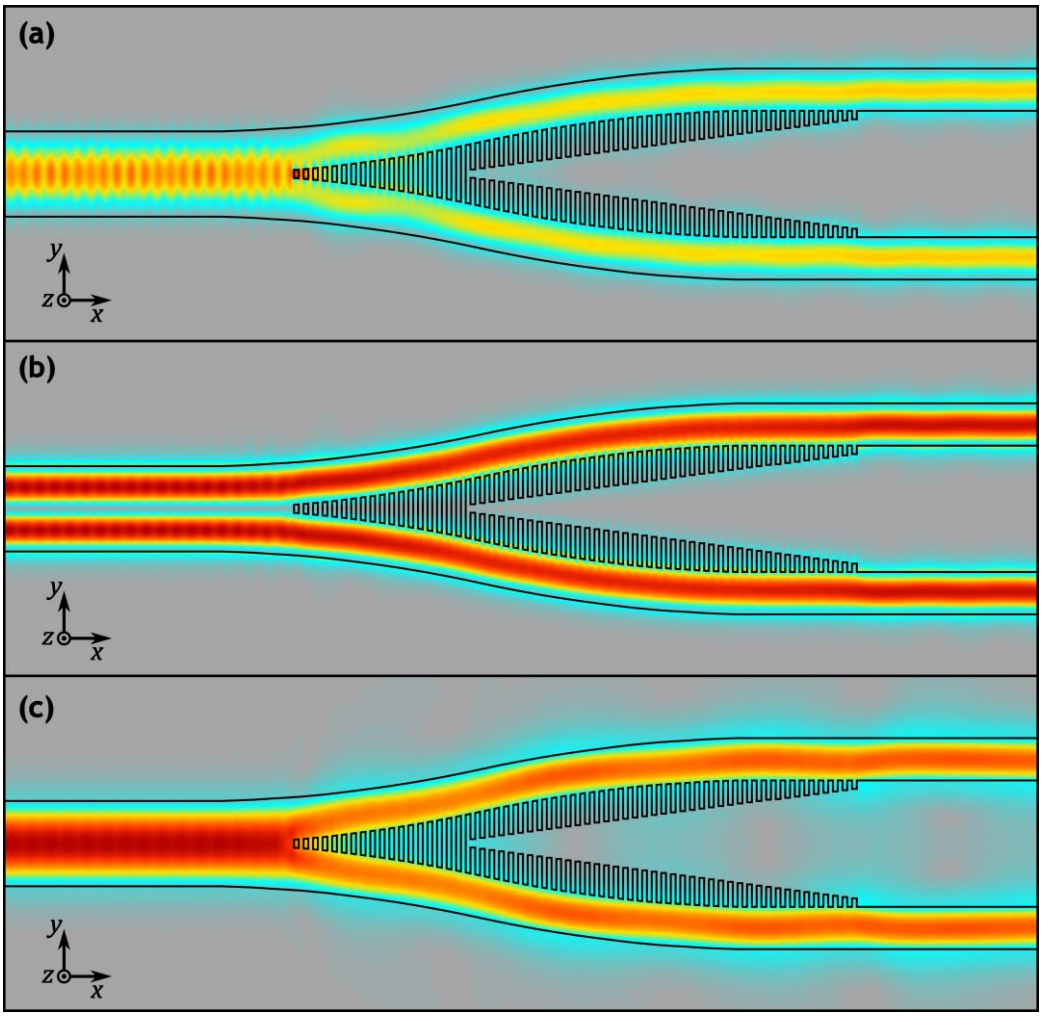

Figure V.2. 3D FDTD simulations of the field propagation through the device at a wavelength of 1560 nm for (a) TE_0 ($|E_y|$), (b) TE_1 ($|E_y|$) and (c) TM_0 ($|E_z|$) modes.

In order to optimize the rest of the geometrical features, S-parameters were calculated through 3D FDTD simulations and used to evaluate the device's excess loss: $EL = 10 \cdot \log_{10}(|S_{21}|^2 + |S_{31}|^2)$, where $|S_{21}|$ and $|S_{31}|$ are the transmission coefficients from the stem to each arm of the Y-junction. The arm length was fixed to L_B = 12.3 μm and the TE_0 mode excess loss was obtained for different values of $L_{SWG} = L_{S1} + L_{S2}$ and L_{S2}, as shown in Figure 2. Preliminary simulations demonstrated that variations in L_{S1} and L_{S2} had a minor impact on the excess losses of the TE_1 mode, and such losses were minimal. This operation matches the predicted response, since the field profile of the TE_1 mode has a zero-field value at the center of the stem waveguide. Consequently, the profile of the TE_1 mode remains unchanged at the branching, as depicted in Figure V.2(b), and the impact of L_{S1} and L_{S2} in TE_1 excess loss is negligible. Therefore, the optimization process focuses exclusively on the TE_0 mode excess loss.

Therefore, the optimization strategies for the proposed device consist mainly of determining the most suitable design for the SWG topology between the splitter arms according to its effect on TE_0,

and then validating the results for TE_1 and TM_0. This optimization process, illustrated in Figure V.3, was accomplished by systematically calculating the S-parameters using 3D FDTD simulations for different values of L_{SWG} and L_{S2}. The simulated excess loss for the TE_0 mode was calculated sweeping different values of L_{SWG} for L_{S2} values of 7.8 μm, 8.0 μm, 8.2 μm, and 8.4 μm, as shown in Figures V.3 (a), (b), (c), and (d), respectively.

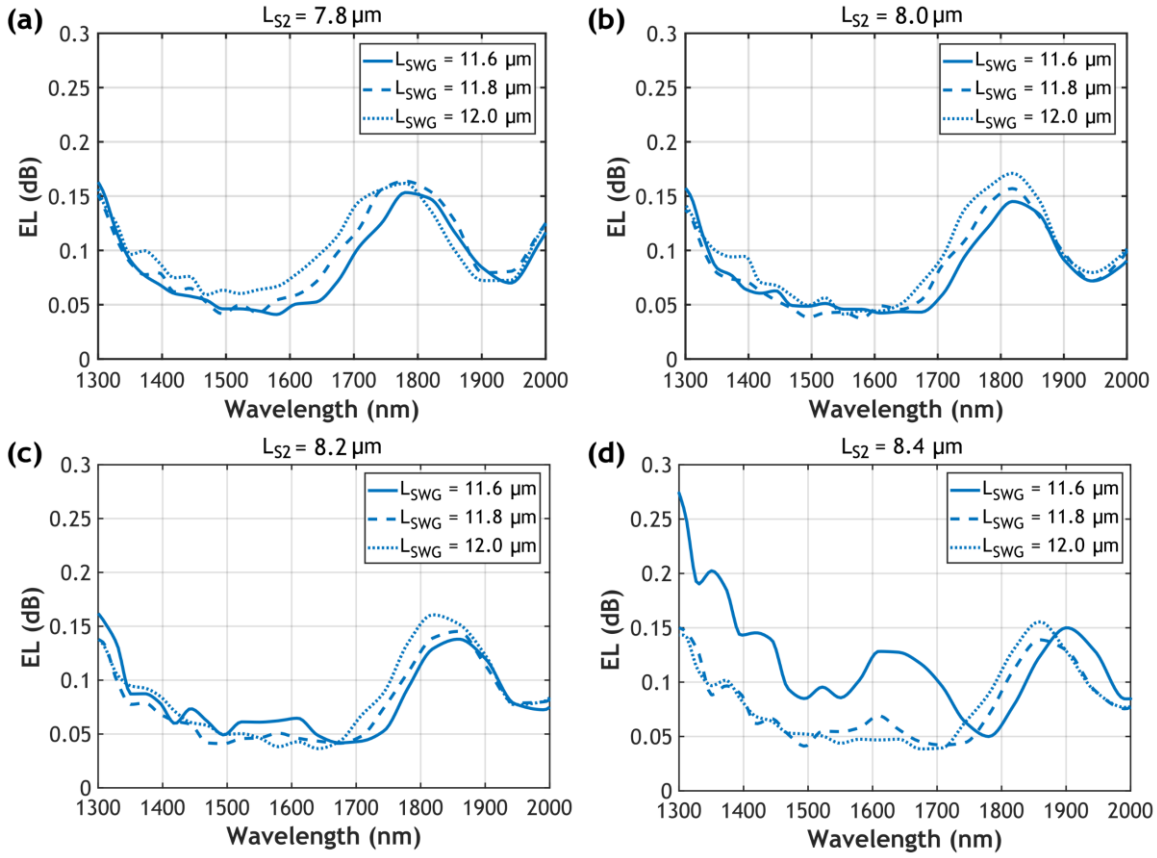

Figure V.3. Simulated excess loss for the TE_0 mode as a function of the wavelength calculated through 3D FDTD simulations for different values of L_{SWG} for (a) L_{S2} = 7.8 μm, (b) L_{S2} = 8.0 μm, (c) L_{S2} = 8.2 μm, and (d) L_{S2} = 8.4 μm.

A larger L_{SWG} tends to shift the best performing region to shorter wavelengths, which can be compensated by increasing L_{S2}. Trade-offs between minimal loss values and curve flatness can also be observed. Based on these results, we judiciously selected the length of the two SWG regions that yield minimal losses across the entire simulated wavelength range (i.e., 1300 — 2000 nm) with L_{SWG} = 11.8 μm and L_{S2} = 8.2 μm.

Figure V.4 shows the simulated EL of the optimized SWG-assisted Y-junction design. The TE_0 mode excess loss remains consistently below 0.2 dB while the TE_1 mode excess loss is less than 0.07 dB, both over an ultra-broad bandwidth of 700 nm (from 1300 to 2000 nm). Therefore, fully covering the E, S, C, L and U telecom bands, partially the O band, and extending up to the 2000 nm waveband. Moreover, the device also offers polarization-independent spectral response at wavelengths below 1800 nm, beyond which leakage losses to the substrate start to become noticeable. Excess loss for the TM_0 mode (EL_{TM0}) is lower than 0.3 dB within the wavelength range from 1300 to 1800 nm.

Tolerances to fabrication deviations of the SWG-assisted Y-junction were evaluated for etching errors of $\Delta\delta$ from the nominal design, while operating for the three modes: TE_0, TE_1, and TM_0, as depicted in Figure V.4 with dotted lines. To account for potential under-etching and over-etching during the fabrication process, adjustments to the geometry of the entire device were induced, considering these errors as absolute variations in the waveguide dimensions. Specifically, the length of the SWG silicon segments (a) was modified to $a' = a + \Delta\delta$ and the widths of the stem and arm waveguides were adjusted to $W_S' = W_S + \Delta\delta$ and $W' = W + \Delta\delta$, respectively. Simulations demonstrate robust fabrication tolerances for the proposed splitter, without performance degradation across the entire 700 nm bandwidth for all TE_0, TE_1, and TM_0 modes.

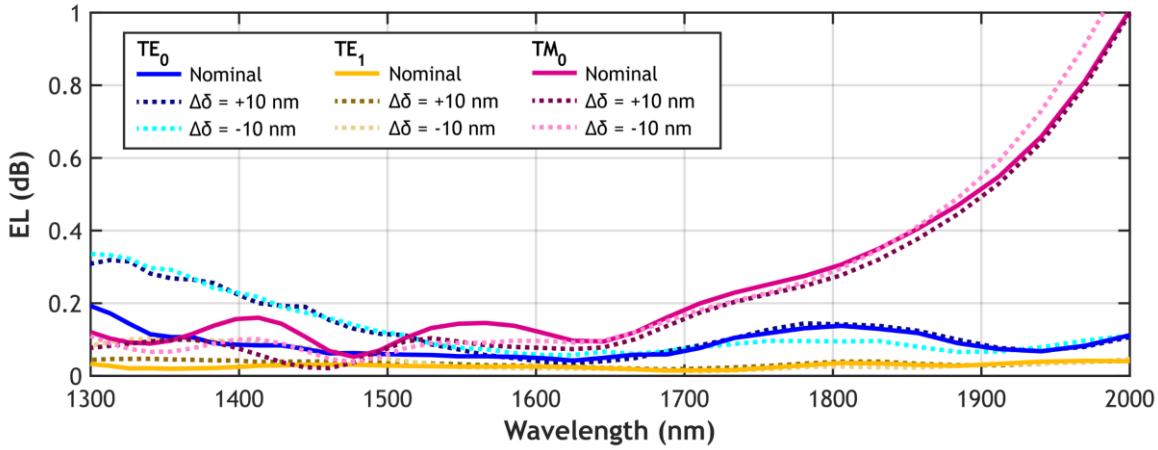

Figure V.4. Excess loss for TE_0 (blue), TE_1 (yellow) and TM_0 (pink) modes for nominal (solid curves) and biased designs with $\Delta\delta$ = ±10 nm (dotted lines) obtained through 3D FDTD simulations.

5.3. Fabrication and experimental characterization

The devices were fabricated on a 220-nm-thick SOI platform with a 2-µm-thick BOX in the same commercial foundry in which the first SWG Y-junction was fabricated [191]. E-beam lithography was used to pattern the Si layer, and etching was performed through an anisotropic reactive ion etching process. Chemical vapor deposition procedure was used to produce the 2.2-µm-thick SiO_2 cladding to cover the Si device layer. The facets of the chip were deep etched, providing smooth trenches around the perimeter of the chip. SWG edge couplers with low-losses and broadband response were included at the input and output facets of the chip to achieve efficient fiber-chip edge coupling [198]. A more in-depth description of the fabrication method can be found in Annex 1.

For the experimental characterization, the same setup described in Chapter IV, Section 4.3, was employed. Accordingly, the same pair of tunable lasers were used to sweep the 1430 — 1505 nm and 1505 — 1680 nm wavelength ranges, respectively. To improve the fidelity of the characterization, the wavelength range was adjusted by reducing the lower end by 10 nm to ensure proper laser operation at shorter wavelengths. Thus, the scanning started at 1430 nm instead of 1420 nm. The lasers were

connected to an optical stage to control the polarization state of incident light precisely. The polarization control stage comprised a three-paddle fiber polarization controller, in addition to an air-fiber bench polarization controller that included a linear polarizer and a half-wave plate. In contrast to the setup used in the previous chapter, the half-wave plate and linear polarizer are replaced with the air-fiber bench polarization controller. This controller integrates the same components (half-wave plate and linear polarizer) but offers a broader operational bandwidth. The light was coupled into the chip SWG edge couplers using a PM lensed optical fiber. A 40× microscope objective collimated the chip output light, directing the beam towards a Glan-laser calcite polarizer. Finally, the beam was focused on a germanium photodetector for data acquisition and subsequent processing.

5.3.1. Measurements of fundamental TE mode

The operation of the SWG-assisted splitters for TE_0 mode was assessed using cascaded structures comprising five of such splitters. In each splitter, the upper arm was routed to the chip output, while the lower arm was connected to the next splitter. This arrangement resulted in a structure with one input and five outputs, as illustrated in the SEM image in Figure V.5 (a), with an inset of the proposed SWG-assisted Y-junction in Figure V.5 (b).

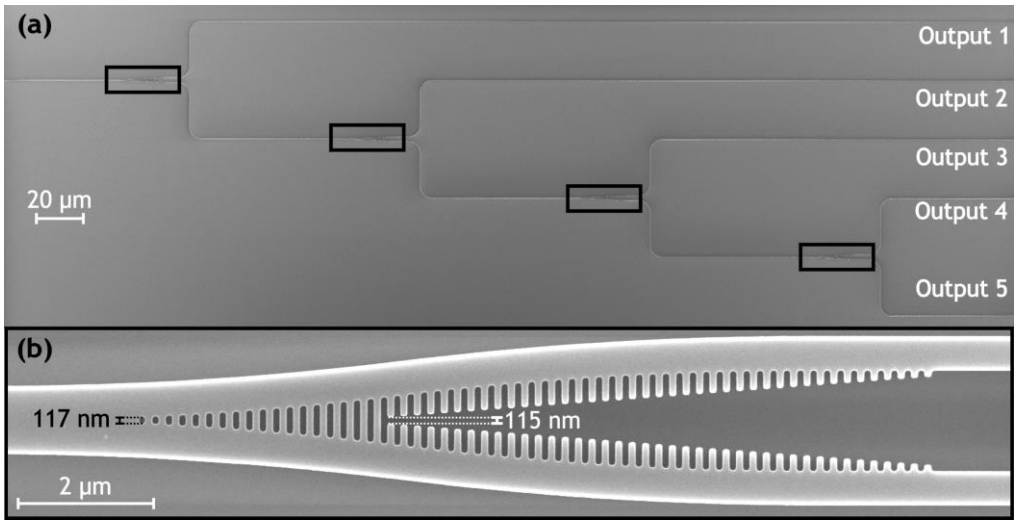

Figure V.5. SEM images of (a) the cascaded structure employed for TE_0 mode characterization. Inset (b) shows a detailed view of the SWG-assisted Y-junction.

Reference structures with the same length, width, and number of bends as each output of the cascaded structure were included on the chip. Specifically, five reference structures, each designed to match a specific output. The first reference $(ref, 1)$ corresponds to output 1 and has 2 bends. The second reference $(ref, 2)$ is equivalent to output 2 and has 4 bends. The third reference $(ref, 3)$ mirrors output 3 and has 6 bends. Fourth $(ref, 4)$ and fifth $(ref, 5)$ references replicate outputs 4 and 5, respectively, and have 8 bends each. The power measured at the output of these reference structures, $P_{ref,i}$ (where i is the reference index) was used to normalize the power measured at each output (P_i) of the cascaded structure as: $P_{N,i} = P_i / P_{ref,i}$. This normalized transmission of the five outputs is presented in Figure V.6, covering the entire measured wavelength range from 1430 nm to 1680 nm. The power measured at each output is in very good agreement with its corresponding target

value, i.e., output 1 is centered at 0.5, output 2 at 0.25, output 3 at 0.125, and outputs 4 and 5 at 0.0625. Note that the small discontinuity observed at the wavelength of 1505 nm is due to the change of laser to perform the wavelength scan.

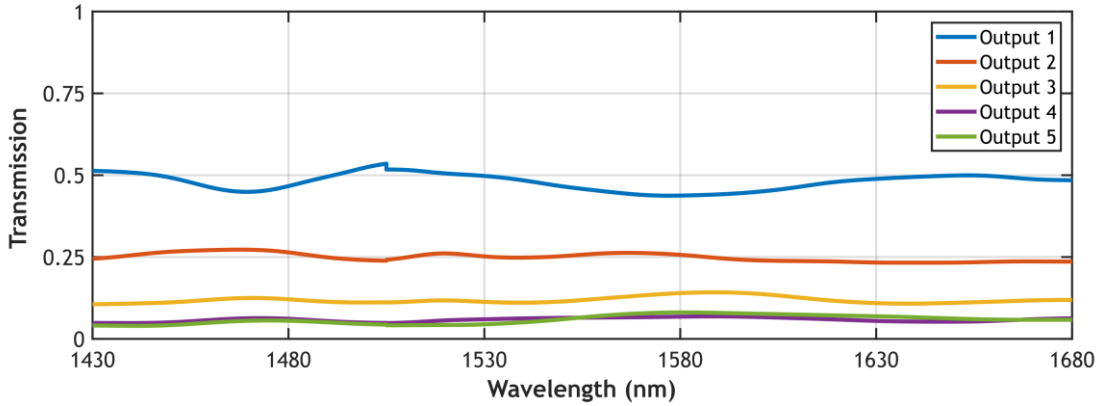

Figure V.6. Normalized transmission spectrum of outputs 1 to 5 measured using cascaded SWG-assisted Y-junctions operating for TE_0 mode.

The excess losses were accurately obtained by linear regression, fitting the power values measured from outputs 1 to 5, while also considering the power imbalance after each stage as follows:

$$EL_1 = 10 \cdot \log_{10}\left(\frac{1}{P_{N,1}+P_{N,2}+P_{N,3}+P_{N,4}+P_{N,5}}\right) \tag{5.1}$$

$$EL_2 = 10 \cdot \log_{10}\left(\frac{1-P_{N,1}}{P_{N,2}+P_{N,3}+P_{N,4}+P_{N,5}}\right) \tag{5.2}$$

$$EL_3 = 10 \cdot \log_{10}\left(\frac{1-P_{N,1}-P_{N,2}}{P_{N,3}+P_{N,4}+P_{N,5}}\right) \tag{5.3}$$

$$EL_4 = 10 \cdot \log_{10}\left(\frac{1-P_{N,1}-P_{N,2}-P_{N,3}}{P_{N,4}+P_{N,5}}\right) \tag{5.4}$$

$$EL_5 = 10 \cdot \log_{10}\left(\frac{1-P_{N,1}-P_{N,2}-P_{N,3}-P_{N,4}}{P_{N,5}}\right) \tag{5.5}$$

The resulting EL_{TE0} is shown in Figure V.7 with solid lines and is the linear regression between EL_1, EL_2, EL_3, EL_4, and EL_5. The excess losses remain below 0.2 dB over the entire measured bandwidth from 1430 to 1680 nm. Experimental results demonstrate a remarkable consistency with simulation predictions (see Figure V.4). Additionally, the power uniformity (PU) at the first output was calculated, defined as the difference between the maximum and minimum output power within the measured bandwidth: $\mathrm{PU} = 10 \cdot \log_{10}(P_{1,max}/P_{1,min})$. The resulting PU for TE_0 operation is 0.88 dB in the entire measured bandwidth.

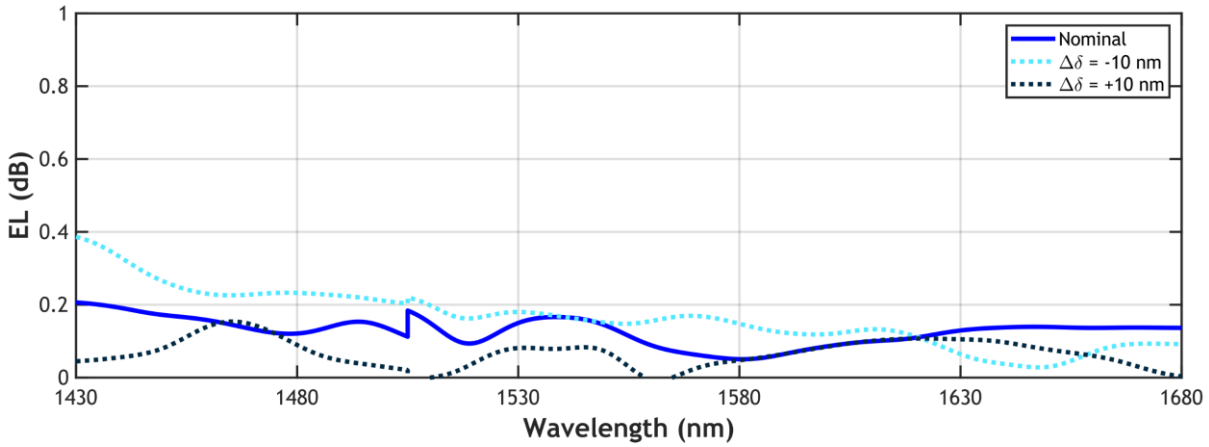

Figure V.7. Measured excess losses for the nominal design (solid lines) and for devices with deviations of $\Delta\delta$ = ±10 nm (dotted lines) for TE_0 mode operation. Note that the discontinuity at 1505 nm results from the laser change for the wavelength scan.

To validate the robustness of the proposed splitter against fabrication deviations, biased devices with induced dimensional variations of $\Delta\delta$ = ±10 nm with respect to the nominal design were fabricated. These devices were similarly arranged in cascaded structures for TE_0 and TE_1 operation. Measured ELs of biased devices are shown in Figure V.7 for TE_0 mode, indicated by dotted lines. The largest performance degradation occurs for over-etching errors ($\Delta\delta$ = -10 nm). Still, losses are lower than 0.4 dB within the full measured bandwidth of 250 nm. These results demonstrate the resilience of the SWG-engineered solution to consistently operate with minimal losses, even in the presence of fabrication-related imperfections.

5.3.1. Measurements of first-order TE mode

To evaluate the operation of the proposed splitter for the TE_1 mode, we incorporated the same cascaded structures used to characterize the TE_0 mode, with the addition of a mode multiplexer preceding each of the five splitters [150]. The mode multiplexer used here is the same one used for TE_1 mode characterization of the SWG Y-junction in the previous chapter. Figure V.8 (a) shows an SEM image of two cascaded auxiliar mode multiplexers with the SWG-assisted Y-junction. An inset of the mode multiplexer is depicted in Figure V.8 (b). When light was injected into the lower branch of the mode multiplexer, TE_1 mode was excited in the stem waveguide of the SWG-assisted Y-junction. This TE_1 mode was then split into the TE_0 modes of the two arms, with the upper arm directed to the chip output and the lower arm directed to the following mode multiplexer. The field distribution ($\Re\{Ey\}$) of TE_0 and TE_1 modes propagating through the structure have been included in Figure V.8.

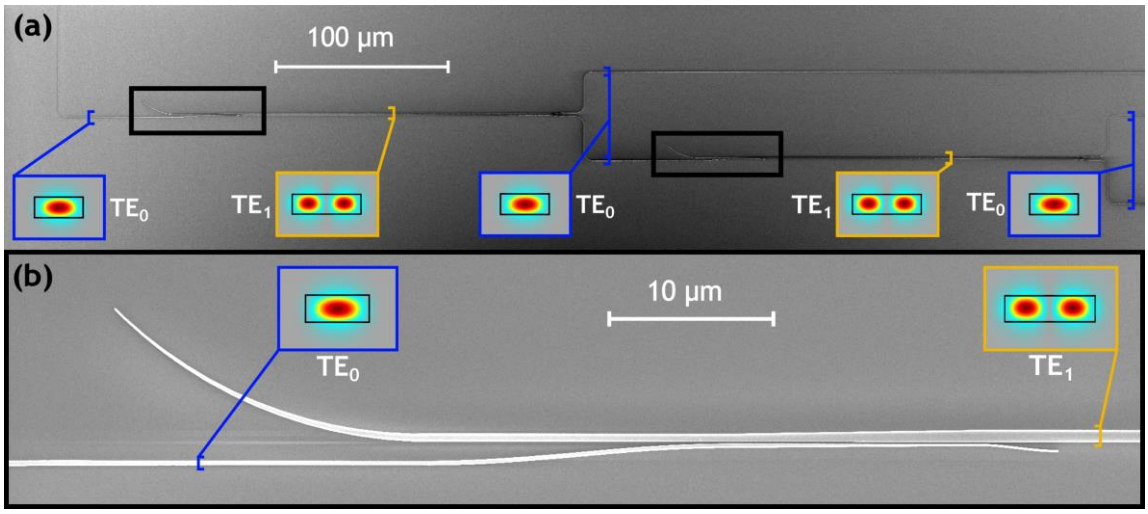

Figure V.8. SEM images of (a) a zoomed cascaded structure employed including mode multiplexers for TE_1 characterization. Inset (b) shows a detailed view of the auxiliary mode multiplexer. In both panels (a) and (b) the field distribution ($\Re\{E_y\}$) of the fundamental and first-order TE modes in different regions of the structure have been included.

Reference structures comprising four mode multiplexers in back-to-back configuration were also incorporated, and the power at the output (P_{mux}) was also measured. In addition, the output power of reference structures ($P_{ref,mux}$), which included waveguides of equivalent width, length and number of bends to those of the back-to-back multiplexers, were also measured to independently determine their contribution. Therefore, the reference power used for the normalization of the cascaded structures is: $P_{ref,i} = P_{ref,mux} - i \cdot (P_{ref,mux} - P_{mux})/4$, where i is the reference index. Then, the normalized power for each output can be calculated as: $P_{N,i}^{(1)} = P_i^{(1)}/(P_{ref,i})$. The superindex (1) is used to differentiate the TE_1 mode operation. The normalized transmission of the five outputs is depicted in Figure V.9, operating for the TE_1 mode across the entire measured wavelength range from 1430 nm to 1680 nm. As for TE_0 mode operation discussed in the preceding section, the power distribution of each output closely aligns with its designated target value. In particular, output 1 is centered at 0.5, output 2 at 0.25, output 3 at 0.125, and outputs 4 and 5 at 0.0625, demonstrating excellent consistency and precision in the device's performance. For the TE_1 mode, excess losses were also accurately obtained using linear regression, fitting the power values measured from outputs 1 to 5. The EL relative to each stage was also calculated using Equations (5.1) to (5.5). The resulting EL_{TE1} is shown in Figure V.10 with solid lines. Similar to the TE_0 mode, the excess losses for TE_1 mode remain below 0.2 dB across the measured bandwidth from 1430 nm to 1680 nm. The experimental results for the TE_1 mode also exhibit consistency with simulation predictions (see Figure V.4). Moreover, PU at the first output was calculated, resulting in a further reduction compared to TE_0 mode, with a PU = 0.66 dB in the complete 1430 — 1680 nm wavelength range.

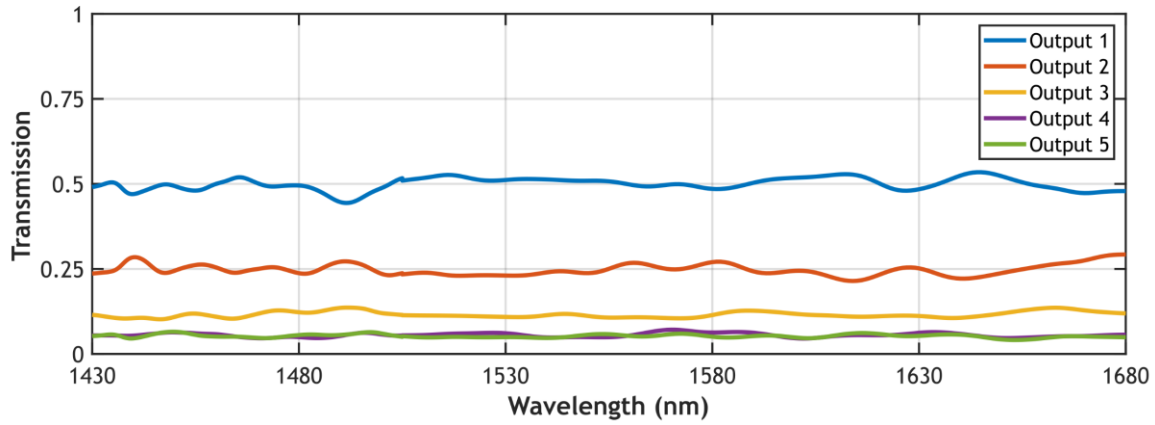

Figure V.9. Normalized transmission spectrum of outputs 1 to 5 measured using cascaded SWG-assisted Y-junctions operating for TE_1 mode. Note that the small discontinuity observed at the wavelength of 1505 nm is due to the change of laser to perform the wavelength scan.

Biased devices with induced dimensional variations of $\Delta\delta$ = ±10 nm relative to the nominal design were included within the cascaded structures with auxiliar mode multiplexer. Subsequently, employing the same procedure of linear regression, the ELs of biased devices were calculated in order to validate the robustness of the proposed splitter against fabrication deviations for TE_1 mode operation. Figure V.9 illustrates the ELs of biased devices with dotted lines. As for the TE_0 mode, the largest performance degradation occurs for over-etching errors ($\Delta\delta$ = -10 nm), with losses remaining under 0.4 dB in the 250 nm measured bandwidth. These results demonstrate the resilience of the proposed SWG-engineered solution to consistently operate with minimal losses for the two first TE modes, even in the presence of fabrication-related imperfections.

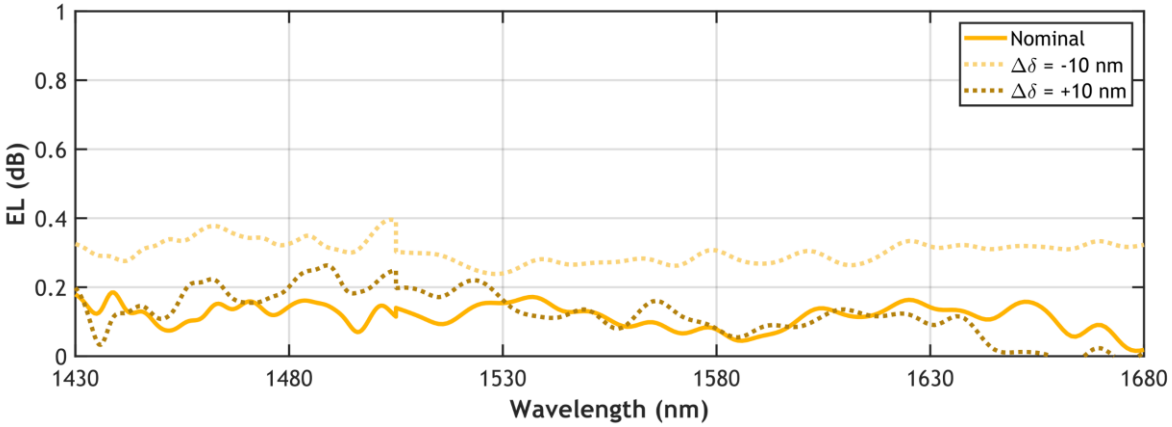

Figure V.10. Measured excess losses for the nominal design (solid lines) and for devices with deviations of $\Delta\delta$ = ±10 nm (dotted lines) for TE_1 mode operation. Note that the discontinuity at 1505 nm results from the laser change for the wavelength scan.

5.3.2. Measurement of the fundamental TM mode

The operation of the SWG-assisted Y-junction for TM_0 mode operation was also examined. Utilizing the same cascaded structures employed for TE_0 mode characterization, TM polarization was excited at the chip input. The bends within the waveguide are critical for light propagation through the structures. The chip includes bends with a radius of 5 µm. These bends are optimized for TE

polarization, resulting in minimal loss and efficient guidance for TE-polarized light within the waveguide structure. However, the behavior of the TM_0 mode differs because of the different orientation of the electric field (along the z-axis) with respect to the waveguide geometry. This results in weak confinement of TM-polarized light within a 220-nm-thick and 500 nm wide Si waveguide. A thicker waveguide layer is typically required for TM operation, which serves the dual purpose of supporting higher-order TM modes and improving polarization confinement within the structure. As a consequence of TM_0 mode weak confinement, radiation occurs at wavelengths beyond 1630 nm at the 5-μm-radii bends. Therefore, the measured bandwidth of the device for TM_0 mode operation is limited to the wavelength range covering from 1430 nm to 1630 nm.

The measured power of these reference structures ($P_{ref,i}^{(2)}$) is used to normalize the measured power of each cascaded stage output ($P_i^{(2)}$) as: $P_{N,i}^{(2)} = P_i^{(2)}/P_{ref,i}^{(2)}$. Note that the superindex (2) is used to differentiate the TM_0 mode operation. Figure V.11 presents the measured normalized transmission of the five outputs, demonstrating the performance of the device operating for TM_0 mode across the measured wavelength spectrum (1430 − 1680 nm). The power distribution across each output is slightly lower than its designated target value. Ideally, output 1 should be centered at 0.5, output 2 at 0.25, output 3 at 0.125, and outputs 4 and 5 at 0.0625. The device still provides efficient power splitting, despite the slight deviation from the intended ratios.

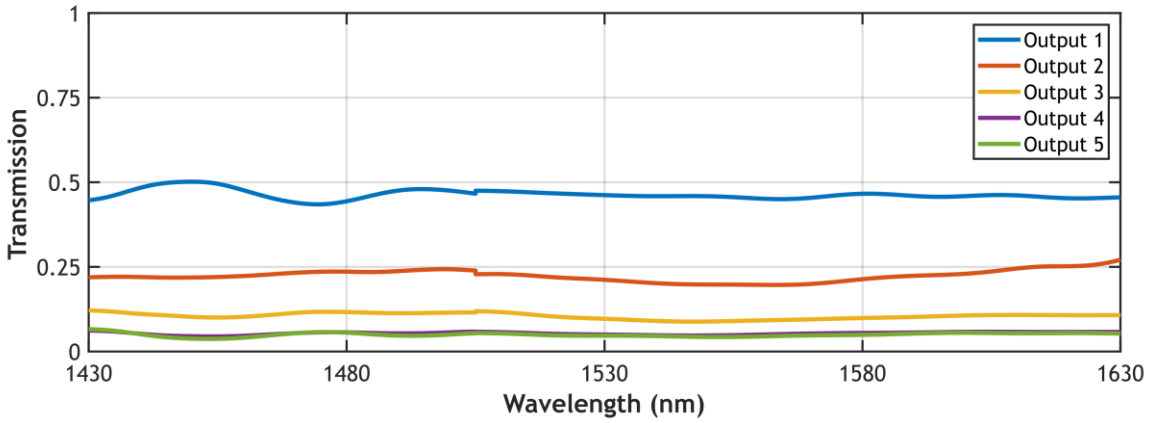

Figure V.11. Normalized transmission spectrum of outputs 1 to 5 measured using cascaded SWG-assisted Y-junctions operating for TM_0 mode.

Figure V.12 shows EL_{TM0}, obtained using the same linear regression analysis of preceding sections. EL_{TM0} measurements for the nominal device are represented with solid line, while biased devices with dimensional variations of $\Delta\delta$ = ±10 nm are plotted with dotted lines. Nevertheless, the device exhibits an excellent performance for TM_0 mode splitting, with EL_{TM0} below 0.4 dB over a wide bandwidth from 1430 to 1630 nm. The excess losses for the splitters with modified dimensions at $\Delta\delta$ = +10 nm are very similar to the losses of the nominal device, achieving an EL_{TM0} <0.4 dB over the same wavelength range. On the other hand, upon over-etching variations of $\Delta\delta$ = -10 nm , the maximum loss in the spectrum is reduced to 0.3 dB. These results demonstrate the

polarization-agnostic response of the proposed splitter, as well as the resilience to typical etching deviations for TM polarization operation.

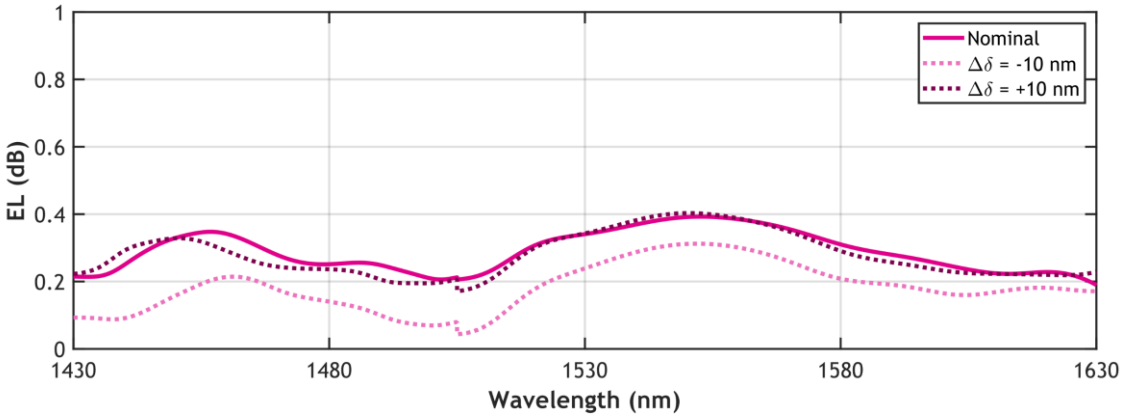

Figure V.12. Measured excess losses for the nominal design (solid lines) and for devices with deviations of $\Delta\delta$ = ±10 nm (dotted lines) for TM_0 operation. Note that the discontinuity at 1505 nm results from the laser change for the wavelength scan.

5.4. Conclusions

In this chapter a metamaterial-assisted silicon 3-dB power splitter for multimode operation over a record broad bandwidth has been proposed and experimentally validated. The unique properties of subwavelength grating metamaterials are leveraged to mitigate the abrupt transition at the tip of conventional Y-junctions, while offering flexible control over the confinement of propagating modes. This approach enables efficient power splitting from the stem waveguide to the S-shaped arms with an outstanding performance for TE_0, TE_1 and TM_0 mode operation. 3D FDTD simulations predict an excess loss lower than 0.2 dB for the TE_0 mode and below 0.07 dB for the TE_1 mode over a wavelength range of 700 nm, which extends from 1300 to 2000 nm. The device also operates for the fundamental TM mode with simulated excess loss under 0.3 dB in the 1300 — 1800 nm wavelength range. Measurements confirm the exceptional power splitting efficiency of the proposed device, with excess losses remaining under 0.2 dB for both fundamental and first-order TE modes in the 1430 to 1680 nm, limited by the lasers available in the setup. The TM_0 mode measurements also exhibit low excess loss of less than 0.4 dB across a 200 nm bandwidth ranging from 1430 to 1630 nm. Furthermore, another significant advantage of the SWG-assisted Y-junction design is its robustness to fabrication errors. Both simulations and experiments prove that the proposed splitter reliably maintains a high-performance response in the presence of fabrication-related geometric variations.

For the sake of comparison, Table 2 summarizes the performance and compares the reported device with several state-of-the-art multimode power splitters based on SOI platforms with a 220-nm-thick waveguide core. To ensure a fair comparison, it should be noted that different authors define the operational bandwidth according to different loss thresholds, indicated therein. Among stand-out devices, Ozcan et al. [130] recently reported a polarization-independent Y-junction, achieving low losses (EL <0.25 dB) and a device length of only 14 μm, but bandwidth is limited to 100 nm. The widest experimental bandwidth (170 nm) is achieved in [188], that is the full-SWG Y-junction presented in

Chapter IV. Despite the broadband and high-performance, the bandwidth for the full-SWG Y-junction is 80 nm smaller for TE_1 mode operation, and still at the expense of greater losses, larger footprint, and no TM operation. The widest simulated performance is achieved by [199], although no experimental validation nor TE_1 operation is provided, and bandwidth is defined for a larger loss threshold. Compared to these alternatives, the SWG-assisted splitter proposed in this thesis represents a substantial advance over current state-of-the-art devices and outperforms them in terms of optical bandwidth with at least 100 nm improvement compared to most prior experimental demonstrations, without increasing the length and maintaining ultra-low losses. Moreover, these results are achieved while preserving an MFS of 100 nm, compatible with state-of-the-art DUV fabrication processes.

A novel SWG-assisted symmetric Y-junction has been demonstrated in this chapter, which is expected to open up a new generation of applications in various areas of silicon photonics, including both established and emerging fields. These applications encompass, but are not limited to, high-capacity multi-band data transmission, LIDAR, multi-target spectroscopy, quantum key distribution, and optical sensing. Moreover, the innovative design strategy proposed herein shows potential for adoption on other high-index contrast material platforms.

To expand the operating bandwidth for larger wavelengths, a thicker BOX layer could be incorporated in the SOI platform. Similarly, the device could operate for higher-order modes redesigning and increasing the width of the stem and arm waveguides. The proposed 3-dB splitter is expected to be essential for advanced and intricate systems that require precise manipulation of optical signals due to its low losses, ultra-broad bandwidth, multimode operation, and robust fabrication tolerances.

Table 2. Comparison of state-of-the-art multimode power splitters using 220-nm-thick silicon core.

Device	Length [μm]	MFS [nm]	Modes	BW_{sim} [nm]	EL_{sim} [dB]	BW_{exp} [nm]	EL_{exp} [dB]
MMI [195]	48	120	TE_0 TE_1	100 (1500 – 1600)	< 0.40	100 (1500 – 1600)	< 0.65
Y-junction [186]	29.15	40	TE_0 TE_1 †	70 (1530 – 1600)	< 0.10	70 (1530 – 1600)	< 0.50
Directional Coupler [200]	2.62	100	TE_0 TM_0	80 (1520 – 1600)	< 1.00	50 (1540 – 1590)	< 1.00
Adiabatic tapers [129]	20	30	TE_0 TM_0	500 (1200 – 1700) 425 (1200 – 1625)	< 0.05* < 0.10*	70 (1530 – 1600)	< 0.19 < 0.14
Y-junction [199]	5	100	TE_0 TM_0	790 (1250 – 2040) 385 (1200 – 1585)	< 0.45 < 1.00	NF	NF
Pixelated meta-structure [201]	5.4	120	TE_0 TE_1	445 (1588 – 2033)	< 0.83	NF	NF
Tapered coupler [194]	13	150	TE_0 TE_1 †	100 (1500 – 1600)	< 0.07 < 0.41	80 (1520 – 1600)	< 1.50
MMI [105]	35.9	100	TE_0 TM_0	160 (1260 – 1420)	< 1.00	NF	NF
Y-junction [130]	14	120	TE_0 TM_0	150 (1500 – 1650)	< 0.10	100 (1500 – 1600)	< 0.25 < 0.23
Y-junction [187], [188] (chapter IV)	41.4	100	TE_0 TE_1	350 (1350 – 1700) 300 (1300 – 1600)	< 0.30 < 0.45	260 (1420 – 1680) 170 (1420 – 1590)	< 0.50 < 1.50
Y-junction (chapter V)	12.3	100	TE_0 TE_1 TM_0	700 (1300 – 2000) 500 (1300 – 1800)	< 0.20 < 0.20 < 0.30	250 (1430 – 1680) 200 (1430 – 1630)	< 0.20 < 0.40

[a] Values marked with an asterisk correspond to values estimated from figures. [b] Devices annotated with a dagger symbol also operate for higher-order modes. NF, Not Fabricated; BW, Bandwidth; EL, Excess Loss; MFS, Minimum Feature Size.

Chapter VI:

ULTRA-BROADBAND MODE CONVERTER

This chapter presents the development of a novel mode conversion architecture using inverse design optimization algorithms and SWG metamaterials. The mode conversion process is achieved through the implementation of two opposing symmetric Y-junctions surrounded by SWG nanostructures. To achieve high- performance, an optimization approach based on inverse design gradient-free algorithms is applied. This methodology aims to exploit the geometric design parameters, thereby allowing multi-parameter optimization for improved operational efficiency. Section 6.1 outlines the intrinsic mode conversion principles underlying symmetric Y-junction architectures. Section 6.2 provides a detailed description of the device design, operating principles, and a complete explanation of the inverse design optimization strategy, including simulation results and delineation of the refined geometric parameters. In addition, Section 6.3 provides a comprehensive account of the measurement setup and experimental protocols used to characterize the fabricated mode converter. Finally, Section 6.4 provides a concise summary of the key results and conclusions derived from both simulations and experiments.

6.1. Introduction
6.2. Device design
6.3. Fabrication and experimental characterization
6.4. Conclusions

6.1. Introduction

The exponential growth of global Internet traffic and the rise of bandwidth-hungry applications accentuate the necessity for the telecommunications industry to move towards next-generation optical systems with higher transmission capacity and lower power consumption [35], [202]. To address this challenge, different multiplexing techniques have been proposed to expand the data transmission capacity of on-chip optical interconnect networks. The dominant silicon photonics optical transceivers rely on wavelength-division multiplexing [37], polarization-division multiplexing (PDM) [203] and mode-division multiplexing systems [38] to encode distinct data channels on the same waveguide. In particular, MDM techniques have attracted a great interest in the last decade as it provides improved data rates by simultaneously transmitting several signals in optical modes of different orders within a single multimode waveguide [39], [204]. Strategies that combine WDM and MDM systems for on-chip and off-chip high-bandwidth-density interconnects have been reported [40]. Also, there have been demonstrations integrating WDM with PDM [203] to enhance link capacity using a single-wavelength light carrier. Multimode silicon photonics involving higher-order modes has proven to be a useful approach in emerging fields such as quantum information processing [41], [148] and on-chip nonlinear photonics [42], [95], [96].

In Chapter III the importance of mode converters in multimode photonic systems was discussed, highlighting their key role to transform a given spatial mode into any other desired mode and vice versa. Broadband, low-loss, and low-crosstalk are critical specifications for the overall high performance of multimode systems. Many mode converters employing different structures have been proposed and, according to their respective operation principle, they can be categorized into four main types: phase matching [152], [153], [154], beam shaping [156], [205], constructive interference of coherent scattering [160], [206] and induced gradient phase [35]. Additionally, structures combining various operation principles have also been reported [100]. Among the aforementioned types of mode converters, devices based on phase matching, beam shaping, and constructive interference of coherence scattering have exhibited characteristics such as low loss, reduced crosstalk, and a strong resilience against fabrication variations. Nevertheless, they are frequently hampered by restricted operational bandwidths or the need for large dimensions.

Mode converters based on induced gradient phase techniques are ultra-compact, broadband, and fabrication-tolerant while maintaining low-loss and low-crosstalk. These devices can be implemented through metasurfaces or metamaterials to assist mode conversion in dielectric waveguides [165], [207]. Mode converters incorporating SWG metamaterials have proven highly successful, showcasing exceptional performance in terms of ultra-low losses, broad operational bandwidths, compact footprints, and robust fabrication tolerances [163], [207], [208], [209].

In this chapter, an innovative mode converter architecture based on two symmetric Y-junctions in back-to-back configuration connected through SWG metamaterials is proposed. The geometrical parameters of the design are optimized through the Powell's gradient-free algorithm, maximizing the modal field conversion between the fundamental and the second-order transverse-electric (TE_2) modes with a compact footprint of only $6.5 \times 2.6\ \mu m^2$. In 3D FDTD simulations, the optimized device

yields an excess loss below 0.75 dB and an extinction ratio (ER) exceeding 10 dB across an extensive bandwidth of 350 nm (1350 nm to 1700 nm). Furthermore, within a 150 nm wavelength range (1472 − 1622 nm), the ER exceeds 20 dB while the EL remains below 0.3 dB. Experimental validation confirms efficient mode conversion in both instances, specifically TE_0-TE_2 and TE_2-TE_0, showing ELs as low as 0.4 dB and ERs exceeding 18 dB across a broadband of 149 nm, extending from 1471 nm to 1620 nm.

6.2. Device design

The device architecture, depicted in Figure VI.1, consists of two symmetric Y-junctions arranged in back-to-back configuration embedded by SWG metamaterials. The geometry comprises a multimode input waveguide of width W_S, ensuring TE_2 mode propagation within the target wavelength range. This input waveguide is divided into two tapered waveguides of length L_T, which constitute the arms of the left symmetric Y-junction. The initial separation between these arms is constrained to the considered MFS and increases to a final separation S, while the width of these arms is reduced to the MFS. The width of the SWG segments increases along with the Y-junction separation, starting from $W_0 = W_S + 2\mathrm{MFS}$ and reaching W_F. The length of the SWG silicon segments also exhibits a linear variation, from a_0 to a_F, for a constant Λ. The geometry has an output multimode waveguide identical to the input one, in which the arms of the right Y-junction converge.

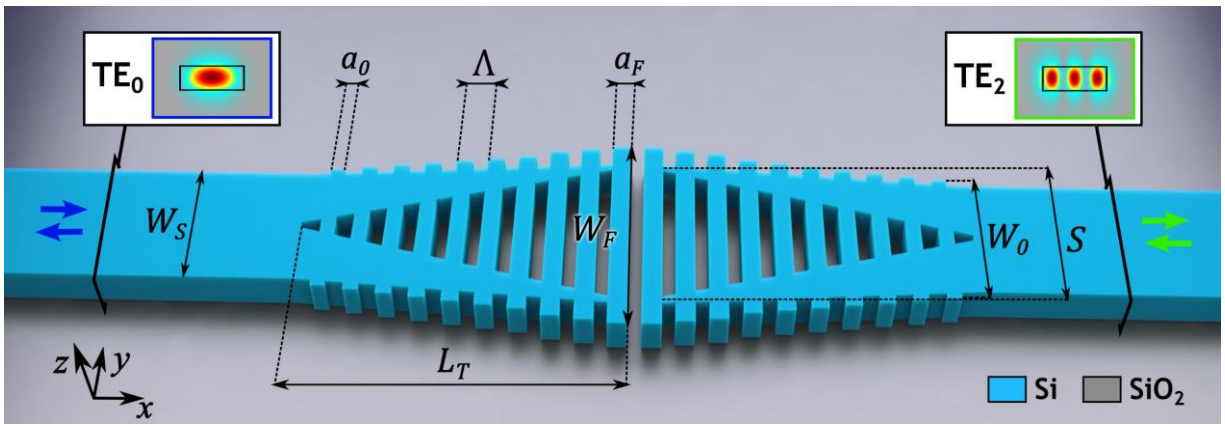

Figure VI.1. Three-dimensional schematic of the proposed SWG mode converter. Insets depict the distribution of the electric field ($\Re\{E_y\}$) in the cross-sectional view of the input/output waveguides.

Efficient mode conversion requires matching the mode profiles of the input and output waveguides to ensure optimal coupling between the desired modes with minimal losses. When the TE_0 mode is excited in the input waveguide, its modal field profile evolves as it propagates through the device, ultimately being fully converted into TE_2 mode at the output waveguide (see section 2.1 below for details). The visual representation of the field profile transformation during the TE_0-TE_2 mode conversion is clearly illustrated in Figure VI.2. It is important to note that the device is reciprocal, i.e., the device also converts an incident TE_2 mode into the output TE_0 mode.

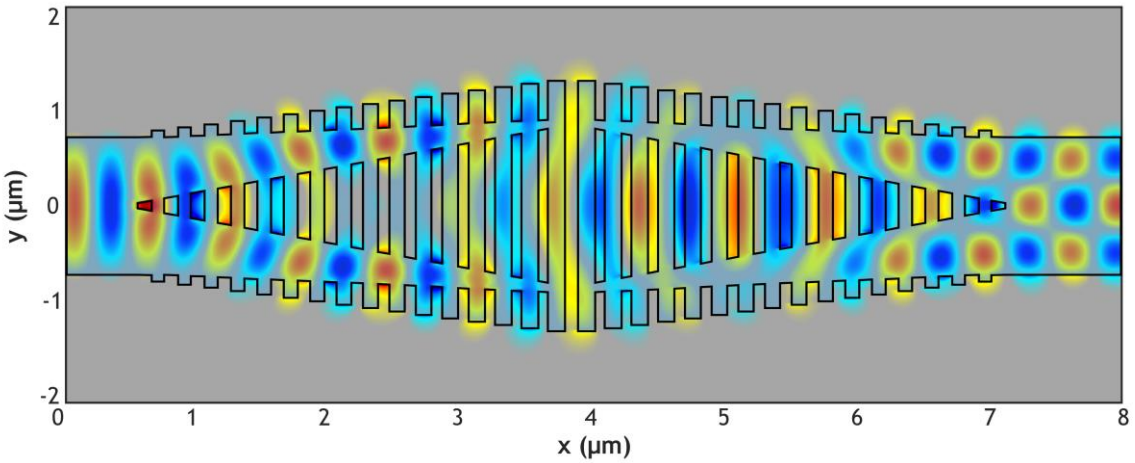

Figure VI.2. Real part of the electric field ($\Re\{E_y\}$) propagating along the device obtained by 3D-FDTD simulation.

6.2.1. Principle of operation

Different studies have addressed the inherent optical mode conversion in symmetric Y-junctions [137], [138], [139]. The input section of a conventional symmetric Y-junction can be seen as a three-layer symmetric waveguide, i.e., three dielectric layers with different refractive indices disposed as cladding-core-cladding. Likewise, the output arm waveguides of a conventional Y-junction is a five-layer symmetric structure: cladding-core-cladding-core-cladding. The transition from the three-layer to the five-layer in the proposed Y-junction structure is schematized in Figure VI.3 (a). The incident field (E_z^i), with a propagation constant k_x, corresponds to that present in a typical three-layer slab waveguide. The field transmitted to the output branching arms waveguides can be approximated by [137]:

$$E_z^t(y) = B(d)E_z^i(y,d)e^{\left(-jcos\theta \int_0^x k_x(x')dx'\right)}e^{(-jk_x|y|sin\theta)} \tag{6.1}$$

where the tilt of the arm waveguides is given by $\theta = atan\left(\frac{S-2MFS}{2L_T}\right)$. With the branching point as the reference origin, the separation between the branching waveguides ($2d$) is given by: $2d = 2xtan(\theta) + MFS$. The reduction in width ($W(x)$) of the tapered arm waveguides can be expressed as: $W(x) = \frac{W_S - MFS}{2} + x\left(\frac{3MFS-W_S}{2L_T}\right)$, being x the distance from the branching point. The electric field $E_z^t(y,d)$ is the corresponding guided-TE mode in a symmetric five-layer waveguide and $B(d)$ is a normalizing factor. The influence of the SWG metamaterial on this device can be conceptualized as an equivalent metamaterial covering the same area as the grating, as illustrated in Figure VI.3 (c). The evolution of the real part of the electric field $E_z(y)$ in the slab structure of Figure VI.3 (a) at the interfaces 1, 2, 3 and 4 is plotted in Figure VI.3 (b). Similarly, the real part of $E_z(y)$ for the Y-junction structure with the equivalent metamaterial of Figure VI.3 (c) is shown in Figure VI.3 (d).

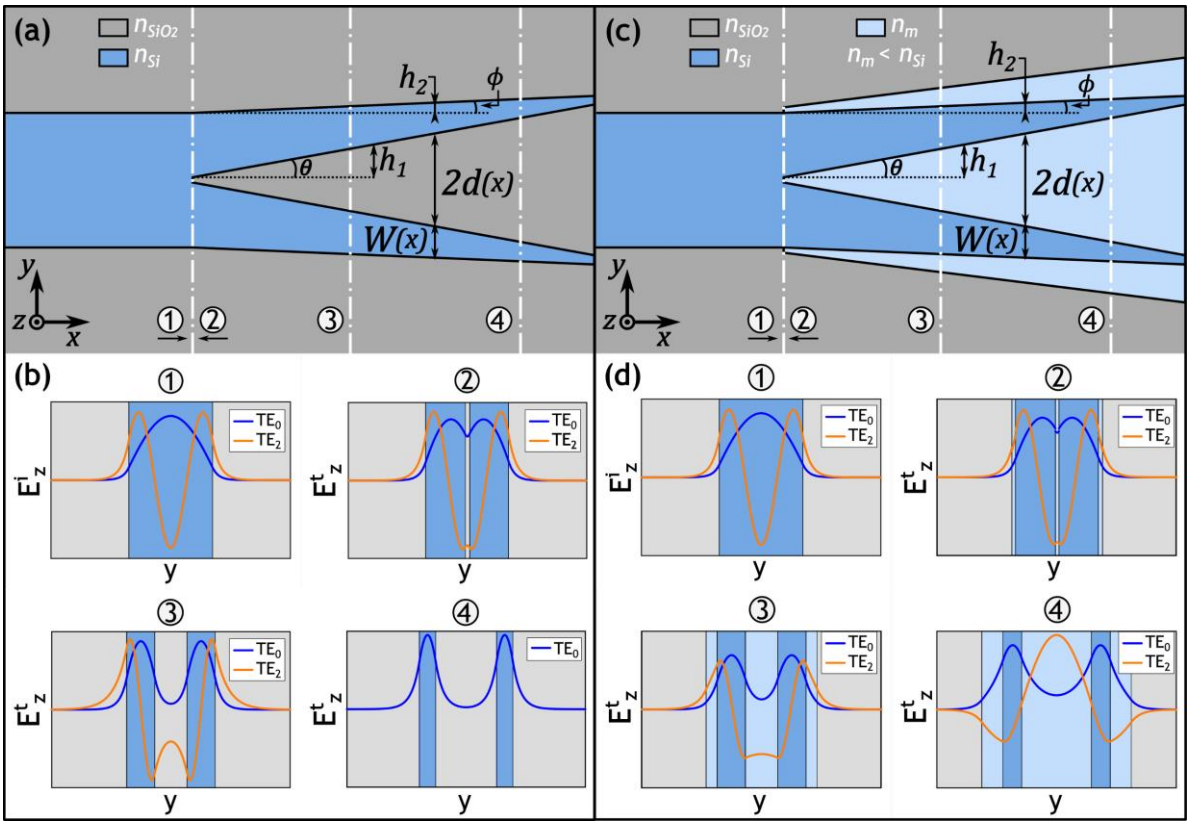

Figure VI.3. (a) Schematic of the symmetric Y-junction used for the mode converter design and (b) $\Re\{E_z\}$ field at specific regions marked as 1, 2, 3 and 4. (c) Schematic the symmetric Y-junction with the SWG structure modeled as an equivalent metamaterial of refractive index n_m and (d) its corresponding $\Re\{E_z\}$ at regions 1, 2, 3 and 4.

Symmetric Y-junctions can only provide mode conversions to even-to-even or odd-to-odd modes because of their mirrored structure relative to the direction of propagation (x-axis). The overlap integral of incident and transmitted fields, calculated at the interface between stem and arms waveguides, quantifies the extent of power exchange between the different optical modes.

The efficacy of power transmission from an input mode of order m to an output mode of order m' hinges on both the branching angle formed by the arms and the discrepancy in propagation constants between the three-layer ($k^i_{x,m}$) and five-layer ($k^t_{x,m'}$) guided wave modes. This can be expressed by the transmitted coupling coefficient [137]:

$$c^t_{m,m'} = \frac{1}{\omega\mu_0}\frac{k^i_{x,m}k^t_{x,m'}}{k^i_{x,m}+k^t_{x,m'}}\int_{-\infty}^{\infty} E^i_{z,m}(E^t_{z,m'})^* dy \qquad (6.2)$$

It is important to note that the propagation constants of the transmitted modes ($k^t_{x,m'}$) are determined by the eigenvalue equations governing the five-layer waveguide structure, which vary as the separation between the arm waveguides increases. Within this structure, the light experiences a phase difference arising from the respective phase associated to the modes propagating through the

arms ($\Phi_{\mathrm{arms}} = n_{eff,strip}k_m$) and the middle SWG metamaterial ($\Phi_{\mathrm{SWG}} = n_{eff,SWG}k_m$) region: $\Delta\Phi = k_m(n_{eff,strip} - n_{eff,SWG})$. This phase difference is responsible for the mode exchange between the TE_0 and TE_2 modes.

The integration of SWG structures in the region of the junction adds another level of complexity to the design process of the proposed device. Additionally, certain geometric parameters of the device vary along the propagation direction to improve mode conversion efficiency. For example, the width of the arm waveguides is progressively reduced, and both the width and length of the SWG segments also change accordingly. Thus, optimization of the device geometry constitutes a substantial challenge due to the high number of interrelated parameters that significantly affect the behavior of the device. To fully exploit the potential of the mode converter topology, an inverse design optimization approach is adopted. This method enables the exploration of all available degrees of freedom in the design space to maximize the mode conversion efficiency. The inverse design process relies on a gradient-based optimization algorithm, iteratively adjusting the design parameters to achieve optimal performance. By systematically refining these parameters, the algorithm aims to enhance the efficiency of mode conversion throughout the device.

6.2.2. Optimization process

Optimization through inverse design offers unprecedented opportunities to push the boundaries of device performance and functionality for integrated photonics as further discussed in Chapter III. Devices that incorporate metamaterials [65], [166] are subjected to topological engineering [141] that often involve multiple interdependent design parameters. Therefore, traditional sequential optimizations become impractical and simultaneous multi-parameter optimizations are required. The mode converter presented in this chapter is developed through an inverse design approach using Powell's gradient-free optimization algorithm [210]. The workflow of this optimization process is summarized in Figure VI.4 (a). This algorithm involves an iterative optimization process that systematically explores conjugated directions within a given parameter space to maximize the target FOM. The parameter space involved in this approach contains the critical geometric parameters of both Y-junctions and subwavelength gratings. The algorithm is initialized with a parameter set and sequentially performs conjugate directional and line searches, thus allowing adaptive updates of the parameter values. This method efficiently navigates multidimensional spaces without requiring gradient information, making it suitable for complex optimization challenges. Additionally, the algorithm considers parameter bounds, restricting geometric values to align with practical design constraints, such as fabrication MFS. Specifically, here the figure of merit represents the modal field transmission from the incident TE_0 mode into the targeted output TE_2 mode ($T_{0,2}$) across the operational wavelength range, obtained through 3D-FDTD simulations. In an ideal scenario, the FOM value should be equal to one, indicating lossless modal conversion between the specified input and output modes.

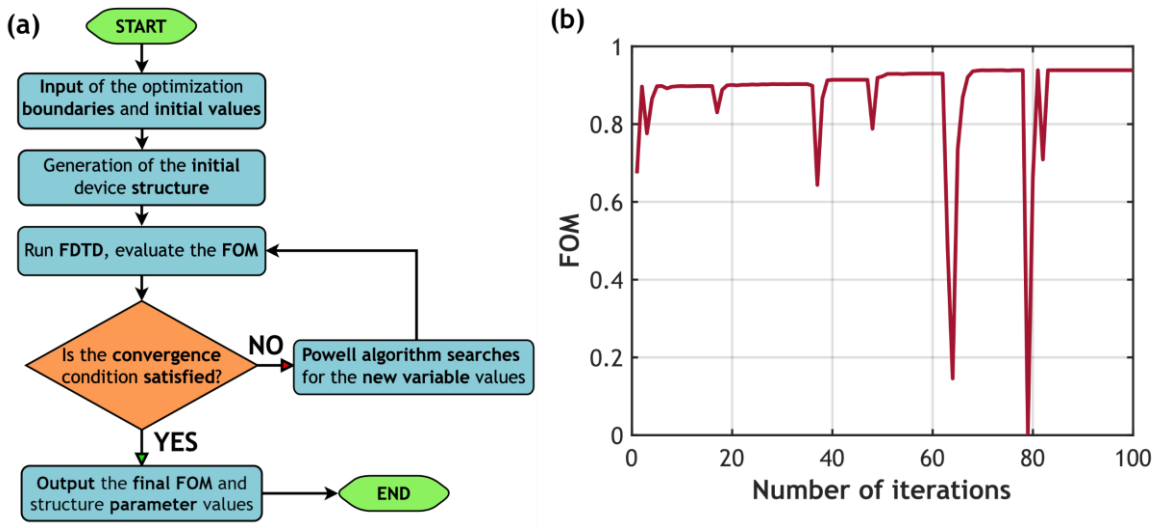

Figure VI.4. (a) Flow chart of the inverse design method using Powell's gradient-free optimization algorithm. (b) Evolution of the figure of merit for each iteration of the optimization process.

The proposed mode converter is developed for an SOI platform with a 220-nm-thick silicon core layer. The MFS of the design is fixed at 60 nm, aligning with the claimed resolution offered by commercial foundries. Certain geometric parameters held constant during the optimization process. For the multimode input and output waveguides, W_S is set at 1.4 μm, ensuring TE_2 mode support meanwhile suppressing higher-order modes for wavelengths between 1350 nm and 1700 nm. For the SWG segments, W_0 is fixed at 1.52 μm, to ensure the MFS restriction, and Λ = 200 nm is selected to avoid radiation and Bragg regimes. On the other hand, the geometric parameters subject to optimization include the duty cycles characterizing the narrower ($DC_0 = a_0/\Lambda$) and wider ($DC_F = a_F/\Lambda$) segments of the SWG, as well as W_F, S, and L_T. Table 3 presents the parameter values used for algorithm initialization, including the paired boundary values that define the minimum and maximum permissible ranges for each parameter. The table further shows the refined parameter values achieved through the Powell algorithm after 100 iterations, highlighting a compact length of only 6.5 μm. Figure VI.4 (b) illustrates the evolution of the figure of merit for each iteration during the entire optimization process.

For this specific device, the excess loss is defined as $EL = 10\log_{10}(T_{0,2})$. Additionally, the extinction ratio is an important metric for evaluating the efficiency of the mode conversion process, describing how effectively the desired mode is produced and undesired output modes are suppressed. The ER is formally defined as the ratio of the power of the converted mode to the power of the original mode, expressed as: $ER = 10\log_{10}(T_{0,0})$. Here $T_{0,0}$ represent the power transmitted from an incident TE_0 mode into the TE_0 mode ($T_{0,0}$) at the output. Figure VI.6 presents the excess loss and extinction ratio for the final mode converter topology, incorporating the optimized geometric design parameters. The proposed device demonstrates simulated EL under 0.75 dB and ER over 10 dB in a 350 nm broad

bandwidth from 1350 nm to 1700 nm. Moreover, in a 150 nm bandwidth covering the 1472 — 1622 nm wavelength range, ER is higher than 20 dB and EL remains below 0.3 dB.

Table 3: Optimization process parameter values.

Parameter	Initial value	Bound min	Bound max	Final value
DC_0	0.60	0.35	0.70	0.47
DC_F	0.60	0.35	0.70	0.65
W_F	2.6 µm	2.0 µm	3.6 µm	2.6 µm
S	1.6 µm	1.0 µm	2.0 µm	1.8 µm
L_T	3.2 µm	1.0 µm	4.0 µm	3.236 µm

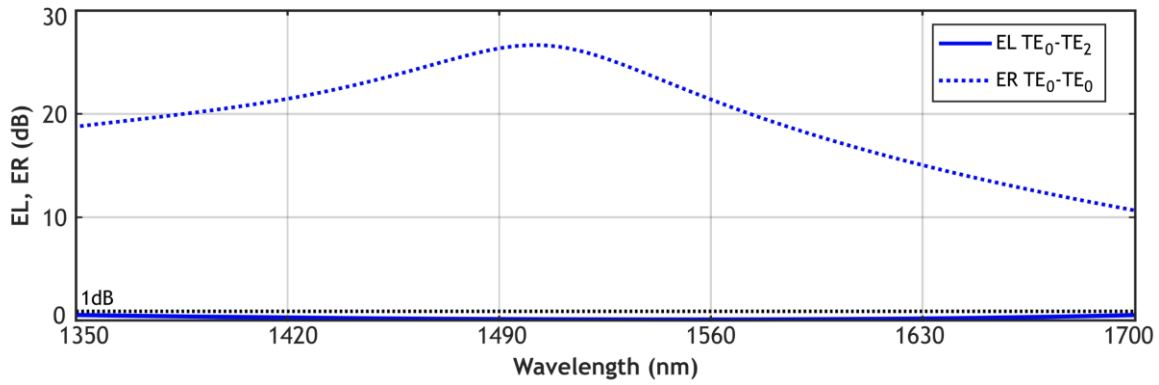

Figure VI.5. Excess loss and extinction ratio of the final optimized design for TE_0 mode input.

6.3. Fabrication and experimental characterization

The fabrication of the proposed ultra-broadband polarization-independent beam splitter was carried out at the facilities of the C2N [211] using SOI wafers with a silicon thickness of 220 nm and a BOX layer of 2 µm. The layout patterns were defined using electron-beam lithography (RAITH EBPG 5200) and then transferred to the silicon layer using reactive ion etching (ICP-DRIE SPTS). SEM images of the fabricated device were collected before the top cladding was deposited (Figure VI.8(a)). A 1.5-µm-thick cladding layer of polymethyl methacrylate (PMMA) was applied to the sample using spin-coating. A more in-depth description of the fabrication method can be found in Annex 1.

The experimental setup used to characterize the mode converter is described in Figure VI.6. Experimental measurements were conducted at the C2N laboratories using two tunable lasers to achieve a combined wavelength range of up to 200 nm, spanning from 1420 nm to 1620 nm. The lasers were connected to an optical component tester (Yenista CT400) through a standard optical fiber to enable automated measurements over the entire wavelength range. A three-paddle polarization controller was used to manage the polarization state of the light at the output of the CT400. The single-mode optical fiber from the polarization controller was mounted on a goniometer, placed on a micropositioning stage, to ensure precise injection of the light into the chip at the appropriate radiation angle of the grating. Optimized grating couplers for TE polarization, whose principle of operation is explained in Chapter II (section 2.2.3), enabled the coupling of light into and out of the chip. Another cleaved single-mode optical fiber, attached to a second goniometer, collected the light

from the chip at the appropriate grating radiation angle, directing it to the photodetector of the CT400. To achieve optimal alignment and efficient coupling across the entire measured spectrum during the wavelength scans, the tilt angle between the input and output cleaved single-mode fibers and the chip's grating coupler interfaces were carefully adjusted. The collected data from the CT400 was sent to a computer for post-processing, analysis, and interpretation.

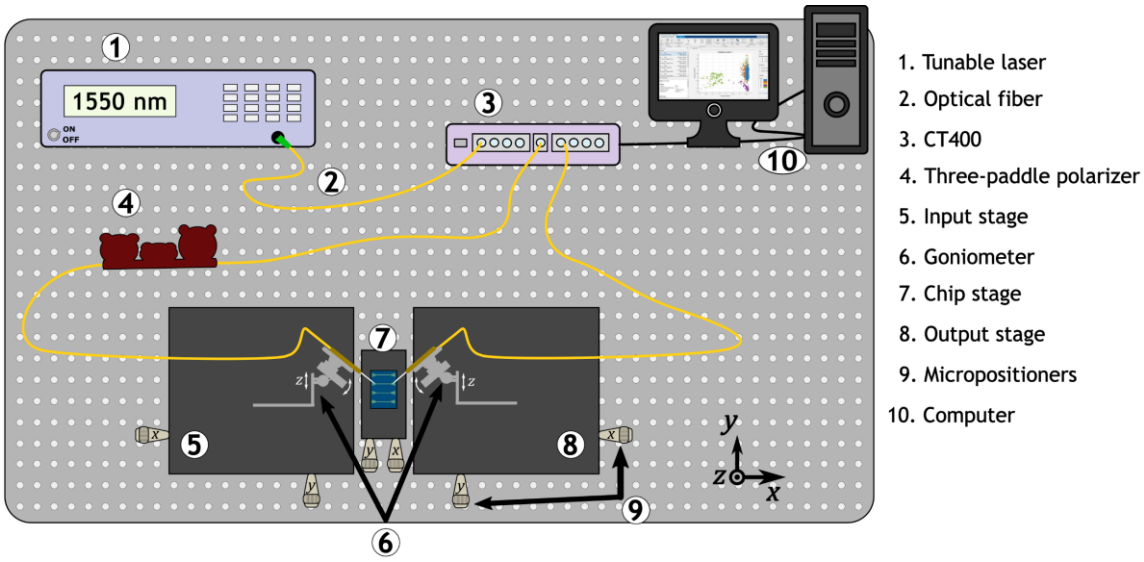

Figure VI.6. Schematic of the measurement setup used to characterize the fabricated mode conversion device.

The SEM image in Figure VI.7 (a) illustrates the on-chip characterization structure used to extract the excess loss and extinction ratios of the proposed device. Additionally, Figure IV.7 (b) offers a detailed SEM view of the fabricated mode converter. The structure consisted of two high-performance mode (de)multiplexers [39], one dedicated to light injection into the mode converter and the other for subsequent mode demultiplexing. This configuration featured three input and three output single-mode waveguides, enabling precise control over the excitation of the first three TE modes: TE_0, TE_1, and TE_2. By selectively injecting light into the first, second, or third input waveguide of the mode multiplexer, the TE_0, TE_1, or TE_2 mode was respectively excited at the input waveguide of the mode converter. Subsequently, after the light passes through the mode converter, the output demultiplexer reciprocally extracted each mode as the fundamental mode of its corresponding output waveguide. Specifically, the TE_0, TE_1, or TE_2 mode proceeding from the mode converter was effectively coupled to the fundamental mode of the first, second, or third output waveguide, respectively. A comprehensive description of the operating principles and performance characteristics of the mode multiplexer/demultiplexer architecture is meticulously detailed in [39]. In addition, the chip also included reference waveguides in order to normalize the power transmission of the mode converter. The configuration of these reference structures mirrored that of the mode multiplexer-mode converter-mode demultiplexer shown in Figure VI.7 (a) but replacing the mode converter with a multimode waveguide of the same length ($2L_T + \Lambda - a_F$) and width (W_S). The measured power of the reference structure when injecting light at the input waveguide p = 1, 2, 3,

at the output q = 1, 2, 3, is P_{pq}^{ref}. Similarly, the measured power for the structures comprising the mode converter is P_{pq}^{mc}. It is noteworthy that when light is injected into the first waveguide (p = 1), the maximum power will be observed at the first output waveguide (q = 1) for the reference structure, whereas for the structures with the mode converter, the maximum power will be detected at the third output waveguide (q = 3). Reciprocally, when light is injected into the third waveguide (p = 3), demonstrates maximum power transmission into the third output waveguide (q = 3) for the reference structure, whereas the maximum power transmission will be detected at the first output waveguide (q = 1) for the structures with the mode converter. Since the mode converter does not impact the TE_1 mode, the behavior of both the reference structures and those incorporating the mode conversion device is consistent. As such, the excess loss and can be determined as follows:

$$EL_{TE0-TE2} = 10\log_{10}\left(\frac{P_{13}^{mc}}{\sqrt{P_{11}^{ref}P_{33}^{ref}}}\right) \tag{6.3}$$

$$EL_{TE2-TE0} = 10\log_{10}\left(\frac{P_{31}^{mc}}{\sqrt{P_{11}^{ref}P_{33}^{ref}}}\right) \tag{6.4}$$

$$EL_{TE1} = 10\log_{10}\left(\frac{P_{22}^{mc}}{P_{22}^{ref}}\right) \tag{6.5}$$

The extinction ratios for undesired output modes are determined using the following expressions:

$$ER_{TE0-TE0} = 10\log_{10}\left(\frac{P_{11}^{mc}}{P_{13}^{mc}}\right) \tag{6.6}$$

$$ER_{TE0-TE1} = 10\log_{10}\left(\frac{P_{12}^{mc}}{P_{13}^{mc}}\right) \tag{6.7}$$

$$ER_{TE2-TE2} = 10\log_{10}\left(\frac{P_{33}^{mc}}{P_{31}^{mc}}\right) \tag{6.8}$$

$$ER_{TE2-TE1} = 10\log_{10}\left(\frac{P_{32}^{mc}}{P_{31}^{mc}}\right) \tag{6.9}$$

$$ER_{TE1-TE0} = 10\log_{10}\left(\frac{P_{21}^{mc}}{P_{22}^{mc}}\right) \tag{6.10}$$

$$ER_{TE1-TE2} = 10\log_{10}\left(\frac{P_{23}^{mc}}{P_{22}^{mc}}\right) \tag{6.11}$$

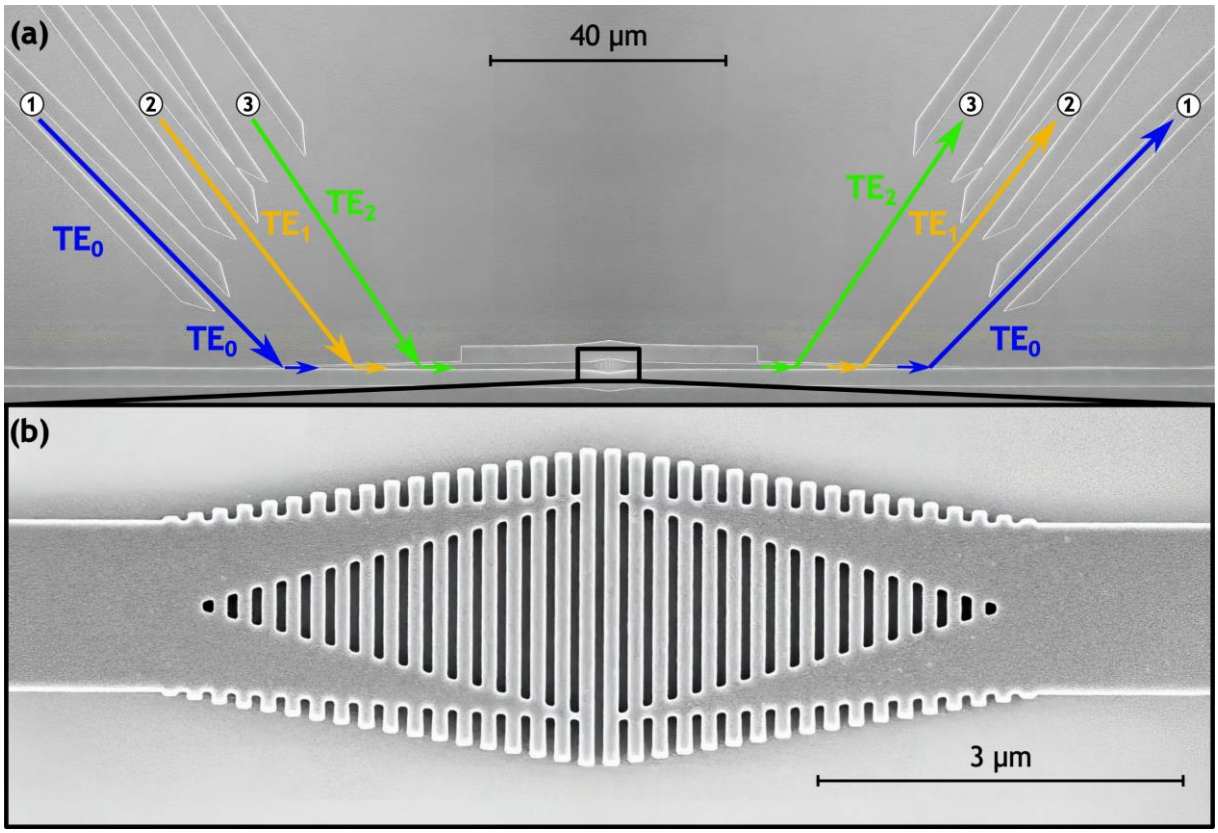

Figure VI.7. SEM images of (a) the MDM architecture used for the device characterization and (b) a magnified view of the fabricated mode converter.

Figure VI.8 (a) presents the ELs and ERs measured for the fabricated device when injecting the TE_0 or TE_2 mode. The performance of the device for the TE_1 mode transmission is also shown in Figure VI.8 (b). For the conversion from the input TE_0 mode into the output TE_2 mode, the device demonstrates experimental EL under 0.35 dB across the measured bandwidth ranging from 1420 nm to 1620 nm. The reciprocal process of TE_2-TE_0 modal conversion exhibits measured EL below 0.52 dB in the same 200 nm broad bandwidth. In both instances of mode conversion, specifically TE_0-TE_2 and TE_2-TE_0, the device exhibits EL as low as 0.4 dB and ER exceed 18 dB across a broadband of 149 nm extending from 1471 nm to 1620 nm. Additionally, ER remains above 10 dB over the whole 200 nm measured bandwidth. As shown in Figure VI.8 (b), the proposed converter architecture does not affect the propagation of the TE_1 mode. When the TE_1 mode is injected into the mode converter, it efficiently propagates through the device with EL under 0.6 dB and ER above 17 dB within the measured wavelength range of 1420 – 1620 nm. These experimental results demonstrate the effectiveness of the device achieving high extinction ratios and ensuring efficient conversion with minimal losses.

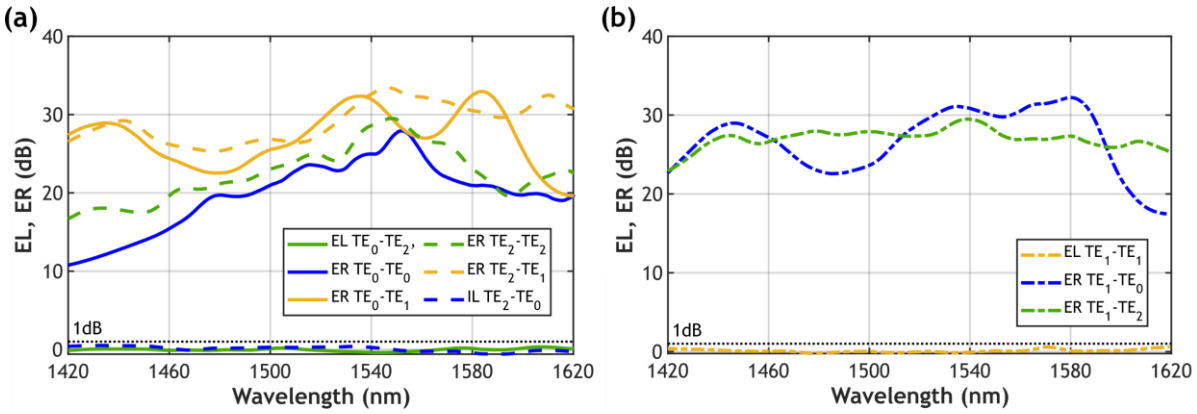

Figure VI.8. Measured EL and ER for TE_0 mode (blue), TE_1 mode (yellow), and TE_2 mode (green) when injecting (a) TE_0 (solid lines) and TE_2 (dashed lines), and (b) TE_1 mode (dash-dot lines).

6.4. Conclusions

In this chapter, a metamaterial-engineered mode converter for TE polarization that operates over a broad bandwidth has been proposed and experimentally demonstrated. The device design presented here achieves efficient mode conversion, leveraging the inherent modal properties of symmetric Y-junctions combined with SWG metamaterials. Powell's gradient-free optimization algorithm is used to maximize the figure of merit, representing the modal field transmission from TE_0 mode to TE_2 mode, by iteratively adjusting all relevant design geometric parameters. In 3D FDTD simulations, the final optimized design demonstrates EL below 0.75 dB and an ER exceeding 10 dB over a broad bandwidth covering from 1350 nm to 1700 nm. Within a 150 nm wavelength range (1472 — 1622 nm), the ER exceeds 20 dB while the EL remains below 0.3 dB. Experimental validation confirms the high performance of the design, showcasing effective mode conversion between fundamental and second order TE modes, with low EL and high ER. Specifically, for TE_0-TE_2 mode conversion, the EL is below 0.35 dB, and for the reciprocal process (TE_2-TE_0), it is under 0.52 dB across the entire measured bandwidth from 1420 nm to 1620 nm. In both instances of mode conversion, specifically TE_0-TE_2 and TE_2-TE_0, the device exhibits EL as low as 0.4 dB and ER exceed 18 dB across a broadband of 149 nm extending from 1471 nm to 1620 nm.

Table 4 provides a summary of the performance of the demonstrated device alongside several state-of-the-art TE_0-TE_2 mode converters, in order to perform a comparative analysis. Among all the reviewed state-of-the-art devices, the largest bandwidth experimentally reported is achieved using SWG and asymmetric tapers in [207], demonstrating EL under 1.8 dB and ER greater than 9 dB in a bandwidth of 81 nm. The mode converter proposed in [212] exhibits the lowest measured losses, showing EL of less than 0.3 dB and ER greater than 9 dB in a 50 nm bandwidth. The device reported in [213] exhibits the broadest simulated bandwidth, with EL less than 2 dB and ER greater than 12 dB over a wavelength range covering 300 nm, but only proving experimental bandwidth of 45 nm. In comparison to these alternative solutions, the mode converter proposed and experimentally demonstrated in this chapter represents a significant improvement over current state-of-the-art devices, offering enhanced functionality in several aspects. It notably outperforms existing devices in

Table 4: Comparison of state-of-the-art TE_0-TE_2 mode converters.

		Simulation			Experiment		
Structure	**Length [μm]**	**EL [dB]**	**ER [dB]**	**BW [nm]**	**EL [dB]**	**ER [dB]**	**BW [nm]**
Asymmetric tapers [206]	19.317	<0.08*	NR	60 (1520-1580)	NF		
Shallow-etched SWG [165]	6.736	<1*	>12.5*	20 (1545-1565)	<0.5	>10	20 (1545-1565)
SWG and asymmetric tapers [207]	4.9	<0.8	>15	100 (1510-1610)	<1.8	>10	81 (1480-1561)
Slot waveguides [212]	2.4	<0.22	>18	50 (1520-1570)	<0.3	>9	50 (1520-1570)
Substrip dielectric waveguides [213]	2.2	<2*	>12*	300 (1400-1700)	<3*	>12*	45 (1535-1580)
Polygonal slot waveguides [214]	24	<0.1*	>20	100 (1500-1600)	NF		
SWG-assisted tapers [215]	4.98	<0.19	>17.36	100 (1500-1600)	NF		
Waveguide-width-modulation [216]	6.5	<0.283	NR	100 (1500-1600)	NF		
Two-etch bragg grating [217]	65.3	<3	>21	24.5 (1540.5-1565)*	NR		
SWG symmetric Y-junctions (this work)	6.542	<0.75	>16	315 (1350-1665)	<0.4	>18	149 (1471-1620)

Values marked with an asterisk correspond to estimations from figures. NR, not reported; NF, not fabricated; IL, insertion loss; ER, extinction ratio; BW, bandwidth.

terms of optical bandwidth, showing almost a two-fold increase over the most broadband experimental demonstrations to date. Furthermore, the device achieves highly efficient mode conversion, with an insertion loss of less than 0.4 dB and an extinction ratio exceeding 18 dB over a wavelength range of 149 nm. Notably, such performance is achieved while maintaining a compact design with an overall length of only 6.5 μm.

The presented SWG mode converter stands as a pioneering solution in the field, distinguished by its notable combination of augmented bandwidth, efficiency, and compact design. These compelling attributes underline the device's considerable potential in ultrahigh-density MDM systems for advanced multimode optical communication and signal processing applications. Furthermore, the device is also expected to find application in emerging fields, such as in quantum information processing or on-chip nonlinear photonics.

Chapter VII:

CONCLUSION

This thesis presents the conceptualization, design and optimization, and comprehensive experimental characterization of a number of innovative and distinctive photonic devices. The concluding chapter provides a concise overview of the advancements made in the field of silicon photonics within the framework of this thesis, emphasizing the impact of these devices and their potential applications. Section 7.1 offers a detailed analysis of the achievements attained for each reported device, providing both a comprehensive discussion and a forward-looking perspective. Section 7.2 examines the potential avenues for further research that can be derived from the ongoing endeavors. Ultimately, section 7.3 summarizes the impact and outcomes resulting from the culmination of this thesis.

7.1. Discussion and outlook

7.2. Applications and future work

7.3. Impact of the present research

7.1. Discussion and outlook

The research conducted in this doctoral thesis is focused on the conceptualization, design, optimization, and experimental characterization of highly-efficient foundational components for next-generation PICs. A number of pioneering structures incorporating SWG metamaterials have been developed to perform power splitting and modal conversion operations. Exploiting SWG structures allows the creation of metamaterials with finely tuned optical properties, making this design approach a powerful tool for the development of silicon photonic devices with high-performance and novel functionalities, all without compromising the simplicity of the fabrication process.

7.1.1. Efficient power splitting based on a full-subwavelength Y-junction

Efficient power splitting is a fundamental operation in silicon photonic integrated circuits to perform on-chip light distribution or facilitating the implementation of complex structures. Although a myriad of approaches has been proposed for power splitting, state-of-the-art devices are hampered by limited operational bandwidth, sensitivity to fabrication errors or large footprints. The proposed novel architecture is based on a Y-junction comprising full SWG metamaterial waveguides. This innovative design effectively demonstrates broadband performance and robust resilience against fabrication variations with minimal losses, especially for single-mode operation. The development of the full-SWG Y-junction device is the outcome of a collaboration with the NRC.

The power splitter has been meticulously engineered for fabrication using diverse methods, each providing different resolutions. One scenario considers high-resolution processes capable of attaining patterns with a minimum size of 50 nm, whereas the other scenario considers the utilization of processes offering resolutions of 100 nm. For the high-resolution scenario (MFS = 50 nm), simulated excess losses for the fundamental mode are below 0.1 dB in an ultra-broad bandwidth of 300 nm (1400 — 1700 nm), and under 0.3 dB for the first-order mode in the 1300 — 1600 nm wavelength range. Considering a 100 nm MFS, the design exhibits EL for both TE_0 and TE_1 modes below 0.5 dB in a 300 nm bandwidth (1300 — 1600 nm). In contrast to a conventional Y-junction splitter, the proposed device achieves a significant reduction of the TE_0 loss at the central design wavelength (1550 nm), decreasing from 0.99 dB to only 0.12 dB. This improvement is accomplished with a negligible impact on the TE_1 loss. Moreover, the device demonstrates robust fabrication tolerances to etching errors up to ±20 nm, particularly for the TE_0 mode. The theoretical design, optimization, and simulated performance of the full-SWG Y-junction were published in [187].

An extensive experimental characterization of the device corroborates the simulated performance, demonstrating a measured excess loss for the fundamental TE mode lower than 0.3 dB for MFS = 50 nm and below 0.5 dB for MFS = 100 nm, in a 260 nm bandwidth (1420 — 1680 nm). Characterization of the first-order TE mode was performed in combination with a mode multiplexer, showing excess loss lower than 1 dB over a 100 nm bandwidth (1475 — 1575 nm) for the 50 nm MFS. SWG Y-junctions with deterministically induced errors of −10 nm and +10 nm were also measured to analyze resilience to over- and under-etching errors, showing robust fabrication tolerances only for the fundamental TE mode. The complete experimental characterization of the proposed device was published in [188].

7.1.2. Achromatic subwavelength-assisted power splitter

In this thesis, a metamaterial-assisted silicon 3-dB power splitter for multimode operation over a record broad bandwidth has been proposed and experimentally validated. This device relies on a symmetric Y-junction with conventional waveguides as arms and stem but features a SWG-metamaterial-assisted transition between them. The unique properties of subwavelength grating metamaterials are leveraged to mitigate the abrupt transition at the tip of conventional Y-junctions, while offering flexible control over the confinement of propagating modes. This ensures that the modes propagating through each branching arm waveguide do not experience an abrupt refractive index change. As a result, the device showcases low losses across multiple modes with relaxed fabrication tolerances over an unprecedented ultra-broad bandwidth. Moreover, this innovative design allows for dual-polarization operation.

Rigorous 3D FDTD simulations predict an excess loss lower than 0.2 dB for the TE_0 mode and below 0.07 dB for the TE_1 mode over a wavelength range of 700 nm, which extends from 1300 to 2000 nm. The device also operates for the fundamental TM mode with simulated excess loss under 0.3 dB in the 1300 — 1800 nm wavelength range. Measurements confirm the exceptional power splitting efficiency of the proposed device, with excess losses remaining under 0.2 dB for both fundamental and first-order TE modes in the 1430 to 1680 nm, limited by the lasers available in the setup. The TM_0 mode measurements also exhibit low excess loss of less than 0.4 dB across a 200 nm bandwidth ranging from 1430 to 1630 nm. Furthermore, another significant advantage of the SWG-assisted Y-junction design is its robustness to fabrication errors. Both simulations and experiments prove that the proposed splitter reliably maintains a high-performance response in the presence of fabrication-related geometric variations. These results stem from collaboration with the NRC and are currently under review in a high-impact scientific journal ranked in the first quartile (Q1) and a preprint has been published in arXiv [218].

7.1.3. Ultra-broadband mode converter

One of the significant contributions of this thesis is the proposal of a design strategy for the realization of high-performance optical mode conversion within a single waveguide. This innovative approach has led to the development of an ultra-compact mode converter design that exhibits efficient mode conversion across a broad bandwidth. During design, the use of SWG metamaterials and inverse design algorithms were strategically combined to exploit the inherent modal properties of symmetric Y-junctions. Specifically, an inverse design optimization technique leveraging a direct search algorithm is employed to maximize a figure of merit. This figure of merit serves as a representative metric of the modal field transmission from TE_0 mode into TE_2 mode, achieved through iterative adjustments to all relevant design geometric parameters. Simulations show for the optimized device EL below 0.75 dB and an ER exceeding 10 dB over a broad bandwidth covering from 1350 nm to 1700 nm. Within a 150 nm wavelength range (1472 — 1622 nm), the ER exceeds 20 dB while the EL

remains below 0.3 dB. Experimental validation confirms the high performance of the design, showcasing effective mode conversion between fundamental and second order TE modes, with low EL and high ER. Specifically, for TE_0-TE_2 mode conversion, the EL is below 0.35 dB, and for the reciprocal process (TE_2-TE_0), it is under 0.52 dB across the entire measured bandwidth from 1420 nm to 1620 nm. In both instances of mode conversion, specifically TE_0-TE_2 and TE_2-TE_0, the device exhibits EL as low as 0.4 dB and ER exceed 18 dB across a broadband of 149 nm extending from 1471 nm to 1620 nm.

The SWG mode converter concept was proposed by the author of this thesis, and the design and optimization process performed during a short research stay of three months in the micro and nano-photonics devices on silicon platform (MINAPHOT) group of the C2N. The fabrication and device measurement were performed by members of the MINAPHOT group who had access to the cleanroom and characterization laboratories. Currently, these findings are undergoing rigorous peer review in a high-impact scientific journal positioned within the Q1 of its respective field.

7.2. Applications and future work

The devices conceived in this thesis exhibit an outstanding performance, being suitable for demanding applications such as including neuromorphic photonics [44], 5G-6G communications [45], quantum photonics [46], LIDAR [26], spectrometry [48], and sensing [49].

Given the significant potential of these advanced photonic building blocks, there is a clear intention to continue the development of high-performance integrated devices, while also exploring more intricate systems in the near future. Outlined herein are the ongoing research initiatives and several potential directions for future investigations.

7.2.1. High-performance power splitting applications

The two power splitting architectures devised in this thesis, namely the full-SWG and the SWG-assisted Y-junctions, hold promise for integration within complex systems. For instance, they hold significant potential in mode-division multiplexing systems, where they can effectively manage the first two transverse electric modes. Moreover, their suitability for fundamental mode operation, distinguished by notable improvements compared to existing devices, positions them as ideal candidates for integration into spatial heterodyne Fourier transform spectrometers, where precision and performance are crucial.

7.2.2. Mode conversion with adaptable splitting ratio

The structure developed for mode conversion not only facilitates a complete power exchange from the fundamental into the second-order transverse-electric mode, but also offers additional functionalities through careful engineering of the mode converter architecture. Specifically, it can yield a device wherein excitation with TE_0 mode results in the simultaneous output of both TE_0 and TE_2 modes, with the power ratio between them adjustable through design parameters. This versatility holds particular significance in the realm of quantum computing, especially in systems relying on

transverse-mode encoding. In quantum computing, the ability to manipulate and control different modes of light is crucial for tasks such as quantum state preparation. Further research in this area promises to deepen the potential applications and benefits of this innovative device such as quantum information processing.

7.2.3. Bimodal sensors

Integrated interferometers, including various structures such as those employing Mach-Zehnder interferometers, ring resonators, and directional couplers, are pivotal in the advancement of photonic devices tailored for on-chip applications. These applications span from optical communication networks to integrated sensors, where compactness and performance are paramount. The operational principles and design methodologies established for the development of the mode converter proposed in this thesis provide a potential avenue for the realization of bimodal sensors. The exploitation of the interference phenomena between the fundamental and second-order transverse electric modes within the waveguide enables the engineering of a bimodal sensor. The investigation and advancement of bimodal sensors represent a pivotal research area within the domain of integrated photonics, offering promising prospects for innovation and technological advancement of lab-on-chip systems.

7.2.4. Synergistic combination of SWG metamaterials with inverse design

The integration of SWG metamaterials with a variety of inverse design methodologies, particularly in conjunction with machine learning algorithms, presents a promising pathway for conducting multiparameter optimizations. This approach allows for the comprehensive exploration of all available degrees of freedom pertaining to the geometrical parameters of the subwavelength nanostructures. By harnessing the capabilities of machine learning algorithms, which excel at identifying intricate patterns within vast datasets, researchers can efficiently navigate the complex design space inherent in SWG metamaterials. Through iterative optimization processes, these methods can uncover optimal configurations that maximize desired performance metrics, such as enhanced light-matter interactions, tailored dispersion properties, and optimized modal characteristics. This synergy between SWG metamaterials and advanced inverse design techniques holds immense potential for unlocking novel functionalities and pushing the boundaries of integrated photonics towards unprecedented levels of performance and versatility.

7.3. Impact of the present research

The course of this thesis has led to notable advancements in the domains of power splitting and mode conversion, providing essential building blocks for the next generation of photonic integrated circuits. These breakthroughs enable the development of applications requiring higher capacities and

energy-efficient consumption, including optical communications and interconnects, nonlinear photonics, programmable photonics, and quantum computing.

The advancements made in this doctoral thesis have generated significant scientific interest, leading to the publication of 8 articles in high-impact journals (refer to Appendix B), with a total of 41 citations. Of these publications, 4 articles have been authored as the primary investigator, with 2 currently under review in Q1 journals. Additionally, the remaining 4 publications have been co-authored as a result of different collaborations. These findings have been disseminated through 16 presentations at international conferences, including 5 invited talks. The international scope of this work was further enhanced through research secondments at the Centre de Nanosciences et de Nanotechnologies, Strathclyde University, and the University of Málaga, as well as collaborations with the National Research Council of Canada and Alcyon Photonics S.L.

The research outcomes of this thesis have also attracted significant technological interest, as notably demonstrated by the Spanish patent application (P202330198) for the integrated SWG-assisted power splitter. In addition, an international extension under the Patent Cooperation Treaty (PCT) has been initiated (PCT/ES2024/070152). Furthermore, the patent application process is underway for the integrated mode converter structure. These patent applications underscore the strong potential for industrial applicability of the developed devices, highlighting their relevance in advancing technological innovation.

Appendix A:

SILICON-ON-INSULATOR FABRICATION PROCESSES

The fabrication of SOI PICs is done by lithography, a technique widely used in microelectronics and other industries for creating patterns on a substrate [219]. The general steps involved in lithographic processes, depicted in Figure A.1, are the following:

1. Substrate preparation: The process begins with the preparation of the SOI wafer, as shown in Figure A.1(a). The sample undergoes a cleaning hydro-fluoric solution before being placed in the spin-coater machine.
2. Photoresist deposition: Photoresist, a light-sensitive material with positive or negative characteristics, is spin-coated onto the substrate. For a positive photoresist, exposure to light weakens the resist, creating areas that will dissolve. In contrast, for a negative photoresist, exposure to light toughens the resist, forming areas that will remain intact. In this context, a negative photoresist is considered for Figures A.1(c)-(h). The photoresist is spin-coated onto the sample, as illustrated in Figure A.1(b), and then baked on a hot plate to evaporate solvents and enhance adhesion.
3. Patterning: This step involves transferring a mask, containing the desired waveguides and devices pattern, onto the photoresist-coated sample. The mask, acting as a translucent sheet with opaque and transparent regions, defines the pattern. Here, the resolution of the WGs is determined based on the resolution of the method employed to inscribe the mask onto the photoresist, which is essentially the MFS that can be reliably patterned. The two main methods are: e-beam lithography and photolithography. In the first one, the sample is exposed to an electron beam that sequentially writes structures in the resist pixel by pixel (Figure A.1 (c)), achieving extremely small features with an MFS typically around 50 nm [220]. The second method, photolithography, involves exposing the resist through a mask to define devices

(Figure A.1(d)) [221]. Photolithography processes are categorized based on the light utilized, such as ultraviolet lithography, DUV lithography, extreme ultraviolet lithography, and X-ray lithography. Hence, the wavelength of the light employed is critical for determining the achievable MFS, with recent improvements in photolithography techniques enabling resolutions in the order of 100-200 nm [43].

4. Development: After exposure, the photoresist is immersed in a developer solution, dissolving parts of the resist on the sample. For positive photoresist, the exposed areas dissolve, while for negative photoresist, the unexposed areas dissolve (Figure A.1(e)).
5. Etching: The sample is subjected to an etching process, typically a dry etching process employing high-energy ions. This process removes material from areas not protected by the developed photoresist, transferring the pattern to the sample (Figure A.1(f)).
6. Resist cleaning: The remaining photoresist is removed from the substrate, leaving behind the patterned features (Figure A.1(g)). The sample is submerged into butanone (metiletilcetona) and then a mixture of sulfuric acid and hydrogen peroxide, known as piranha, is utilized to eliminate remaining organic residues. Subsequently, oxygen plasma is employed to clean off any residues or contaminants from prior processes.
7. Cladding deposition: In many cases, a cladding layer is deposited to protect the guiding silicon layer (Figure A.1(h)). For a SiO_2 layer, the deposition is achieved using plasma-enhanced chemical vapor deposition (PECVD).

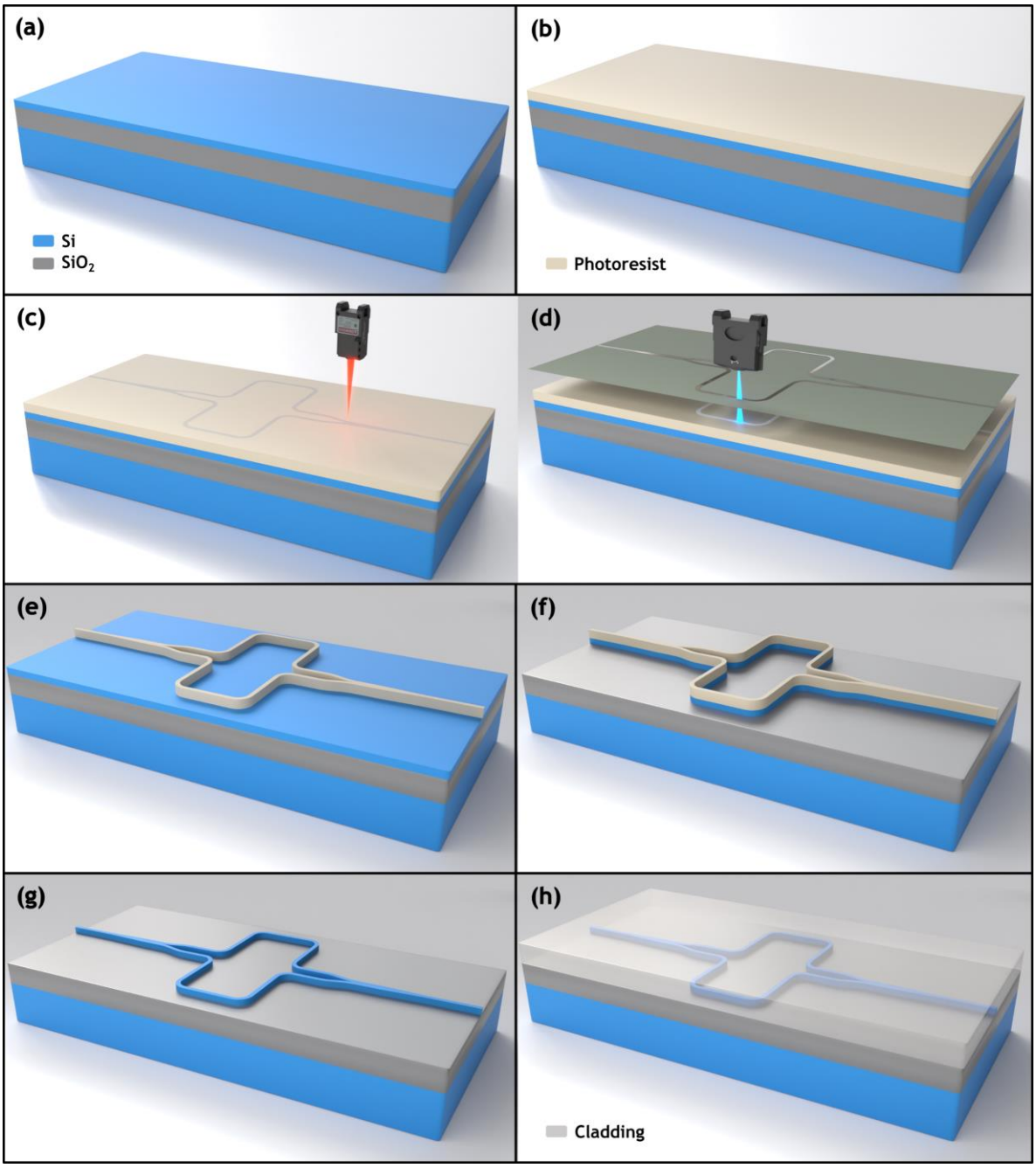

Figure A.1. Schematic representation of the lithographic process for device fabrication on a SOI wafer (a) Sample preparation for photoresist deposition. (b) Sample after photoresist spin-coating. (c) E-beam lithography. (d) Photolithography. (e) Sample after light exposure and development considering a negative photoresist. (f) Sample after etching the material from areas not protected by the photoresist. (g) The photoresist is removed from the substrate. (h) Deposition of a cladding layer.

Appendix B:

SCIENTIFIC-TECHNOLOGICAL OUTPUT

International journal papers

1. **R. Fernandez de Cabo**, D. González-Andrade, P. Cheben, & A. V. Velasco. "High-performance on-chip silicon beamsplitter based on subwavelength metamaterials for enhanced fabrication tolerance." *Nanomaterials*, vol. 11, no. 5, p. 1304, May 2021, doi: 10.3390/nano11051304.
   JIF: 5.7
   Rank (JCR): Q1, 44/178 in PHYSICS, APPLIED (2021).
   Cites: 19 (Google scholar)
2. D. González-Andrade, **R. Fernández de Cabo**, J. Vilas, I. Olivares, A. Días, J. M. Luque-González, J. G. Wangüemert-Pérez, A. Ortega-Moñux, I. Molina-Fernández, R. Halir, P. Cheben, & A. V. Velasco. "Mode converter and multiplexer with a subwavelength phase shifter for extended broadband operation." *IEEE Photonics Technology Letters,* vol. 33, no. 22, p. 1262-1265, Sep 2021, doi: 10.1109/LPT.2021.3116439.
   JIF: 2.4
   Rank (JCR): Q2, 147/344 in ENGINEERING, ELECTRICAL & ELECTRONIC (2021).
   Cites: 9 (Google scholar)
3. **R. Fernández de Cabo**, J. Vilas, P. Cheben, A. V. Velasco, & D. González-Andrade, "Experimental characterization of an ultra-broadband dual-mode symmetric Y–junction based on metamaterial waveguides," *Optics & Laser Technology*, vol. 157, p. 108742, Jan. 2023, doi: 10.1016/j.optlastec.2022.108742.
   JIF: 5.0
   Rank (JCR): Q1, 25/178 in PHYSICS, APPLIED (2022).
   Cites: 8 (Google scholar)

4. D. González-Andrade, I. Olivares, **R. Fernández de Cabo**, J. Vilas, A. Dias, & A. V. Velasco. "Broadband three-mode converter and multiplexer based on cascaded symmetric Y-junctions and subwavelength engineered MMI and phase shifters." *Optics & Laser Technology*, vol. 164, p. 109513, Sep 2023, doi: 10.1016/j.optlastec.2023.109513.
   JIF: 5.0
   Rank (JCR): Q1, 25/178 in PHYSICS, APPLIED (2022).
   Cites: 3 (Google scholar)
5. J. Vilas, **R. Fernández de Cabo**, I. Olivares, D. González-Andrade, A. V. Velasco, & A. Dias. "Low-loss directional coupler for the C, L and U bands based on subwavelength gratings." *IEEE Photonics Technology Letters*, vol. 35, p. 1331-1334, Dec 2023, doi: 10.1109/LPT.2023.3325660.
   JIF: 2.6
   Rank (JCR): Q2, 149/352 in ENGINEERING, ELECTRICAL & ELECTRONIC (2022).
   Cites: 1 (Google scholar)
6. **R. Fernández de Cabo**, D. González-Andrade, P. Cheben, & A. V. Velasco. "Extending the spectral operation of silicon power splitters through subwavelength nanotechnology." *arXiv e-prints* (2024): arXiv-2403. (Under review)
7. **R. Fernández de Cabo**, A. Sánchez-Sánchez, Y. Yang, D. Melati, C. Alonso-Ramos, A. V. Velasco & D. González-Andrade. "Broadband mode converter based on gradient-free optimized subwavelength Y-junctions." (Under review).
8. J. Vilas, I. Olivares, M. Gómez-Castaño, I. Ayuso, P. Medeiros, **R. Fernández de Cabo**, A. V. Velasco, & A. Dias "Broadband and low-crosstalk mode multiplexer based on subwavelength-assisted phase-matching." (Under review).

International conferences

1. **R. Fernández de Cabo**, D. González-Andrade, P. Cheben, & A. V. Velalsco. "Y-junction power splitter engineered through subwavelength metamaterials." *2020 IEEE Photonics Conference (IPC)*. IEEE, 2020.
2. **R. Fernández de Cabo**, D. González-Andrade, P. Cheben, & A. V. Velalsco. "Y-junction beamsplitter engineered through subwavelength metamaterials." *Integrated Optics: Design, Devices, Systems and Applications VI*. Vol. 11775. SPIE Optics+Optoelectronics, 2021.
3. **R. Fernández de Cabo**, D. González-Andrade, P. Cheben, & A. V. Velalsco. "Fabrication-tolerant Y-junction for high-performance power division using subwavelength silicon metamaterials." *2021 IEEE 17th International Conference on Group IV Photonics (GFP)*. IEEE, 2021.
4. **R. Fernández de Cabo**, J. Vilas, P. Cheben, A. V. Velasco, & D. González-Andrade. "Ultra-broadband silicon beam-splitter based on subwavelength metamaterials." *2022 Photonics North (PN)*. IEEE, 2022.
5. **R. Fernández de Cabo**, J. Vilas, P. Cheben, A. V. Velasco, & D. González-Andrade. "Experimental characterization of a high-performance Y-junction enhanced with subwavelength

grating metamaterials (Conference Presentation)." *Metamaterials, Metadevices, and Metasystems 2022*. SPIE Optics+Photonics, 2022.

6. A. V. Velasco, **R. Fernández de Cabo**, D. González-Andrade, J. Vilas, I. Olivares, A. Dias, J. M. Luque-González, J. G. Wangüemert-Pérez, A. Ortega-Moñux, I. Molina-Fernández, R. Halir, & P. Cheben. "Subwavelength-structured metamaterials for broadband mode conversion and multiplexing." *2022 Photonics North (PN)*. IEEE, 2022. (Invited)
7. A. V. Velasco, D. González-Andrade, **R. Fernández de Cabo**, J. Vilas, I. Olivares, A. Dias, J. G. Wangüemert-Pérez, J. M. Luque-González, A. Ortega-Moñux, I. Molina-Fernández, R. Halir, & P. Cheben. "Subwavelength metamaterials for broadband mode multiplexing and power splitting in silicon waveguides." *European Conference on Integrated Optics (ECIO)*. 2022.
8. **R. Fernández de Cabo.** "Silicon photonics subwavelength metamaterials for high-performance power division." *Humboldt meets Leibniz: Emerging Topics in Optics and Photonics*. 2022.
9. J. Vilas, **R. Fernández de Cabo**, D. González-Andrade, I. Olivares, A. V. Velasco & A. Días. "High-performance power splitter based on subwavelength gratings with customizable splitting ratio." *Humboldt meets Leibniz: Emerging Topics in Optics and Photonics. 2022*.
10. D. González-Andrade, **R. Fernández de Cabo**, J. Vilas, T. T. D. Dinh, J. M. Luque-González, D. Oser, G. Aubin, F. Amar, D. Pérez-Galacho, I. Olivares, A. Dias, R. Halir, A. Ortega-Moñux, J. G. Wangüemert-Pérez, I. Molina-Fernández, E. Cassan, D. Marris-Morini, P. Cheben, L. Vivien, A. V. Velasco, & C. Alonso-Ramos. "Silicon photonic mode multiplexers based on subwavelength metamaterials and on-chip beamforming." *Smart Photonic and Optoelectronic Integrated Circuits 2023*. Vol. 12425. SPIE Photonics West, 2023. (Invited)
11. J. Vilas, **R. Fernández de Cabo**, I. Olivares, D. González-Andrade, A. Días & A. V. Velasco. "Experimental demonstration of a low-loss broadband directional coupler based on subwavelength gratings metamaterials." *European Conference on Integrated Optics (ECIO)*. 2023.
12. P. Cheben, J. H. Schmid, P. Ginel-Moreno, S. Khajavi, R. Korček, W. Fraser, D. Sirmaci, A. F. Hinestrosa, J. M. Luque-González, D. Pereira-Martín, A. Sánchez-Postigo, A. Hadij-ElHouati, D. Benedikovič, A. Ortega-Moñux, J. G. Wangüemert-Pérez, I. Molina-Fernández, R. Halir, W. N. Ye, D. Melati, C. Alonso-Ramos, D. González-Andrade, L. Vivien, I. Staude, J. Zhang, M. Milanizadeh, D-X. Xu, Y. Grinberg, R. Cheriton, S. Janz, S. Wang, M. Vachon, M. Dado, **R. Fernández de Cabo**, & A. V. Velasco. "Subwavelength-Engineered Metamaterial Devices for Integrated Photonics." *2023 23rd International Conference on Transparent Optical Networks (ICTON)*. IEEE, 2023. (Invited)
13. P. Cheben, J. H. Schmid, W. N. Ye, D. Benedikovič, P. Ginel-Moreno, S. Khajavi, J. M. Luque-González, A. F. Hinestrosa, D. Pereira-Martín, A. Hadij-ElHouati, R. Korček, W. Fraser, A. Sánchez-Postigo, A. Ortega-Moñux, J. G. Wangüemert-Pérez, I. Molina-Fernández, R. Halir, D. Melati, C. Alonso-Ramos, D. González-Andrade, L. Vivien, J. Zhang, M. Milanizadeh, D.-X. Xu,

Y. Grinberg, S. Janz, R. Cheriton, S. Wang, M. Vachon, M. Dado, **R. Fernández de Cabo**, & A. V. Velasco. “High performance silicon photonic devices with subwavelength metamaterials.” *International Conference on Metamaterials, Photonic Crystals and Plasmonics (META)*. 2023. (Invited)

14. A. V. Velasco, D. González-Andrade, **R. Fernández de Cabo**, J. Vilas, I. Olivares, A. Dias, J. M. Luque-González, J. G. Wangüemert-Pérez, A. Ortega-Moñux, I. Molina-Fernández, R. Halir, & P. Cheben. "Advanced metamaterial devices for broadband mode conversion and multiplexing." *Integrated Photonics Research, Silicon and Nanophotonics*. Optica Publishing Group, 2023. (Invited)
15. **R. Fernández de Cabo**, J. Vilas, P. Cheben, A. V. Velasco, & D. González-Andrade. "Subwavelength silicon metamaterials for high-performance and fabrication-tolerant power splitting." *Solar Energy and Light-Emitting Devices*. Optica Publishing Group, 2023.
16. **R. Fernández de Cabo**, A. V. Velasco, P. Cheben, & D. González-Andrade. " Achromatic subwavelength-assisted power splitter for next-generation silicon photonics." *2024 IEEE Si Photonics Conference*. IEEE, 2024.

Patent applications

1. **R. Fernández de Cabo**, A. V. Velasco, & D. González-Andrade. “Dispositivo divisor de potencia integrado en guías de onda.” **P202330198**, 2023.
2. **R. Fernández de Cabo**, A. V. Velasco, & D. González-Andrade. “Dispositivo divisor de potencia integrado en guías de onda.” **PCT/ES2024/070152**, 2024.
3. **R. Fernández de Cabo**, A. V. Velasco, & D. González-Andrade. “Conversor de modos integrado en guías de onda.” **P202430377**, 2024.

Awards

- Madrid City Council awards R. Fernández de Cabo in the 2022 Talent and Technology Awards for the work titled "High-performance Photonic Power Divider based on Subwavelength Metamaterials".

BIBLIOGRAPHY

[1] Tom Mader, "Driving the era of silicon photonics with integrated lasers," Jan. 17, 2023.

[2] G. E. Moore, "Cramming More Components Onto Integrated Circuits," *Proceedings of the IEEE*, vol. 86, no. 1, pp. 82–85, Jan. 1998, doi: 10.1109/JPROC.1998.658762.

[3] V. Agarwal, M. S. Hrishikesh, S. W. Keckler, & D. Burger, "Clock rate versus IPC," in *Proceedings of the 27th annual international symposium on Computer architecture - ISCA '00*, New York, New York, USA: ACM Press, 2000, pp. 248–259. doi: 10.1145/339647.339691.

[4] K. Likharev, "Electronics Below 10 nm," in *Nano and Giga Challenges in Microelectronics*, Elsevier, 2003, pp. 27–68. doi: 10.1016/B978-044451494-3/50002-0.

[5] R. L. Uy, "Beyond multi-core: A survey of architectural innovations on microprocessor," in *2014 International Conference on Humanoid, Nanotechnology, Information Technology, Communication and Control, Environment and Management (HNICEM)*, IEEE, Nov. 2014, pp. 1–6. doi: 10.1109/HNICEM.2014.7016212.

[6] S. E. Miller, "Integrated Optics: An Introduction," *Bell System Technical Journal*, vol. 48, no. 7, pp. 2059–2069, Sep. 1969, doi: 10.1002/j.1538-7305.1969.tb01165.x.

[7] Ansheng Liu *et al.*, "Wavelength Division Multiplexing Based Photonic Integrated Circuits on Silicon-on-Insulator Platform," *IEEE Journal of Selected Topics in Quantum Electronics*, vol. 16, no. 1, pp. 23–32, 2010, doi: 10.1109/JSTQE.2009.2033454.

[8] H. Ren, X. Li, Q. Zhang, & M. Gu, "On-chip noninterference angular momentum multiplexing of broadband light," *Science*, vol. 352, no. 6287, pp. 805–809, May 2016, doi: 10.1126/science.aaf1112.

[9] Z. Zhou, R. Chen, X. Li, & T. Li, "Development trends in silicon photonics for data centers," *Optical Fiber Technology*, vol. 44, pp. 13–23, Aug. 2018, doi: 10.1016/j.yofte.2018.03.009.

[10] C. Lam, Hong Liu, B. Koley, Xiaoxue Zhao, V. Kamalov, & V. Gill, "Fiber optic communication technologies: What's needed for datacenter network operations," *IEEE Communications Magazine*, vol. 48, no. 7, pp. 32–39, Jul. 2010, doi: 10.1109/MCOM.2010.5496876.

[11] Jeff W. Hockert, "Integrated Photonics Set to Light Up the Data Center," *Intel Tech*, May 11, 2021.

[12] L. Chrostowski & M. Hochberg, *Silicon Photonics Design*. Cambridge University Press, 2015. doi: 10.1017/CBO9781316084168.

[13] M. A. Butt, "Integrated Optics: Platforms and Fabrication Methods," *Encyclopedia*, vol. 3, no. 3, pp. 824–838, Jun. 2023, doi: 10.3390/encyclopedia3030059.

[14] D. D'Agostino *et al.*, "Low-loss passive waveguides in a generic InP foundry process via local diffusion of zinc," *Optics Express*, vol. 23, no. 19, p. 25143, Sep. 2015, doi: 10.1364/OE.23.025143.

[15] X.-Y. Han *et al.*, "Recent Progress of Imprinted Polymer Photonic Waveguide Devices and Applications," *Polymers*, vol. 10, no. 6, p. 603, May 2018, doi: 10.3390/polym10060603.

[16] J. Halldorsson, N. B. Arnfinnsdottir, A. B. Jonsdottir, B. Agnarsson, & K. Leosson, "High index contrast polymer waveguide platform for integrated biophotonics," *Optics Express*, vol. 18, no. 15, p. 16217, Jul. 2010, doi: 10.1364/OE.18.016217.

[17] Y. Qi & Y. Li, "Integrated lithium niobate photonics," *Nanophotonics*, vol. 9, no. 6, pp. 1287–1320, Jun. 2020, doi: 10.1515/nanoph-2020-0013.

[18] D. Sun *et al.*, "Microstructure and domain engineering of lithium niobate crystal films for integrated photonic applications," *Light: Science & Applications*, vol. 9, no. 1, p. 197, Dec. 2020, doi: 10.1038/s41377-020-00434-0.

[19] Z. Yan *et al.*, "A monolithic InP/SOI platform for integrated photonics," *Light: Science & Applications*, vol. 10, no. 1, p. 200, Sep. 2021, doi: 10.1038/s41377-021-00636-0.

[20] M. Tang *et al.*, "Integration of III-V lasers on Si for Si photonics," *Progress in Quantum Electronics*, vol. 66, pp. 1–18, Aug. 2019, doi: 10.1016/j.pquantelec.2019.05.002.

[21] V. Passaro, C. Tullio, B. Troia, M. Notte, G. Giannoccaro, & F. Leonardis, "Recent Advances in Integrated Photonic Sensors," *Sensors*, vol. 12, no. 11, pp. 15558–15598, Nov. 2012, doi: 10.3390/s121115558.

[22] N. L. Kazanskiy, S. N. Khonina, & M. A. Butt, "Advancement in Silicon Integrated Photonics Technologies for Sensing Applications in Near-Infrared and Mid-Infrared Region: A Review," *Photonics*, vol. 9, no. 5, p. 331, May 2022, doi: 10.3390/photonics9050331.

[23] G. Yurtsever, B. Považay, A. Alex, B. Zabihian, W. Drexler, & R. Baets, "Photonic integrated Mach-Zehnder interferometer with an on-chip reference arm for optical coherence tomography," *Biomedical Optics Express*, vol. 5, no. 4, p. 1050, Apr. 2014, doi: 10.1364/BOE.5.001050.

[24] J. Wang, F. Sciarrino, A. Laing, & M. G. Thompson, "Integrated photonic quantum technologies," *Nature Photonics*, vol. 14, no. 5, pp. 273–284, May 2020, doi: 10.1038/s41566-019-0532-1.

[25] A. W. Elshaari, W. Pernice, K. Srinivasan, O. Benson, & V. Zwiller, "Hybrid integrated quantum photonic circuits," *Nature Photonics*, vol. 14, no. 5, pp. 285–298, May 2020, doi: 10.1038/s41566-020-0609-x.

[26] X. Zhang, K. Kwon, J. Henriksson, J. Luo, & M. C. Wu, "A large-scale microelectromechanical-systems-based silicon photonics LiDAR," *Nature*, vol. 603, no. 7900, pp. 253–258, Mar. 2022, doi: 10.1038/s41586-022-04415-8.

[27] P. Ghelfi *et al.*, "Photonics in Radar Systems: RF Integration for State-of-the-Art Functionality," *IEEE Microwave Magazine*, vol. 16, no. 8, pp. 74–83, Sep. 2015, doi: 10.1109/MMM.2015.2441591.

[28] H. Mekawey, M. Elsayed, Y. Ismail, & M. A. Swillam, "Optical Interconnects Finally Seeing the Light in Silicon Photonics: Past the Hype," *Nanomaterials*, vol. 12, no. 3, p. 485, Jan. 2022, doi: 10.3390/nano12030485.

[29] B. Jalali & S. Fathpour, "Silicon Photonics," *Journal of Lightwave Technology*, vol. 24, no. 12, pp. 4600–4615, Dec. 2006, doi: 10.1109/JLT.2006.885782.

[30] A. Rahim, T. Spuesens, R. Baets, & W. Bogaerts, "Open-Access Silicon Photonics: Current Status and Emerging Initiatives," *Proceedings of the IEEE*, vol. 106, no. 12, pp. 2313–2330, Dec. 2018, doi: 10.1109/JPROC.2018.2878686.

[31] V. Stojanović *et al.*, "Monolithic silicon-photonic platforms in state-of-the-art CMOS SOI processes [Invited]," *Optics Express*, vol. 26, no. 10, p. 13106, May 2018, doi: 10.1364/OE.26.013106.

[32] R. Soref, D. Buca, & S.-Q. Yu, "Group IV Photonics: Driving Integrated Optoelectronics," *Optics and Photonics News*, vol. 27, no. 1, p. 32, Jan. 2016, doi: 10.1364/OPN.27.1.000032.

[33] R. A. Soref & J. P. Lorenzo, "Single-crystal silicon: a new material for 1.3 and 1.6 μm integrated-optical components," *Electronics Letters*, vol. 21, no. 21, p. 953, 1985, doi: 10.1049/el:19850673.

[34] S. Shekhar *et al.*, "Roadmapping the next generation of silicon photonics," *Nature Communications*, vol. 15, no. 1, p. 751, Jan. 2024, doi: 10.1038/s41467-024-44750-0.

[35] Y. Su, Y. Zhang, C. Qiu, X. Guo, & L. Sun, "Silicon Photonic Platform for Passive Waveguide Devices: Materials, Fabrication, and Applications," *Advanced Materials Technologies*, vol. 5, no. 8, Aug. 2020, doi: 10.1002/admt.201901153.

[36] N. Margalit, C. Xiang, S. M. Bowers, A. Bjorlin, R. Blum, & J. E. Bowers, "Perspective on the future of silicon photonics and electronics," *Applied Physics Letters*, vol. 118, no. 22, May 2021, doi: 10.1063/5.0050117.

[37] H. Yu *et al.*, "800 Gbps Fully Integrated Silicon Photonics Transmitter for Data Center Applications," in *Optical Fiber Communication Conference (OFC) 2022*, Washington, D.C.: Optica Publishing Group, 2022, p. M2D.7. doi: 10.1364/OFC.2022.M2D.7.

[38] D. Dai & J. E. Bowers, “Silicon-based on-chip multiplexing technologies and devices for Peta-bit optical interconnects,” *Nanophotonics*, vol. 3, no. 4–5, pp. 283–311, Aug. 2014, doi: 10.1515/nanoph-2013-0021.

[39] D. González-Andrade *et al.*, “Spatial and Polarization Division Multiplexing Harnessing On-Chip Optical Beam Forming,” *Laser & Photonics Reviews*, vol. 17, no. 11, Nov. 2023, doi: 10.1002/lpor.202300298.

[40] L.-W. Luo *et al.*, “WDM-compatible mode-division multiplexing on a silicon chip,” *Nature Communications*, vol. 5, no. 1, p. 3069, Jan. 2014, doi: 10.1038/ncomms4069.

[41] A. Mohanty, M. Zhang, A. Dutt, S. Ramelow, P. Nussenzveig, & M. Lipson, “Quantum interference between transverse spatial waveguide modes,” *Nature Communications*, vol. 8, no. 1, p. 14010, Jan. 2017, doi: 10.1038/ncomms14010.

[42] K. R. Mojaver & O. Liboiron-Ladouceur, “On-chip Optical Phase Monitoring in Multi-Transverse-Mode Integrated Silicon-based Optical Processors,” *IEEE Journal of Selected Topics in Quantum Electronics*, pp. 1–8, 2022, doi: 10.1109/JSTQE.2022.3209023.

[43] S. Y. Siew *et al.*, “Review of Silicon Photonics Technology and Platform Development,” *Journal of Lightwave Technology*, vol. 39, no. 13, pp. 4374–4389, Jul. 2021, doi: 10.1109/JLT.2021.3066203.

[44] B. J. Shastri *et al.*, “Photonics for artificial intelligence and neuromorphic computing,” *Nature Photonics*, vol. 15, no. 2, pp. 102–114, Feb. 2021, doi: 10.1038/s41566-020-00754-y.

[45] Z. Wei, Z. Wang, J. Zhang, Q. Li, J. Zhang, & H. Y. Fu, “Evolution of optical wireless communication for B5G/6G,” *Progress in Quantum Electronics*, vol. 83, p. 100398, May 2022, doi: 10.1016/j.pquantelec.2022.100398.

[46] D. Bonneau, J. W. Silverstone, & M. G. Thompson, “Silicon Quantum Photonics,” 2016, pp. 41–82. doi: 10.1007/978-3-642-10503-6_2.

[47] Q. Shi *et al.*, “Progress in wearable electronics/photonics—Moving toward the era of artificial intelligence and internet of things,” *InfoMat*, vol. 2, no. 6, pp. 1131–1162, Nov. 2020, doi: 10.1002/inf2.12122.

[48] D. González-Andrade *et al.*, “Broadband Fourier-transform silicon nitride spectrometer with wide-area multiaperture input,” *Optics Letters*, vol. 46, no. 16, p. 4021, Aug. 2021, doi: 10.1364/OL.438361.

[49] A. L. Washburn & R. C. Bailey, “Photonics-on-a-chip: recent advances in integrated waveguides as enabling detection elements for real-world, lab-on-a-chip biosensing applications,” *The Analyst*, vol. 136, no. 2, pp. 227–236, 2011, doi: 10.1039/C0AN00449A.

[50] H. Kogelnik, “Theory of Dielectric Waveguides,” 1975, pp. 13–81. doi: 10.1007/978-3-662-43208-2_2.

[51] G. Lifante, *Integrated Photonics: Fundamentals*. Wiley, 2003. doi: 10.1002/0470861401.

[52] J. B. Driscoll, X. Liu, S. Yasseri, I. Hsieh, J. I. Dadap, & R. M. Osgood, "Large longitudinal electric fields (E_z) in silicon nanowire waveguides," *Optics Express*, vol. 17, no. 4, p. 2797, Feb. 2009, doi: 10.1364/OE.17.002797.

[53] G. Floquet, "Sur les équations différentielles linéaires à coefficients périodiques," *Annales scientifiques de l'École normale supérieure*, vol. 12, pp. 47–88, 1883, doi: 10.24033/asens.220.

[54] F. Bloch, "Über die Quantenmechanik der Elektronen in Kristallgittern," *Zeitschrift fur Physik*, vol. 52, no. 7–8, pp. 555–600, Jul. 1929, doi: 10.1007/BF01339455.

[55] J. Shibayama, A. Yamahira, T. Mugita, J. Yamauchi, & H. Nakano, "A finite-difference time-domain beam-propagation method for TE- and TM-wave analyses," *Journal of Lightwave Technology*, vol. 21, no. 7, pp. 1709–1715, Jul. 2003, doi: 10.1109/JLT.2003.814392.

[56] J. D. Joannopoulos, S. G. Johnson, J. N. Winn, & R. D. Meade, *Photonic Crystals*. Princeton University Press, 2011. doi: 10.2307/j.ctvcm4gz9.

[57] S. Armaghani, A. Rostami, & H. Mirtagioglu, "Bragg grating based entangled biphoton dispersion management," *Physica Scripta*, vol. 98, no. 10, p. 105112, Oct. 2023, doi: 10.1088/1402-4896/acfb4a.

[58] K. Iga & Y. Kokubun, Eds., *Encyclopedic Handbook of Integrated Optics*, vol. 114. CRC Press, 2005. doi: 10.1201/9781420027815.

[59] C. Pérez-Armenta *et al.*, "Narrowband Bragg filters based on subwavelength grating waveguides for silicon photonic sensing," *Optics Express*, vol. 28, no. 25, p. 37971, Dec. 2020, doi: 10.1364/OE.404364.

[60] M. A. Butt, N. L. Kazanskiy, & S. N. Khonina, "Advances in Waveguide Bragg Grating Structures, Platforms, and Applications: An Up-to-Date Appraisal," *Biosensors*, vol. 12, no. 7, p. 497, Jul. 2022, doi: 10.3390/bios12070497.

[61] D. Pereira-Martín *et al.*, "Complex spectral filters in silicon waveguides based on cladding-modulated Bragg gratings," *Optics Express*, vol. 29, no. 11, p. 15867, May 2021, doi: 10.1364/OE.420696.

[62] F. Van Laere *et al.*, "Compact Focusing Grating Couplers for Silicon-on-Insulator Integrated Circuits," *IEEE Photonics Technology Letters*, vol. 19, no. 23, pp. 1919–1921, Dec. 2007, doi: 10.1109/LPT.2007.908762.

[63] D. Benedikovic *et al.*, "High-efficiency single etch step apodized surface grating coupler using subwavelength structure," *Laser & Photonics Reviews*, vol. 8, no. 6, Nov. 2014, doi: 10.1002/lpor.201400113.

[64] P. Cheben *et al.*, "Recent advances in metamaterial integrated photonics," *Advances in Optics and Photonics*, vol. 15, no. 4, p. 1033, Dec. 2023, doi: 10.1364/AOP.495828.

[65] P. Cheben, R. Halir, J. H. Schmid, H. A. Atwater, & D. R. Smith, "Subwavelength integrated photonics," *Nature*, vol. 560, no. 7720, pp. 565–572, Aug. 2018, doi: 10.1038/s41586-018-0421-7.

[66] P. Wang, "Group velocity of light in uniaxial crystals," *Applied Optics*, vol. 60, no. 7, p. 1987, Mar. 2021, doi: 10.1364/AO.416686.

[67] J. M. Luque-González *et al.*, "A review of silicon subwavelength gratings: building break-through devices with anisotropic metamaterials," *Nanophotonics*, vol. 10, no. 11, pp. 2765–2797, Aug. 2021, doi: 10.1515/nanoph-2021-0110.

[68] P. Yeh, A. Yariv, & C.-S. Hong, "Electromagnetic propagation in periodic stratified media I General theory*," *Journal of the Optical Society of America*, vol. 67, no. 4, p. 423, Apr. 1977, doi: 10.1364/JOSA.67.000423.

[69] S. M. Rytov, "Electromagnetic Properties of a Finely Stratified Medium," 1956.

[70] J. D. Sarmiento-Merenguel *et al.*, "Controlling leakage losses in subwavelength grating silicon metamaterial waveguides," *Optics Letters*, vol. 41, no. 15, p. 3443, Aug. 2016, doi: 10.1364/OL.41.003443.

[71] A. Ortega-Moñux *et al.*, "Disorder effects in subwavelength grating metamaterial waveguides," *Optics Express*, vol. 25, no. 11, p. 12222, May 2017, doi: 10.1364/OE.25.012222.

[72] P. Cheben *et al.*, "Refractive index engineering with subwavelength gratings for efficient microphotonic couplers and planar waveguide multiplexers," *Optics Letters*, vol. 35, no. 15, p. 2526, Aug. 2010, doi: 10.1364/OL.35.002526.

[73] R. Halir *et al.*, "Waveguide sub-wavelength structures: a review of principles and applications," *Laser & Photonics Reviews*, vol. 9, no. 1, pp. 25–49, Jan. 2015, doi: 10.1002/lpor.201400083.

[74] J. Gonzalo Wangüemert-Pérez *et al.*, "Evanescent field waveguide sensing with subwavelength grating structures in silicon-on-insulator," *Optics Letters*, vol. 39, no. 15, p. 4442, Aug. 2014, doi: 10.1364/OL.39.004442.

[75] R. Sumi, N. Das Gupta, & B. K. Das, "Integrated optical Mach-Zehnder interferometer with a sensing arm of sub-wavelength grating waveguide in SOI," in *2017 IEEE SENSORS*, IEEE, Oct. 2017, pp. 1–3. doi: 10.1109/ICSENS.2017.8234125.

[76] M. A. Butt, S. N. Khonina, & N. L. Kazanskiy, "Device performance of standard strip, slot and hybrid plasmonic μ-ring resonator: a comparative study," *Waves in Random and Complex Media*, vol. 31, no. 6, pp. 2397–2406, Nov. 2021, doi: 10.1080/17455030.2020.1744769.

[77] R. Halir *et al.*, "Ultra-broadband nanophotonic beamsplitter using an anisotropic sub-wavelength metamaterial," *Laser & Photonics Reviews*, vol. 10, no. 6, pp. 1039–1046, Nov. 2016, doi: 10.1002/lpor.201600213.

[78] L. B. Soldano & E. C. M. Pennings, "Optical multi-mode interference devices based on self-imaging: principles and applications," *Journal of Lightwave Technology*, vol. 13, no. 4, pp. 615–627, Apr. 1995, doi: 10.1109/50.372474.

[79] Z. Jafari & A. Zarifkar, "Fabrication-friendly subwavelength-structure-assisted waveguide for dispersion engineering," *Applied Optics*, vol. 55, no. 32, p. 9084, Nov. 2016, doi: 10.1364/AO.55.009084.

[80] D. González-Andrade *et al.*, "Ultra-broadband nanophotonic phase shifter based on subwavelength metamaterial waveguides," *Photonics Research*, vol. 8, no. 3, p. 359, Mar. 2020, doi: 10.1364/PRJ.373223.

[81] R. Halir *et al.*, "Colorless directional coupler with dispersion engineered sub-wavelength structure," *Optics Express*, vol. 20, no. 12, p. 13470, Jun. 2012, doi: 10.1364/OE.20.013470.

[82] Q. Zhong *et al.*, "Focusing-curved subwavelength grating couplers for ultra-broadband silicon photonics optical interfaces," *Optics Express*, vol. 22, no. 15, p. 18224, Jul. 2014, doi: 10.1364/OE.22.018224.

[83] P. Jean, A. Gervais, S. LaRochelle, & W. Shi, "Slow Light in Subwavelength Grating Waveguides," *IEEE Journal of Selected Topics in Quantum Electronics*, vol. 26, no. 2, pp. 1–8, Mar. 2020, doi: 10.1109/JSTQE.2019.2933788.

[84] B. Ni & J. Xiao, "Subwavelength-grating-based compact and broadband TE-pass polarizer for slot waveguides on a SOI platform," *Journal of the Optical Society of America B*, vol. 36, no. 8, p. 2126, Aug. 2019, doi: 10.1364/JOSAB.36.002126.

[85] A. Herrero-Bermello, J. M. Luque-Gonzalez, A. V. Velasco, A. Ortega-Monux, P. Cheben, & R. Halir, "Design of a Broadband Polarization Splitter Based on Anisotropy-Engineered Tilted Subwavelength Gratings," *IEEE Photonics Journal*, vol. 11, no. 3, pp. 1–8, Jun. 2019, doi: 10.1109/JPHOT.2019.2912335.

[86] H. Xu, D. Dai, & Y. Shi, "Ultra-Broadband and Ultra-Compact On-Chip Silicon Polarization Beam Splitter by Using Hetero-Anisotropic Metamaterials," *Laser & Photonics Reviews*, vol. 13, no. 4, Apr. 2019, doi: 10.1002/lpor.201800349.

[87] S. Wu & J. Xiao, "Compact polarization rotator for silicon-based cross-slot waveguides using subwavelength gratings," *Applied Optics*, vol. 56, no. 17, p. 4892, Jun. 2017, doi: 10.1364/AO.56.004892.

[88] H. Xu & Y. Shi, "Subwavelength-grating-assisted silicon polarization rotator covering all optical communication bands," *Optics Express*, vol. 27, no. 4, p. 5588, Feb. 2019, doi: 10.1364/OE.27.005588.

[89] J. Chen & J. Xiao, "Ultracompact silicon-based polarization splitter and rotator based on asymmetric directional couplers with subwavelength gratings," *Journal of the Optical Society of America B*, vol. 39, no. 1, p. 345, Jan. 2022, doi: 10.1364/JOSAB.447359.

[90] M. Borhan Mia, N. Jaidye, I. Ahmed, S. Z. Ahmed, & S. kim, "Broadband integrated polarization splitter and rotator using subwavelength grating claddings," *Optics Express*, vol. 31, no. 3, p. 4140, Jan. 2023, doi: 10.1364/OE.479195.

[91] J. M. Luque-González *et al.*, "Tilted subwavelength gratings: controlling anisotropy in metamaterial nanophotonic waveguides," *Optics Letters*, vol. 43, no. 19, p. 4691, Oct. 2018, doi: 10.1364/OL.43.004691.

[92] J. M. Luque-González *et al.*, "Bricked Subwavelength Gratings: A Tailorable On-Chip Metamaterial Topology," *Laser & Photonics Reviews*, vol. 15, no. 6, Jun. 2021, doi: 10.1002/lpor.202000478.

[93] C. Li, M. Zhang, H. Xu, Y. Tan, Y. Shi, & D. Dai, "Subwavelength silicon photonics for on-chip mode-manipulation," *PhotoniX*, vol. 2, no. 1, p. 11, Jul. 2021, doi: 10.1186/s43074-021-00032-2.

[94] S. Bernabé *et al.*, "Silicon photonics for terabit/s communication in data centers and exascale computers," *Solid-State Electronics*, vol. 179, p. 107928, May 2021, doi: 10.1016/j.sse.2020.107928.

[95] L.-T. Feng *et al.*, "On-chip transverse-mode entangled photon pair source," *npj Quantum Information*, vol. 5, no. 1, p. 2, Jan. 2019, doi: 10.1038/s41534-018-0121-z.

[96] E. A. Kittlaus, N. T. Otterstrom, & P. T. Rakich, "On-chip inter-modal Brillouin scattering," *Nature Communications*, vol. 8, no. 1, p. 15819, Jul. 2017, doi: 10.1038/ncomms15819.

[97] X. Xu *et al.*, "Self-calibrating programmable photonic integrated circuits," *Nature Photonics*, vol. 16, no. 8, pp. 595–602, Aug. 2022, doi: 10.1038/s41566-022-01020-z.

[98] L. Liao *et al.*, "High speed silicon Mach-Zehnder modulator," *Optics Express*, vol. 13, no. 8, p. 3129, 2005, doi: 10.1364/OPEX.13.003129.

[99] C. Sun, Y. Yu, M. Ye, G. Chen, & X. Zhang, "An ultra-low crosstalk and broadband two-mode (de)multiplexer based on adiabatic couplers," *Scientific Reports*, vol. 6, no. 1, p. 38494, Dec. 2016, doi: 10.1038/srep38494.

[100] D. Gonzalez-Andrade *et al.*, "Ultra-Broadband Mode Converter and Multiplexer Based on Sub-Wavelength Structures," *IEEE Photonics Journal*, vol. 10, no. 2, pp. 1–10, Apr. 2018, doi: 10.1109/JPHOT.2018.2819364.

[101] S. Tomofuji, S. Matsuo, T. Kakitsuka, & K. Kitayama, "Dynamic switching characteristics of InGaAsP/InP multimode interference optical waveguide switch," *Optics Express*, vol. 17, no. 26, p. 23380, Dec. 2009, doi: 10.1364/OE.17.023380.

[102] Y. Liu & H. Hu, "Silicon optical phased array with a 180-degree field of view for 2D optical beam steering," *Optica*, vol. 9, no. 8, p. 903, Aug. 2022, doi: 10.1364/OPTICA.458642.

[103] A. Rahim *et al.*, "Taking silicon photonics modulators to a higher performance level: state-of-the-art and a review of new technologies," *Advanced Photonics*, vol. 3, no. 02, Apr. 2021, doi: 10.1117/1.AP.3.2.024003.

[104] B. Bai, H. Shu, X. Wang, & W. Zou, "Towards silicon photonic neural networks for artificial intelligence," *Science China Information Sciences*, vol. 63, no. 6, p. 160403, Jun. 2020, doi: 10.1007/s11432-020-2872-3.

[105] C. Pérez-Armenta *et al.*, "Polarization-independent multimode interference coupler with anisotropy-engineered bricked metamaterial," *Photonics Research*, vol. 10, no. 4, p. A57, Apr. 2022, doi: 10.1364/PRJ.446932.

[106] A. Kumar, M. Gupta, P. Pitchappa, N. Wang, M. Fujita, & R. Singh, "Terahertz topological photonic integrated circuits for 6G and beyond: A Perspective," *Journal of Applied Physics*, vol. 132, no. 14, Oct. 2022, doi: 10.1063/5.0099423.

[107] H. F. Talbot, "LXXVI. Facts relating to optical science. No. IV," *The London, Edinburgh, and Dublin Philosophical Magazine and Journal of Science*, vol. 9, no. 56, pp. 401–407, Dec. 1836, doi: 10.1080/14786443608649032.

[108] R. Ulrich & G. Ankele, "Self-imaging in homogeneous planar optical waveguides," *Applied Physics Letters*, vol. 27, no. 6, pp. 337–339, Sep. 1975, doi: 10.1063/1.88467.

[109] A. Maese-Novo *et al.*, "Wavelength independent multimode interference coupler," *Optics Express*, vol. 21, no. 6, p. 7033, Mar. 2013, doi: 10.1364/OE.21.007033.

[110] Ansys, "Multi-Mode Interference (MMI) Coupler." [Online]. Available: https://optics.ansys.com/hc/en-us/articles/360042305194-Multi-Mode-Interference-MMI-Coupler

[111] B. M. A. Rahman, N. Somasiri, C. Themistos, & K. T. V. Grattan, "Design of optical polarization splitters in a single-section deeply etched MMI waveguide," *Applied Physics B*, vol. 73, no. 5–6, pp. 613–618, Oct. 2001, doi: 10.1007/s003400100680.

[112] D. P. Nair & M. Menard, "A Compact Low-Loss Broadband Polarization Independent Silicon 50/50 Splitter," *IEEE Photonics Journal*, vol. 13, no. 4, pp. 1–7, Aug. 2021, doi: 10.1109/JPHOT.2021.3091539.

[113] S. Hassan & D. Chack, "Design and analysis of polarization independent MMI based power splitter for PICs," *Microelectronics Journal*, vol. 104, p. 104887, Oct. 2020, doi: 10.1016/j.mejo.2020.104887.

[114] E. A. J. Marcatili, “Dielectric Rectangular Waveguide and Directional Coupler for Integrated Optics,” *Bell System Technical Journal*, vol. 48, no. 7, pp. 2071–2102, Sep. 1969, doi: 10.1002/j.1538-7305.1969.tb01166.x.

[115] E. A. J. Marcatili, L. L. Buhl, & R. C. Alferness, “Experimental verification of the improved coupled-mode equations,” *Applied Physics Letters*, vol. 49, no. 25, pp. 1692–1693, Dec. 1986, doi: 10.1063/1.97268.

[116] C. Chen, *Foundations for Guided-Wave Optics*. Wiley, 2006. doi: 10.1002/0470042222.

[117] W.-P. Huang, “Coupled-mode theory for optical waveguides: an overview,” *Journal of the Optical Society of America A*, vol. 11, no. 3, p. 963, Mar. 1994, doi: 10.1364/JOSAA.11.000963.

[118] COSMOL, “Wave Optics Module: Directional Coupler.” Accessed: May 03, 2024. [Online]. Available: https://cn.comsol.com/press/gallery/?filter=comsol+multiphysics+version+4.3b

[119] Z. Zhang, X. Hu, & J. Wang, “On-chip optical mode exchange using tapered directional coupler,” *Scientific Reports*, vol. 5, no. 1, p. 16072, Nov. 2015, doi: 10.1038/srep16072.

[120] Y. Ding, J. Xu, F. Da Ros, B. Huang, H. Ou, & C. Peucheret, “On-chip two-mode division multiplexing using tapered directional coupler-based mode multiplexer and demultiplexer,” *Optics Express*, vol. 21, no. 8, p. 10376, Apr. 2013, doi: 10.1364/OE.21.010376.

[121] B. J. Luff, R. Wilson, D. J. Schiffrin, R. D. Harris, & J. S. Wilkinson, “Integrated-optical directional coupler biosensor,” *Optics Letters*, vol. 21, no. 8, p. 618, Apr. 1996, doi: 10.1364/OL.21.000618.

[122] X. Chen, W. Liu, Y. Zhang, & Y. Shi, “Polarization-insensitive broadband 2 × 2 3 dB power splitter based on silicon-bent directional couplers,” *Optics Letters*, vol. 42, no. 19, p. 3738, Oct. 2017, doi: 10.1364/OL.42.003738.

[123] Z. Lu *et al.*, “Broadband silicon photonic directional coupler using asymmetric-waveguide based phase control,” *Optics Express*, vol. 23, no. 3, p. 3795, Feb. 2015, doi: 10.1364/OE.23.003795.

[124] R. K. Gupta, S. Chandran, & B. K. Das, “Wavelength-Independent Directional Couplers for Integrated Silicon Photonics,” *Journal of Lightwave Technology*, vol. 35, no. 22, pp. 4916–4923, Nov. 2017, doi: 10.1109/JLT.2017.2759162.

[125] J. Vilas, R. Fernandez De Cabo, I. Olivares, D. Gonzalez-Andrade, A. V. Velasco, & A. Dias-Ponte, “Low-Loss Directional Coupler for the C, L and U Bands Based on Subwavelength Gratings,” *IEEE Photonics Technology Letters*, vol. 35, no. 24, 2023, doi: 10.1109/LPT.2023.3325660.

[126] C. Ye & D. Dai, “Ultra-Compact Broadband 2 × 2 3 dB Power Splitter Using a Subwavelength-Grating-Assisted Asymmetric Directional Coupler,” *Journal of Lightwave Technology*, vol. 38, no. 8, pp. 2370–2375, Apr. 2020, doi: 10.1109/JLT.2020.2973663.

[127] H. Yun, W. Shi, Y. Wang, L. Chrostowski, & N. A. F. Jaeger, “2×2 adiabatic 3-dB coupler on silicon-on-insulator rib waveguides,” P. Cheben, J. Schmid, C. Boudoux, L. R. Chen, A. Delâge,

S. Janz, R. Kashyap, D. J. Lockwood, H.-P. Loock, and Z. Mi, Eds., Oct. 2013, p. 89150V. doi: 10.1117/12.2037968.

[128] J. Xing *et al.*, "Silicon-on-insulator-based adiabatic splitter with simultaneous tapering of velocity and coupling," *Optics Letters*, vol. 38, no. 13, p. 2221, Jul. 2013, doi: 10.1364/OL.38.002221.

[129] Y. Wang, S. Gao, K. Wang, & E. Skafidas, "Ultra-broadband and low-loss 3 dB optical power splitter based on adiabatic tapered silicon waveguides," *Optics Letters*, vol. 41, no. 9, p. 2053, May 2016, doi: 10.1364/OL.41.002053.

[130] C. Ozcan, M. Mojahedi, & J. Stewart Aitchison, "Short, broadband, and polarization-insensitive adiabatic Y-junction power splitters," *Optics Letters*, vol. 48, no. 18, p. 4901, Sep. 2023, doi: 10.1364/OL.500240.

[131] H. Yun, L. Chrostowski, & N. A. F. Jaeger, "Ultra-broadband 2 × 2 adiabatic 3 dB coupler using subwavelength-grating-assisted silicon-on-insulator strip waveguides," *Optics Letters*, vol. 43, no. 8, p. 1935, Apr. 2018, doi: 10.1364/OL.43.001935.

[132] R. Hu, L. Sun, Z. Zhang, Q. Sun, Y. Pan, & Y. Su, "Ultrabroadband and compact 2 × 2 3-dB coupler based on trapezoidal subwavelength gratings," *Optics Express*, vol. 31, no. 14, p. 23542, Jul. 2023, doi: 10.1364/OE.485816.

[133] J. D. Love & N. Riesen, "Single-, Few-, and Multimode Y-Junctions," *Journal of Lightwave Technology*, vol. 30, no. 3, pp. 304–309, Feb. 2012, doi: 10.1109/JLT.2011.2179976.

[134] Henry W. M. & Love J. D., "Asymmetric multimode Y-junction splitters," *Optical and Quantum Electronics*, vol. 29, pp. 379–392, Mar. 1997, doi: 10.1023/A:1018582912154.

[135] J. B. Driscoll, R. R. Grote, B. Souhan, J. I. Dadap, M. Lu, & R. M. Osgood, "Asymmetric Y junctions in silicon waveguides for on-chip mode-division multiplexing," *Optics Letters*, vol. 38, no. 11, p. 1854, Jun. 2013, doi: 10.1364/OL.38.001854.

[136] K. Shirafuji & S. Kurazono, "Transmission characteristics of optical asymmetric Y junction with a gap region," *Journal of Lightwave Technology*, vol. 9, no. 4, pp. 426–429, Apr. 1991, doi: 10.1109/50.76654.

[137] A. Garcia-Valenzuela, "Large-angle transmission and mode conversion characteristics of symmetric multimode Y-junction couplers," *Optical Engineering*, vol. 33, no. 4, p. 1032, Apr. 1994, doi: 10.1117/12.166932.

[138] W. Burns & A. Milton, "Mode conversion in planar-dielectric separating waveguides," *IEEE Journal of Quantum Electronics*, vol. 11, no. 1, pp. 32–39, Jan. 1975, doi: 10.1109/JQE.1975.1068511.

[139] M. Kuznetsov, "Radiation loss in dielectric waveguide Y-branch structures," *Journal of Lightwave Technology*, vol. 3, no. 3, pp. 674–677, 1985, doi: 10.1109/JLT.1985.1074216.

[140] M. H. Eskiyerly, A. Garcia-Valenzuela, & M. Tabib-Azar, "Mode conversion and large-angle transmission in symmetric multimode Y-junction couplers," M. Tabib-Azar and D. L. Polla, Eds., Mar. 1993, pp. 70–82. doi: 10.1117/12.141231.

[141] Y. Zhang *et al.*, "A compact and low loss Y-junction for submicron silicon waveguide," *Optics Express*, vol. 21, no. 1, p. 1310, Jan. 2013, doi: 10.1364/OE.21.001310.

[142] C. Sun, J. Zhao, Z. Wang, L. Du, & W. Huang, "Broadband and high uniformity Y junction optical beam splitter with multimode tapered branch," *Optik*, vol. 180, pp. 866–872, Feb. 2019, doi: 10.1016/j.ijleo.2018.12.013.

[143] W. Chang *et al.*, "Inverse design and demonstration of an ultracompact broadband dual-mode 3 dB power splitter," *Optics Express*, vol. 26, no. 18, p. 24135, Sep. 2018, doi: 10.1364/OE.26.024135.

[144] D. González-Andrade *et al.*, "Polarization- and wavelength-agnostic nanophotonic beam splitter," *Scientific Reports*, vol. 9, no. 1, p. 3604, Mar. 2019, doi: 10.1038/s41598-019-40497-7.

[145] X. Liu, Y. Zhao, Z. Zhu, H. Liu, & F. Gan, "Particle Swarm Optimized Compact, Low Loss 3-dB Power Splitter Enabled by Silicon Columns in Silicon-on-Insulator," *Photonics*, vol. 10, no. 4, p. 419, Apr. 2023, doi: 10.3390/photonics10040419.

[146] M. Danaie, R. Nasiri Far, & A. Dideban, "Design of a High-Bandwidth Y-Shaped Photonic Crystal Power Splitter for TE Modes," *International Journal of Optics and Photonics*, vol. 12, no. 1, pp. 33–42, Jan. 2018, doi: 10.29252/ijop.12.1.33.

[147] A. Berry, N. Anand, S. Anandan, & P. Krishnan, "High-Performance Eight-Channel Photonic Crystal Ring Resonator–Based Optical Demultiplexer for DWDM Applications," *Plasmonics*, vol. 16, no. 6, pp. 2073–2080, Dec. 2021, doi: 10.1007/s11468-021-01463-0.

[148] L.-T. Feng *et al.*, "On-chip coherent conversion of photonic quantum entanglement between different degrees of freedom," *Nature Communications*, vol. 7, no. 1, p. 11985, Jun. 2016, doi: 10.1038/ncomms11985.

[149] "Recent advances in mode converters for a mode division multiplex transmission system," *Opto-Electronics Review*, Jan. 2024, doi: 10.24425/opelre.2021.135825.

[150] D. Dai *et al.*, "10-Channel Mode (de)multiplexer with Dual Polarizations," *Laser & Photonics Reviews*, vol. 12, no. 1, Jan. 2018, doi: 10.1002/lpor.201700109.

[151] H. Xu, C. Liu, D. Dai, & Y. Shi, "Direct-access mode-division multiplexing switch for scalable on-chip multi-mode networks," *Nanophotonics*, vol. 10, no. 18, pp. 4551–4566, Dec. 2021, doi: 10.1515/nanoph-2021-0441.

[152] D. Dai, Y. Tang, & J. E. Bowers, "Mode conversion in tapered submicron silicon ridge optical waveguides," *Optics Express*, vol. 20, no. 12, p. 13425, Jun. 2012, doi: 10.1364/OE.20.013425.

[153] Ming-Chan Wu, Fu-Chen Hsiao, & Shuo-Yen Tseng, "Adiabatic Mode Conversion in Multimode Waveguides Using Chirped Computer-Generated Planar Holograms," *IEEE Photonics Technology Letters*, vol. 23, no. 12, pp. 807–809, Jun. 2011, doi: 10.1109/LPT.2011.2138127.

[154] H. Qiu *et al.*, "Silicon mode multi/demultiplexer based on multimode grating-assisted couplers," *Optics Express*, vol. 21, no. 15, p. 17904, Jul. 2013, doi: 10.1364/OE.21.017904.

[155] U. D. Dave & M. Lipson, "Efficient Conversion to Very High Order Modes in Silicon Waveguides," in *Conference on Lasers and Electro-Optics*, Washington, D.C.: OSA, 2019, p. SM3J.6. doi: 10.1364/CLEO_SI.2019.SM3J.6.

[156] Y. Huang, G. Xu, & S.-T. Ho, "An Ultracompact Optical Mode Order Converter," *IEEE Photonics Technology Letters*, vol. 18, no. 21, pp. 2281–2283, Nov. 2006, doi: 10.1109/LPT.2006.884886.

[157] B. B. Oner, K. Üstün, H. Kurt, A. K. Okyay, & G. Turhan-Sayan, "Large bandwidth mode order converter by differential waveguides," *Optics Express*, vol. 23, no. 3, p. 3186, Feb. 2015, doi: 10.1364/OE.23.003186.

[158] M. Turduev, B. B. Oner, I. H. Giden, & H. Kurt, "Mode transformation using graded photonic crystals with axial asymmetry," *Journal of the Optical Society of America B*, vol. 30, no. 6, p. 1569, Jun. 2013, doi: 10.1364/JOSAB.30.001569.

[159] J. B. Driscoll *et al.*, "A 60 Gb/s MDM-WDM Si photonic link with < 07 dB power penalty per channel," *Optics Express*, vol. 22, no. 15, p. 18543, Jul. 2014, doi: 10.1364/OE.22.018543.

[160] J. Leuthold, J. Eckner, E. Gamper, P. A. Besse, & H. Melchior, "Multimode interference couplers for the conversion and combining of zero- and first-order modes," *Journal of Lightwave Technology*, vol. 16, no. 7, pp. 1228–1239, Jul. 1998, doi: 10.1109/50.701401.

[161] V. Liu, D. A. B. Miller, & S. Fan, "Ultra-compact photonic crystal waveguide spatial mode converter and its connection to the optical diode effect," *Optics Express*, vol. 20, no. 27, p. 28388, Dec. 2012, doi: 10.1364/OE.20.028388.

[162] J. Lu & J. Vučković, "Objective-first design of high-efficiency, small-footprint couplers between arbitrary nanophotonic waveguide modes," *Optics Express*, vol. 20, no. 7, p. 7221, Mar. 2012, doi: 10.1364/OE.20.007221.

[163] D. Ohana & U. Levy, "Mode conversion based on dielectric metamaterial in silicon," *Optics Express*, vol. 22, no. 22, p. 27617, Nov. 2014, doi: 10.1364/OE.22.027617.

[164] J. Guo *et al.*, "Ultra-Compact and Ultra-Broadband Guided-Mode Exchangers on Silicon," *Laser & Photonics Reviews*, vol. 14, no. 7, Jul. 2020, doi: 10.1002/lpor.202000058.

[165] H. Wang, Y. Zhang, Y. He, Q. Zhu, L. Sun, & Y. Su, "Compact Silicon Waveguide Mode Converter Employing Dielectric Metasurface Structure," *Advanced Optical Materials*, vol. 7, no. 4, Feb. 2019, doi: 10.1002/adom.201801191.

[166] R. Halir *et al.*, "Subwavelength-Grating Metamaterial Structures for Silicon Photonic Devices," *Proceedings of the IEEE*, vol. 106, no. 12, pp. 2144–2157, Dec. 2018, doi: 10.1109/JPROC.2018.2851614.

[167] J. Huang *et al.*, "Digital nanophotonics: the highway to the integration of subwavelength-scale photonics," *Nanophotonics*, vol. 10, no. 3, pp. 1011–1030, Jan. 2021, doi: 10.1515/nanoph-2020-0494.

[168] H. Zhou *et al.*, "Dielectric Metasurfaces Enabled Ultradensely Integrated Multidimensional Optical System," *Laser & Photonics Reviews*, vol. 16, no. 4, Apr. 2022, doi: 10.1002/lpor.202100521.

[169] L. Sanchis, A. Håkansson, D. López-Zanón, J. Bravo-Abad, & J. Sánchez-Dehesa, "Integrated optical devices design by genetic algorithm," *Applied Physics Letters*, vol. 84, no. 22, pp. 4460–4462, May 2004, doi: 10.1063/1.1738931.

[170] C. M. Lalau-Keraly, S. Bhargava, O. D. Miller, & E. Yablonovitch, "Adjoint shape optimization applied to electromagnetic design," *Optics Express*, vol. 21, no. 18, p. 21693, Sep. 2013, doi: 10.1364/OE.21.021693.

[171] J. C. Meza, "Steepest descent," *WIREs Computational Statistics*, vol. 2, no. 6, pp. 719–722, Nov. 2010, doi: 10.1002/wics.117.

[172] M. P. Bendsøe & O. Sigmund, "Extensions and applications," in *Topology Optimization*, Berlin, Heidelberg: Springer Berlin Heidelberg, 2004, pp. 71–158. doi: 10.1007/978-3-662-05086-6_2.

[173] J. Lu & J. Vučković, "Nanophotonic computational design," *Optics Express*, vol. 21, no. 11, p. 13351, Jun. 2013, doi: 10.1364/OE.21.013351.

[174] D. Melati *et al.*, "Mapping the global design space of nanophotonic components using machine learning pattern recognition," *Nature Communications*, vol. 10, no. 1, p. 4775, Oct. 2019, doi: 10.1038/s41467-019-12698-1.

[175] Z. Wang *et al.*, "93-THz ultra-broadband and ultra-low loss Y-junction photonic power splitter with phased inverse design," *Optics Express*, vol. 31, no. 10, p. 15904, May 2023, doi: 10.1364/OE.489550.

[176] Y. Chen & J. Xiao, "Ultracompact and broadband silicon-based polarization-independent 1 × 2 power splitter using a shallowly etched multimode interference coupler," *Journal of the Optical Society of America B*, vol. 38, no. 10, p. 3064, Oct. 2021, doi: 10.1364/JOSAB.428649.

[177] X. Li, H. Xu, X. Xiao, Z. Li, J. Yu, & Y. Yu, "Compact and low-loss silicon power splitter based on inverse tapers," *Optics Letters*, vol. 38, no. 20, p. 4220, Oct. 2013, doi: 10.1364/OL.38.004220.

[178] L. Han, B. P.-P. Kuo, N. Alic, & S. Radic, "Ultra-broadband multimode 3dB optical power splitter using an adiabatic coupler and a Y-branch," *Optics Express*, vol. 26, no. 11, p. 14800, May 2018, doi: 10.1364/OE.26.014800.

[179] D. Yang, H. Tian, & Y. Ji, "High-bandwidth and low-loss photonic crystal power-splitter with parallel output based on the integration of Y-junction and waveguide bends," *Optics Communications*, vol. 285, no. 18, pp. 3752–3757, Aug. 2012, doi: 10.1016/j.optcom.2012.05.022.

[180] Z. Weissman, E. Marom, & A. Hardy, "Very low-loss Y-junction power divider," *Optics Letters*, vol. 14, no. 5, p. 293, Mar. 1989, doi: 10.1364/OL.14.000293.

[181] H. Sasaki & I. Anderson, "Theoretical and experimental studies on active Y-junctions in optical waveguides," *IEEE Journal of Quantum Electronics*, vol. 14, no. 11, pp. 883–892, Nov. 1978, doi: 10.1109/JQE.1978.1069695.

[182] S. Serecunova, D. Seyringer, F. Uherek, & H. Seyringer, "Design and optimization of optical power splitters for optical access networks," *Optical and Quantum Electronics*, vol. 54, no. 6, p. 365, Jun. 2022, doi: 10.1007/s11082-022-03620-z.

[183] N. Yang & J. Xiao, "A compact silicon-based polarization-independent power splitter using a three-guide directional coupler with subwavelength gratings," *Optics Communications*, vol. 459, p. 125095, Mar. 2020, doi: 10.1016/j.optcom.2019.125095.

[184] M. Lu *et al.*, "Ultra-compact TE-mode-pass power splitter based on subwavelength gratings and hybrid plasmonic waveguides on SOI platform," *Optics Communications*, vol. 498, p. 127250, Nov. 2021, doi: 10.1016/j.optcom.2021.127250.

[185] L. Xu *et al.*, "Compact high-performance adiabatic 3-dB coupler enabled by subwavelength grating slot in the silicon-on-insulator platform," *Optics Express*, vol. 26, no. 23, p. 29873, Nov. 2018, doi: 10.1364/OE.26.029873.

[186] L. Lu, D. Liu, M. Yan, & M. Zhang, "Subwavelength adiabatic multimode Y-junctions," *Optics Letters*, vol. 44, no. 19, p. 4729, Oct. 2019, doi: 10.1364/OL.44.004729.

[187] R. Fernández de Cabo, D. González-Andrade, P. Cheben, & A. V. Velasco, "High-Performance On-Chip Silicon Beamsplitter Based on Subwavelength Metamaterials for Enhanced Fabrication Tolerance," *Nanomaterials*, vol. 11, no. 5, p. 1304, May 2021, doi: 10.3390/nano11051304.

[188] R. Fernández de Cabo, J. Vilas, P. Cheben, A. V. Velasco, & D. González-Andrade, "Experimental characterization of an ultra-broadband dual-mode symmetric Y–junction based on metamaterial waveguides," *Optics & Laser Technology*, vol. 157, p. 108742, Jan. 2023, doi: 10.1016/j.optlastec.2022.108742.

[189] O. Karker, R. Bange, E. Bano, & V. Stambouli, “Optimizing interferences of DUV lithography on SOI substrates for the rapid fabrication of sub-wavelength features,” *Nanotechnology*, vol. 32, no. 23, p. 235301, Jun. 2021, doi: 10.1088/1361-6528/abe3b6.

[190] T. Ito & S. Okazaki, “Pushing the limits of lithography,” *Nature*, vol. 406, no. 6799, pp. 1027–1031, Aug. 2000, doi: 10.1038/35023233.

[191] Applied Nanotools Inc., “NanoSOI Fabrication Service.” Accessed: May 03, 2024. [Online]. Available: https://www.appliednt.com/nanosoi-fabrication-service/

[192] Lumerical, “Lumerical 3D FDTD solver.” Accessed: May 03, 2024. [Online]. Available: https://www.ansys.com/products/optics/fdtd

[193] J. H. Schmid *et al.*, “Refractive Index Engineering With Subwavelength Gratings in Silicon Microphotonic Waveguides,” *IEEE Photonics Journal*, vol. 3, no. 3, pp. 597–607, Jun. 2011, doi: 10.1109/JPHOT.2011.2139198.

[194] W. Chen *et al.*, “Broadband multimode 3 dB optical power splitter using tapered couplers,” *Optics Express*, vol. 30, no. 26, p. 46236, Dec. 2022, doi: 10.1364/OE.471397.

[195] H. Shiran, G. zhang, & O. Liboiron-Ladouceur, “Dual-mode broadband compact 2 × 2 optical power splitter using sub-wavelength metamaterial structures,” *Optics Express*, vol. 29, no. 15, p. 23864, Jul. 2021, doi: 10.1364/OE.423882.

[196] Z. Weissman, A. Hardy, & E. Marom, “Mode-Dependent Radiation Loss in Y-Junctions and Directional Couplers,” in *The Sixteenth Conference of Electrical and Electronics Engineers in Israel*, IEEE, pp. 1–4. doi: 10.1109/EEIS.1989.720183.

[197] R. Baets & P. E. Lagasse, “Calculation of radiation loss in integrated-optic tapers and Y-junctions,” *Applied Optics*, vol. 21, no. 11, p. 1972, Jun. 1982, doi: 10.1364/AO.21.001972.

[198] P. Cheben, D.-X. Xu, S. Janz, & A. Densmore, “Subwavelength waveguide grating for mode conversion and light coupling in integrated optics,” *Optics Express*, vol. 14, no. 11, p. 4695, 2006, doi: 10.1364/OE.14.004695.

[199] Y. Zhou, C. Yin, W. Liu, E. Xing, J. Tang, & J. Liu, “Design of an ultra-broadband and low-loss 3 dB power splitter from the 1.25 to 2.04 μm wave band,” *Applied Optics*, vol. 61, no. 32, p. 9449, Nov. 2022, doi: 10.1364/AO.470157.

[200] A. Zhang *et al.*, “Ultra-compact polarization-independent 3 dB power splitter in silicon,” *Optics Letters*, vol. 46, no. 19, p. 5000, Oct. 2021, doi: 10.1364/OL.439320.

[201] J. Xu, Y. Liu, X. Guo, Q. Song, & K. Xu, “Inverse design of a dual-mode 3-dB optical power splitter with a 445 nm bandwidth,” *Optics Express*, vol. 30, no. 15, p. 26266, Jul. 2022, doi: 10.1364/OE.463274.

[202] P. J. Winzer, D. T. Neilson, & A. R. Chraplyvy, “Fiber-optic transmission and networking: the previous 20 and the next 20 years [Invited],” *Optics Express*, vol. 26, no. 18, p. 24190, Sep. 2018, doi: 10.1364/OE.26.024190.

[203] J. Wang, S. He, & D. Dai, "On-chip silicon 8-channel hybrid (de)multiplexer enabling simultaneous mode- and polarization-division-multiplexing," *Laser & Photonics Reviews*, vol. 8, no. 2, Mar. 2014, doi: 10.1002/lpor.201300157.

[204] J. Wang & Y. Long, "On-chip silicon photonic signaling and processing: a review," *Science Bulletin*, vol. 63, no. 19, pp. 1267–1310, Oct. 2018, doi: 10.1016/j.scib.2018.05.038.

[205] B.-T. Lee & S.-Y. Shin, "Mode-order converter in a multimode waveguide," *Optics Letters*, vol. 28, no. 18, p. 1660, Sep. 2003, doi: 10.1364/OL.28.001660.

[206] D. Chen, X. Xiao, L. Wang, Y. Yu, W. Liu, & Q. Yang, "Low-loss and fabrication tolerant silicon mode-order converters based on novel compact tapers," *Optics Express*, vol. 23, no. 9, p. 11152, May 2015, doi: 10.1364/OE.23.011152.

[207] Z. Guo, J. Xiao, & S. Wu, "Experimental demonstration of a flexible and high-performance mode-order converter using subwavelength grating metamaterials," *Optics Express*, vol. 31, no. 6, p. 10744, Mar. 2023, doi: 10.1364/oe.484384.

[208] Z. Li *et al.*, "Controlling propagation and coupling of waveguide modes using phase-gradient metasurfaces," *Nature Nanotechnology*, vol. 12, no. 7, pp. 675–683, Jul. 2017, doi: 10.1038/nnano.2017.50.

[209] D. Ohana, B. Desiatov, N. Mazurski, & U. Levy, "Dielectric Metasurface as a Platform for Spatial Mode Conversion in Nanoscale Waveguides," *Nano Letters*, vol. 16, no. 12, pp. 7956–7961, Dec. 2016, doi: 10.1021/acs.nanolett.6b04264.

[210] M. J. D. Powell, "An efficient method for finding the minimum of a function of several variables without calculating derivatives," *The Computer Journal*, vol. 7, no. 2, pp. 155–162, Feb. 1964, doi: 10.1093/comjnl/7.2.155.

[211] Centre for Nanoscience and Nanotechnology (C2N), "C2N Technological Facilities." Accessed: May 03, 2024. [Online]. Available: https://www.c2n.universite-paris-saclay.fr/en/platforms/technology-facility/

[212] Y. Zhao *et al.*, "Ultra-compact silicon mode-order converters based on dielectric slots," *Optics Letters*, vol. 45, no. 13, p. 3797, Jul. 2020, doi: 10.1364/ol.391748.

[213] B. E. Abu-elmaaty, M. S. Sayed, R. K. Pokharel, & H. M. H. Shalaby, "General silicon-on-insulator higher-order mode converter based on substrip dielectric waveguides," *Applied Optics*, vol. 58, no. 7, p. 1763, Mar. 2019, doi: 10.1364/AO.58.001763.

[214] L. Hao *et al.*, "Efficient TE-Polarized Mode-Order Converter Based on High-Index-Contrast Polygonal Slot in a Silicon-on-Insulator Waveguide," *IEEE Photonics Journal*, vol. 11, no. 2, pp. 1–10, Apr. 2019, doi: 10.1109/JPHOT.2019.2907640.

[215] Z. Cheng *et al.*, "Sub-wavelength grating assisted mode order converter on the SOI substrate," *Optics Express*, vol. 27, no. 23, p. 34434, Nov. 2019, doi: 10.1364/OE.27.034434.

[216] Z. Chen, T. Lin, X. Liu, & H. Lv, "Ultra-Compact Broadband In-Line Mode Converter Based on a Width-Modulated Silicon Waveguide," *IEEE Photonics Journal*, vol. 13, no. 2, pp. 1–7, Apr. 2021, doi: 10.1109/JPHOT.2021.3066198.

[217] R. Xiao *et al.*, "On-chip mode converter based on two cascaded Bragg gratings," *Optics Express*, vol. 27, no. 3, p. 1941, Feb. 2019, doi: 10.1364/OE.27.001941.

[218] R. Fernández de Cabo, D. González-Andrade, P. Cheben, & A. V. Velasco, "Extending the spectral operation of silicon power splitters through subwavelength nanotechnology," *arXiv*. 2024. doi: 10.48550/arXiv.2403.15781.

[219] E. Sharma *et al.*, "Evolution in Lithography Techniques: Microlithography to Nanolithography," *Nanomaterials*, vol. 12, no. 16, p. 2754, Aug. 2022, doi: 10.3390/nano12162754.

[220] M. Eissa, T. Mitarai, T. Amemiya, Y. Miyamoto, & N. Nishiyama, "Fabrication of Si photonic waveguides by electron beam lithography using improved proximity effect correction," *Japanese Journal of Applied Physics*, vol. 59, no. 12, p. 126502, Dec. 2020, doi: 10.35848/1347-4065/abc78d.

[221] Y. Huang, Q. Zhao, L. Kamyab, A. Rostami, F. Capolino, & O. Boyraz, "Sub-micron silicon nitride waveguide fabrication using conventional optical lithography," *Optics Express*, vol. 23, no. 5, p. 6780, Mar. 2015, doi: 10.1364/OE.23.006780.